ISBN 978-82-326-3762-1 (printed ver.)
ISBN 978-82-326-3763-8 (electronic ver.)
ISSN 1503-8181

NTNU
Norwegian University of
Science and Technology

Daniel Wehner

Doctoral thesis

Doctoral theses at NTNU, 2019:80

NTNU
Norwegian University of Science and Technology
Thesis for the Degree of
Philosophiae Doctor
Faculty of Engineering
Department of Geoscience and Petroleum

NTNU

Doctoral theses at NTNU, 2019:80

Daniel Wehner

Experimental Studies of the Acoustic Signal generated by Marine Seismic Sources

NTNU
Norwegian University of
Science and Technology

Daniel Wehner

Experimental Studies of the Acoustic Signal generated by Marine Seismic Sources

Thesis for the Degree of Philosophiae Doctor

Trondheim, March 2019

Norwegian University of Science and Technology
Faculty of Engineering
Department of Geoscience and Petroleum

NTNU
Norwegian University of
Science and Technology

NTNU
Norwegian University of Science and Technology

Thesis for the Degree of Philosophiae Doctor

Faculty of Engineering
Department of Geoscience and Petroleum

ISBN 978-82-326-3762-1 (printed ver.)
ISBN 978-82-326-3763-8 (electronic ver.)
ISSN 1503-8181

Doctoral theses at NTNU, 2019:80

Printed by NTNU Grafisk senter

Abstract

Marine seismic acquisition is the most commonly used geophysical technique to image the subsurface for different purposes, e.g. exploration of reservoirs or investigation of subduction zones as areas where earthquakes are generated. The acquisition consists of a sound source emitting the signal into the subsurface and dedicated sensors which receive the reflected signals from the subsurface structures of interest. The most common sound source used in marine seismics over the last 50 years is the airgun. The airgun is a mechanical device releasing high pressurized air from a chamber into the surrounding water within a few milliseconds. The acoustic source signal consists of a sharp peak when the pressurized air is released followed by an oscillation corresponding to the expanding and contracting air bubble in water. The main advantages of the airgun are its signal repeatability and long lifetime. However, the emitted frequency bandwidth is limited by the oscillation period and the destructive interference of the direct downgoing wavefield with the first reflection from the sea surface, referred to as the ghost. In recent years there has been increasing interest in improving two major aspects of the sound source in marine seismic acquisition. The first aspect is the enhancement of emitted low frequency signals ($<$ 5 Hz) which are beneficial for imaging of deep targets, especially below salt or basalt structures which scatter and reflect most of the higher frequencies. In addition, low frequencies are beneficial for velocity model building in full waveform inversion. The second aspect is the reduction of high frequencies ($>$ 100-200 Hz) which can have an impact on marine life, e.g. masking communication or behavioural disturbances. Therefore, alternative source types, e.g. marine vibrators, are developed and investigations are conducted on how to tune the signal emitted by airguns.

The thesis consists of several, individual manuscripts where the acoustic signal generated by single marine seismic sources, especially from airguns, is experimentally investigated. Several experiments are conducted to study the mechanisms that have an impact on the low frequency content of the emitted sound signal. First, the signal generated by the rising airgun bubble is investigated separately from the main peak and oscillating bubble by dedicated experiments with rising buoys and the results are compared to measured airgun signatures. Secondly, the impact of the spherical wave front on the ghost reflection is studied for different source-interface distances in a tank experiment. Third, the impact of the interaction between the airgun bubble and sea surface on the source signature is investigated for very shallow source depths and the variations of the oscillating bubble and ghost reflection are discussed. In addition, the signal emitted into air is analyzed for these shallow seismic sources. Another study deals with the reduction of high frequency emission from seismic airguns. The impact of bubble curtains surrounding an airgun on the source signature and high frequency emission are investigated for different bubble curtain configurations.

The results from the rising airgun bubble indicate a low frequency signal emitted by this movement. However, the signal strength is low and seems to have no significant impact in marine seismic acquisition. The results for the spherical wave front indicate that the low frequency signal ($<$ 1-2 Hz) could be enhanced with decreasing source depth. However, the noise level at this frequency band is usually strong and it needs to be further investigated how large the impact could be in field applications. The results from the source-interface interaction indicate that the low frequency signal ($<$ 5 Hz) is strongly enhanced when the airgun bubble bursts directly at the water surface and no oscillations occur. This effect seems to be promising to enhance the low frequency signal in field applications. The results from the bubble curtain surrounding the airgun indicate a gradually decreasing frequency content above 50 Hz with increasing air injection into the bubble curtain. Hence, bubble curtains could potentially be considered to reduce high frequency emissions from airguns.

Preface

This thesis is submitted to the Norwegian University of Science and Technology (NTNU) for partial fulfillment of the requirements for the degree of philosophiae doctor.

This doctoral work has been performed at the Department of Geoscience and Petroleum, NTNU, Trondheim, with Professor Martin Landrø as supervisor.

The research was funded by the European Union's Horizon 2020 research and innovation programme under the Marie Skłodowska-Curie grant agreement No 641943 within the project WAVES.

Acknowledgements

My particular gratitude goes to my supervisor Prof. Martin Landrø for his great guidance and for simply being a good person. He was always available for discussions, hinting the way when needed while supporting the freedom to develop my own ideas. His enthusiasm about science is catching and a huge motivation.

I am grateful for the support of the technical staff at the IGP department who built equipment for my experiments or fixed stuff that I broke. A big thanks to Noralf, Steffen, Terje, Håkon and Tim Cato (at IES). I am also thankful for the support of the administration at IGP who helped with all non-technical issues.

I am thankful for being a part of the WAVES project where I met and learnt from super smart people and got introduced into a broad spectrum of research, from medical imaging to infrasound in the atmosphere.

I am grateful to a number of people that contributed to my research, assisted me during my PhD or were involved in other experiments where I learnt a lot about different topics, e.g. ultrasound and marine mammals. Thanks to Børge Arntsen, Lasse Amundsen, Harald Westerdahl, Nathalie Favretto-Cristini, Peter Svensson and Marianne Rasmussen.

I like to thank Anton Ziolkowski, Jan Langhammer and Rune M. Holt for serving on the thesis committee.

I enjoyed the work environment at the department and the scientific discussions with the people from IGP. Thanks to Anna, Babak, Benjamin, Filipe, Gilberto, Hamid, Ivan, Izzie, Kjetil, Marcin, Stian, Vegard, Yuriy, ... to name a few.

I am thankful for the support from my parents which made my way into science easily possible.

Table of Contents

Abstract **i**

Preface **iii**

Acknowledgements **v**

Table of Contents **ix**

List of Tables **xi**

List of Figures **xxi**

1 Introduction **1**
- 1.1 Marine Seismic Acquisition . . . 3
- 1.2 Marine Seismic Sources . . . 4
  - 1.2.1 The Source Ghost . . . 5
  - 1.2.2 The Airgun . . . 7
  - 1.2.3 Alternative Sources . . . 13
- 1.3 Marine Seismic Receiver . . . 14
  - 1.3.1 Seismic Streamer . . . 14
  - 1.3.2 Ocean Bottom Surveys (OBS) . . . 16
- 1.4 Noise Sources and Environmental Impact . . . 17
  - 1.4.1 Noise in Seismic Acquisition . . . 17
  - 1.4.2 Marine Seismic Survey Impact on the Environment . . . 19
- 1.5 Contributions . . . 20
- 1.6 Experimental data availability . . . 22

2 Low-frequency acoustic signal created by rising air-gun bubble **23**
- 2.1 Abstract . . . 23
- 2.2 Introduction . . . 24
- 2.3 Theory . . . 25

2.4 Modeling . . . 28
2.5 Experiments . . . 29
  2.5.1 Buoy experiment in the tank . . . 30
  2.5.2 Buoy experiment in the field . . . 31
  2.5.3 Airgun experiment in the field . . . 32
2.6 Results . . . 33
  2.6.1 Buoy in the tank . . . 33
  2.6.2 Buoy in the field . . . 35
  2.6.3 Airgun in the field . . . 37
2.7 Discussion . . . 38
2.8 Conclusions . . . 42
2.9 Acknowledgements . . . 42

3 Frequency-depth dependent spherical reflection response from the sea surface - A transmission experiment 43
3.1 Abstract . . . 43
3.2 Introduction . . . 44
3.3 Theory . . . 46
3.4 Experiments . . . 48
  3.4.1 Experiment A: Source in Water . . . 49
  3.4.2 Experiment B: Source in Air . . . 50
  3.4.3 Source Signature and Repeatability . . . 51
3.5 Modeling . . . 55
3.6 Results . . . 56
  3.6.1 Experiment A: Source in Water . . . 57
  3.6.2 Experiment B: Source in Air . . . 59
3.7 Discussion . . . 59
3.8 Conclusion . . . 65
3.9 Acknowledgements . . . 65

4 The Impact on Low Frequencies from Very Shallow Air Guns in Marine Seismic Acquisition - An Experimental Study 67
4.1 Abstract . . . 67
4.2 Introduction . . . 68
4.3 Theory . . . 70
4.4 Experiments . . . 73
  4.4.1 Water tank experiments . . . 73
  4.4.2 Field experiments . . . 75
4.5 Results . . . 75
  4.5.1 Water tank measurements . . . 76
  4.5.2 Field measurements . . . 78
  4.5.3 Energy vs. Depth . . . 80
4.6 Discussion . . . 81
4.7 Conclusion . . . 86
4.8 Acknowledgements . . . 87

5 The Coupling of Marine Seismic Source Signals into Air 89
5.1 Abstract . . . 89
5.2 Introduction . . . 90
5.3 Theory . . . 91
5.4 Experiments . . . 92
5.5 Results . . . 94
5.6 Discussion . . . 100
5.7 Conclusion . . . 106
5.8 Acknowledgements . . . 106

6 The Impact of Bubble Curtains on Seismic Air Gun Signatures and its High Frequency Emission 107
6.1 Abstract . . . 107
6.2 Introduction . . . 108
6.3 Theory . . . 109
6.4 Experiments . . . 113
6.5 Results . . . 115
  6.5.1 Acoustic Signal . . . 115
  6.5.2 Bubble Curtain . . . 122
6.6 Discussion . . . 124
6.7 Conclusion . . . 127
6.8 Acknowledgements . . . 128

7 Concluding remarks 129

A Tube wave monitoring - detect shear modulus and S-wave velocity changes in the formations surrounding wells 135
A.1 Abstract . . . 135
A.2 Introduction . . . 136
A.3 Theory . . . 138
  A.3.1 Relation between tube wave and shear modulus . . . 138
  A.3.2 Shear modulus change due to CO_2 injection . . . 141
A.4 Experiments . . . 142
A.5 Results . . . 144
  A.5.1 Recorded Waves in Boreholes . . . 145
  A.5.2 Tube Wave and S-Wave Velocity/Shear Modulus Estimation . . . 149
A.6 Mechanisms changing the Shear Modulus . . . 154
  A.6.1 CO_2 injection . . . 154
  A.6.2 Engineering Applications . . . 157
A.7 Discussion . . . 157
  A.7.1 Sensitivity analysis of borehole parameter . . . 157
  A.7.2 Field scenario example . . . 160
A.8 Conclusions . . . 162
A.9 Acknowledgments . . . 162

Bibliography 163

List of Tables

2.1 Essential parameters of the three buoys used for the experiments. 30
2.2 Amplitude of main impulse, $A(f_1)$, and rising bubble signal, $A(f_2)$, after travelling through 3D medium with common medium parameters (v_m, Q) for a sandstone (Mavko et al., 1998). 39
2.3 Near-field amplitude of signal from rising bubble for source depth of z_s = 7.5 m. Measured single air gun amplitude for $R \leq 1$ m and computed amplitude for bigger bubble radii $R > 1$ m using the proposed model. . . 41
2.4 Computed far-field amplitudes (in bar) for the low frequency signal from a rising air gun bubble after travelling through a 3 km thick 3D medium with velocity v_m and quality factor Q. The amplitude is given for different source depths z_s and radii R of the bubble. 41

A.1 Important parameters of the shallow well 1 and deep well 2. 143

List of Figures

1.1 Simple sketch of a common marine seismic acquisition set up in 2D. Possible wave path for signals reflected from geological structures in the subsurface are illustrated. 4

1.2 (a) Sketch illustrating parameters used for the computation of reflection coefficient R_c and geometry for source and receiver position. The dashed arrow indicates the additional travel paths r_g for the ghost signal. (b) Ghost spectrum $|G(\omega)|$ for different incident angles θ_1 6

1.3 Top: Reflected spike function from the sea surface for two different source depths z_s, assuming R_c = -0.9994. Bottom: Corresponding frequency spectra, that can also be described by the ghost function (Equation 1.9). . 7

1.4 Simple sketch of an airgun and photos from a 1.6 in^3 gun fired in a water tank at different times as indicated (illustrations from Langhammer (1994)). 8

1.5 Top: Acoustic signature generated by a single 200 in^3 airgun fired at different depths z_s. Modelled at 1000 m distance from the source and corrected for geometrical spreading with $1/r$, without the impact from the ghost. Bottom: Corresponding frequency spectra. 9

1.6 Top: Acoustic signature generated by a single 200 in^3 airgun fired at different depths z_s (as in Figure 1.5). Modelled at 1000 m distance from the source and corrected for geometrical spreading with $1/r$, with the ghost and R_c = -0.9994. Bottom: Corresponding frequency spectra. 10

1.7 Common geometry of a seismic source array consisting of 3 sub-arrays, indicated by its source depths z_{s1}, z_{s2} and z_{s3} (Landrø et al., 2013). A single gun is shown as a circle and its volume is given in in^3. Sub-array 3 (bottom) has the same source volume as sub-array 1. Photos show a random single sub-array (*courtesy of PGS*) and a full source, consisting of two source arrays with 3 sub-arrays each, towed behind a vessel (*courtesy of the International Association of Geophysical Contractors. Used with permission*). 11

1.8 Top: Acoustic signature generated by the source array shown in Figure 1.7 for different depths of the sub-arrays. Modelled at 1000 m distance from the source and corrected for geometrical spreading with $1/r$, with the ghost and R_c = -0.9994. Bottom: Corresponding frequency spectra. . . . 12

1.9 Common seismic streamer set up for 3D seismic acquisition. For 2D acquisition only one streamer is towed behind the vessel (Figure 1.1). 15

1.10 Noise recorded along the traces of a 3000 m long streamer towed at 9-12 m depth with a sample rate of 2 ms for two different weather conditions. Data is shown without a low-cut filter (solid line) and with a 5.3 Hz low-cut filter applied (dashed line) (data reproduced from Landrø et al. (1989)). 18

1.11 Ship traffic noise along the traces of a 3000 m long streamer towed at 9-12 m depth with a sample rate of 2 ms for two different ships passing by at different distances with approximate average distance indicated. The shot noise is recorded for a time window of 10-14 s after the shot was fired. The data is filtered with a 5.3 Hz low-cut filter (data reproduced from Landrø et al. (1989)). 19

2.1 Empirical relation between drag coefficient and Reynolds number from experimental data (Morrison, 2013). The area between dashed lines indicates expected Reynolds numbers for our experiments. 27

2.2 (a) Pressure distribution around sphere at laminar flow (Michelson, 1970) and (b) modified pressure distribution for turbulent flow according to results of Achenbach (1972). The flow direction is vertical, pointing in negative z-direction. (c) Experimental data from (Achenbach, 1972) for a turbulent flow around a fixed sphere. All amplitudes are normalized to the maximum positive pressure value. 28

2.3 Cross-section of setup for buoy experiments in the tank. The depth and width of the tank are indicated and the length is 3.00 m to each side of the buoy. H1, H2, H3 and H4 denote the hydrophones, z_s the release depth of the buoy and x the offset between source and receiver. 30

2.4 Cross-section of setup for buoy experiments in the field. H1 and H2 denote the hydrophones, z_s the release depth of the buoy and x the offset between source and receiver. 31

2.5 Cross-section of setup for air gun experiments in the field. The gun is fired at four different depth z_s (3 m, 5 m, 7.5 m, 10 m) and the vertical offset z_r is constant. 32

2.6 Modeled (solid line) vs. video measured (crosses) depth position of buoy B in the tank during rising (top) and modeled (solid) vs. video measured (crosses) velocity of buoy B in the tank during rising (bottom). 33

2.7 (a) Measured (top) and modeled signal (bottom) for the rising buoy A from a depth of z_s = 0.50 m. (b) Measured (top) and modeled signal (bottom) for the rising buoy A from a depth of z_s = 0.80 m in the tank according to Figure 2.3. The vertical dotted line indicates the time when the center of the buoy is at the water surface. 34

2.8 (a) Measured (top) and modeled signal (bottom) for the rising buoy B from a depth of z_s = 0.50 m. (b) Measured (top) and modeled signal (bottom) for the rising buoy B from a depth of z_s = 0.80 m in the tank according to Figure 2.3. The vertical dotted line indicates the time when the center of the buoy is at the water surface. 35

2.9 (a) Sequence of pictures from rising buoy with time step of 50 ms. (b) Modeled (solid line) vs. video measured (crosses) depth position of buoy C in the field during rising (top) and modeled (solid) vs. video measured (crosses) velocity of buoy C in the field during rising (bottom). 36

2.10 Recordings of H1 (top) and H2 (bottom) for release depths of 1.5 m, 2.5 m and 3.5 m according to Figure 2.4. The signals are aligned to the buoy breaking the surface (at 2.9 s), indicated by the vertical dotted line. 36

2.11 (a) Recorded air gun signature, 150 Hz low pass filtered, at hydrophone according to Figure 2.5. (b) Zoom on recorded data between 0.5 s and 3.5 s, 5 Hz low pass filtered (solid line). Modeled signature of rising sphere (dashed line); the model stops when the sphere reaches the surface. Notice the different amplitude scale between (a) and (b). 38

2.12 Possible array design for creating one big air bubble to enhance the proposed low frequency signal. A bubble with $R \approx 3$ m could be expected for these number of air guns. 40

3.1 Spherical wave incident on a flat interface and important parameters for the computation of R_{sph} (top). Plane wave incident on a flat interface and important parameters for the computation of R_{pp} (bottom) 47

3.2 Plane wave reflection coefficient (solid line) and spherical wave reflection response for two different source depths (dotted and dashed line) at the water-air interface as a function of frequency. 48

3.3 (a) Photo of the water tank with dimensions 6 m x 2.5 m x 1.4 m. (b) Underwater photo with gun port of watergun on the left side (red arrow) and hydrophones in the middle. 50

3.4 Schematic sketch of the experimental set up using the watergun as a source in water. Numbers in brackets indicate the coordinates (x,y,z) in meters. . 50

3.5 (a) Photo of the signalgun and near field hydrophone indicated by red the arrow. (b) Top view of the experimental set up with signalgun (red arrow) and hydrophones (blue arrow). 51

3.6 Schematic sketch of the experimental set up using the signalgun as a source in air. Numbers in brackets indicate the coordinates (x,y,z) in meters. . . . 51

3.7 Recorded signal at hydrophone H2 in air (black) and H5 in water (blue) according to Figure 3.4. The signal of H2 in air is multiplied by a factor of 250. The source was fired at z_s = 0.3 m. The signal is filtered with a 10 - 100 Hz (top), 10 - 200 Hz (middle) and 10 - 300 Hz (bottom) bandpass filter. Photos show a top view of the created water jet while the watergun is fired according to different times. The position of the watergun is sketched. 52

3.8 Relative difference $\mu(\delta A)$ between the mean maximum recorded amplitude and the difference amplitude between repeated shots for the signal filtered within 10 - 100 Hz for experiment A. For the hydrophones in air (black) and water (blue). 53
3.9 Recorded signal at hydrophone H2 in air (black) and H1 in water (blue) according to Figure 3.6. The source was fired at z_s = -0.3 m. The signal is filtered with a 10 - 100 Hz (top), 10 - 200 Hz (middle) and 10 - 300 Hz (bottom) bandpass filter. Photos show a side view of the signalgun while it is fired according to different times. 54
3.10 (a) Modeled results at receiver H5 (Figure 3.4) for three different settings using the watergun signature. (b) Modeled results at receiver H2 (Figure 3.6) for three different settings using the signalgun signature. 56
3.11 (a) Measured amplitude ratio for different source depths according to Experiment A1. The amplitudes are corrected for geometrical spreading. The ratios are shown for different bandpass filters. The dashed line shows T_{pp}. (b) Modeled amplitude ratios for the same Experiment. 57
3.12 (a) Measured amplitude ratio for different horizontal receiver offsets in air according to Experiment A2. The amplitudes are corrected for geometrical spreading. The ratios are shown for different bandpass filters. The dashed line shows T_{pp}. (b) Modeled amplitude ratios for the same Experiment. . 58
3.13 (a) Measured amplitude ratio for different source elevations according to Experiment B. The amplitudes are corrected for geometrical spreading. The ratios are shown for different bandpass filters. (b) Modeled amplitude ratios for the same Experiment. 59
3.14 Results from the tank and free-field model of experiment A within frequency band of 10 Hz - 100 Hz. The deghosted results are computed from the free-field and homogeneous model. Theoretical plane wave transmission coefficient T_{pp} (dashed line). 60
3.15 Measured, deghosted, results within frequency band of 10 Hz - 100 Hz (asterisk), spherical wave transmission response T_{sph} for 10 Hz and 100 Hz (dotted lines) and plane wave transmission coefficient T_{pp} (dashed line) for different source depths z_s. 61
3.16 Comparison of ghost functions G using the plane wave (R_{pp}) and spherical wave (R_{sph}) reflection assuming two different source depths z_s. The spectra are normalized to the maximum value within the displayed frequency range. 62
3.17 (a) Results from the tank and free-field model of experiment B within frequency band of 10 Hz - 100 Hz. The deghosted results are computed from the free-field and homogeneous model. Theoretical plane wave transmission coefficient T_{pp} (dashed line). (b) Zoom in on plot (a). 63

4.1 Change of bubble time period T_b in an infinite medium (T_{RW}) and close to a free surface (r = -1) for the different models, T_{He} and T_{HL}. T_b is modelled for different air gun sizes of 100 (solid), 500 (dashed) and 1200 (dotted) in^3 and a firing pressure of 137 bar. The circles indicate the maximum bubble period. 71

4.2 Spike functions and their ghost reflections from the sea surface (top) and the corresponding frequency spectra (bottom). Dashed lines indicate a prefect reflection at the surface. Solid lines indicate a reduced ghost reflection with amplitudes given as A_{gh}, computed from Equation 4.7. 72

4.3 Sketch of experimental set up in the water tank. The hydrophones are indicated as H_1, H_2 and H_3 where the x-, y- and z-coordinates in meters are given in brackets. The water depth in the tank is 1.25 m and the width and length of the tank are 2.5 m and 6 m, respectively. 74

4.4 Sketch of experimental set up in the field. The hydrophone is indicated as H_f where the x- and z-coordinates in meters are given in brackets. The water depth in the fjord is around 390 m. 75

4.5 Measurements at H_1 of 12 in^3 air gun fired in water tank at different depths (top) and the corresponding frequency spectra (middle) and a zoom on the low frequency part (bottom). A 300 Hz low-pass filter is applied to the data. 76

4.6 Photos of air gun fired at a depth of 0.15 m (taken by Stian Rørheim). The time between each photo is 13 ms. 77

4.7 Measured bubble time period of 12 in^3 air gun for different depths fired in the water tank compared to theoretical curves from Rayleigh-Willis equation, Herring and Haavik (Eq. 4.1, 4.2, 4.3). The gray area indicates source depths which are smaller than four times the maximum bubble radius. . . 78

4.8 Measurements of 1200 in^3 air gun fired in the fjord at different depths (top) and the corresponding frequency spectra (middle) and a zoom on the low frequency part (bottom). A 300 Hz low-pass filter is applied to the data. 79

4.9 Measured bubble time period of 1200 in^3 air gun for different depths fired in the fjord compared to theoretical curves from Rayleigh-Willis equation, Herring and Haavik (Eq. 4.1, 4.2, 4.3). The gray area indicates source depths which are smaller than four times the maximum bubble radius. . . 80

4.10 Estimated, normalized energy E using Equation 4.10 computed for different source depths for the tank experiments in air and water (top) and the field experiments (bottom). 82

4.11 (a) Sketch illustrating the critical pressure p_c needed to disturb the surface area with the radius d. (b) Photos taken by camera 1 shown in Figure 4.3 of the air gun fired at different depths with a firing pressure of 80 bar. The photos are taken shortly after the main bubble radius was reached, at ca. 0.045 s (Figure 4.5). 83

4.12 Characteristic depths for different gun volumes V_g and a firing pressure of 137 bar as explained in point I to V. R_{max} is the maximum bubble radius, T_b the bubble time period, z_s the source depth, p_s the emitted acoustic pressure at the surface and p_c the critical pressure as indicated in Figure 4.11(a). 85

5.1 Sketch illustrating the displacement h of the water surface caused by an oscillating bubble underwater. 92

5.2 Sketch of experimental set up in the water tank for Experiment A. The hydrophones are indicated as H_5 and H_6 where the x-, y- and z-coordinates in meters are given in brackets. The water depth in the tank is 1.25 m and the width and length of the tank are 2.5 m and 6 m, respectively. 93

5.3 Sketch of experimental set up in the water tank for Experiment B. The hydrophones are indicated as H_1, H_2, H_3 and H_4 where the x-, y- and z-coordinates in meters are given in brackets. The water depth in the tank is 1.25 m and the width and length of the tank are 2.5 m and 6 m, respectively. 93

5.4 Measurements of watergun signature at H_5 and H_6 (Figure 5.2) for different source depths z_s. Indicated is also the ratio between the source depth z_s and maximum cavity radius R_{mc}. Signal is 300 Hz low-pass filtered. . 95

5.5 Measurements of airgun signature at H_1 and H_4 (Figure 5.3) for different source depths z_s. Indicated is also the ratio between the source depth z_s and maximum bubble radius R_{mb}. Signal is 300 Hz low-pass filtered. . . 96

5.6 Ratio of maximum peak amplitude measured in air A_{air} and water A_{water} for both experiments depending on the ratio between the source depth z_s and maximum bubble size R_m. R_m is replaced with R_{mc} and R_{mb} for the respective experiment. Computed for a 300 Hz low-pass filtered signal. Dashed line shows theoretical ratio using the plane wave transmission coefficient T_p. 97

5.7 (a) Photos at water surface for airgun experiment B fired at different source depths z_s taken ca. 20 ms after airgun is fired, when bubble radius R is close to its maximum. Sketch shows the set up and how max(h) is measured. (b) Measured maximum surface displacement h for different source depths. Shaded area indicates the error. Grey line is the normalized measured acoustic pressure in water for the airgun fired at z_s = 0.3 m. . . 98

5.8 Measurements of airgun signature in air at H_2, H_3 and H_4 (Figure 5.3) with different band-pass filters applied as indicated, corrected for spreading with $1/r$ and aligned in time. The source depth is z_s = 0.3 m. Note the different amplitude scales for each plot. 99

5.9 2D section of experimental set up shown in Figure 5.3. The transmitted signal into air from a monopole sound source is sketched accounting only for homogeneous waves (black) and including the evanescent part (grey), adopted from Calvo et al. (2013). 101

5.10 Modelled bubble radius R and surface displacement h vertically above the source. The critical radius R_c, when the bubble breaks the surface, is reached at 1. The black dashed line indicates the modelled bubble radius when it does not break the water-air interface. A 150 Hz low-pass filter is applied to $\ddot{h}$. 102

5.11 Measured (solid) and modelled (dotted) signals from the 12 in^3 airgun recorded in water at H_1 and in air at H_4 as indicated in Figure 5.3 for different source depths z_s. Measured and modelled data are normalized to each maximum value, respectively. A 150 Hz low-pass filter is applied to the data. 103

5.12 Photos of airgun fired at a different source depths z_s taken at different times as indicated. The source depths correspond to the recordings shown in Figure 5.11. Pressure recordings and camera are not synchronized. . . 104
5.13 Continuation of Figure 5.12. 105

6.1 Modelled signature of 12 in^3 airgun fired with 80 bar at a depth of z_s = 0.6 m and 400 Hz low-pass filtered. Top: varying heat transfer γ. Middle: varying parameter c'_∞, ρ'_∞ with Φ (Eq. 6.6, 6.8). Bottom: varying initial radii R'_0 with Φ, assuming R_{bc} = 3 cm (Eq. 6.9). 112
6.2 Extinction cross-section σ_e (Equation 6.12) that indicates the sound attenuation for different bubble radii a. 113
6.3 Photos and sketch of experimental set up in the water tank. The hydrophones are indicated as H_1 and H_2 where the x-, y- and z-coordinates in meters are given in brackets. The water depth in the tank is 1.25 m and the width (y-direction) and length (x-direction) of the tank are 2.5 m and 6 m, respectively. 114
6.4 Underwater photos of tube ring around air gun ports with different amounts of injected air. Pressure indicates the value measured at the inlet valve for the air supply. 115
6.5 Underwater photos of metal frame attached to air gun with different amounts of injected air. Pressure indicates the value measured at the inlet valve for the air supply. 115
6.6 Comparison of signal measured at H_2 without devices, with tube ring and with metal frame attached to the gun. No air bubble curtain is present. Signal is 400 Hz low-pass filtered. 116
6.7 Comparison of signal measured at H_2 without and with bubble curtain of different amounts of injected air using the tube ring as shown in Figure 6.4. Signal is 400 Hz low-pass filtered and the shaded area indicates errorbars from the measurements (only in frequency spectrum). 117
6.8 Comparison of signal measured at H_2 without and with bubble curtain of different amounts of injected air using the tube ring as shown in Figure 6.4. Signal is 2000 Hz low-pass filtered and the shaded area indicates errorbars from the measurements (only in frequency spectrum). 118
6.9 Comparison of signal measured at H_2 without and with bubble curtain of different amounts of injected air using the metal frame as shown in Figure 6.5. Signal is 400 Hz low-pass filtered and the shaded area indicates errorbars from the measurements (only in frequency spectrum). 119
6.10 Comparison of signal measured at H_2 without and with bubble curtain of different amounts of injected air using the metal frame as shown in Figure 6.5. Signal is 2000 Hz low-pass filtered and the shaded area indicates errorbars from the measurements (only in frequency spectrum). 120
6.11 Bubble time period T_b and primary-to-bubble ratio P/B for all experimental settings as indicated. The signal is 150 Hz low-pass filtered. . . . 121

6.12 Zoom on main peak in Figure 6.7 and 6.9 and the slope of the main peak for all experiments. Errorbars are indicated as shaded area. Slope is computed as summed gradient between start of signal (t = 0 s) and main peak amplitude and signal is 400 Hz low-pass filtered. 121

6.13 Zoom on main peak in Figure 6.8 and 6.10 and the slope of the main peak for all experiments. Errorbars are indicated as shaded areas. Slope is computed as summed gradient between start of signal (t = 0 s) and main peak amplitude and signal is 2000 Hz low-pass filtered. 122

6.14 (a) Top view of Figure 6.3 showing the path for the wall reflections and the bubble curtain dimensions. (b) Estimated sound velocity and air saturation inside bubble curtain using Equation 6.14 and 6.8. 123

6.15 Comparison of measured (top) and modelled (bottom) acoustic pressure for the ring set up using the estimated saturation values Φ (Figure 6.14(b)) and dimensions of bubble curtain (Figure 6.4). Model accounts for all effects explained in Figure 6.1. Signal is 400 Hz low-pass filtered. 125

6.16 Comparison of measured (top) and modelled (bottom) acoustic pressure for the frame set up using the estimated saturation values Φ (Figure 6.14(b)) and dimensions of bubble curtain (Figure 6.5). Model accounts for all effects explained in Figure 6.1. Signal is 400 Hz low-pass filtered. 126

7.1 Sketch illustrating the frequency spectrum of a single airgun signature in the far-field computed with a conventional airgun model (I). The deviations from the model caused by mechanisms discussed in chapter 2, 3 (II), chapter 4 (III) and chapter 6 (IV) are shown and explained in more detail in the text. 130

7.2 Field experiments suggested to continue the work presented in this thesis. The experiments A, B and C are explained in more detail in the text. . . . 132

A.1 Borehole set up and the important parameters for the relation between the tube wave and S-wave within the geological formation. 139

A.2 Relation between the tube wave velocity v_t and S-wave velocity v_s (top) and shear modulus μ_s (bottom) within the formation surrounding the well for different settings. 140

A.3 Experimental set up inside the workhall. The shallow, 30 m, (well 1) and deep, 95 m, borehole (well 2) are shown on topview and cross-section. The stars indicate the positions of the hammer source with r_s = 0.15 m. The shallowest hydrophone is indicated by H-24 with a regular spacing of 1 m to the next receiver. 144

A.4 Stacked traces for the experiment in the shallow well 1 (left) and for the experiment in the deep well 2 (right). 145

A.5 Smoothed, mean frequency spectra for a time window of 1 s of all shots in well 1 as solid lines for the different tests (top) and for the test in well 2 (bottom). The dotted lines illustrate the corresponding noise spectra. The amplitudes are normalized to the maximum value of all recordings. . . . 146

A.6 Smoothed, mean frequency spectra for time windows of 16 s of passive recordings in the shallow and deep well at different times with recording lengths of 21 h (shallow: 10/17), 4 h (shallow: 03/18) and 11 h (deep: 10/17). 147
A.7 Stacked traces for the experiment in the shallow well 1, filtered within frequency bands of (a) 50 - 450 Hz and (b) 0 - 150 Hz. Stacked traces for the experiment in the deep well 2, filtered within frequency bands of (c) 50 - 450 Hz and (d) 0 - 150 Hz. 148
A.8 Normalized f-k spectrum of a single shot conducted in the shallow well 1 (left) and deep well 2 (right). The black line indicates the fitted line for the velocity estimation and the purple line is the picked maximum amplitude at each frequency. 149
A.9 Estimated velocities using the slope in the f-k-domain for each hammer shot (blue) and the average value (red) for all experiments in the shallow well, as test 1: September 2017, test 2: October 2017, test 3: March 2018 and test 4: May 2018 (from top to bottom). 151
A.10 Estimated velocities using the slope in the f-k-domain for each hammer shot (blue) and the average value (red) for the experiment in the deep well. 152
A.11 Relation between the tube wave v_t and S-wave velocity v_s (top) and shear modulus μ_s (bottom) for well 1 (black) and well 2 (red). The dotted lines indicate the corresponding error bars within the tube wave is measured and the resultant v_s and μ_s range. 153
A.12 Relative variation of shear modulus and S-wave velocities due to dissolution effects in the formation for different amounts of injected CO_2 using the empirical relation from Vanorio et al. (2011) for different overburden pressures (in brackets). The amount of injected pore volume is without unit as indicated in Equation A.8. 155
A.13 Relative variation of shear modulus and S-wave velocities due to precipitation of halite in the pore space with an initial porosity of $\Phi = 30\%$. 156
A.14 Relative variation of shear modulus and S-wave velocities due to changes in pore pressure for sandstones (black) and carbonates (red). The overburden confining stress is 15 MPa and initial pore pressure is 7.5 MPa. 156
A.15 Sensitivity study of the relation between the tube and shear modulus for different parameters. The dotted line indicates the relation for the experimental set up of well 1, the same as in Figure A.11 (black, solid line). Each plot illustrates the variation of one parameter with (a) borehole diameter d_b, (b) casing thickness d_{cas}, (c) tool thickness r_{min}, (d) shear modulus of tool μ_t, (e) bulk modulus of borehole fluid K_f, (f) temperature of borehole fluid T, (g) shear modulus of casing μ_c, (h) coupling between casing and formation β. 159
A.15 Figure continued. 160
A.16 Modelled change of shear modulus μ_s for a sandstone formation at approximately 750 m depth during CO_2 injection and the corresponding change of the tube wave velocity v_t. The injection starts at t_1 and ends at t_2. At t_3 the initial pore pressure is reached. 161

Chapter 1

Introduction

In marine seismic surveys large acquisition systems, consisting of several sources and receivers, are used to map the geological structures in the subsurface for different interests, e.g. exploration of reservoirs. For most seismic applications it is desirable to emit and record a signal in a broad bandwidth ranging from approximately 1 Hz to 200 Hz. In the early days of marine seismic exploration, in the 1940's and 1950's, dynamite and similar explosives were the conventional sound sources used in the surveys (Landrø and Amundsen, 2018). In the beginning the explosives were detonated at large depths or at the sea bottom and later on it became common practice to deploy the dynamite with floating devices at a few meters below the sea surface. In 1969, the use of explosives was prohibited by most governments due to safety risks and environmental reasons, e.g. fish kill (Landrø and Amundsen, 2018). Therefore, several alternative sources were developed in the 1960's and the airgun, developed by Stephen Chelminski, came off as the winner from the competition. The airgun, which is a mechanical device releasing high pressure air into the water within a few milliseconds, is still the most common source in marine seismic acquisition today. The acoustic signal from this source is characterized by a sharp peak, generated when the air is released, followed by several smaller peaks caused by the oscillating air bubble. The emitted frequency content is mainly influenced by the source depth due to two different effects and for the low frequency content these effects seem to counteract each other (Hegna and Parkes, 2011; Landrø and Amundsen, 2014a). The first effect is the oscillation period of the air bubble. This period decreases with increasing source depth and hence reduces the energy content at the low frequency end of the spectrum. The second effect is the constructive and destructive interference of the direct downgoing wavefield from the source with the first reflected wavefield from the sea surface, referred to as the ghost (van Melle and Weatherburn, 1953). The destructive interference leads to notches in the spectrum at specific frequencies depending on the source depth (Parkes and Hatton, 1986). It should be noted that the ghost effect reduces the energy content at low frequencies for decreasing source depths, in contrast to the oscillating bubble. In addition, for deeper sources the higher ghost notches move to lower frequencies and hence into the seismic frequency band between 1 Hz and 200 Hz.

Motivation: The main motivation for this work is to investigate the emitted frequency range from single marine seismic sources, especially airguns, in more detail. The signal emitted by airguns has often low energy for frequencies below 5 Hz and it emits noticeable signal above 200 Hz. While it would be beneficial to enhance the low frequency part (ten Kroode et al., 2013), the high frequency signal should be attenuated to mitigate the impact on marine life (Gordon et al., 2003; Southall et al., 2007; Cato et al., 2013). In this thesis source mechanisms are experimentally investigated that could have an impact on the low and high frequency end of the seismic frequency band.

The thesis consists of a collection of individual manuscripts, an introduction and a summary part, including an outlook for future investigations. The structure and content of the chapters are as follow:

Chapter 1: In this introductory part the basics of marine seismic acquisition are described and the sources and receivers used for the surveys are illustrated. In addition, potential noise sources are explained and an introduction on the environmental impact of marine seismic acquisition is given. As the thesis investigates mechanisms that impact the source signature, the focus is on the seismic airgun, its oscillating air bubble and the source ghost effect. At the end of this chapter, my contributions to the different publications are listed. In addition, the experimental data is made available as explained in the last section of the chapter.

Chapter 2: The impact of the rising airgun bubble on the acoustic source signature is investigated with dedicated experiments and a simple model. The acoustic signal from a rising buoy that is submerged in water is recorded in tank and field experiments and is compared to airgun signatures recorded in the field. The experimental set up is chosen to separate the effect of the rising bubble from the main impulse and oscillating bubble which normally occur when an airgun is fired. The measured data is compared to a simple model describing the acoustic signal created by a rising sphere in water.

Chapter 3: The effect of the ghost reflection from the water surface on the source signal is investigated in more detail by tank experiments where the distance between the source and interface is varied. We discuss the difference in assuming a spherical wave front for the reflection compared to plane waves. The experiments are repeated in the same way, but with a source located in air. The measured data is compared to modelled results using the Comsol software.

Chapter 4: The interaction between the water-air interface and the airgun source is investigated from tank and field experiments. The airgun is fired at different depths very close to the interface including the depth where the air bubble directly bursts into the surrounding air. The disturbance of the interface is investigated from video recordings and acoustic measurements. In addition, the variations of the oscillating bubble and ghost effect are discussed with a focus on the low frequency content of the source signal.

Chapter 5: This chapter is an extended investigation and discussion to Chapter 3 and 4. However, it can be read as an independent manuscript. We focus on the signals from the seismic sources in water that are recorded in air. The contributions of the signal transmitted through the interface and from the moving water surface are discussed.

Chapter 6: The impact of bubble curtains surrounding the airgun on its source signature and high frequency emission are investigated with dedicated tank experiments. Two different bubble curtains, varying in its size and the way they are fixed to the airgun, are tested and compared to the common airgun signature. We focus on the impact of the bubble curtain on the main peak of the source signature which is mainly responsible for the high frequency emission.

Chapter 7: The main results from all chapters are summarized and discussed in respect to its applicability and use in marine seismic acquisition. A few suggestions are given for future investigations in relation to marine seismic sources.

Appendix: We investigate a potential application of tube waves which are interface waves travelling along boreholes. The idea is to use the tube waves as a monitoring method to detect changes in the formations surrounding the borehole. We conduct experiments in two shallow wells, 95 m and 30 m deep, to study the parameters that impact the tube wave and investigate how accurately the tube wave velocity could be measured. As this study is not related to marine seismic sources, it is part of the appendix. It is included as it contains additional information to some of the extended abstracts mentioned in section 1.5 and might be helpful for future experiments conducted in the well at the Department of Geoscience and Petroleum, NTNU.

1.1 Marine Seismic Acquisition

To image objects that we cannot see with our own eyes, we often make use of waves, like acoustic, elastic or electromagnetic waves, to solve this problem. Examples from our every-day life are medical applications, as ultrasound imaging for a baby in utero, or non-destructive testing on bridges and buildings to check for cracks or other internal structures. Marine seismic acquisition is used in a similar way to image the subsurface below the seafloor. These images can be used to understand geological structures as plate boundaries or faults which cause earthquakes or to map resources as geothermal, gas or oil reservoirs. Figure 1.1 illustrates a common scenario and set up of instruments used to acquire seismic data. For simplicity the illustration is restricted to 2D acquisition while many seismic surveys are conducted in 3D using several streamers dragged parallel behind the vessel. The seismic sources towed behind the vessel generate the acoustic waves which propagate into the subsurface and are reflected from geological structures with different properties (density and wave velocity). The reflected signals are recorded by sensors in the water column or on the sea bottom. From the recorded data images are produced by processing techniques which visualize the structures of the subsurface (Ikelle and Amundsen, 2005). In addition, several noise sources impact the recorded data and overlap with the desired data. In the following sections the seismic sources (1.2), the seismic receivers (1.3) and the noise sources (1.4) in marine seismic acquisition are described in more detail.

In general, a simple description of the problem can be given as (Parkes and Hatton, 1986)

$$x(t) = s(t) * g(t) + n(t) \tag{1.1}$$

where $x(t)$ is the signal recorded at the receiver, $s(t)$ is the signal emitted from the source and $n(t)$ is noise on the data. The response from the subsurface, in which we are interested in, is denoted by $g(t)$. In this simple description the impulse response from the receiver and from the recording system is neglected (Ikelle and Amundsen, 2005).

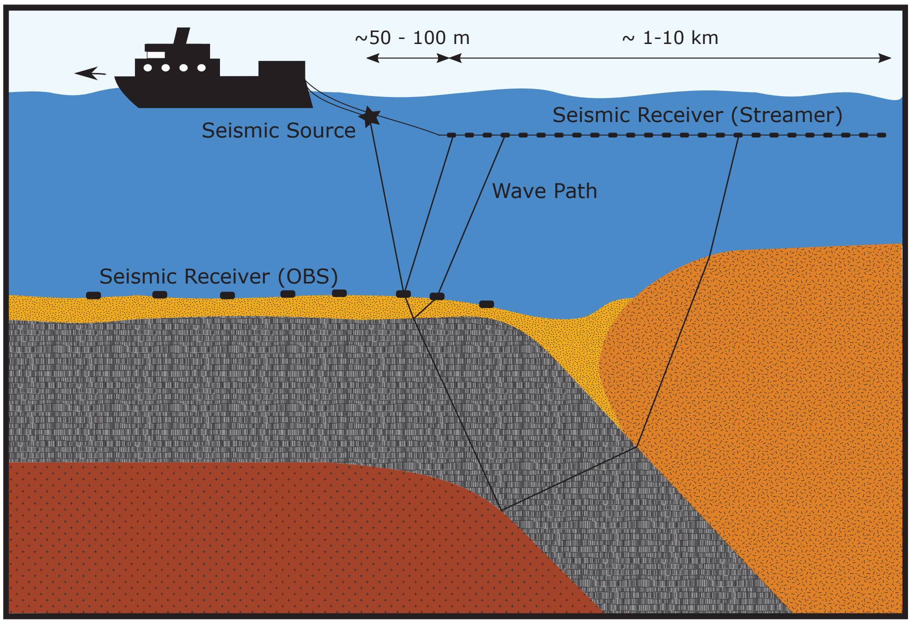

Figure 1.1: Simple sketch of a common marine seismic acquisition set up in 2D. Possible wave path for signals reflected from geological structures in the subsurface are illustrated.

1.2 Marine Seismic Sources

First, the source ghost is described as the impact of the strong reflection from the sea surface is common for all sources in marine seismic acquisition. Then, the acoustic signal generated by the airgun is explained as this is still the most common source and the experiments in this thesis are mostly performed with an airgun. In addition, alternative seismic source types are described which are already in use or in the development.

1.2.1 The Source Ghost

The reflection from the sea surface following the direct downgoing wavefield from a source submerged in water is referred to as the ghost (van Melle and Weatherburn, 1953). As the distance between the source and the sea surface is small compared to the wave length of interest in marine seismic acquisition, the ghost can be considered as an inherent part of the source signature. To illustrate the impact of the ghost on the frequency content of the source signature we compute the signal emitted by a point source located at a depth z_s and recorded at a receiver at the distance r (Figure 1.2(a)). The signal can be described as (Parkes and Hatton, 1986)

$$p(r,t) = \frac{1}{r} p_n(t - \frac{r}{c_1}) + R_c \frac{1}{r + r_g} p_n(t - \frac{r}{c_1} - \frac{r_g}{c_1}) \tag{1.2}$$

where r is the direct distance between the source and receiver and r_g is the distance added to r for the sea surface reflected signal (Figure 1.2(a)). This path can be described assuming a ghost source position above the sea surface with the same vertical distance to the interface as z_s (Parkes and Hatton, 1986). The source signal is denoted by p_n, c_1 is the sound velocity in water and R_c is the reflection coefficient at the sea surface. The additional distance for the ghost source can be approximated in the far-field, when $r \gg r_g$, as

$$r_g \approx 2 z_s \text{cos}(\theta_1) \tag{1.3}$$

where θ_1 is the incident angle on the sea surface (Figure 1.2(a)). The reflection coefficient for a flat fluid-fluid interface, assuming plane waves, can be described as (Kinsler et al., 1962)

$$R_c = \frac{c_2 \rho_2 / \text{cos}(\theta_2) \ - \ c_1 \rho_1 / \text{cos}(\theta_1)}{c_2 \rho_2 / \text{cos}(\theta_2) \ + \ c_1 \rho_1 / \text{cos}(\theta_1)} \tag{1.4}$$

where ρ_i and c_i, with i = 1, 2, denote the density and velocity of the respective layer (Figure 1.2(a)). The incident and reflected angles are indicated as θ_1 and θ_2 is the refracted angle. In case of the sea surface the parameters are ρ_1 = 1000 kg/m^3, c_1 = 1500 m/s, ρ_2 = 1.25 kg/m^3 and c_2 = 334 m/s. These values reveal a reflection coefficient of R_c = -0.9994 for $\theta_1 = 0^o$. The reflection coefficient can vary for different scenarios, e.g. a rough surface topography caused by wind and weather (Parkes and Hatton, 1986).

The frequency spectrum of the signal at a receiver in the far-field, using Equation 1.3, can be received by computing the Fourier transform of equation 1.2 that leads to

$$P(r,\omega) = \frac{1}{r} P_n(\omega) \, e^{i\omega(r/c_1)} + R_c \frac{1}{r} P_n(\omega) \, e^{i\omega((r+r_g)/c_1)} \tag{1.5}$$

where $\omega = 2\pi f$ is the angular frequency, with f as the frequency. As we are in the far-field r_g is neglected in the second decay term $\frac{1}{r}$, but not in the more sensitive phase term. We can separate equation 1.5 into two parts as

$$P(r,\omega) = S(\omega) G(\omega) \tag{1.6}$$

with

$$S(\omega) = \frac{1}{r} P_n(\omega) \, e^{i\omega(r/c_1)} \tag{1.7}$$

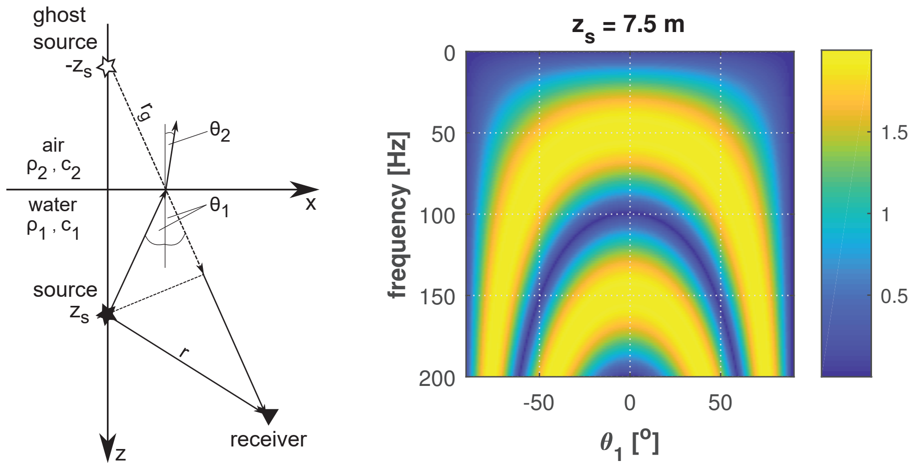

(a) (b)

Figure 1.2: (a) Sketch illustrating parameters used for the computation of reflection coefficient R_c and geometry for source and receiver position. The dashed arrow indicates the additional travel paths r_g for the ghost signal. (b) Ghost spectrum $|G(\omega)|$ for different incident angles θ_1

$$G(\omega) = 1 + R_c\, e^{i\omega(r_g/c_1)} \tag{1.8}$$

where the term $S(\omega)$ is the direct signal to the receiver and the term $G(\omega)$ is the ghost reflection. Therefore, the impact of the ghost on the frequency spectrum of the source signature at the receiver can be described as (Amundsen, 1993)

$$|G(\omega)| = |1 + R_c\, e^{i\omega(r_g/c_1)}| \tag{1.9}$$

This ghost spectrum is shown for different incident angles θ_1 in Figure 1.2(b). It should be noted that Equation 1.9 is only valid in the far-field. For computations in the near-field the correct distance for r_g needs to be found from the geometry. As an example for the ghost impact, the signal recorded at a receiver in the far-field vertically below a point source, which emits a spike function, is modelled and shown in Figure 1.3. The point source is located at two different depths z_s to demonstrate the difference in the ghost notches that are located at (Parkes and Hatton, 1986; Amundsen and Zhou, 2013)

$$f_n = \frac{c_1}{2z_s} n \quad \text{, with} \quad n = 0, 1, 2, ... \tag{1.10}$$

The received pressure signal in the far-field from every point source submerged in water at a single depth has these notches in the frequency spectrum related to its depth. It should be noted that the notch at 0 Hz exists for all source depths.

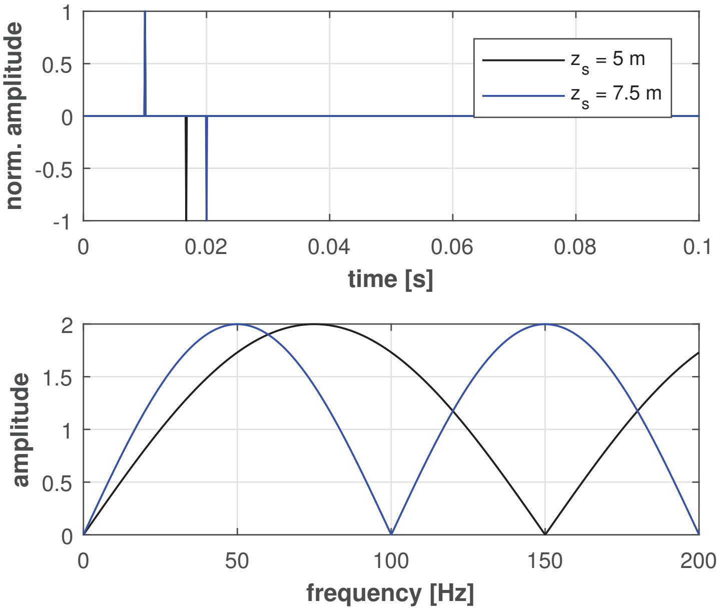

Figure 1.3: Top: Reflected spike function from the sea surface for two different source depths z_s, assuming R_c = -0.9994. Bottom: Corresponding frequency spectra, that can also be described by the ghost function (Equation 1.9).

1.2.2 The Airgun

To understand the signal generated by an airgun, we need to describe the source and the acoustic pressure emitted by the source. The airgun is a mechanical device that releases high pressure air from a chamber into the surrounding water (Giles, 1968). This air forms an expanding bubble due to the higher pressure inside the bubble compared to the water. As it expands the pressure decreases and the bubble reaches a size where the pressure inside the bubble is lower than in the surrounding water. Therefore, the air bubble contracts again and the internal pressure increases. This oscillation is repeated until the bubble reaches the water surface or it is dissipated in water. A sketch of an airgun and photos from one oscillation period while an airgun is fired are shown in Figure 1.4. The sketch indicates the chambers that are filled with compressed air through the pressure cable, the shuttle that opens when the air gun is triggered by the solenoid and the gun ports where the air is released when fired. The maximum bubble radius in Figure 1.4 is reached after 11 ms and at 22 ms the bubble size is close to its minimum due to the contraction.

The first physical description of an oscillating bubble in an inviscid, incompressible and infinite medium was done by Rayleigh (1917). Later, several different models for an oscillating bubble are derived which account for more physical effects, e.g. energy dissipation effects of the bubble, as heat transfer and mass transfer, or compressibility effects (Kirkwood and Bethe, 1942; Gilmore, 1952; Keller and Kolodner, 1956; Plesset and Pros-

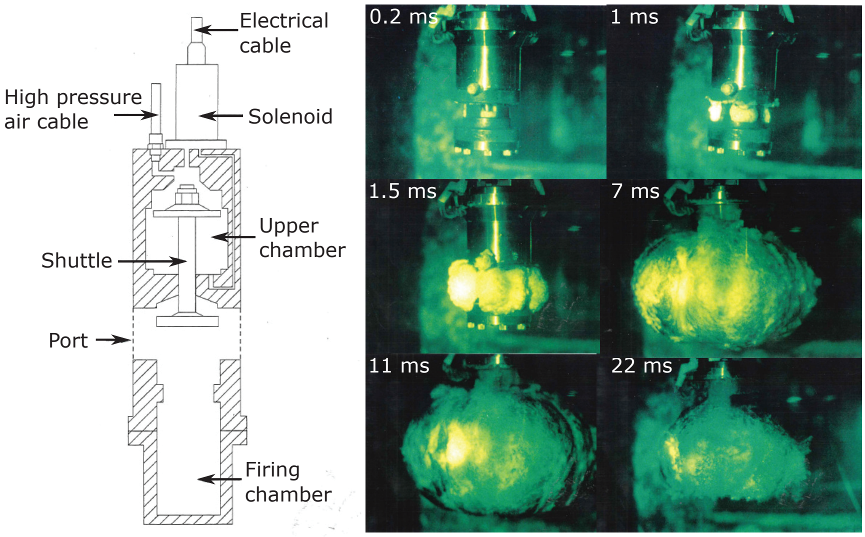

Figure 1.4: Simple sketch of an airgun and photos from a 1.6 in^3 gun fired in a water tank at different times as indicated (illustrations from Langhammer (1994)).

peretti, 1977; Ziolkowski, 1970). For the following description the equation by Kirkwood and Bethe (1942) is used with additional damping factors as given by Landrø and Sollie (1992)

$$\ddot{R} = \frac{\left(1+\frac{\dot{R}}{C}\right)H + \left(1-\frac{\dot{R}}{C}\right)\frac{R}{C}\dot{H} - \frac{3}{2}\left(1-\frac{\dot{R}}{3C}\right)\dot{R}^2 - \alpha\dot{R} + \beta\dot{R}^2}{R\left(1-\frac{\dot{R}}{C}\right)} \tag{1.11}$$

where R, $\dot{R}$ and $\ddot{R}$ are the bubble radius, velocity and acceleration, respectively. The sound velocity in water at the bubble wall is denoted by C and α and β are damping and empirical coefficients accounting for energy losses on the bubble oscillation. H is the enthalpy at the bubble wall given as (Ziolkowski, 1970; Landrø and Sollie, 1992)

$$H = \frac{n(p_\infty + B)}{(n-1)\rho_\infty}\left[\left(\frac{P_b + B}{p_\infty + B}\right)^{(n-1)/n} - 1\right] \tag{1.12}$$

where n and B are constants depending on the fluid and for water $n \approx 7$ and $B \approx 3000$ bar (Gilmore, 1952). The hydrostatic pressure is denoted by p_∞, ρ_∞ is the water density and P_b is the pressure in the liquid at the bubble wall. The sound velocity at the bubble wall can be described as (Ziolkowski, 1970)

$$C = c_\infty\left(\frac{P_b + B}{p_\infty + B}\right)^{(n-1)/2n} \tag{1.13}$$

where c_∞ is the sound velocity in undisturbed water. The pressure at the bubble wall is given as (de Graaf et al., 2014b)

$$P_b = p_\infty\left(\frac{R_0}{R}\right)^{3\gamma} \tag{1.14}$$

where γ is the polytropic index that is γ = 1.4 for adiabtic conditions between the air bubble and surrounding water and γ = 1 for isothermal conditions. The initial bubble radius is denoted as R_0.

The acoustic pressure from an oscillating bubble propagating in an incompressible fluid and measured at a receiver point can be described as (Gilmore, 1952)

$$p(r) = \rho_\infty \frac{R}{r}\Big(H + \frac{(r^3 - R^3)}{r^3}\frac{\dot{R}^2}{2}\Big) \tag{1.15}$$

where r is the distance between the source and the receiver. The term $(r^3 - R^3)/r^3$ vanishes in the far-field when the bubble radius is much smaller than the source-receiver distance, $R \ll r$. In an incompressible fluid the enthalpy H can be approximated as (Gilmore, 1952)

$$H \approx \frac{P_b - p_\infty}{\rho_\infty} \tag{1.16}$$

The modelled acoustic pressure emitted by a 200 in^3 airgun, fired with 137 bar and located at two different source depths z_s, recorded at a receiver vertically below the source at the distance r = 1000 m is shown in Figure 1.5. The source signatures are given in bar-m which means that the signal is corrected for geometrical spreading by multiplying with r. This is commonly done in seismic acquisition to make signatures from different sources, measured at different distances comparable. The ghost reflection is not considered for the

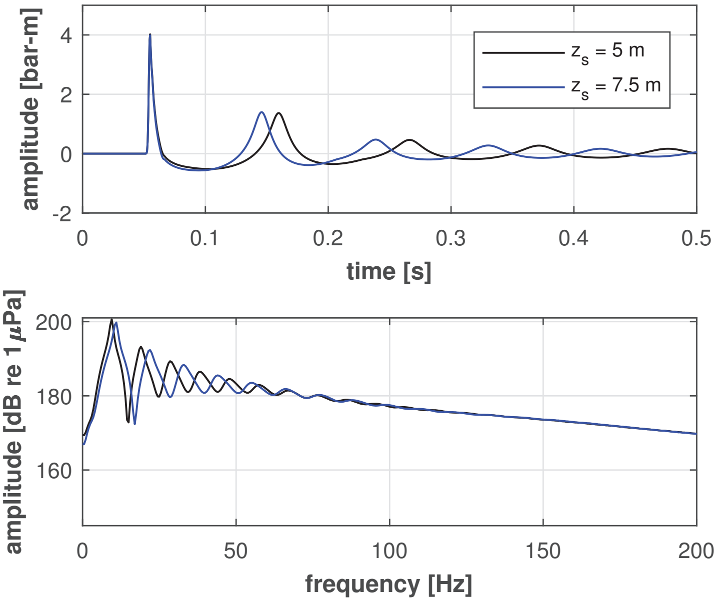

Figure 1.5: Top: Acoustic signature generated by a single 200 in^3 airgun fired at different depths z_s. Modelled at 1000 m distance from the source and corrected for geometrical spreading with $1/r$, without the impact from the ghost. Bottom: Corresponding frequency spectra.

modelling and hence Figure 1.5 illustrates the source signature of the airgun without the impact of the sea surface, but still accounting for different hydrostatic pressure values with varying source depths z_s. In marine seismic acquisition this is referred to as the notional source signature (Ziolkowski et al., 1982). We notice the increase of the bubble time period T_B for shallower sources and how this shifts the spectrum towards lower frequencies. The same computation is repeated, but adding the ghost effect to the modelled pressure at the receiver (Figure 1.6). We notice how the ghost effect creates notches in the spectra at frequencies f_n (Eq. 1.10) and how frequencies are boosted, e.g. between 25 and 75 Hz for the source at z_s = 7.5 m according to Figure 1.3. For frequencies below 10 Hz the spectrum looks very similar for both source depths (Figure 1.6, bottom), indicating that the ghost reflection and bubble effect counteract each other. The main characteristics of the acoustic signature from an airgun can be described by this model and common parameters to characterize the signature are the primary peak amplitude P, the primary peak-to-peak amplitude PP, the bubble time period T_B and the primary-to-bubble ratio P/B (Figure 1.6). These parameters are given for the source strength at 1 m distance from the source which means that the signal is multiplied by r to correct for geometrical spreading. Empirical relations to estimate these source signature characteristics for different source volumes and depths are given by Vaage et al. (1983).

This is a simple model and in practice there are more effects that have an impact on the source signature and bubble oscillation from a single airgun, e.g. the airgun design, heat

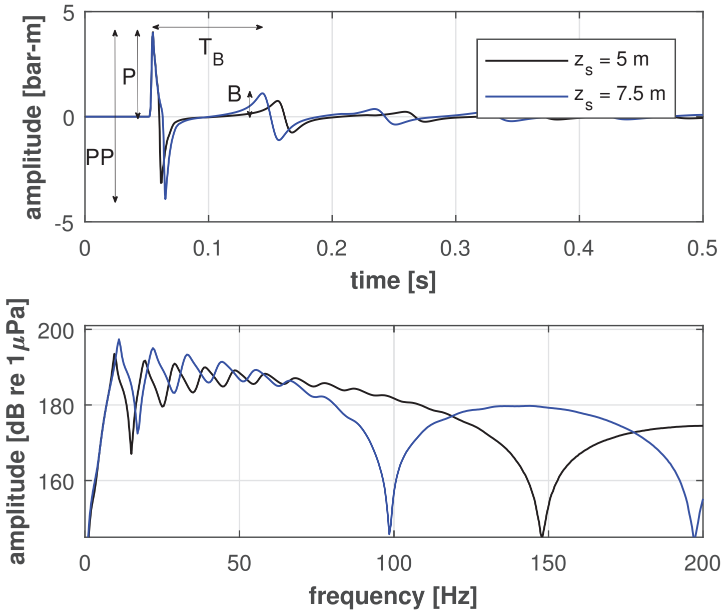

Figure 1.6: Top: Acoustic signature generated by a single 200 in^3 airgun fired at different depths z_s (as in Figure 1.5). Modelled at 1000 m distance from the source and corrected for geometrical spreading with $1/r$, with the ghost and R_c = -0.9994. Bottom: Corresponding frequency spectra.

transfer or viscosity. Studies on the viscosity effect are presented by Langhammer and Landrø (1993a) or King (2016). The heat transfer at the bubble wall is discussed by Plesset and Zwick (1952), Nigmatulin et al. (1981) or Ziolkowski (1982). The effect of water temperature on the bubble oscillation is demonstrated by Langhammer and Landrø (1993b) and Landrø (2014). The impact of the shuttle motion and gun port shapes on the source signature is discussed by Johnston (1982) and Dragoset (1984). How the airgun body itself can impact the bubble oscillations is discussed by Schulze-Gattermann (1972). An overview of several mechanisms acting at the same time is given by Li et al. (2010) or de Graaf et al. (2014b).

We have illustrated the acoustic signature generated by a single airgun. In marine seismic acquisition source arrays which consist of several airguns, typically 25-50, are commonly used (Dragoset, 2000). An example of an airgun source array, consisting of 30 airguns with a total volume of 4470 in^3 and arranged in three sub-arrays is shown in Figure 1.7. The use of arrays has two main benefits. First, the source strength is increased and hence the signal can image deeper areas in the subsurface. Second, the bubble oscillation can be removed by deploying airguns with different volumes in the array. Due to different bubble periods, only the main peaks of the individual airguns add up while the bubble signal vanishes. This leads to a source signature that is closer to an ideal impulsive seismic wavelet that can be handled easier in data processing (Dragoset, 2000). When single airguns are fired close together in an array, the signature of each individual source is influenced by the neighbouring sources (Ziolkowski et al., 1982). How the signature of an airgun array can be computed accounting for these interactions is demonstrated by Ziolkowski et al. (1982) and Parkes et al. (1984).

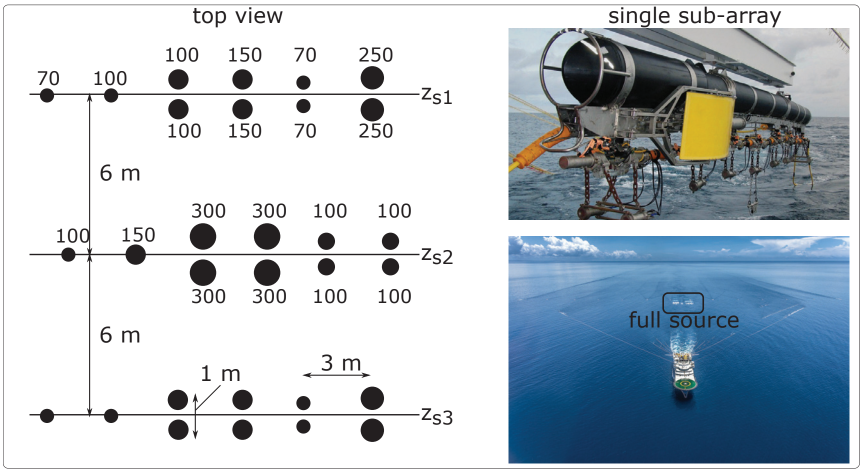

Figure 1.7: Common geometry of a seismic source array consisting of 3 sub-arrays, indicated by its source depths z_{s1}, z_{s2} and z_{s3} (Landrø et al., 2013). A single gun is shown as a circle and its volume is given in in^3. Sub-array 3 (bottom) has the same source volume as sub-array 1. Photos show a random single sub-array (*courtesy of PGS*) and a full source, consisting of two source arrays with 3 sub-arrays each, towed behind a vessel (*courtesy of the International Association of Geophysical Contractors. Used with permission*).

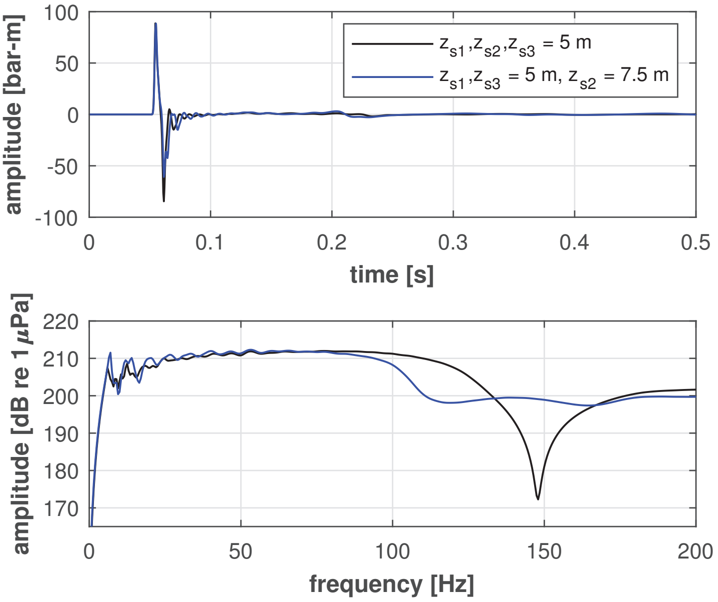

Figure 1.8: Top: Acoustic signature generated by the source array shown in Figure 1.7 for different depths of the sub-arrays. Modelled at 1000 m distance from the source and corrected for geometrical spreading with $1/r$, with the ghost and R_c = -0.9994. Bottom: Corresponding frequency spectra.

The source array can be tuned by deploying sources at different depths (Moldoveanu, 2000; Cambois et al., 2009) or firing individual guns with a small time delay (Abma and Ross, 2013, 2015). This tuning should lead to decreased notches in the frequency spectrum caused by the ghost reflection and hence broadens the usable frequency band. In addition, the time delay between individual airguns can result in a smaller peak amplitude which could reduce the environmental impact Abma and Ross (2015). Further advancements are made in the shot separation in marine seismic acquisition which are commonly large, 25 m - 50 m, to avoid interference with previous shots in the recorded data (Berkhout, 2008). Recent developments in processing (Abma et al., 2015; Robertsson et al., 2016; Jennings et al., 2018) allow for a denser shot point separation, which is referred to as simultaneous source acquisition or blended acquisition. That idea might be expanded to a continuous shooting and recording in marine seismic acquisition as discussed by Hegna et al. (2018).

The signature from the airgun array shown in Figure 1.7 is modelled using the software Nucleus (PGS, 2018) and is shown in Figure 1.8. The source-receiver distance, r = 1000 m, firing pressure, p_f = 137 bar, and source depths z_s are the same as for the single airgun (Figure 1.6). The modelling is performed for a constant source depth of all sub-arrays and for variable source depths between the sub-arrays. For the modelling with variable source depths, the firing time of the deeper sub-array at z_{s2} = 7.5 m is delayed by t_d = 2.5 m / 1500 m/s = 1.7 ms, to align the downgoing signal. We note how the array increases the source strength and reduces the bubble oscillations compared to the signature of a single gun below 100 Hz (Figure 1.6). In addition, the source array with variable source depths fills the notch in the frequency spectrum at 150 Hz related to the ghost (Figure 1.8).

1.2.3 Alternative Sources

The following list gives an overview of common marine seismic sources that are in use today or that are in the development phase. The main working principal of the source is listed together with references for a more detailed description. An overview that also includes sources used in the past can be found in Lugg (1979) or Langhammer (1994) or for new source developments in Mougenot et al. (2015). The conventional airgun is neglected in the list as it was already described in detail.

Marine Vibrator: A moving plate or membrane driven by hydraulic or electromechanical systems that generates a sweep in water. A few field examples of marine vibrators are demonstrated by Jenkerson et al. (1999), Tenghamm and Long (2006), Ozasa et al. (2015) or Pramik et al. (2015). To develop a commercially viable marine vibrator that can produce comparable source output levels as common marine seismic sources, like airguns, a Joint Industry Project (JIP) was initiated in 2011 (Schostak et al., 2015) and first tests from prototypes are presented by Jenkerson et al. (2018) and Roy et al. (2018). If these marine vibrators can produce comparable output to seismic airguns, they would provide several additional advantages. The phase, amplitude and bandwidth of marine vibrators can be controlled with high precision (Jenkerson et al., 2018). These benefits can result in a better source separation for simultaneous source acquisition, a reduced environmental impact due to lower peak amplitudes or a more efficient operation in shallow waters (Jenkerson et al., 2018).

eSource: A newly development airgun that has better control on the air released from the gun chamber to reduce the main peak and hence the high frequency emission. It was development to reduce the impact on marine life while preserving the bandwidth needed for seismic imaging. The development of the source is described by Coste et al. (2014), Gerez et al. (2015) and Groenaas et al. (2016). A comparison between conventional airguns and the eSource is demonstrated by Li and Bayly (2017).

Wolfspar: A large vibrator-type source, that is designed to generate specific ultra-low frequencies needed for the computation of velocity models in full waveform inversion (Dellinger et al., 2016). The first field trial with the Wolfspar source is accomplished in 2018 (Pool et al., 2018).

Tuned Pulsed Sources: An evolution of an airgun that has much larger chamber volumes and lower firing pressures than the conventional airgun (Ronen et al., 2015; Chelminski, 2015). The source is intended to have a slower rise time and lower amplitude of the main peak, a longer bubble time period and should create less cavitation. This can result in an increase of the low frequency content in the source signature while reducing the high frequency emission. A modelling study and a first field test are demonstrated by Watson et al. (2016) and Ronen and Chelminski (2018), respectively.

Waterguns: The source generates a water jet by a rapid movement of a piston. This leads to a collapsing cavity which acts as the acoustic source. The source was first described by Avedik and Combe (1973) and Renard et al. (1974). Investigations of the source signature from waterguns are demonstrated by French and Henson (1978), Fail (1983), Safar

(1984), Safar (1985a), Safar (1985b), Safar (1986), Lugg and Brummitt (1986), Tree et al. (1986) and Landrø et al. (1993). A comparison between airgun and watergun signatures is described by Hutchinson and Detrick (1984) and Deri (1987).

GI Gun: An airgun consisting of two firing chambers, referred to as generator (G) and injector (I) (Landrø, 1992). The air from the generator is released in the same way as for a conventional airgun. The air from the injector is released with a time delay corresponding to the time when the air bubble created from the generator is close to its maximum size. Therefore, the bubble oscillation is strongly reduced and the source signal is characterized by a clean primary pulse (Landrø, 1992).

Sparker: The sudden discharge of high voltage electrical energy at one or more electrodes underwater forms a plasma bubble which rapidly expands and collapses (Lugg, 1979; Langhammer, 1994). Due to the condensation of the steam into water during the bubble growth and collapse, little gas is left in the bubble and only one oscillation occurs (Lugg, 1979).

Boomer: An electromagnetically driven source where a plate is hold against a coil by heavy springs or rubber bumpers (Edgerton and Hayward, 1964; Mosher and Simpkin, 1999). The coil is connected to a capacitor bank that is discharged when the source is triggered. This discharge induces eddy currents inside the plate which leads to rapid repulsion of the plate from the coil. A cavity is formed due to the movement of the plate which acts as the acoustic source (Edgerton and Hayward, 1964). A seismic survey with a boomer source that images a fluvial channel system and shallow gas accumulations is presented by Müller et al. (2002).

1.3 Marine Seismic Receiver

So far we discussed marine seismic sources (Figure 1.1) and how the emitted signature from an airgun looks like. To receive the desired information about the subsurface we need to record the emitted signal with suitable sensors. We discuss two common seismic receiver types which differ in their positioning (Figure 1.1) and in the physical quantities that they measure. First, we describe seismic streamers which are towed behind the vessel. Second, ocean bottom surveys are described which are conducted at the sea bottom.

1.3.1 Seismic Streamer

Streamers are long cables equipped with hydrophones that measure the acoustic pressure in water. In addition, the dual sensor streamer developed by PGS is able to record the vertical particle motion (Tenghamm et al., 2007). The streamers are towed behind the vessel and they are filled with fluid or foam so that they float in water. Additional devices are mounted to the streamers to control and measure its depths and positioning in water (IAGC and OGP, 2011; IAGC, 2013). More detailed studies about seismic streamers and their positioning are demonstrated by Pedersen and Sørensen (2001) and Grindheim et al. (2017). The main components are shown in Figure 1.9 and their main function is explained below.

1. Deflector: controls the spread and position when several streamers are towed parallel behind the vessel in 3D surveys.
2. Front buoy: controlling the depth and position of the streamer.
3. Birds: mounted at several locations along the streamer to control the depth and steering of the cable.
4. Tail buoy: measure the streamer position and to act as a warning sign for the submerged streamer visible on the surface.
5. Acoustic Positioning System and Magnetic Compasses: to measure the orientation and position of the streamer

The sensors are grouped into smaller sections, commonly 12.5 m or 25 m, to reduce the noise generated by the streamer on a single hydrophone (Figure 1.9). The signals from

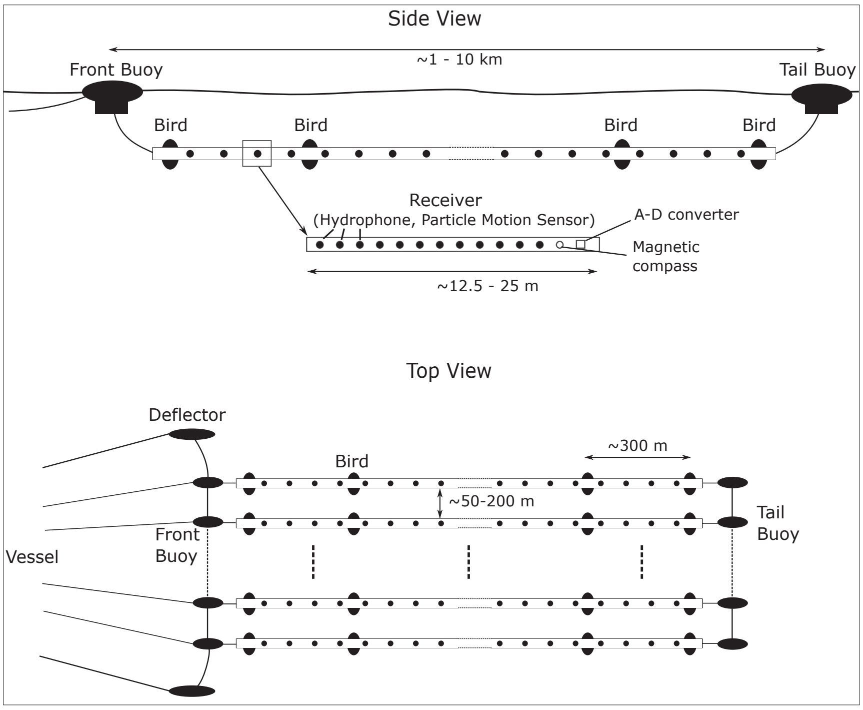

Figure 1.9: Common seismic streamer set up for 3D seismic acquisition. For 2D acquisition only one streamer is towed behind the vessel (Figure 1.1).

each group are digitized as an averaged signal, called trace, and send to the processing center on-board the vessel. The hydrophones are able to record signals stronger than about 2 μbar for frequencies above 5 Hz that is the noise level in calm weather conditions (Landrø et al., 1989; IAGC, 2013). For frequencies below 5 Hz the noise levels could be about 7-8 times stronger. In rough weather conditions these noise levels can be increased by a factor of 3-4. It should be mentioned that there is a streamer system designed for high resolution, shallow subsurface imaging, referred to as P-cable system (Planke and Berndt, 2002; Planke et al., 2009; Petersen et al., 2010). The system consists of 12-24 short streamers, about 25 m long, with a small spacing of about 10 m between each streamer. A smaller source size than for conventional 3D seismic is used.

The recorded signals on the streamer are effected by the ghost similar to the source (Figure 1.2(b)) that creates notches in the frequency band of the data depending on the towing depth. For the receiver side there are two main solutions in seismic acquisition to tackle the ghost problem. The first is the already mentioned dual sensor that measures pressure and vertical particle motion. The pressure is reflected with opposite polarity from the sea surface while the ghost signal for the particle motion has the same polarity as the incident wave field. Therefore, the pressure and particle motion can be used complementary to remove the ghost effect (Carlson et al., 2007; Tenghamm et al., 2007). The second solution is the towing of a slanted streamer, so that the sensors are at different depths. Therefore, the diversity of the notches can be used to compensate for the ghost effect (Soubaras and Lafet, 2013; Dhelie et al., 2014). In addition, further processing techniques might be used to remove the ghost from the measured data (e.g. Amundsen and Zhou (2013), Mayhan and Weglein (2013) or Hicks et al. (2014)).

1.3.2 Ocean Bottom Surveys (OBS)

Surveys with receivers located at the ocean bottom can be performed with different systems (IAGC and OGP, 2011; Landrø and Amundsen, 2018). The first consists of single nodes which are planted into the seafloor. These surveys can be performed by remotely operated vehicles (ROVs) that set out and recover the receivers at seabed. Alternatively, the nodes can be attached to a steel wire that lowers the rope with the receivers directly from a vessel and later they are recovered again by the vessel. Another system uses cables with sensors inside. The cables are deployed on the seabed from the vessel and either stay connected to the vessel which records the data or the cables are attached to buoys where the data can be saved (Landrø and Amundsen, 2018).

Ocean bottom receivers are commonly equipped with four sensors measuring the pressure and the particle velocity in the vertical and two perpendicular horizontal directions. A few advantages of OBS surveys compared to seismic streamer acquisition should be mentioned. First, there is a higher flexibility of acquisition geometries as the cables are fixed on the seafloor and the shooting vessel can operate at nearly any pattern above the receiver array (Landrø and Amundsen, 2018). Second, the recording of shear waves can reveal more information about the subsurface in addition to recordings of pressure waves only. This includes information about different fluids in the rock formations as shear waves are insensitive to the fluid content or investigations of anisotropy which could be estimated from shear wave splitting (Crampin, 1985). In addition, ocean bottom receivers could be permanently installed at the ocean floor (van Gestel et al., 2008; Bertrand et al., 2014). Although the installation of permanent systems is expensive, the accuracy for time-lapse measurements can be improved. Permanently installed system can also be used to conduct time-lapse investigations using noise recordings over longer time periods (Mordret et al., 2014; de Ridder and Biondi, 2015). Another technology development is the step from electric sensors to fiber optic sensor technology which can have a longer life-time, higher dynamic range and could be less expensive (Eriksrud et al., 2009).

1.4 Noise Sources and Environmental Impact

Beside the desired signal that contains information about the subsurface, several other signals are recorded by the seismic sensors which are considered as noise (Equation 1.1). We elaborate more on the noise sources in the first part of this section and list references tackling the problem of removing the noise. In the second part, the environmental impact, e.g. the influence on marine mammals, of seismic acquisition is discussed as research on that topic has increased within the last years. This part serves more as an introduction with literature recommendations for the interested reader.

1.4.1 Noise in Seismic Acquisition

The most common noise sources that have an impact on the data recorded in marine seismic acquisition are swell and flow noise caused by the flow surrounding the streamer and interference noise that is related to nearby seismic vessels, previous shot noise or ship traffic (Elboth, 2010). These noise sources are mostly valid for streamer data while receiver at the ocean bottom are less or not at all effected by these mechanisms. The strongest noise occurs below 2-3 Hz related to hydrostatic pressure fluctuations caused by ocean swell (Smith, 1999; Elboth et al., 2009, 2010a). The ocean waves also cause turbulent flow along the streamer generating noise mainly between 2-15 Hz (Elboth et al., 2010a). An additional noise source for frequencies below 15 Hz might be bulge waves that travel along the streamer cable (Bjelland, 1993; Dowling, 1998; Elboth, 2010). The noise levels on streamer data for different weather conditions and sea states are demonstrated by Landrø et al. (1989) or Smith (1999). An example for the impact of weather noise on a seismic streamer is shown in Figure 1.10. Note that the counting starts at the tail buoy of the streamer and hence the streamer at 3000 m is closest to the towing vessel. The rms amplitude is computed as an average of 5 recordings for each trace with a recording length of 7 s. It should be mentioned that the noise level is almost the same for both sea states when the low-cut filter is applied.

The impact of interference noise, e.g. from other seismic vessels or previous shots, is demonstrated by Lynn et al. (1987) and Landrø (2008). Only considering the previous shot as the noise source Landrø (2008) demonstrate on an example that it takes longer

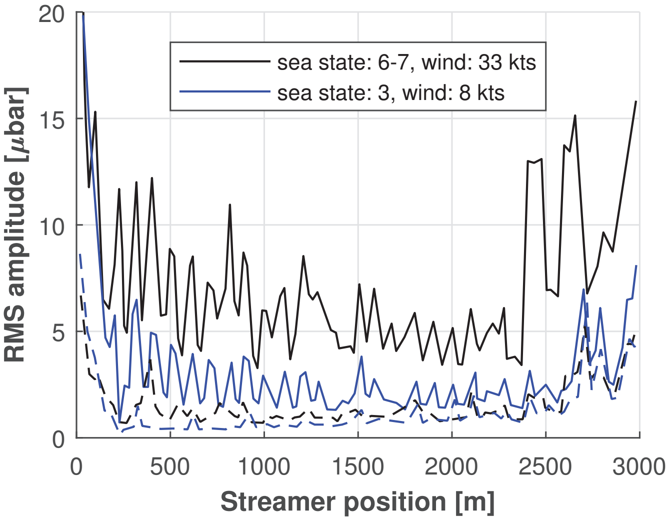

Figure 1.10: Noise recorded along the traces of a 3000 m long streamer towed at 9-12 m depth with a sample rate of 2 ms for two different weather conditions. Data is shown without a low-cut filter (solid line) and with a 5.3 Hz low-cut filter applied (dashed line) (data reproduced from Landrø et al. (1989)).

than the commonly used 10 s shot separation to reach the ambient noise level on the receiver again. Therefore, the shot noise could be important for measurements as time-lapse seismic where a high signal-to-noise ratio is important to resolve small changes in the subsurface. An example for the impact of ship traffic and shot noise on a seismic streamer is shown in Figure 1.11. The two ships, tanker and coastal ship, pass by the end of the streamer and hence they are closest to the streamer position at 0 m. For the tanker the distance is around 8 km to streamer position at 0 m and ca. 10 km to the end at 3000 m (Landrø et al., 1989). For the shot noise a time window between 10 - 14 s is chosen as the common interval between shots in seismic acquisition is 10 s. It should be noted that both, the traffic and shot noise, are above the noise level from the weather noise (Figure 1.10, dashed lines).

Potential methods to remove the noise from the measured data during signal processing are discussed by Schonewille et al. (2008), Elboth et al. (2010b) or Dondurur and Karsli (2012). In particular for the interference noise methods are presented by Fookes et al. (2003), Brittan et al. (2008) or Gulunay (2008). Reducing the flow noise on streamers during acquisition could be achieved by coating the streamer with a material that makes the surface hydrophobic (Elboth et al., 2012). The noise caused by the bulge wave propagating within the streamer could be reduced by incorporating a stiff package that encloses the hydrophone (Dowle and Maples, 2006).

Other noise sources, which are not discussed here, but could have an impact for particular cases are instrument noise, propeller cavitation noise or general background noise (Elboth, 2010).

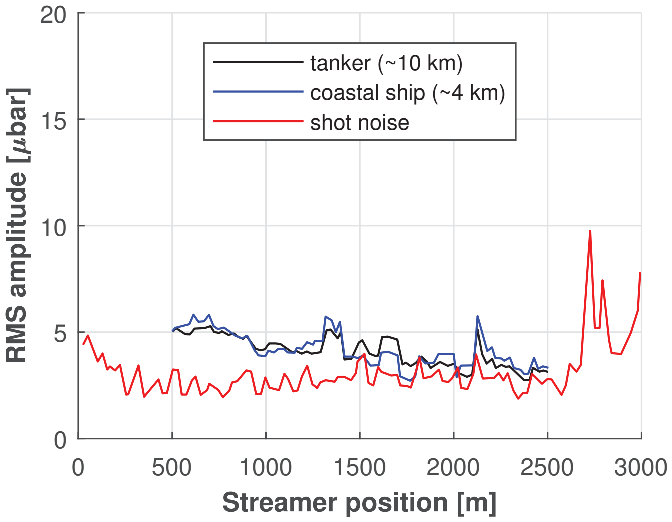

Figure 1.11: Ship traffic noise along the traces of a 3000 m long streamer towed at 9-12 m depth with a sample rate of 2 ms for two different ships passing by at different distances with approximate average distance indicated. The shot noise is recorded for a time window of 10-14 s after the shot was fired. The data is filtered with a 5.3 Hz low-cut filter (data reproduced from Landrø et al. (1989)).

1.4.2 Marine Seismic Survey Impact on the Environment

Marine seismic acquisition is one anthropogenic contributor to the increased noise level in the oceans within the last decades. The increased ship traffic, pile driving for offshore constructions or naval activities are further examples. Overviews of anthropogenic and natural noise sources in the ocean are given by Hatch and Wright (2007), Dahl et al. (2007), Hildebrand (2009) or André et al. (2011). The impact of marine seismic acquisition on marine life is mostly investigated for cetaceans which include whales, dolphins and porpoises. The sound impact is often evaluated considering two measures that are the sound pressure level (SPL) accounting for the peak amplitude of the signal and the sound exposure level (SEL) accounting for the emitted energy with time (Southall et al., 2007). The impact on marine mammals could be divided into three main categories that range from behavioural changes caused by noise, acoustic interference with signals used for communication and localization to physiological damage of the hearing system of marine mammals (Richardson et al., 1995; Nowacek et al., 2007). Hearing thresholds are defined by Southall et al. (2007) for the cetaceans in three groups which are sensitive in different frequency bands. These groups are defined as low-frequency (LF-) cetaceans, mid-frequency (MF-) cetaceans and high-frequency (HF-) cetaceans which are sensitive in the frequency ranges between 7 Hz - 22 kHz, 150 Hz - 160 kHz and 200 Hz - 180 kHz, respectively. As marine seismic source signals, especially from airguns, are strongest below 150 Hz they interact most with the LF-cetaceans which include mainly baleen whales (Southall et al., 2007). Airguns also emit signal above 150 Hz which are often of no interest for seismic imaging and hence could be reduced. The high frequencies from seismic acquisition are related, for instance, to the steep rise time of the main peak when the air is rapidly released from the airgun (Groenaas et al., 2016) or due to cavitation processes as discuss by Khodabandeloo (2018). Studies on the impact of seismic airgun surveys on baleen whales are presented by Di Iorio and Clark (2010), Dunlop et al. (2015), Dunlop et al. (2016) or Cato et al. (2013). The impact on the hearing of harbor porpoises after exposure to airguns is discussed by Kastelein et al. (2017). The influence of a single watergun on odontocetes, which are toothed whales, is investigated by Finneran et al. (2002). Concepts on how to monitor marine mammals and mitigate the impact of seismic surveys on marine life are presented by Nowacek et al. (2015) and Racca and Bröker (2018). How injury zones or protection areas around seismic sources are computed is demonstrated by Laws (2012), Breitzke and Bohlen (2012), Ainslie et al. (2016) or Tulett and Laws (2016). When marine mammals are observed within this zone the acquisition needs to be stopped. Kragh et al. (2012) and Laws (2013) discuss ways to reduce the seismic source strength without sacrificing too much quality of the recorded seismic data. Alternative marine seismic sources that could reduce the environmental impact were also discussed in Section 1.2.3. Further studies on the impact of seismic surveys on fish are presented by Wardle et al. (2001), Popper (2005), Fewtrell and McCauley (2012) or Carroll et al. (2017).

1.5 Contributions

In the following my contributions to the articles presented in this thesis are listed together with additional work that was performed during the period of my PhD.

Paper 1 (Chapter 2) Wehner, D., and M. Landrø, 2017. Low-frequency acoustic signal created by rising air-gun bubble. Geophysics 82(6), P119-P128.
The work was performed by Daniel Wehner as the lead researcher and author. Martin Landrø participated as a supervisor.

Paper 2 (Chapter 3) Wehner, D., Landrø, M., Amundsen, L., and H. Westerdahl, 2018. Frequency-depth-dependent spherical reflection response from the sea surface - a transmission experiment. Geophysical Journal International 214(2), 1206-1217.
The work was performed by Daniel Wehner as the lead researcher and author. Martin Landrø participated as a supervisor. Lasse Amundsen contributed with comments to the data analysis, discussion and the manuscript. Harald Westerdahl contributed with comments to the discussion and assisted with the Comsol model.

Paper 3 (Chapter 4) Wehner, D., Landrø, M., and L. Amundsen. The Impact on Low Frequencies from Very Shallow Air Guns in Marine Seismic Acquisition - An Experimental Study. *Submitted to Geophysics in October 2018.*
The work was performed by Daniel Wehner as the lead researcher and author. Martin Landrø participated as a supervisor. Lasse Amundsen shared the data from the field experiment and contributed to the discussion and analysis.

Extended Discussion (Chapter 5) Wehner, D., Svensson, P., and M. Landrø. The Coupling of Marine Seismic Source Signals into Air. *Extended investigation and discussion*

on Chapter 3 and 4
The work was performed by Daniel Wehner as the lead researcher and author. Martin Landrø participated as a supervisor. Peter Svensson helped with the modelling of the acoustic signal generated by a moving surface and contributed with comments to the discussion and manuscript.

Paper 4 (Chapter 6) Wehner, D., and M. Landrø. The Impact of Bubble Curtains on Seismic Air Gun Signatures and its High Frequency Emission. *Manuscript in preparation*.
The work was performed by Daniel Wehner as the lead researcher and author. Martin Landrø participated as a supervisor.

Paper 5 (Appendix) Wehner, D., Borges, F., Liu, Y., and M. Landrø. Tube wave monitoring - detect shear modulus and S-wave velocity changes in the formations surrounding wells. *Manuscript in preparation*.
The work was performed by Daniel Wehner as the lead researcher and author. Martin Landrø participated as a supervisor. Filipe Borges modelled the changes of the shear modulus for CO_2 injection, helped with the velocity estimation of the tube wave, wrote some parts of the manuscript related to the changes caused by CO_2 injection, assisted for some experiments and contributed to the discussion. Yi Liu helped with the velocity estimation of the tube wave.

Below, additional conference proceedings and technical articles are listed which are not included in this thesis

Wehner, D., Liu, Y., and M. Landrø, 2017. Estimate the Shear Wave Velocity Close to Wells from Tube Waves - An Experimental Study. EAGE Fourth Sustainable Earth Sciences Conference, Tu SES4 12.

Landrø, M., Wehner, D., Vedvik, N., and P. Ringrose, 2017. Detecting and Mapping Gas Leakage Events in Shallow Marine Sediments. EAGE/SEG Research Workshop Trondheim, Th CO2 04.

Borges, F., Wehner, D., and M. Landrø, 2018. Calculation of Tube Wave Velocity in a Shallow Borehole Using Passive Seismic Recordings. 80th EAGE Conference and Exhibition, Extended Abstracts,Th P4 03.

Wehner, D., and M. Landrø, 2018. The Impact of Bubbly Water on Airgun Signatures. EAGE Marine Acquisition Workshop, We MA 09.

Wehner, D., Borges, F., and M. Landrø, 2018. Using Well Operation Noise To Estimate Shear Modulus Changes From Measured Tube Waves - A Feasibility Study, Fifth CO2 Geological Storage Workshop, Fr CO2 04.

Landrø, M., Wehner, D., Vedvik, N., Ringrose, P., Løv Løhre, N. and K. Berteussen. Gas flow through shallow sediments - laboratory experiments compared to passive and active seismic field data. *Submitted to the International Journal of Greenhouse Gas Control in September 2018*.

1.6 Experimental data availability

Parts of the data from the experiments presented in this thesis are accessible on the site below via the item Research Data.
`https://explore.openaire.eu/search/project?projectId=corda__h2020::4fd88476be793fa7221dfd08861eb938`

For further information and questions about the data you could directly contact the author via:
`https://www.researchgate.net/profile/Daniel_Wehner2`

In addition, an interesting study on airgun measurements was conducted within the E&P Sound and Marine Life Joint Industry Project, referred to as Svein Vaage Broadband Airgun Study (Mattson, 2010). It is planned to make the data freely available within 2019 and further information can be found on the website from the JIP, Sound and Marine Life (2018) and Bröker et al. (2018).

Chapter 2

Low-frequency acoustic signal created by rising air-gun bubble

Daniel Wehner[1] **and Martin Landrø**[2]
[1] *NTNU, Department of Geoscience and Petroleum, 7031 Trondheim, Norway*
[2] *NTNU, Department of Electronic Systems, 7491 Trondheim, Norway*

published in Geophysics, Vol. 82, No. 6 (November-December 2017); P. P119-P128. DOI: 0.1190/GEO2016-0674.1

2.1 Abstract

In the seismic industry there is increasing interest in generating and recording low frequencies, which leads to better data quality and can be important for full waveform inversion. The air gun is a seismic source with a signal that consists of the main impulse (1), oscillating bubble (2) and rising of this air bubble (3). However, there has been little investigation of the third characteristic. We demonstrate a low frequency signal that could be created by the rising air bubble and show the contribution to the low frequency content in seismic acquisition. We use a simple theory and modeling of rising spheres in water and compute the acoustic signal created by this effect. We conduct tank and field experiments with a submerged buoy that is released from different depths and record the acoustic signal with hydrophones along the rising path. The experiments simulate the signal from the rising bubble separated from the other two effects (1,2). Furthermore, we use data recorded below a single air gun fired at different depths to investigate if we can observe the proposed signal. We find that the rising bubble creates a low frequency signal. Compared to the main impulse and the oscillating bubble effect of an air gun signal, the contribution of the rising bubble is weak, in the order of 1/900 depending on bubble size. By using large air gun arrays tuned to create one big bubble, the contribution of the signal could be increased.

The enhanced signal could be important for deep targets or basin exploration as the low frequency signal is less attenuated.

2.2 Introduction

The interest in enhancing the low frequency content in seismic data has increased within the last years as there are three main benefits due to broadband seismic data. Low frequencies reduce the sidelobes of wavelets leading to higher resolution, they penetrate deeper into the earth as they suffer less from attenuation and low frequency data are important for seismic inversion (ten Kroode et al., 2013). A general overview of recent advances in broadband seismic is given by Robertsson et al. (2013) who divide the topic in benefits of low frequency data, new methods in processing, imaging processes and advances in acquisition of low frequency data. This study focuses on acquisition and more precisely on a source mechanism of seismic air guns that potentially could create low frequencies.

In marine seismic acquisition the data recording has improved due to two main approaches. On one hand, data is recorded with variable depth streamers. Dhelie et al. (2014) show data from a snake streamer acquisition where the receivers are located at different depths while Soubaras and Lafet (2013) explain processing techniques for variable streamer depth acquisition. Additionally, Hicks et al. (2014) demonstrate that advanced processing of flat streamer data could reveal similar results as advanced processing of variable depth streamer. On the other hand, multi-component receivers are used to measure pressure and particle velocity (Carlson et al., 2007) at the same depth. Using proper processing techniques, both methods reduce the notches in the frequency spectrum that are related to the ghost reflections from the surface (Ikelle and Amundsen, 2005). The improved data quality is achieved by separation of the up- and downgoing wave field. Furthermore, Landrø et al. (2014) suggest to use geophones instead of hydrophones at the ocean bottom to record more signal in the low frequency band.

On the source side, Moldoveanu (2000) suggests to fire air guns on a vertical source array configuration where two air gun arrays are located at different depths. These arrays can be fired simultaneously or with a little time delay between individual air guns (Abma and Ross, 2013). Firing source arrays at different depths with a time delay to create a constructive downgoing wave field is beneficial for low frequencies (Cambois et al., 2009). Shooting the air guns at variable depths is another approach to improve the frequency content of the signal (Haavik and Landrø, 2015). These methods are still under investigation and the more complicated the shooting pattern the more demanding is the processing of the data. If the processing can be handled, the sequential shooting at various depths seems promising for an increased low frequency signal.

As the previous developments are related to array design, there are also improvements on single sources. Coste et al. (2014) present a new design of air guns that reduces amplitudes at high frequencies to mitigate the effect on marine mammals. In addition, major research efforts are carried out on marine vibrators. On land, seismic vibrators can produce low frequency signals very efficiently and reproducible (Wei et al., 2012). In the marine area, this is still challenging. However, Pramik et al. (2015) and Ozasa et al. (2015) show promising results for this technique. Furthermore, Meier et al. (2015) illustrate a marine dipole source that would increase especially the energy content at the low frequency end of the spectrum. Recently, an ”FWI-friendly” vibrator-type source that focuses on creating ultra-low frequencies is presented by Dellinger et al. (2016).

In this paper we like to explore a mechanism from seismic air guns that could be partly responsible for the creation of low frequencies. Landrø and Amundsen (2014a) discussed the impact of source depth on the low frequency output where they found enhanced low frequencies (below 1 Hz) for shallow source depths at 3.00 m compared to 7.50 m. Based on this result, they suggested that these low frequencies could be created by the rising of the air gun bubble in the water column (Landrø and Amundsen, 2014b). We present a simple theory and modeling that explains the signal from a rising sphere that is extensively studied in fluid dynamics. Furthermore, we compare the theoretical results with data recorded during tank and field experiments where a submerged buoy is released from different water depths. The experiment should separate the signal created by the rising bubble from the main impulse and oscillating behavior of the air gun bubble which are much stronger in amplitude. Additionally, we check the model against single air gun recordings from different depths to demonstrate that the acoustic signal of a rising air bubble can be measured. Finally, we investigate the exploitation of the signal for real applications in seismic exploration and crustal studies. The results should prove the existence of the signal from a rising air gun bubble and hence reinforce the proposed mechanism by Landrø and Amundsen (2014b).

2.3 Theory

We are interested in the acoustic signal created by a rising air bubble only. Therefore, the movement of a sphere through a fluid and the corresponding pressure distribution around the sphere are described.

If a sphere is submerged in water, gravity, buoyancy and drag are the forces acting on the object. The problem is well described in fluid dynamics where it is seen similar to the flow around a fixed sphere (Morrison, 2013). The force balance, assuming that the movement is in z-direction only, is given as (Morrison, 2013)

$$F_B - F_G - F_D = ma_z \;, \tag{2.1}$$

with

$$F_B = V\rho_f g \;, \tag{2.2}$$

$$F_D = \frac{1}{2}\rho_f C_D A v_z^2 \;, \tag{2.3}$$

$$F_G = V\rho_s g \;, \tag{2.4}$$

where F_B is the buoyancy, F_D the drag and F_G the gravitational force. The volume and cross-sectional area of the sphere are denoted by $V = \frac{4}{3}\pi R^3$ and $A = \pi R^2$ with radius R, while ρ_s is its density and m the mass. The density of the fluid is ρ_f, g is the gravitational acceleration and C_D is the drag coefficient that depends on the fluid type. The vertical velocity and acceleration is denoted by v_z and a_z, respectively. Equation 2.1 can be reorganized to solve for the acceleration

$$a_z = \frac{F_B - F_G - F_D}{m} \; . \tag{2.5}$$

Integration of Eq. 2.5 gives us the velocity, and further integration gives the position of the sphere (Halliday et al., 2003).

$$v_z = \int a_z dt \tag{2.6}$$

$$z = \int v_z dt \tag{2.7}$$

The velocity v_z is an important quantity for the source term of the acoustic signal as we will see later. The buoyancy and gravitational force are constant assuming that the size and density of the sphere are not changing and g is constant. However, the drag force depends on v_z and C_D (Eq. 2.3) that change over time. The drag coefficient C_D is dependent on the Reynolds number that discriminates between laminar and turbulent flow and is given as (Morrison, 2013)

$$Re = \frac{v_z D}{\nu} \; , \tag{2.8}$$

where D is the diameter of the sphere and ν the kinematic viscosity of the fluid. The empirical relation between drag coefficient and Reynolds number is shown in Figure 2.1 (Morrison, 2013). So far we are able to describe the movement of a rising sphere assuming perfect spherical shape with a constant size and density.

The pressure distribution surrounding the sphere created from this movement depends on the flow regime, whether it is laminar or turbulent. For laminar flow the pressure distribution C_P is given as (Michelson, 1970)

$$C_P = 2\frac{R^3}{r^3} - 3\frac{R^3}{r^3}sin^2(\theta) - \frac{R^6}{r^6}cos^2(\theta) - \frac{R^6}{4r^6}sin^2(\theta) \; , \tag{2.9}$$

where r is the distance to the observation point and θ is the angle surrounding the sphere. Figure 2.2(a) shows the pressure around a sphere for laminar flow where the amplitude is normalized to the maximum value. For Reynolds numbers higher than $Re = 2100$ turbulent flow is expected (Reynolds, 1883). Achenbach (1972) already performed flow experiments around a fixed sphere within a turbulent flow regime where the pressure behind the sphere changes with respect to laminar flow. Figure 2.2(c) shows results for different Reynolds numbers where we have negative pressure behind the sphere instead of positive pressure as in the laminar case. We modify Eq. 2.9 according to the experimental results from Achenbach (1972). The pressure distribution from 0 to 110 degrees is assumed to be the

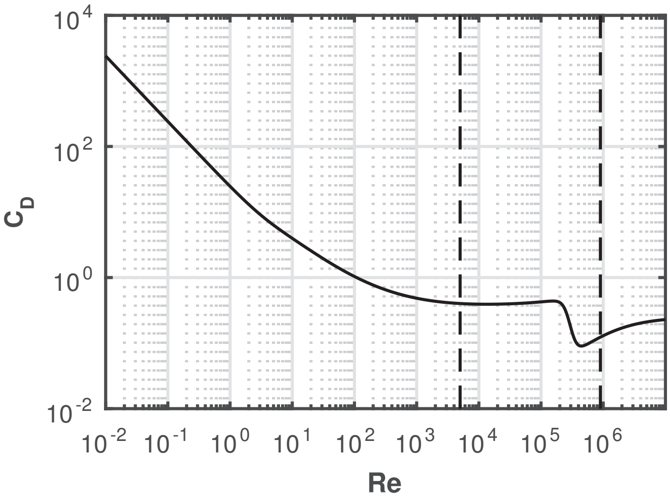

Figure 2.1: Empirical relation between drag coefficient and Reynolds number from experimental data (Morrison, 2013). The area between dashed lines indicates expected Reynolds numbers for our experiments.

same as for the laminar case, whereas the pressure distribution from 110 to 180 degrees is set to a fixed value taken from the angle at 110 degrees. This leads to a negative pressure behind the sphere (Figure 2.2(b)) fitting the experimental data from Achenbach (1972).

The source strength which gives the acoustic energy density emitted by the rising sphere is controlled by its velocity v_z (Eq. 2.6). A terminal, constant velocity will be achieved when the forces (Eq. 2.1) are in balance which defines the upper limit for the source strength. The source term can be written as (Morrison, 2013)

$$S = \frac{\rho_f v_z^2}{2} \, . \tag{2.10}$$

The modified Eq. 2.9 combined with Eq. 2.10 is the pressure field emitted from the rising sphere in the near-field with an amplitude decay of $\frac{R^3}{r^3}$ (Eq. 2.9). Hence, the near-field pressure is given as

$$p_{near} = S\, C_P \, . \tag{2.11}$$

We estimate the transition between near- and far-field r_{far} at three times the source size that is described by the radius R. In the far-field the amplitude decay is $\frac{R}{r}$ according to (Gilmore, 1952) and the emitted pressure can be written as

$$p_{far} = S\, C_P(r_{far})\, \frac{R}{r} \, . \tag{2.12}$$

Here, we assume that the movement of a rising sphere is similar to the movement of the wall of an oscillating bubble as described by Gilmore (1952). This assumption is valid for the movement vertically below the sphere. For radiating angles deviating from the vertical line this assumption is less exact as the movement from the sphere is only upwards and not towards the center as during an oscillation of a sphere. Furthermore, the pressure calculations hold for the case of an incompressible fluid. This could be assumed as the rising velocity of the sphere is much smaller than the velocity of acoustic sound in water (Gilmore, 1952). However, this is a simple theory describing the acoustic pressure emitted by a rising sphere which we think is comparable to the rising of an air gun bubble.

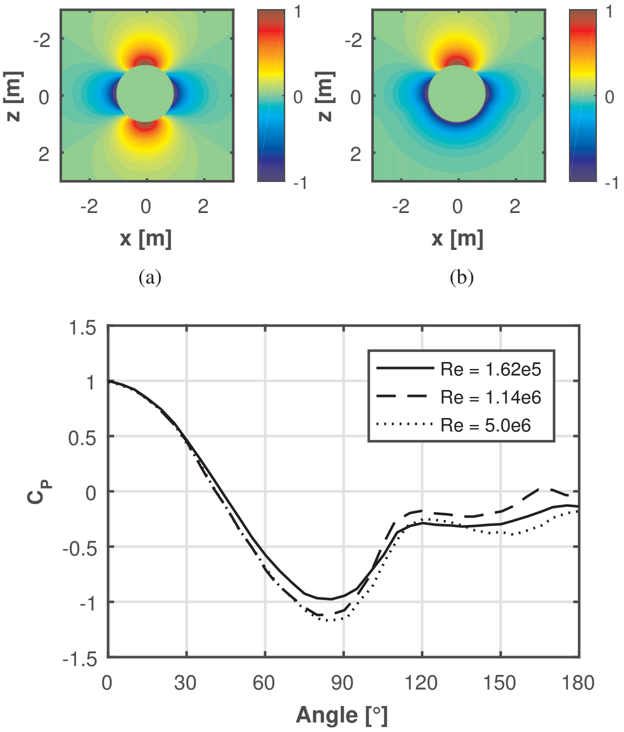

(a) (b)

(c)

Figure 2.2: (a) Pressure distribution around sphere at laminar flow (Michelson, 1970) and (b) modified pressure distribution for turbulent flow according to results of Achenbach (1972). The flow direction is vertical, pointing in negative z-direction. (c) Experimental data from (Achenbach, 1972) for a turbulent flow around a fixed sphere. All amplitudes are normalized to the maximum positive pressure value.

2.4 Modeling

The movement and acoustic pressure from the rising sphere are modeled according to the theory. The problem is solved with a finite difference approach using a two-stage explicit

Runge-Kutta method (LeVeque, 2007)

$$U^{mid} = U^n + \frac{1}{2} f(U^n) \Delta t \; , \tag{2.13}$$

$$U^{n+1} = U^n + f(U^{mid}) \; , \tag{2.14}$$

where U denotes the depth z, velocity v_z, or acceleration a_z of the sphere, and Δt is the time step, where the time $t = n\Delta t$ ($n = 1, 2, ...$). The initial depth z^0 is known and we assume an initial velocity v_z^0 close to zero which we can use to compute the initial acceleration a_z^0. First, the quantities v_z and z are computed between two adjacent time steps with the Euler method according to Eq. 2.13.

$$v^{mid} = v^n + \frac{1}{2} a^n \Delta t \tag{2.15}$$

$$z^{mid} = z^n + \frac{1}{2} v^n \Delta t \tag{2.16}$$

In a second step the drag coefficient, using the Reynolds number (Eq. 2.8) and empirical relations (Fig. 2.1), and the drag force (Eq. 2.3) can be computed for the midpoint. Hence, we can calculate the acceleration a^{mid} (Eq. 2.5) at the same position. We can use these values to compute our quantities for the next time step

$$v^{n+1} = v^n + a^{mid} \Delta t \; , \tag{2.17}$$

$$z^{n+1} = z^n + v^{mid} \Delta t \; . \tag{2.18}$$

Now, we can compute the drag coefficient, drag force, and acceleration a^{n+1} for the new time step and repeat the scheme. As we have the description of the moving sphere (z, v_z, a_z) at all times, we can use the velocity to model the pressure field surrounding it using Eq. 2.11 and 2.12.

The two-stage explicit Runge-Kutta method has second order accuracy (LeVeque, 2007). But keep in mind that we make several assumptions to simplify the problem as stated at the end of the Theory section.

2.5 Experiments

We perform experiments in a water tank and in open sea where submerged buoys of different sizes are released from several depths. We denote the three different buoy sizes by bouy A, B and C. Due to practical reasons buoy A and B are used in the tank while buoy B and C are used in the field experiment. The important parameters of all buoys are listed in Table 2.1. In both experiments Bruel & Kjær hydrophones of the type 8105 are used which have a frequency range between 0.1 Hz and 180 kHz. Additionally, the rising buoy is recorded on video in the tank and field experiment to measure the depth at different time steps and hence the velocity of the buoy.

Furthermore, we use data from an air gun experiment where a single gun was fired at different depths in open sea (Landrø and Amundsen, 2014b).

Buoy dimensions			
Buoy name	A	B	C
Radius, R [m]	0.10	0.12	0.145
Mass, m [kg]	0.7	1.1	2.0
Effective density, ρ_b, [kg/m^3]	167	152	157

Table 2.1: Essential parameters of the three buoys used for the experiments.

2.5.1 Buoy experiment in the tank

Figure 2.3 shows the setup for the tank experiment. The depth and width of the tank are indicated in the figure and the length is 6.00 m, around 3.00 m to each side of the buoy. A weight at the bottom and a rope are used to submerge and release the buoy from four different depths denoted by z_s. A four hydrophone array is placed along the rising path of the buoy where the first one (H1) is closest to the water surface. A video camera, located at half the depth z_s, records the rising sphere with 30 fps which means that a photo is taken every 33 ms.

The major advantage of the tank experiment is the high accuracy that can be achieved for the release depth z_s, the depth of the hydrophones and the offset between source and

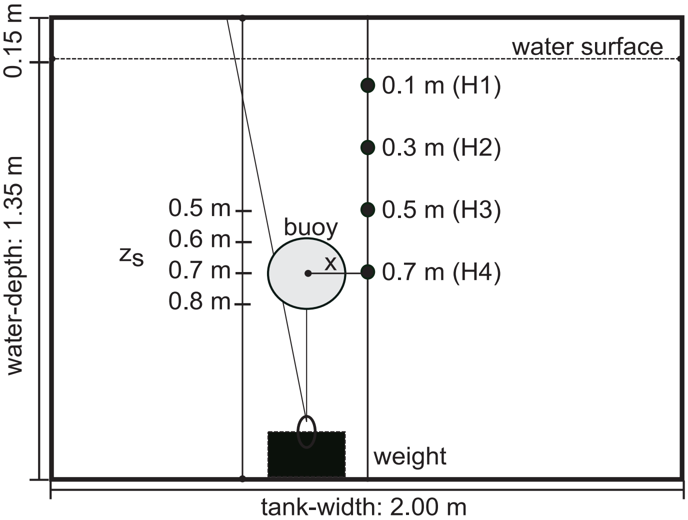

Figure 2.3: Cross-section of setup for buoy experiments in the tank. The depth and width of the tank are indicated and the length is 3.00 m to each side of the buoy. H1, H2, H3 and H4 denote the hydrophones, z_s the release depth of the buoy and x the offset between source and receiver.

receiver. However, some issues occur during the experiment which should be mentioned. The rising buoy creates small gravity waves while it gets close to the surface that could interfere with the signal of interest. Due to the limited size, side and surface reflections are expected. We think these are negligible as we conduct the test in the middle of the tank and measure the signal very close to the source. Although we have high precision of the receiver and source geometry, the buoy is not a perfect sphere and turbulences are created while the buoy rises. Therefore, the buoy is not rising along a straight vertical line which could lead to errors in offset and hence in the amplitude estimation.

2.5.2 Buoy experiment in the field

The field experiment is conducted in a fjord in Norway and the setup is similar to the tank experiment (Figure 2.4). During this test only two hydrophones are available. The release depths z_s and the offset x are larger compared to the tank experiment. Due to practical reasons, buoy B and C are used for these tests. The rising buoy was again recorded by a video camera located approximately at half the release depth.

The test was carried out to reproduce the signal from the tank experiment without a limiting medium in x- and y-direction. One major disadvantage of this test is less accuracy in the

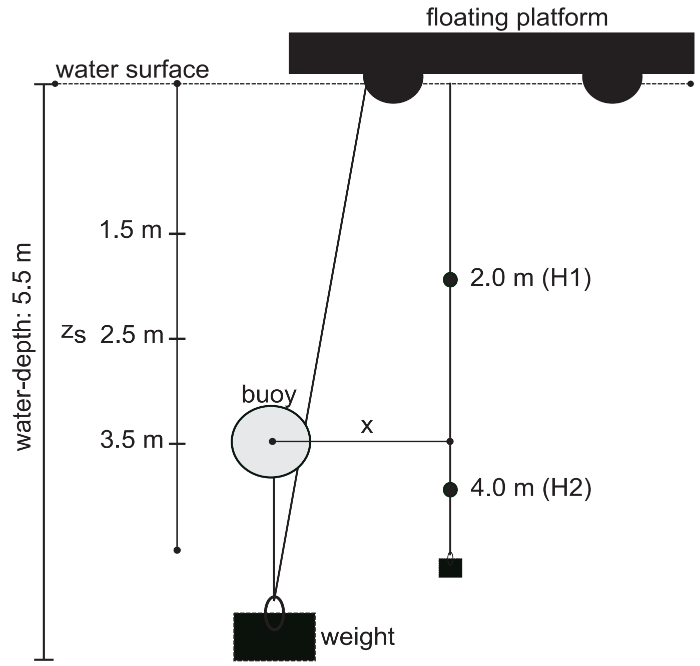

Figure 2.4: Cross-section of setup for buoy experiments in the field. H1 and H2 denote the hydrophones, z_s the release depth of the buoy and x the offset between source and receiver.

position of the buoy and hydrophones, because the visibility within the water was less than 4 meters and the experiment was influenced by tidal effects. This led to errors for the release depth within ± 0.8 m. As already mentioned the buoy is not rising along a straight vertical line. This effect is more pronounced if the release depth is increased. Additionally, the background noise is higher than in the tank experiment which was also increased by a fishing farm a few hundred meters away.

2.5.3 Airgun experiment in the field

We use air gun data recorded during a field test in a Norwegian fjord some years ago (Landrø and Amundsen, 2014b). A single 600 cubic inch air gun was fired at four different depths which are 3 m, 5 m, 7.5 m and 10 m, respectively (Figure 2.5). A hydrophone recorded the signal at a constant distance of 20 m below the air gun. The total water depth was 390 m and the weather conditions were excellent what led to good repeatability of single shots at the same depth. That an air gun creates stable signatures is demonstrated by Dragoset et al. (1987). The signatures of the air gun fired at the same depth show similar characteristics for the signal under investigation.

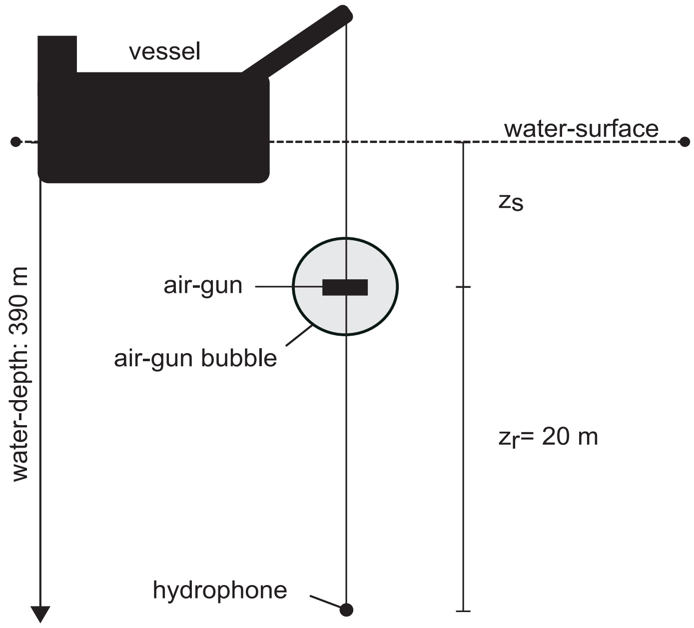

Figure 2.5: Cross-section of setup for air gun experiments in the field. The gun is fired at four different depth z_s (3 m, 5 m, 7.5 m, 10 m) and the vertical offset z_r is constant.

2.6 Results

The results of the buoy experiments in the tank, field and the air gun data will be compared with the model to demonstrate that the proposed negative acoustic signal is created by a rising bubble and that it is measurable. The amplitudes of the acoustic signal are given in bar and 1 bar = 10^5 Pa.

2.6.1 Buoy in the tank

First, we compare the video recorded data with the modeled movement of a sphere to show that the simple theory is a good approximation explaining the mechanism that is responsible for the signal we are looking for. In Figure 2.6 the modeled depth and velocity for the release of buoy B at z_s = 0.75 m is compared with depth measurements taken from the video. The measured velocity is computed from the depth data. The maximum error between a measured and modeled depth is approximately 6 cm. This could be due to the simplified model, but also to errors in the depth measurement as only one photo every 33 ms is taken. We also recognize that the velocity reaches the terminal, constant velocity at 0.25 s, before it slows down. The decreasing velocity in the model is due to less buoyancy forces when the buoy is partly above the water surface. The good fit between the modeled and measured movement confirms that the main behavior of the buoy is described by the model.

We compare the measured acoustic signal from the rising buoy in the tank with the mod-

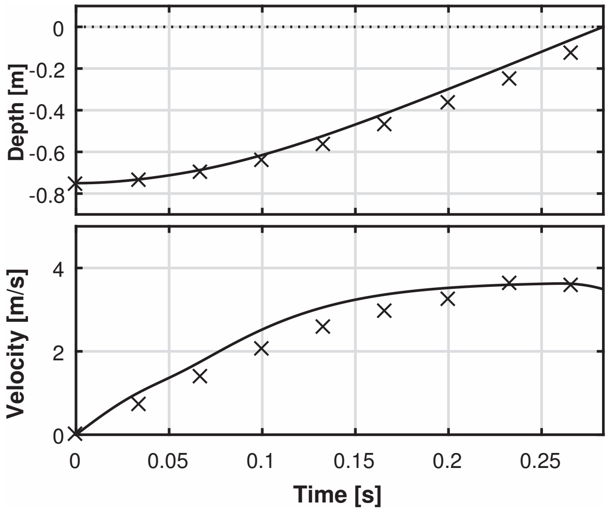

Figure 2.6: Modeled (solid line) vs. video measured (crosses) depth position of buoy B in the tank during rising (top) and modeled (solid) vs. video measured (crosses) velocity of buoy B in the tank during rising (bottom).

eled signal using the proposed theory. It should be mentioned that the recorded data is not processed. Figure 2.7 illustrates the measured and modeled data for buoy A for two different release depths and an offset of x = 0.15 m. The time starts when the buoy is released and the model stops when the center of the buoy has reached the surface which is indicated by the vertical dotted line in the figure. We observe that the model has a good fit with the measured data showing the negative signal that we expect when the buoy passes the hydrophone. Also the duration of the signal increases while the source depth increases (Figure 2.7(b)). The difference in amplitude between measured and modeled data could be due to the fact that the buoy is not rising along a straight vertical path and hence the offset in the experiment is changing while it is constant in the model. That is confirmed as the difference in amplitudes is more pronounced for the deeper release depths where the rising path could deviate more from a straight vertical line. The amplitudes for the negative signal of H1 and H2 in Figure 2.7(b) are very similar indicating that the buoy could have reached the terminal velocity. This is not the case for the shallow release depth (Figure 2.7(a)) as the rising time is too short to reach the terminal velocity. The signal after the buoy has reached the surface, behind the dotted line, is probably related to gravity waves in the tank due to the buoy breaking the surface.

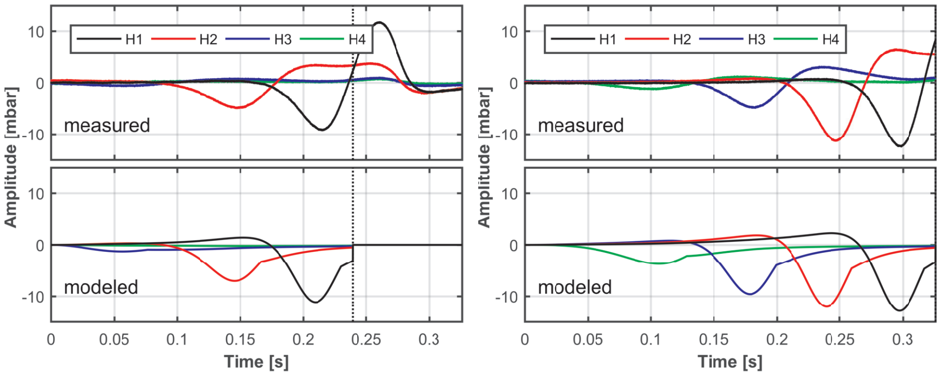

(a)

(b)

Figure 2.7: (a) Measured (top) and modeled signal (bottom) for the rising buoy A from a depth of z_s = 0.50 m. (b) Measured (top) and modeled signal (bottom) for the rising buoy A from a depth of z_s = 0.80 m in the tank according to Figure 2.3. The vertical dotted line indicates the time when the center of the buoy is at the water surface.

In Figure 2.8 we compare the measured and modeled data for the same release depths, but using buoy B and an offset of x = 0.18 m. The model fits the measured data well with some differences in the amplitude. These are probably also due to changing offsets while the buoy is rising. It should be noticed that the duration of the signal is shorter for buoy B than A as the buoyancy of the bigger buoy is higher and hence it rises faster. The higher velocity v_z leads to higher amplitudes that could be observed if you compare Figure 2.7 and 2.8 carefully. The difference should be bigger if the same offset in both experiments is used.

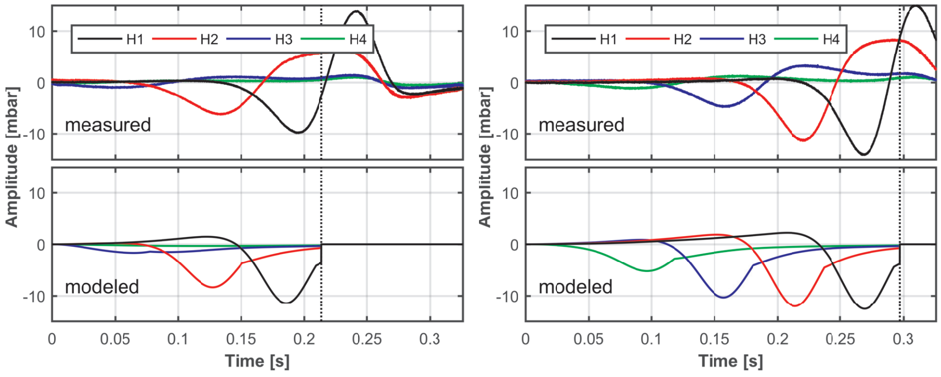

(a)

(b)

Figure 2.8: (a) Measured (top) and modeled signal (bottom) for the rising buoy B from a depth of z_s = 0.50 m. (b) Measured (top) and modeled signal (bottom) for the rising buoy B from a depth of z_s = 0.80 m in the tank according to Figure 2.3. The vertical dotted line indicates the time when the center of the buoy is at the water surface.

2.6.2 Buoy in the field

We can verify the model once more by comparing it with the video recordings acquired during the field experiment. The modeled and measured depth and velocity are shown in Figure 2.9(b). Additionally, a sequence of pictures illustrates the data used for measuring the depth (Figure 2.9(a)). The sequence starts at the upper left and finishes at the lower right panel while going from left to right. The time step between the pictures is 50 ms while a picture every 8 ms exists for the plots of Figure 2.9(b). We observe that the model predicts a faster rising than the measured data with a maximum error of 13 cm for a depth point. The deviation is higher than for the tank experiment which could be due to the increased release depth. Therefore, the rising path deviates even more from a straight line which leads to errors in the estimated rising time. Additionally, the release of the buoy was more complicated because of the deep water depth and simple release mechanism, what could also create deviations between modeled and measured rising times.

Due to the high uncertainties in the release depth and the offset it is difficult to adjust the model to these conditions. Therefore, we only use the measured data from different depths and both hydrophones (Figure 2.4) to demonstrate that the same signal is created in open sea and for bigger offsets. The recorded signal for three release depths and an offset of x = 1.25 m for buoy C can be seen in Figure 2.10. The acoustic signal is 45 Hz low pass filtered to remove background noise (e.g. electrical noise) and the signals are aligned to the high amplitude, high frequency signal at approximately 2.9 s (dashed line). This signal is related to the time when the buoy breaks the surface and hits the platform (Figure 2.4) which is therefore a good trigger at the end of the rising path.

We notice the higher noise level within the first second of the recording, but also that a

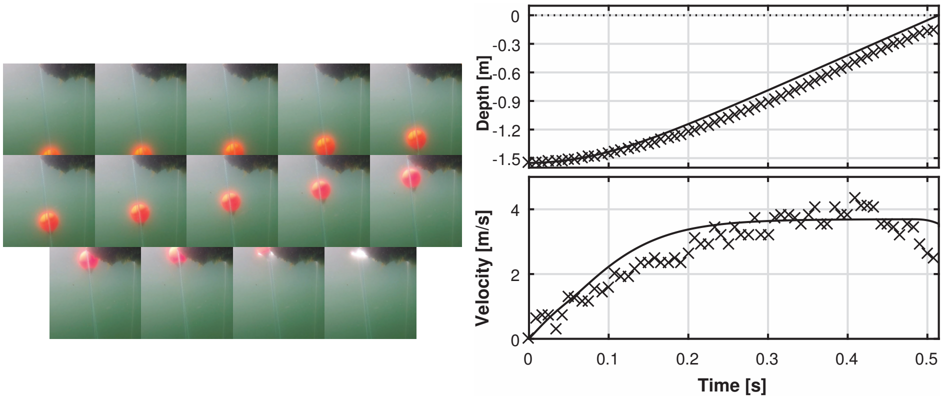

(a) (b)

Figure 2.9: (a) Sequence of pictures from rising buoy with time step of 50 ms. (b) Modeled (solid line) vs. video measured (crosses) depth position of buoy C in the field during rising (top) and modeled (solid) vs. video measured (crosses) velocity of buoy C in the field during rising (bottom).

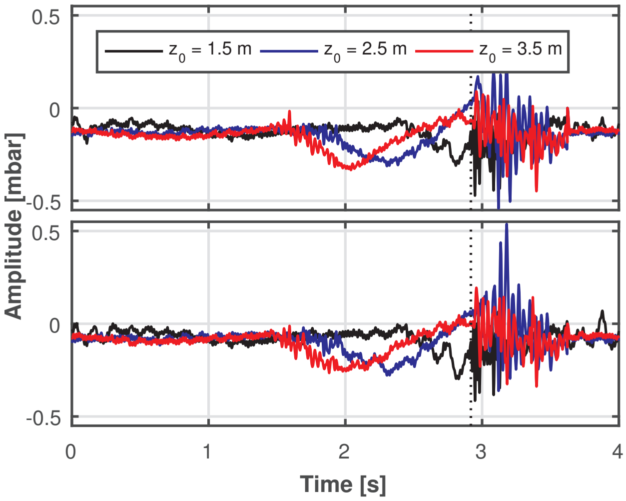

Figure 2.10: Recordings of H1 (top) and H2 (bottom) for release depths of 1.5 m, 2.5 m and 3.5 m according to Figure 2.4. The signals are aligned to the buoy breaking the surface (at 2.9 s), indicated by the vertical dotted line.

negative pressure signal starts around 1.5 s for the deepest release (red curve) and later for the shallower releases. As the hydrophones are deeper than the buoy for most time during the rising, this demonstrates the negative pressure below the buoy. Also the duration of the signal increases with increasing depth. The amplitudes at each hydrophone are similar for all depths which is reasonable if we assume that the terminal velocity is achieved 0.25 s after the release (Figure 2.9(b)). Furthermore, we observe higher amplitudes for H1 which is explained by the shorter offset to the buoy while it rises. It should be also mentioned that the negative signal has more high frequency noise than in the tank. This could be due to the higher background noise or to high turbulences as buoy C reaches higher velocities than A and B in the tank.

2.6.3 Airgun in the field

We need to estimate the size and density of the air gun bubble to compare our model with the measured data. The Rayleigh equation is used to estimate the radius of the air gun bubble and then different percentages of the maximum radius are used for the modeling. This should be a simple approximation to account for the oscillating bubble, as different radii have different rising velocities. For the biggest air bubble according to the shallowest firing depth we use a radius of 75 $\%$ of the maximum value, that is 1 m. The radii of deeper firing depths are chosen the same way with percentages of 70 $\%$, 65 $\%$ and 60 $\%$, respectively. These differences should account for more and shorter oscillations that occur at deeper depths. Additionally, the bubble gets more dissolved during longer rising paths and therefore further away from a spherical shape. The density of the air gun bubble is assumed to be 230 kg/m^3, estimated from a fit to the modeled data. The deviation from the density of air is due to the oscillating effect where the air is expanded and compressed. Furthermore, the air gun bubble is not a perfect sphere and can contain water particles that increase its density.

Figure 2.11(a) shows the recorded air gun signal 20 m below the source which is fired at four different depths. The main impulse occurs at time t = 0 s and the amplitude scale is cut at 15 mbar to get more focus on the signal afterwards. We observe that the amplitude of the oscillating bubble increases and its period decreases with increasing water depth. In Figure 2.11(b) the same signal is plotted, but zoomed to a different time window and filtered with a 5 Hz low pass filter. The difference in amplitude scale between Figure 2.11(a) and 2.11(b) should be noticed. Additionally, the modeled signal of a rising sphere is displayed in Figure 2.11(b) (dotted lines). The model stops when the center of the sphere is at the surface and therefore it is shorter for shallow release depths.

On one hand, we observe that the negative signal has the biggest amplitude for the shallowest firing depth; that could be related to the biggest bubble radius while the amplitude is decreasing for deeper source depths. On the other hand, the duration of the negative signal increases with increasing source depths. This is probably related to the longer rising path. Furthermore, the signal is smooth for the shallowest source depth whereas it becomes more indistinct with increasing depth. This could be due to the fact that the air bubble gets more dissolved on its rising path and this is more pronounced for longer ways. In addition, the amplitude decreases gradually after its maximum negative value which could be explained by the increasing distance between the rising bubble and the hydrophone. In general, the amplitude fit between the modeled and measured data is quite good and also the increasing period fits to some extent. There are still several deviations between the modeled and measured data. These are probably due to the simplified model neglecting the oscillations of the bubble and compressible flow. However, the goal was to separate

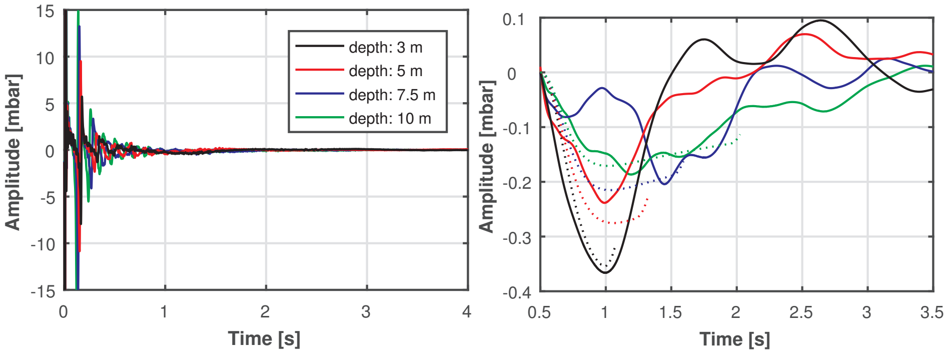

(a) (b)

Figure 2.11: (a) Recorded air gun signature, 150 Hz low pass filtered, at hydrophone according to Figure 2.5. (b) Zoom on recorded data between 0.5 s and 3.5 s, 5 Hz low pass filtered (solid line). Modeled signature of rising sphere (dashed line); the model stops when the sphere reaches the surface. Notice the different amplitude scale between (a) and (b).

the signal of a rising bubble from the oscillating effect and the main features of decreasing amplitude and increasing period with increasing source depth are explained by the model.

2.7 Discussion

We were able to measure a low frequency acoustic signal created by a rising sphere by dedicated buoy experiments. The signal found in the air gun data is likely to be the rising air bubble which would confirm the far-field radiation of this acoustic signal. The simple theory and model is in good agreement with the experimental data and hence reinforces the proposed mechanism. However, the contribution of this effect compared to the main impulse and oscillating behavior from the air gun bubble seems to be very small (Figure 2.11). For a source depth of z_s = 7.5 m the near-field amplitude for the main impulse is 3.5 bar-m and for the rising bubble signal 0.0038 bar-m, while the main frequencies of both signals are 60 Hz and 2 Hz, respectively. This leads to an amplitude ratio in the near-field of 1:900 for the single air gun experiment, which would differ depending on the bubble size.

For a better comparison of both signal strengths we illustrate a simple example of reflection seismic. The 3D model consists of a thin water layer where the source and receiver are located at a depth of z_s = 7.5 m and z_r = 30 m, respectively. Below the water layer the acoustic medium consists of a homogeneous sand layer with a thickness of d = 3000 m on top of a homogeneous half-space. The interface simulates the target area for our reflection example. We like to estimate the amplitudes of both signals recorded at the receiver after travelling through the medium as the impact of attenuation and source ghost depends on the frequency. The amplitudes at the receiver can be estimated as

$$A(f_i) = A_0(f_i)\, R\, G\, e^{\left(\frac{\pi f_i z}{Q v_m}\right)}\, H(f_i)\,, \tag{2.19}$$

where the medium velocity v_m and quality factor Q are assumed to be constant, z is the distance the signal has travelled and $A_0(f_i)$ is the near-field amplitude. The main frequencies of the impulse and rising air gun bubble are indicated by f_1 and f_2, respectively, with i = 1,2. The reflection coefficient at the interface to the half-space and the geometrical spreading are given as R and $G = \frac{1}{z}$, while $H(f_i) = |2\sin(\frac{2\pi f_i z_s}{c})|$ is the source ghost function with c as the sound velocity in water.

Results for amplitudes $A(f_i)$ for different combinations of medium velocities v_m and Q-values are listed in Table 2.2. For the computation the reflection coefficient is assumed to be $R = 0.2$ according to a velocity and density change of 10% between both layers. We observe that the higher the attenuation (smaller Q) or slower the velocity the smaller are the amplitudes $A(f_i)$. Additionally, the advantage of low frequencies becomes obvious. The impact of different medium parameters on the low frequency signal from the rising bubble is less compared to the high frequency signal and hence the low frequency signal is especially valuable for media with low v- and Q-values. However, the noise on streamer data in rough weather has amplitudes around 46e-6 bar for frequencies below 5 Hz and 6e-6 bar for higher frequencies (Landrø et al., 1989). During calm weather the noise level could be reduced by a factor of 3 or 4, leading to optimal noise amplitudes around 11e-6 bar for the low and 1.5e-6 bar for the high frequencies. While the signal of the main impulse is above the noise level, the signal of the rising bubble is too low to be recorded. Therefore, we need to find a way to enhance the signal and increase its contribution in the far-field.

v_m [m/s]	Q	$A(f_1)$ [bar]	$A(f_2)$ [bar]
3000	150	18.0e-6	0.014e-6
3000	300	63.2e-6	0.015e-6
4000	150	33.7e-6	0.015e-6
4000	300	86.5e-6	0.016e-6

Table 2.2: Amplitude of main impulse, $A(f_1)$, and rising bubble signal, $A(f_2)$, after travelling through 3D medium with common medium parameters (v_m, Q) for a sandstone (Mavko et al., 1998).

Our experimental data is recorded from a single air gun, whereas in practice big arrays and clusters are used for exploration. Therefore, an obvious solution is to tune air gun arrays in the way that they create one big bubble (Hopperstad et al., 2012). The main advantage of these hyperclusters is that the bubble time period, and at the same time the low frequency output, is increased. However, enhancements of even lower frequencies could be due to the rising of a big bubble. As a thought experiment we assume an air gun cluster with a circular shape (Figure 2.12) which could possibly create one big bubble. We compute new near-field amplitudes using our modeling for a rising sphere. We take the same density for the bubble as for the single air gun bubble, but increase the radius for the bubble created by the proposed array design which is towed at 7.5 m depth. This array configuration could, in theory, be expanded to create even bigger bubbles. In practice, clusters are limited to the strength of mechanical structures and the supply of high pressure air into one small location. This simple example should only illustrate which bubble sizes are roughly required to create applicable signals. Further investigation needs to be done on the separation between single guns, whether a frequency-locked array or an array with coalesced bubbles is optimal for the enhancement of this source mechanism (Laws et al., 1990). For bigger air bubbles, the source depth is also an important factor that needs to be taken into account.

Results for the achieved near-field amplitude for the low frequency signal at 2 Hz could be enhanced as seen in Table 2.3 according to our thought experiment. The first four amplitudes up to a radius of 1 m are measured from the experimental data where different radii result from the difference in source depth. The amplitudes for bigger radii are modeled assuming a rising sphere. If we were able to create a big bubble with R = 15 m, near-field amplitudes of the low frequencies would be increased by a factor of approximately 450 compared to a single air gun.

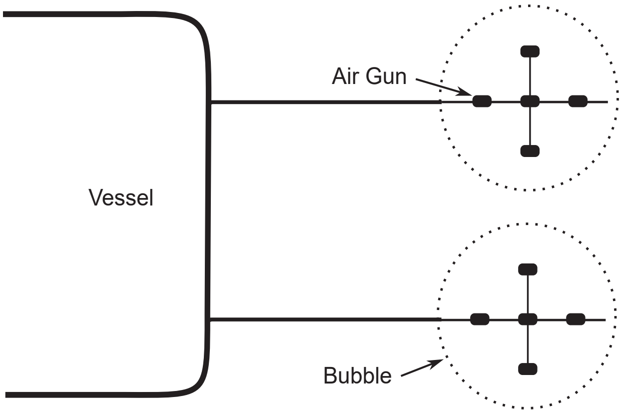

Figure 2.12: Possible array design for creating one big air bubble to enhance the proposed low frequency signal. A bubble with $R \approx 3$ m could be expected for these number of air guns.

For field applications we have to take the attenuation, geometrical spreading, reflection coefficient and especially the source ghost effect into account (Eq. 2.19). Therefore, we compute the far-field amplitudes for the low frequency signal after it has travelled through the same 3D medium as used earlier. Again, we assume two different velocities v_m and Q-values (Table 2.4). We also assume that the source is fired at three different depths z_s to demonstrate the impact of the ghost. We use a main frequency of 2 Hz, but it should be noted that this frequency will slightly change according to the source depth.

Two main features should be noted from the results in Table 2.4. First, the well known effect of increased amplitudes in low frequencies with increasing source depth can be seen, assuming that the bubble size is constant. Secondly, the signal strength will be

bubble radius R [m]	amplitude [bar-m]
0.66	0.0030
0.75	0.0038
0.86	0.0049
1	0.0065
3	0.0520
6	0.2090
9	0.6180
12	1.5120
15	3.1830

Table 2.3: Near-field amplitude of signal from rising bubble for source depth of z_s = 7.5 m. Measured single air gun amplitude for $R \leq 1$ m and computed amplitude for bigger bubble radii $R > 1$ m using the proposed model.

case 1: v_m = 3000 [m/s], Q = 150				
z_s [m]	R = 6 m	R = 9 m	R = 12 m	R = 15 m
7.5	8.05e-7	2.38e-6	5.82e-6	12.3e-6
10	1.07e-6	3.17e-6	7.76e-6	16.3e-6
15	1.61e-6	4.75e-6	11.6e-6	24.5e-6
case 2: v_m = 4000 [m/s], Q = 300				
7.5	8.48e-7	2.51e-6	6.13e-6	13.0e-6
10	1.13e-6	3.34e-6	8.17e-6	17.2e-6
15	1.69e-6	5.00e-6	12.2e-6	25.8e-6

Table 2.4: Computed far-field amplitudes (in bar) for the low frequency signal from a rising air gun bubble after travelling through a 3 km thick 3D medium with velocity v_m and quality factor Q. The amplitude is given for different source depths z_s and radii R of the bubble.

above the noise level for calm weather conditions, if the bubble radius exceeds 12 m. The amplitudes of the low frequency signal could be higher, if we are interested in diving waves as we can neglect the reflection coefficient. Changing the array design could also have negative impacts on the overall signal output which was not investigated here. However, we demonstrated that there could be contributions from this source mechanism to the low frequency end of the spectrum.

The maximum size of an air gun bubble that is achievable in field applications is mainly an engineering issue and is not addressed in our investigations. Another approach to make the signal from the rising air gun bubble applicable is to reduce the low frequency noise on the recorded data. A better signal to noise ratio at these frequencies might be achieved by the usage of 4C ocean bottom recordings instead of streamer data (Halliday et al., 2015; Landrø et al., 2014).

2.8 Conclusions

The proposed mechanism that a moderate part of low frequencies could be created by the rising air gun bubble could be confirmed from tank and field experiments which are supported by a simple model. Further contributions could be due to the spike shape of the main impulse. The signal from the rising air gun bubble shows increasing length and decreasing amplitude with increasing source depth, while it is clearer for shallow source depths where less dissolution of the bubble on its rising path is expected. These features agree with the theory and model. The contribution from the rising bubble signal to the frequency spectrum of a single air gun source in the far-field is insignificant. However, there could be contributions from this mechanism if huge air gun clusters are used and tuned as suggested here. This might could exploit the mechanism to make it feasible for exploration purposes, especially for investigations of deep targets and crustal studies. The estimations are made on a simple model and therefore it needs further investigations whether this mechanism can contribute significantly within field applications. This involves more complex modeling with different array designs and studies of field data.

2.9 Acknowledgements

We acknowledge the European Union's Horizon 2020 research and innovation programme under the Marie Skłodowska-Curie grant agreement No 641943 for the funding of Daniel Wehner's PhD project within WAVES. We like to thank Statoil ASA for contributing the air gun recordings where Å. S. Pedersen and M. Thomson have designed and conducted the field work. We like to acknowledge the technical team at IPT for their support to the experimental setup. Daniel Wehner thanks Kjetil E. Haavik for fruitful discussions. Martin Landrø acknowledges financial support from the Norwegian Research Council. The editor and unknown reviewers are acknowledged for their constructive comments.

Chapter 3

Frequency-depth dependent spherical reflection response from the sea surface - A transmission experiment

Daniel Wehner[1], Martin Landrø[2], Lasse Amundsen[3] and Harald Westerdahl[4]
[1] *NTNU, Department of Geoscience and Petroleum, 7031 Trondheim, Norway*
[2] *NTNU, Department of Electronic Systems, 7491 Trondheim, Norway*
[3] *Statoil Research Centre, 7053 Trondheim, Department of Geoscience and Petroleum, Trondheim, 7031 Norway.*
[4] *Statoil Research Centre, 7053 Trondheim.*

published in Geophysical Journal International, Vol. 214, Issue 2 (August 2018); P. 1206-1217. DOI: 10.1093/gji/ggy196

3.1 Abstract

In academia and the industry, there is increasing interest in generating and recording low seismic frequencies, which lead to better data quality, deeper signal penetration and can be important for full-waveform inversion. The common marine seismic source in acquisition is the air gun which is towed behind a vessel. The frequency content of the signal produced by the air gun mainly depends on its source depth as there are two effects which are presumed to counteract each other. First, there is the oscillating air bubble generated by the air gun which leads to more low frequencies for shallow source depths. Secondly, there is the interference of the downgoing wave with the first reflection from the sea surface, referred to as the ghost, which leads to more low frequencies for deeper source depths. It is still under debate whether it is beneficial to place the source shallow or deep to generate the strongest signal for frequencies below 5 Hz. Therefore, the ghost effect is studied in more detail by measuring the transmission at the water-air interface. We conduct experiments in a water tank where a small-volume seismic source is fired at different depths below the water surface to investigate how the ghost varies with frequency and depth. The signal from the seismic source is recorded with hydrophones inside water and air during the test to estimate the transmitted signal through the interface. In a second test, we perform experiments with an acoustic source located in air which is fired at different elevations above the water surface. The source in air is a starter gun and the signals are again recorded in water and air. The measured data indicates an increasing transmission of the signal through the water-air interface when the source is closer to the water surface which leads to a decreasing reflection for sources close to the surface. The measured results are compared with modeled data and the existing theory. The observed increase in transmission for shallow source depths could be explained by the theory of a spherical wave front striking the interface instead of assuming a plane wave front. The difference can be important for frequencies below 1 Hz. The results suggest that deploying a few sources very shallow during marine seismic acquisition could be beneficial for these very low frequencies. In addition, the effect of a spherical wave front might be considered for modeling far field signatures of seismic sources for frequencies below 1 Hz.

3.2 Introduction

The almost perfect reflection of acoustic waves at the water-air interface is a well known effect in many applications. In seismic acquisition the first reflection from the sea surface that follows the downgoing source signal is referred to as the ghost which is a main problem for generating low frequencies. The signal created by a single marine seismic source like the air gun or water gun propagates spherically in all directions. Due to the short time delay, the ghost reflection is overlapping with the downgoing wave field. This leads to unwanted effects as certain frequencies vanish due to destructive interference depending on the source depth. Especially, low frequencies approaching 0 Hz are thought to vanish completely due to the ghost. This assumption is correct for a reflection coefficient of -1 which is independent of frequency and source depth. In practice this approximation often seems to be sufficient. However, a more detailed description of the reflection from the sea surface depending on source depth and frequency could lead to new considerations in seismic acquisition and better processing of seismic data.

There are several effects which can have an impact on the ghost reflection. First, the source signature can vary due to interaction between the source and an interface like the sea surface. The impact on cavities or air bubbles close to the water surface was studied by several authors on small scales, mostly in the range of mm. Chahine (1977) and Blake and Gibson (1981) performed experiments with electrodes to create cavities near the water-air interface. They conclude on a distance between the cavity and interface within the cavity is interacting with the boundary. This happens when the cavity-interface distance is less than three times the maximum radius of the cavity. A numerical study of the interaction between a bubble and the water-air interface is illustrated by Wang et al. (1996). For seismic sources there are studies on the interaction of air bubbles in clustered air gun arrays when they are close to each other (Strandenes and Vaage, 1992). Due to these interactions the source signature is changing (Giles and Johnston, 1973) as neighbouring source bubbles act as a boundary. The changing bubble time period caused by the interaction of clustered guns is demonstrated by Barker and Landrø (2012).

Secondly, the reflection coefficient can vary due to the shape and properties of the interface itself. The changing reflection coefficient for different surface topographies, due to wind and weather, is described in theory by many authors (Brekhovskikh and Lysanov, 1991; Hovem, 2007; Jensen et al., 2011). This weather effect mainly has an impact on high seismic frequencies as demonstrated by Kryvohuz and Campman (2017). Klüver and Tabti (2015) illustrate how the reflection coefficient could be estimated from dual-sensor streamer data. Additionally, recent theoretical analyses demonstrates that a monopole sound source would radiate more acoustic energy into air than expected if the source depth is much less than the emitted acoustic wavelength (Godin, 2006; McDonald and Calvo, 2007; Godin, 2008; Glushkov et al., 2013). This phenomenon is caused by the evanescent component of the wave inside water which can be converted to a homogeneous wave inside air for specific wave numbers. Calvo et al. (2013) and Voloshchenko and Tarasov (2013) conducted acoustic experiments using sound sources ranging from 1 kHz to 20 kHz and they verified the increased signal transmission from water to air for shallow source depths relative to the wavelength. Another theoretical study by Deng et al. (2012) illustrates a similar effect for a moving point source underwater. Therefore, it might be possible to use recorded sound in air emitted from marine seismic sources to measure properties of the atmosphere.

Thirdly, an almost perfect, frequency independent reflection coefficient is based on the assumption of plane wave propagation. However, marine seismic sources emit spherical waves which cause a frequency and depth dependent reflection as shown by Brekhovskikh and Lysanov (1991) and Aki and Richards (2002). The spherical reflection response deviates most from the plane wave reflection coefficient for low frequencies, or more precisely for wavelength larger than the source-interface distance. This effect is demonstrated by Li et al. (2017a), Li et al. (2017b) and Yan et al. (2017) for AVO (amplitude versus offset) analysis of seismic data between two acoustic media.

This research opens up on the question if the reflected signal from the surface decreases for shallow source depths relative to the emitted wavelength. If this is the case, the destructive interference within the low frequency range between the initially downgoing wave field and ghost reflection is less than in a model of a constant reflection coefficient close to -1 and that would be beneficial for generating low frequencies. Recently presented experimental results from Amundsen et al. (2017) indicate an increased low frequency signal for shallow large-volume single-gun sources. We conduct experiments in a water tank to measure the transmitted signal from sources at varying distances to the water-air interface. We focus on the transmission and reflection from a source placed in water. In addition, a second experiment with a source in air is conducted. The transmission from air to water is discussed by many authors in ocean acoustics for large ranges (Hudimac, 1957; Young, 1973; Lubard and Hurdle, 1976). The sources are placed in water and air to investigate the transmission from both sides of the interface. The experimental results should provide a better understanding of the transmitted and reflected signal when the source is fired close to the sea surface and hence the depth is small compared to the acoustic wavelength. We compare the reflection from the sea surface assuming models for plane and spherical waves. The change of the reflected signal within the low frequency band is of special interest.

3.3 Theory

We are interested in the transmitted and reflected signal at the water-air interface and how this might change with source depth and frequency. Therefore, the plane wave reflection coefficient and spherical wave reflection response for a flat interface between two acoustic media are compared (Figure 3.1).

Plane waves are characterized by a constant phase and amplitude on the plane that is perpendicular to the direction of propagation (Kinsler et al., 1962). These planes are indicated as lines in 2D in Figure 3.1 (bottom). From this assumption, the plane wave reflection and transmission coefficients at a flat fluid-fluid interface are defined as (Kinsler et al., 1962)

$$R_{pp} = \frac{\rho_2 c_2/cos(\theta_2) \; - \; \rho_1 c_1/cos(\theta_1)}{\rho_2 c_2/cos(\theta_2) \; + \; \rho_1 c_1/cos(\theta_1)} \tag{3.1}$$

$$T_{pp} = \frac{2 \; \rho_2 c_2/cos(\theta_2)}{\rho_2 c_2/cos(\theta_2) \; + \; \rho_1 c_1/cos(\theta_1)} \tag{3.2}$$

where ρ_i and c_i with $i = 1, 2$, denote the density and velocity of the respective layer (Figure 3.1). The incident and reflected angle is indicated by θ_1 and θ_2 is the angle of refraction where θ_2 can be computed following Snell's law as (Huygens, 1690)

$$\theta_2 = \text{arcsin}\Big(\frac{c_2 \; sin(\theta_1)}{c_1}\Big). \tag{3.3}$$

At the water-air interface changes of the reflection and transmission coefficient for varying angles θ_1 are small, ranging from R_{pp} = -0.9994 at θ_1 = 0^o to R_{pp} = -1 at θ_1 = 90^o. The relation between reflection and transmission for a flat surface can be written as

$$R_{pp} = T_{pp} - 1 \tag{3.4}$$

Spherical waves that are incident and reflected from an interface can be expressed as the superposition of cylindrical waves following Sommerfeld's integral (Aki and Richards, 2002). The spherical wave reflection response at a flat fluid-fluid interface can be described

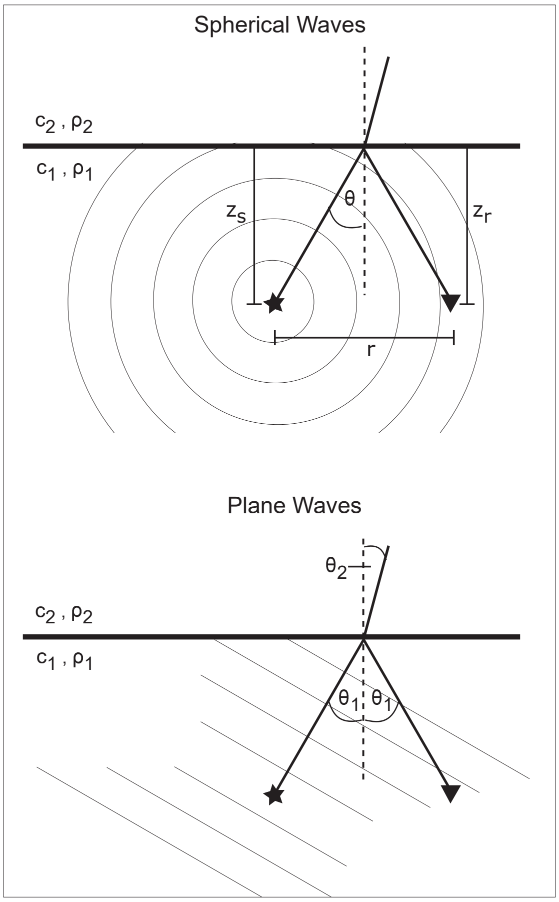

Figure 3.1: Spherical wave incident on a flat interface and important parameters for the computation of R_{sph} (top). Plane wave incident on a flat interface and important parameters for the computation of R_{pp} (bottom)

as the ratio between the reflected and incident wave and is given as (Li et al., 2017a; Ursenbach and Haase, 2006)

$$R_{sph} = \frac{\int_1^0 R_{pp}(x)\ \Psi\ dx + i\int_0^\infty R_{pp}(ix)\ \Phi\ dx}{\int_1^0\ \Psi\ dx + i\int_0^\infty\ \Phi\ dx} \tag{3.5}$$

$$\Psi = J_0(\omega r\sqrt{1-x^2}/c_1)e^{(i\omega x(z_r+z_s)/c_1)} \tag{3.6}$$

$$\Phi = J_0(\omega r\sqrt{1+x^2}/c_1)e^{(-\omega x(z_r+z_s)/c_1)} \tag{3.7}$$

where ω is the angular frequency, r is the horizontal offset between source and receiver, while z_r and z_s are the receiver-interface and source-interface distance, respectively (Figure 3.1, top). The integration variable is $x = cos(\theta_1)$ and J_0 is the zero-order Bessel function. As it depends also on the source and receiver depth and not only on the medium parameters, the spherical wave reflection is defined as a response rather than a coefficient. The same relation as in Equation 3.4 can be used to obtain the reflection response from measured transmitted signals

$$R_{sph} = T_{sph} - 1 \tag{3.8}$$

We notice that the plane wave reflection coefficient R_{pp} changes only with angle of incidence, whereas the spherical wave reflection response R_{sph} depends on the incident angle, frequency, source and receiver depths. The difference between both equations is illustrated in Figure 3.2 for varying frequencies and source depths. For the computation we use v_1 = 1500 m/s, ρ_1 = 1000 kg/m^3 for the parameters of water and v_2 = 340 m/s, ρ_2 = 1.25 kg/m^3 for those in air. We assume that the source and receiver depth are the same as the seismic source is so close to the water-air interface, that the ghost reflection is an inherent part of the source signature. Although the difference is small, the question remains if it can be recognized on measured data.

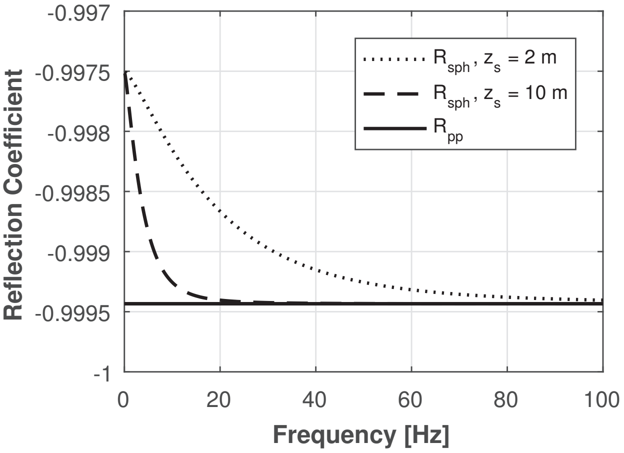

Figure 3.2: Plane wave reflection coefficient (solid line) and spherical wave reflection response for two different source depths (dotted and dashed line) at the water-air interface as a function of frequency.

3.4 Experiments

Two experiments are conducted to investigate the impact on the reflected and transmitted signal in relation to source depth and frequency. We perform a first experiment where a source is fired in water (A) and a second one where a source is fired in air (B). All experiments are performed in a water tank with a length of 6 m, a width of 2.5 m and the depth is 1.4 m, respectively (Figure 3.3(a)). The walls of the tank are equipped with 5 cm thick foam mattresses. Although it does not act as perfectly absorbing boundaries, previous tests showed an improved signal reception with smaller side reflections. For both experiments different receiver geometries are used to investigate the dependence of the transmitted signal on the source depth and incident angle on the water-air interface. Brüel & Kjær hydrophones of the type 8105 are used as receivers which have a frequency range from 0.1 Hz to 100 kHz. The hydrophones have the same sensitivity in water and air up to a frequency of 3 kHz. Therefore, we use the the same hydrophones to recorded the signal in air. Due to the fact that we use strong sources, the lower sensitivity compared to microphones is not an issue for our experiment. The receivers are not coupled to the tank during the experiments to avoid impacts on the measured low frequencies.

3.4.1 Experiment A: Source in Water

The source is a S15 water gun with one cylindrical gun port which is build for borehole applications (Figure 3.3(b)). The gun has a volume of 15 in^3 (ca. 0.25 l) for the water chamber as indicated by the model number S15. The water gun generates a high velocity water jet when the water is pushed out from the gun chamber. Due to the high velocity a cavity is created which collapses when the water jet slows down. The cylindrical gun port shape allows us to generate a cavity at a quite accurate position compared to the common radial gun ports with several openings. For more details on the water gun the reader is referred to Landrø et al. (1993). We conduct one experiment to investigate the impact of source depth on the vertically transmitted signal. A second experiment is performed where the receivers in air are moved to different offsets to investigate the impact of incident angle on the transmitted signal. The experimental set ups are as follows.

1. First, three hydrophones are located vertically above the estimated location of the cavity in air with a distance of z_r = -0.3 m, -0.2 m and -0.1 m to the water-air interface, while $y_r = y_s = 0$. We denote these hydrophones as H1, H2 and H3 (Figure 3.4). Then the water gun is fired three times at different source depths z_s, ranging from 0.2 m to 0.8 m with an increment of 0.1 m. Afterwards, the same experiment is repeated while the three hydrophones are located inside the water at depths of z_r = 0.3 m, 0.5 m, 0.7 m and a horizontal offset of y_r = 0.3 m between the cavity and receiver. We denote these hydrophones as H4, H5 and H6 (Figure 3.4). The offset in x-direction is estimated to be the same for the source and receivers which means $x_r = x_s$. This is the best acquisition we could get due to practical considerations in the laboratory.

2. For the second test, the source depth is constant at z_s = 0.3 m and the position of hydrophones H4, H5 and H6 is the same as in the first experiment. The receivers H1, H2 and H3 are moved to different y_r positions, ranging from 0 m to 0.6 m with an increment of 0.1 m, while x_r and z_r are also constant. For each receiver position the source is fired three times.

(a) (b)

Figure 3.3: (a) Photo of the water tank with dimensions 6 m x 2.5 m x 1.4 m. (b) Underwater photo with gun port of watergun on the left side (red arrow) and hydrophones in the middle.

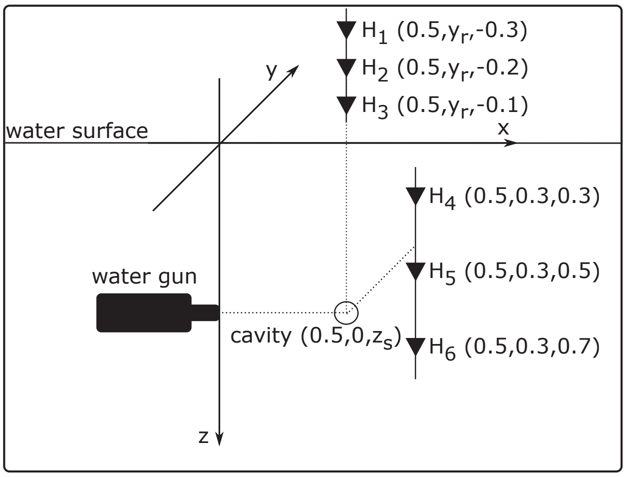

Figure 3.4: Schematic sketch of the experimental set up using the watergun as a source in water. Numbers in brackets indicate the coordinates (x,y,z) in meters.

3.4.2 Experiment B: Source in Air

The source is a Stalker R1 2.5″ gun that has a caliber of 0.38 in. (9 mm) and blank bullets, which for instance is used in athletics. The propellant of the bullet has a weight of 0.56 g and a caloric equivalent of 3.06 kJ/g which leads to a released energy of approximately 1.71 kJ for one blank bullet. The signalgun is fixed to the metal frame of the tank above the water surface and a near field hydrophone is attached to it (Figure 3.5(a)). The near field hydrophone is used to measure the source signature and trigger the recording during the experiments. Similar to experiment A, we conducted a test to investigate the impact of source elevation on the vertically transmitted signal. The experimental set up is as follows.

1. One hydrophone is placed inside water at a depth of z_r = 0.05 m indicated by H1.

The second hydrophone, H2, is located in air at z_r = -0.05 m (Figure 3.6). They are both located at $x_r = y_r$ = 0 m. The signalgun is also placed at $x_s = y_s$ = 0 m. During this test the source is moved to different elevations z_s, ranging from -0.2 m to -0.8 m with an increment of -0.1 m. At each source position the signalgun is fired four times.


(a) (b)

Figure 3.5: (a) Photo of the signalgun and near field hydrophone indicated by red the arrow. (b) Top view of the experimental set up with signalgun (red arrow) and hydrophones (blue arrow).

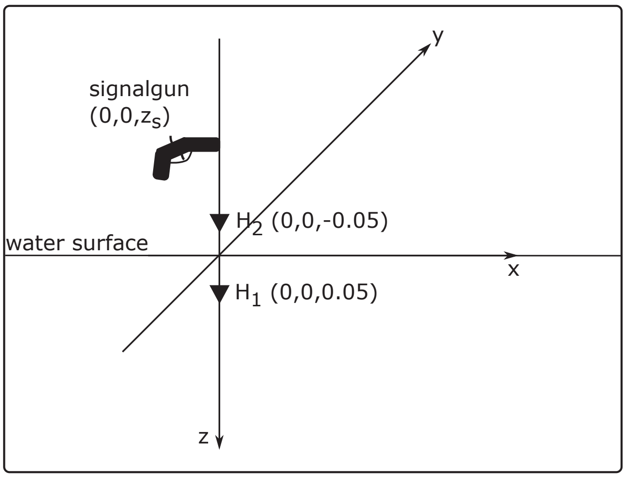

Figure 3.6: Schematic sketch of the experimental set up using the signalgun as a source in air. Numbers in brackets indicate the coordinates (x,y,z) in meters.

3.4.3 Source Signature and Repeatability

For the later estimation of the transmitted signal the maximum amplitudes of the signal recorded in water and air are compared. Therefore, the source signatures and their repeatability are investigated.

Figure 3.7 illustrates the signal recorded in water and air which is created by the watergun in experiment A for different frequency bands. The signature is characterized by a small positive peak between 0.01 s and 0.02 s when the water is pushed out of the gun chamber, followed by a negative peak due to the growing cavity. The main peak around 0.04 s is created by the collapse of the cavity. A second peak at 0.053 s can be recognized which is due to an oscillation of the cavity. The photos in Figure 3.7 illustrate the shape of the water jet at different times after the water gun is fired while the cavity is difficult to identify from these pictures. The water jet velocity can be roughly estimated from the pictures which leads to an averaged value of 30 m/s. For the lowest frequencies (Figure 3.7, top) both signals have almost the same shape, indicating that we can recorded the same signal in air

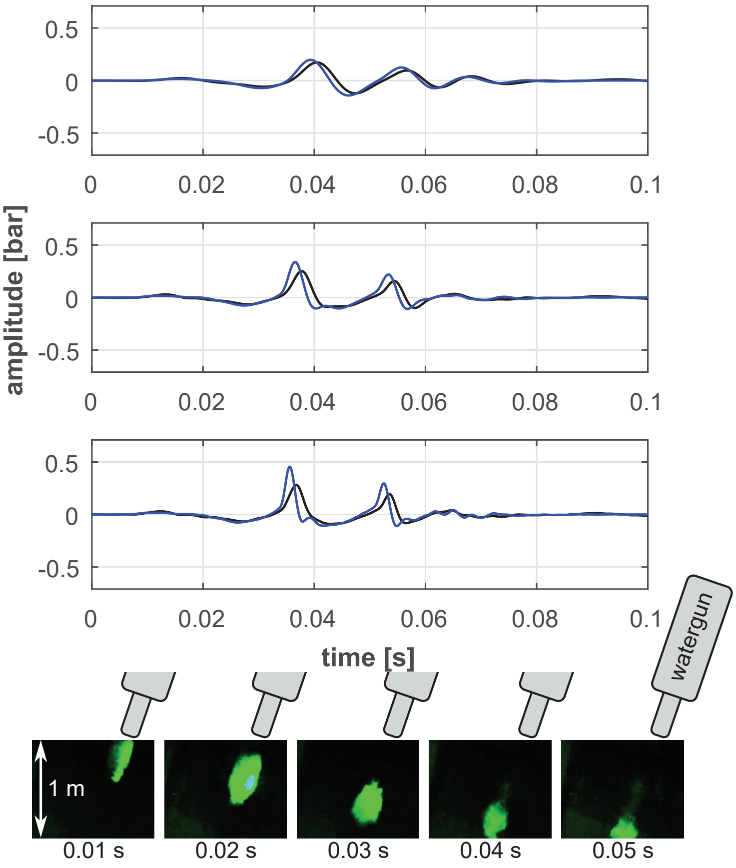

Figure 3.7: Recorded signal at hydrophone H2 in air (black) and H5 in water (blue) according to Figure 3.4. The signal of H2 in air is multiplied by a factor of 250. The source was fired at z_s = 0.3 m. The signal is filtered with a 10 - 100 Hz (top), 10 - 200 Hz (middle) and 10 - 300 Hz (bottom) bandpass filter. Photos show a top view of the created water jet while the watergun is fired according to different times. The position of the watergun is sketched.

and water. The time difference between both recordings fits to the source-receiver distance and the slower sound velocity in air compared to water. The phase within the different frequency bands is shifted due to the applied filter while the amplitude is unaffected which is important for our investigation. We notice that including higher frequencies in the signal (Figure 3.7, bottom) leads to more deviations between the signal in water and air which can be observed around 0.04 s and 0.06 s.

As the signal in water and air is not recorded at the same time during experiment A, the repeatability of the source signal is important. Therefore, we compare the relative difference of the maximum amplitude for one hydrophone Hi between repeated shots at the same depth as

$$\delta A(Hi) = \frac{\Delta A_{max}(Hi)}{A_{max}(Hi)} * 100 \tag{3.9}$$

where $A_{max}(Hi)$ is the mean maximum amplitude recorded at one hydrophone while i = 1, 2, 3 for the receivers in air and i = 4, 5, 6 for the receivers in water, respectively. The mean difference of the maximum amplitude between each repeated shot at the same depth is $\Delta A_{max}(Hi) = |A^n_{max}(Hi) - A^m_{max}(Hi)|$ where n = m = 1, 2, 3 indicate the shot number at each source depth z_s. The difference $\Delta A_{max}(Hi)$ is computed for all combinations of n and m, except for $n = m$. Then the mean value of all hydrophones in air is calculated as

$$\mu(\delta A) = \frac{1}{N}\sum_{i=1}^{N} \delta A(Hi) \tag{3.10}$$

where N is the total number of hydrophones which is three in our case. The same is repeated for the measurements in water and the results for each source depth are illustrated in Figure 3.8. It should be noted that the repeatability is better for deeper source depths as the cavity created near the surface is within the minimum operation depth of the water

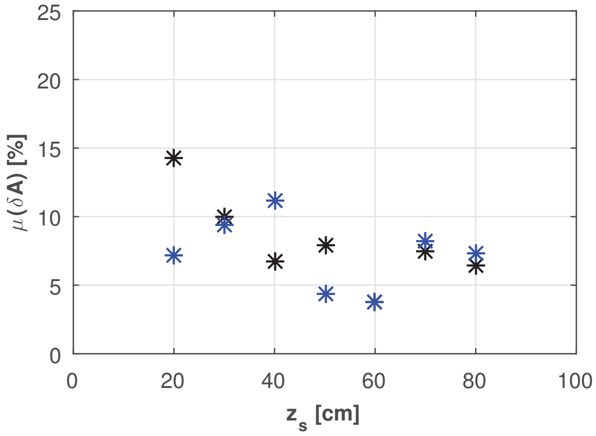

Figure 3.8: Relative difference $\mu(\delta A)$ between the mean maximum recorded amplitude and the difference amplitude between repeated shots for the signal filtered within 10 - 100 Hz for experiment A. For the hydrophones in air (black) and water (blue).

gun. The important aspect is that amplitude changes between repeated shots are less than changes due to varying source depth.

Figure 3.9 illustrates the signal recorded in water and air which is created by the signalgun in experiment B for different frequency bands. The signature is characterized by a main positive peak around 0.004 s which is caused by the firing of the signalgun. This can be seen on the photos taken during the shot (Figure 3.9). It should be mentioned that the photos and pressure recordings are not synchronized and hence there could be small deviations in time. The signal after the main peak could be caused by reverberations of the signalgun. Although the signal is weak for the lowest frequency range, the shape of

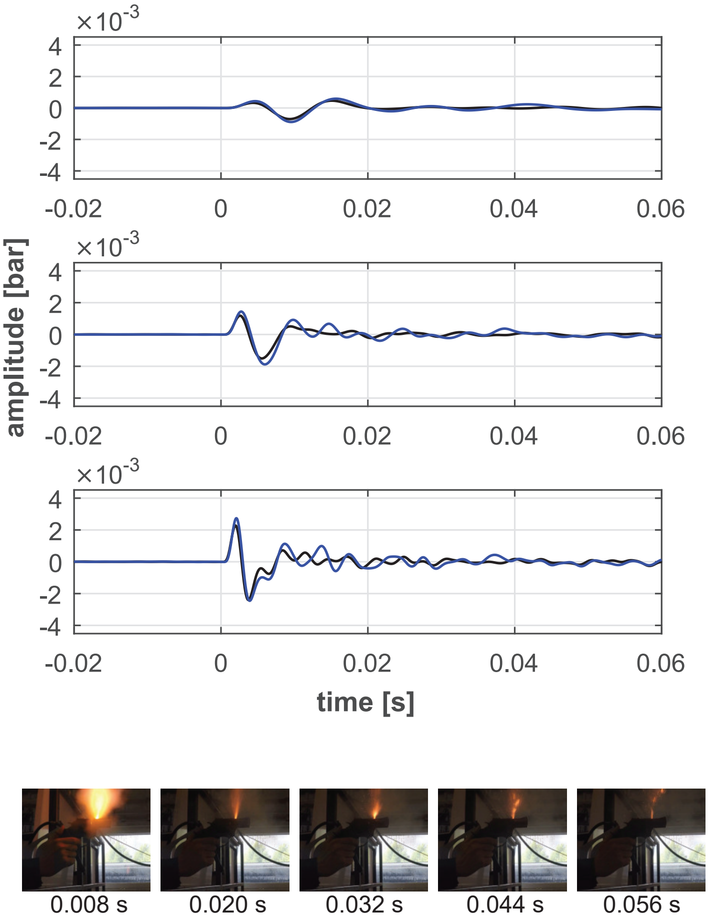

Figure 3.9: Recorded signal at hydrophone H2 in air (black) and H1 in water (blue) according to Figure 3.6. The source was fired at z_s = -0.3 m. The signal is filtered with a 10 - 100 Hz (top), 10 - 200 Hz (middle) and 10 - 300 Hz (bottom) bandpass filter. Photos show a side view of the signalgun while it is fired according to different times.

the main peak is similar for all plots (Figure 3.9), again indicating that we can recorded the same signal in air and water. The small time difference between both peaks fits to the source-receiver distance and the slower sound velocity in air compared to water. For higher frequencies deviations between the signal in water and air are stronger pronounced, especially after the main peak. However, we only consider the main peak for further investigations of the transmitted signal.

During experiment B the receivers are placed in water and air at the same time while the source is fired. Therefore, the repeatability investigation is not relevant. However, the radiation pattern of the signalgun is assumed to be more complex than a collapsing cavity. Therefore, we measure the radiation pattern of the signalgun in different planes (x-z and x-y) according to our experimental set up (Figure 3.6). We conclude that the signal emitted below the z_s-x plane in which the signalgun is located is similar in all directions.

3.5 Modeling

A modeling study is conducted to compare the measured results with modeled data and to investigate the impact of the tank dimensions on the experimental results. We simulate the data solving the 3D Helmholtz equation in a finite element scheme using the Comsol software. The maximum frequency of investigation is f_{max} = 300 Hz and the minimum velocity in the model is v_{min} = 340 m/s, leading to a minimum wavelength of λ_{min} = 1.13 m. A minimum of n = 8 mesh elements per wavelength and a time step of t_{step} = 1.25e-4 s is used which indicates a CFL (Courant-Friedrichs-Lewy) number of CFL = 0.3 (Courant et al., 1928). These parameters reveal a stable and accurate simulation in our case. As input source an averaged, measured near field source signature is implemented where the mean measured watergun signal from all experiments A is computed and filtered to the frequency range of investigation. The same is done for the modeling of experiment B where the source is in air. Therefore, the source depth and receiver offsets are the only parameters that change during the modeling according to the experimental set up. As we are mainly investigating the ratio between the maximum amplitude of the signal in air and water, this is an adequate approximation of the source.

An important issue for the experimental results is the limited size of the water tank. Although damping material is placed at the walls, side reflections will have a small impact on the measured data. Therefore, we simulate the transmitted signal within three different settings:

1. Tank Model: compute the transmission within a tank model according to the experimental set up. The 3D tank model consists of the metal tank, a foam layer, the water and a surrounding air medium.
2. Free-Field Model: compute the transmission for a two layer medium (water and air) without any tank boundaries using the same acquisition geometry as in the experiment.

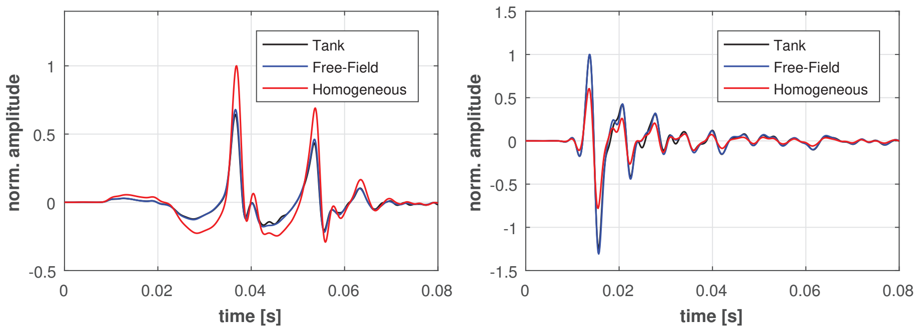

(a) (b)

Figure 3.10: (a) Modeled results at receiver H5 (Figure 3.4) for three different settings using the watergun signature. (b) Modeled results at receiver H2 (Figure 3.6) for three different settings using the signalgun signature.

3. Homogeneous Model: compute the wave propagation within a homogeneous (either water or air) medium using the same acquisition geometry as in the experiment.

The modeled results of all three settings at one receiver position are illustrated in Figure 3.10(a) for experiment A and in Figure 3.10(b) for experiment B. It should be noted that the results from the homogeneous model are close to the source input as the signatures are only influenced by geometrical spreading. There are small differences between the tank and free-field model which are caused by the limited size of our water tank. They are considered to be negligible as they are already difficult to identify. The results from the homogeneous model differ most from the other two which is caused by the reflected signal from the interface itself. Therefore, the results from the homogeneous model could be used to separate the incident and reflected wave.

There are some drawbacks in the modeling that should be mentioned. The implemented source signatures are not recorded exactly at the source position and might be already influenced by the experimental set up itself. In addition, the metal frame above the water surface (Figure 3.3 (a)) is not taken into account in the model due to complexity. This could especially lead to deviations between modeled and measured results for the experiment where the source is placed in air.

3.6 Results

The results from the transmission experiments in the water tank are compared with the modeled results to investigate a potential impact of the transmitted signal on source depth and frequency.

3.6.1 Experiment A: Source in Water

For a rough estimation of the transmission coefficient we compute the ratio between the mean maximum amplitude of all hydrophones in air H_{air} to those in water H_{water} as a function of the source depth z_s as

$$\frac{H_{air}}{H_{water}}(z_s) = \frac{1}{M}\left(\sum_{i}^{3}\sum_{j}^{3}\frac{A_{max}(Hi)}{A_{max}(Hj)}\,\frac{r_i}{r_j}\right) \tag{3.11}$$

where the total number of combinations is $M = i \cdot j$, r_i and r_j denote the source receiver distance for each individual hydrophone. The indices i = 1, 2, 3 and j = 4, 5, 6 denoted the hydrophones in air and water (Figure 3.4). The multiplication by r_i/r_j corrects for geometrical spreading. The linear assumption is found to be the best choice by comparing measured amplitudes at all hydrophones located in air after correction. The results for different source depths z_s are illustrated in Figure 3.11(a). The error bars indicate the standard deviation calculated from all ratios of each depth. The ratio is computed for three different frequency bands. Frequencies below 10 Hz are filtered out as the signal to noise ratio is too small for these low frequencies. The modeled results for the same acquisition geometry and frequency bands are shown in Figure 3.11(b). The modeled results agree well with the measured data, indicating the same trend and almost the same values for the ratio H_{air}/H_{water}. The deviations could be due to measuring inaccuracies or from the modelling as discussed in the Section Modeling.

First, we notice that the measured transmitted signal is 3 to 10 times higher than the expected theoretical value T_{pp} for plane waves. The plane wave transmission coefficient is computed using Equation 3.2 with a density and velocity of $\rho_2 = 1.25\frac{kg}{m^3}$ and $c_2 = 340\frac{m}{s}$ in air and $\rho_1 = 1000\frac{kg}{m^3}$ and $c_1 = 1500\frac{m}{s}$ in water, respectively. We assume a vertical incident angle ($\theta = 0$) as the receivers are directly above the source. In addition, more sig-

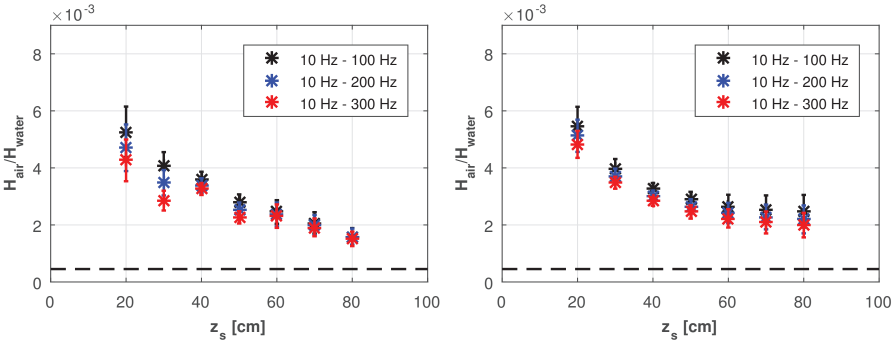

(a) (b)

Figure 3.11: (a) Measured amplitude ratio for different source depths according to Experiment A1. The amplitudes are corrected for geometrical spreading. The ratios are shown for different bandpass filters. The dashed line shows T_{pp}. (b) Modeled amplitude ratios for the same Experiment.

nal is transmitted into the air when the source is closer to the interface. This general trend agrees with the theory of a spherical wave transmission response (Figure 3.2). It should be mentioned that more signal seems to be transmitted for lower frequencies (Figure 3.11(a), black). However, these differences are small and within the error range of our measurements and hence it could not be verified with this data. The trend of increased transmission for lower frequencies could be better observed in the modeled data (Figure 3.11(b)).

In experiment A2 the source depth is constant and the hydrophones H1, H2, and H3 (Figure 3.4) are moved to different offsets to investigate the impact of the incident angle on the transmitted signal. The ratio is computed in the same way as before using Equation 3.11 but for a constant source depth and varying angles θ. The results are illustrated in Figure 3.12(a). The modelled results for the same acquisition geometry and frequency bands are shown in Figure 3.12(b). There is a good fit between the measured and modeled data, while the modeled H_{air}/H_{water} ratios are slightly lower than the measured values.

The results reveal a constant transmission until an angle of approximately $\theta = 45°$. For larger angles the ratio decreases similar to the trend of a plane wave transmission coefficient. However, the theoretical T_{pp} predicts a relative decrease of 50% for the transmitted signal at 60° compared to 0°. The decrease of the measured and modeled ratios is not as strong as the one predicted by the plane wave transmission coefficient. It should be mentioned that there is a small deviation between the amplitude ratios in Figure 3.11(a) and 3.12(a) at zero-offset and a source depth of $z_s = 0.3$ m, although they should be the same. This is due to the fact that both values are computed from different tests.

It has to be noted that both tests reveal a higher ratio than expected for the plane wave transmission coefficient what could be an indication for the impact of the spherical wavefront.

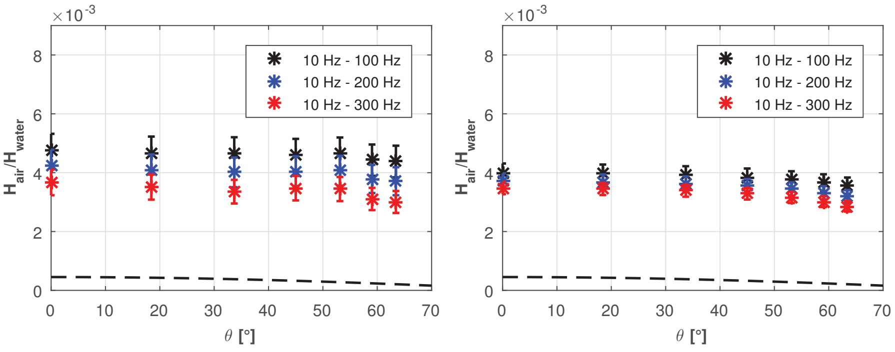

(a) (b)

Figure 3.12: (a) Measured amplitude ratio for different horizontal receiver offsets in air according to Experiment A2. The amplitudes are corrected for geometrical spreading. The ratios are shown for different bandpass filters. The dashed line shows T_{pp}. (b) Modeled amplitude ratios for the same Experiment.

3.6.2 Experiment B: Source in Air

The results for different source elevations z_s are illustrated in Figure 3.13(a). The ratio is computed using Equation 3.11, while it is reversed as the source is in air during this experiment. Hence, the ratio H_{water}/H_{air} is calculated for three different frequency bands. The modelled results are illustrated in Figure 3.13(b). A trend of increasing ratios for smaller source-interface distances can be seen in the measured and modeled data, while there is a difference between both data sets up to 0.4 in the ratio for the shallowest source elevations. It should be mentioned that the variation of the ratios between different source-interface distances is higher than the results from experiment A.

The higher ratios within the measured data could be due to side reflections from metal frames and other obstacles which are part of the construction above the tank (Figure 3.3) as these are not taken into account during the modeling. The steeper increase of the ratios for small source elevations z_s compared to experiment A could be caused by the short distance of the receivers to the interface. Therefore, the interference of the down- and upgoing wavefield for the receiver in air has a bigger impact than during experiment A. In general, it should be noted that a similar behaviour in the modeled and measured data can be observed.

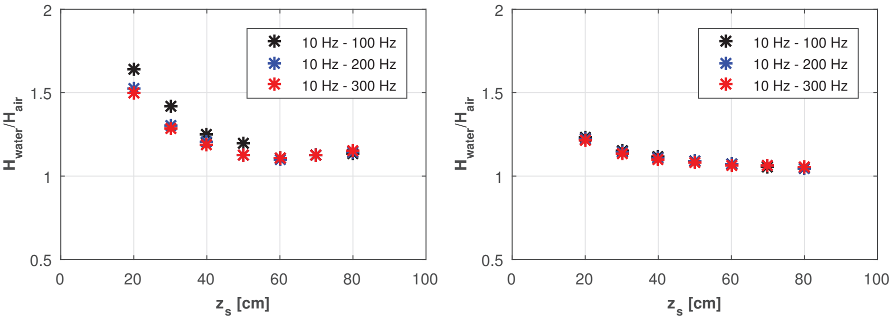

(a)

(b)

Figure 3.13: (a) Measured amplitude ratio for different source elevations according to Experiment B. The amplitudes are corrected for geometrical spreading. The ratios are shown for different bandpass filters. (b) Modeled amplitude ratios for the same Experiment.

3.7 Discussion

The experimental and modeling results reveal a dependency of the transmitted signal on the source-interface distance, as well as a potential dependency on frequency which might be partly explained by the spherical shape of the wavefront. The reflection coefficient can be computed from the results using Equation 3.4 and 3.8. How these findings could impact marine seismic acquisition is investigated in more detail and hence we focus primarily on the source inside water, before we elaborate more on the reversed experiment B.

First, it should be noted that the results are influenced by the reflection from the interface itself. The amplitude recorded in water during experiment A is mainly an interference of the direct wave and the ghost reflection from the water surface. For a better quantification of the transmission and reflection coefficient we use the results from the homogeneous model to remove the ghost effect from our data. Therefore, the ratio of the modeled amplitude from a homogeneous water medium and the modeled amplitude in air from the free-field model is computed. We denote these results as deghosted and they are illustrated in Figure 3.14. This leads to a smaller transmission as the amplitude in a homogeneous model is higher than the amplitude including the interface (Figure 3.10(a)). However, the ratio is still higher than expected for the plane wave transmission coefficient. In addition, Figure 3.14 illustrates that the difference between the ratio modeled in our experimental tank set up and in the free-field is small. This is a promising result as a similar trend could be expected in field applications.

For a better comparison of the experimental results to the theory of a plane wave transmission coefficient and spherical wave transmission response we use the difference from the deghosted and free-field model (Figure 3.14) to remove the ghost effect from our experimental data. The difference is subtracted from the measured ratios in experiment A1 to get a better estimation of the transmission coefficient. Then, the spherical wave transmission response T_{sph} is computed for two frequencies according to the frequency range of the measured data. The results are shown in Figure 3.15 in comparison with the plane wave transmission coefficient T_{pp}. The error bars indicate the standard deviation computed from all measured ratios of each depth according to Equation 3.11. We notice that the measured

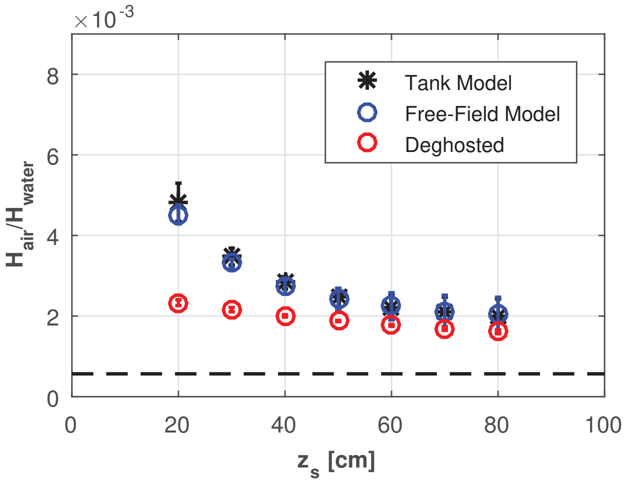

Figure 3.14: Results from the tank and free-field model of experiment A within frequency band of 10 Hz - 100 Hz. The deghosted results are computed from the free-field and homogeneous model. Theoretical plane wave transmission coefficient T_{pp} (dashed line).

transmission coefficient is closer to the spherical wave theory than to the plane wave assumption T_{pp}, although the fit is not perfect. That the deghosted values for the shallowest sources are even higher than $T_{sph}(10\text{ Hz})$ could be explained by the larger deviation between the tank and free-field model for the shallower depth (Figure 3.14). Further differences could be due to inaccuracies of the measured data or the deghosting method which is based on modeled results. The maximum increase of the spherical transmission response is five times that of the plane wave coefficient for source depths approaching the water-air interface.

It could be concluded from the results that the spherical wave transmission response has a better fit to the observations which should be the same for the reflection. However, the difference to the plane wave coefficient is small. To illustrate how different reflection coefficients could impact the frequency content in marine seismic acquisition regarding the source signal we assume linear superposition of the downgoing and surface reflected pressure. Then the frequency spectrum of the source ghost could be computed as

$$G = 1 + R\, e^{(i\omega 2 z_s cos(\theta)/c_1)} \tag{3.12}$$

for vertical incidence ($\theta = 0°$) and two different source depths z_s. The reflection coefficient R is replaced by R_{pp} and R_{sph}, respectively, where the coefficients are similar to those plotted in Figure 3.2. The normalized spectra are shown in Figure 3.16. The difference between both assumptions is small and barely visible for frequencies above 1 Hz. For the deep source, at 5 m depth, the difference is noticeable for frequencies below 0.1 Hz, with an increase of 3.5 dB for R_{sph} at 0.05 Hz compared to R_{pp}. The impact on the shallower source, at 1 m depth, could be already recognized below 1 Hz, with an increase of 5 dB for R_{sph} at 0.2 Hz. Following this example, the difference between conventional

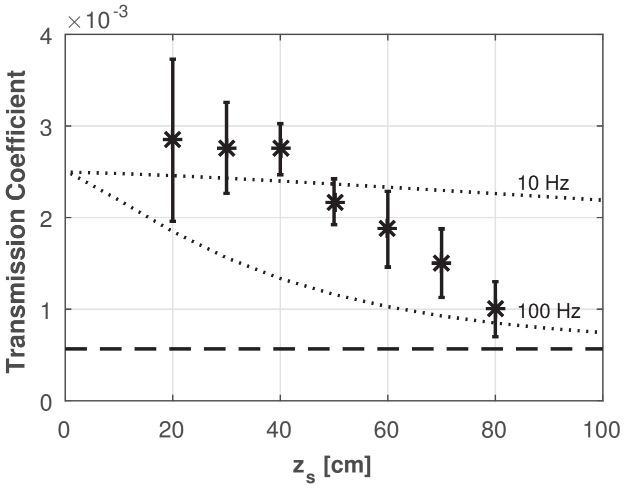

Figure 3.15: Measured, deghosted, results within frequency band of 10 Hz - 100 Hz (asterisk), spherical wave transmission response T_{sph} for 10 Hz and 100 Hz (dotted lines) and plane wave transmission coefficient T_{pp} (dashed line) for different source depths z_s.

calculations of the far field ghost assuming a constant reflection and the assumption of a spherical wave front is negligible above 0.1 Hz for typical source array depths of 5 m and deeper. Assuming a source array at 1 m depth the difference would be negligible above 1 Hz as the difference is less than 0.5 dB in the computed far field spectrum and less than 0.1 dB for frequencies above 2 Hz. It should be noted that these differences in the ghost effect barely vary as a function of angle for those low frequencies. If the bubble oscillation is taken into account which creates a stronger low frequency signal for shallower depths, very shallow sources might be beneficial for frequencies below 1 Hz. This would be in agreement with findings illustrated by Landrø and Amundsen (2014a). Therefore, further tests with an over-/under-configuration might be considered where a few sources are placed very shallow, about 1 m below the sea surface. The source depth might be limited by practical issues when towing sources that shallow. An investigation on the source ghost effect for different source depths is demonstrated by Haavik and Landrø (2015), however the shallowest source depths in this study is 3 m. Due to high noise levels at these frequencies caused by ocean swell, 4C ocean-bottom receivers are preferable to recognize this effect as they have a better signal-to-noise ratio at these low frequencies (Landrø et al., 2014; Halliday et al., 2015).

For the modeled results from experiment B the same deghosting method as for experiment A is performed which leads to a big change of the estimated ratio (Figure 3.17(a)). We notice again that the difference between the tank and free-field model is small. A close view on the deghosted ratio illustrates that the results are lower than the theoretical plane wave transmission coefficient (Figure 3.17(b)). This is expected from Equation 3.4 if more signal is transmitted, as for a total reflection where $R = 1$, it follows $T = 2$ and for a total transmission where $R = 0$, it follows $T = 1$. The discussion is restricted on the modeled deghosted results as the deviation between modeled and measured data is too large.

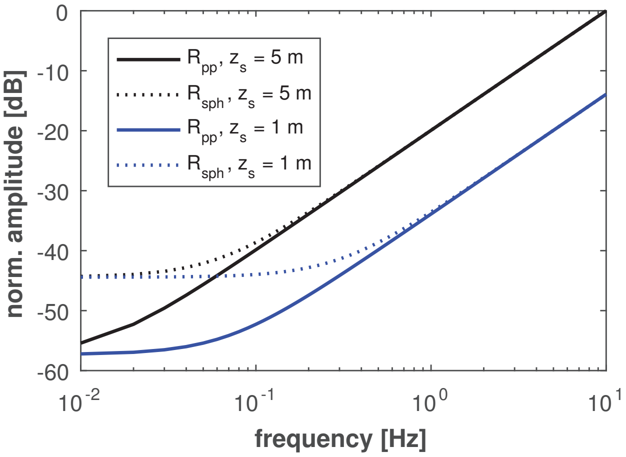

Figure 3.16: Comparison of ghost functions G using the plane wave (R_{pp}) and spherical wave (R_{sph}) reflection assuming two different source depths z_s. The spectra are normalized to the maximum value within the displayed frequency range.

Therefore, the deghosting of the measured data from modeled results is not applicable for experiment B. It is difficult to conclude on a depth dependency or a quantification of the transmission coefficient from these results. However, they give some evidence that the impact of the spherical wave front might be observed as higher transmission ratios than the plane wave coefficient are observed.

It should be pointed out that all results and the theory is valid for a flat fluid-fluid interface and is not accounting for surface topography caused by weather and swell. In field applications, the effect of a rough sea surface cannot be neglected and surface topography also leads to frequency dependent reflection. The impact on reflection and scattering from rough interfaces is discussed by many authors, which for instance is summarized by Ogilvy (1987). Whether the surface can be considered as rough or smooth can be defined by the Rayleigh parameter (Hovem, 2007)

$$\chi = 2k\sigma cos(\theta) \tag{3.13}$$

where σ is the mean height of the ocean waves at the sea surface and $k = (2\pi f)/v_1$ the wave number with frequency f and sound speed in water v_1. For values of $\chi \ll 1$ the sea surface can be assumed to be acoustically smooth. For a source in water with a frequency of f = 1 Hz, a mean wave height of σ = 3 m and a vertical incident acoustic wave we get χ = 0.0251 according to Equation 3.13. As this number is much smaller than 1, a rough sea surface should have a negligible impact on the low frequency part of the ghost as the main observed difference from our results is for frequencies of 1 Hz and below. However, for frequencies above 1 Hz the weather effect could be more pronounced for these parameters following the example from Klüver and Tabti (2015). Therefore, it could be assumed that phase changes of the reflected signal from a rough sea surface might be mainly caused by the surface topography for frequencies above 1 or 2 Hz, while the phase changes for frequencies below 1 Hz could be mainly due to the spherical wave front. This simple assumption depends on the roughness of the sea surface and could change for different

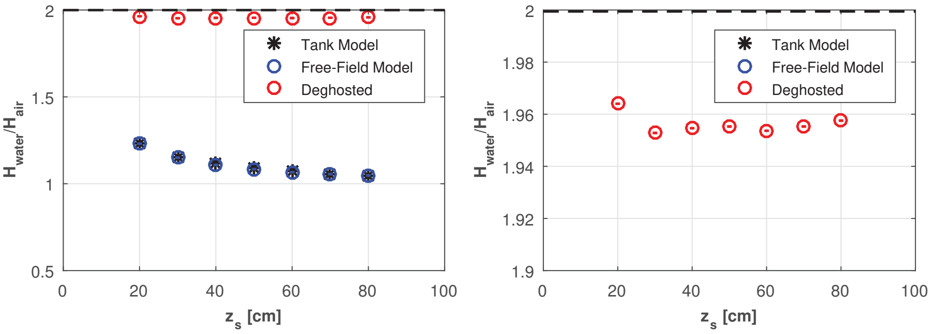

(a) (b)

Figure 3.17: (a) Results from the tank and free-field model of experiment B within frequency band of 10 Hz - 100 Hz. The deghosted results are computed from the free-field and homogeneous model. Theoretical plane wave transmission coefficient T_{pp} (dashed line). (b) Zoom in on plot (a).

sea states. When the source is located in air, the transmission from air into water is more influenced by the same surface roughness as the wave number k is larger in air due a lower sound velocity. This leads to a Rayleigh parameter of χ = 0.1109 for f = 1 Hz, σ = 3 m and v_2 = 340 m/s. Therefore, a small surface topography could lead to an increased transmission from air to water (Lubard and Hurdle, 1976).

Furthermore, two other effects acting on the transmission should be discussed which were mentioned in the introduction. First, there could be an increased transmission from water to air due to the evanescent part of the wave field as discussed by Godin (2008) and McDonald and Calvo (2007). Following the derivation of McDonald and Calvo (2007), a monopole point source that approaches $kz_s \rightarrow 0$ radiates up to 1.1% of the power, that would be radiated into the unbounded medium, into air, where k is the wave number and z_s the source depth. For a source approaching $kz_s \rightarrow \infty$ the radiated power into air relative to that radiated into unbounded water would be 0.028% and hence is much lower compared to a source close to the interface ($kz_s \rightarrow 0$). For our experiments the range of kz_s is roughly between 0.01 - 1 and therefore this effect might influence the results. The experimental kz_s range would lead to a radiated power which is 35 times higher compared to the value in unbounded water for kz_s = 0.01. For kz_s = 1 the value should be 1.5 times higher. It should be mentioned that McDonald and Calvo (2007) describe the radiated power while we estimate the transmitted signal from peak pressure measurements. We can compare our measurements to the results of Calvo et al. (2013) who also evaluate pressure measurements corresponding to the same theory. They obtain similar results in the range around kz_s = 0.1, whereas for values approaching kz_s = 0.01 they achieve higher transmitted values than the results presented here. Hence, it should be noted that an increased transmission due to evanescent waves might partly influence the achieved measurements. However, the results fit also with the theoretical spherical wave reflection response and the different ghost function (Figure 3.16) can still be expected. It should be mentioned that the enhanced transmission might be an explanation why we hear airguns during marine seismic acquisition louder than expected while a sufficient amount could be also transmitted through the hull of the seismic vessel.

Secondly, the physical interaction of the source and interface could lead to changes of the source signature and would have an impact on the measured data in air and water. The limit within interaction between the cavity and the interface happens is $z_s < 3\, r_{cav}$, where r_{cav} is the maximum radius of the cavity (Chahine, 1977). The minimum source depths within our experiments is z_s = 0.2 m. We can estimate the cavity radius from the collapse time τ of the measured data as (Rayleigh, 1917)

$$\tau = 0.915\, r_{cav} \sqrt{\frac{\rho_w}{p_0}} \tag{3.14}$$

where ρ_w is the water density, p_0 the hydrostatic pressure and 0.915 is an exact number derived from gamma functions by Rayleigh (1917). With a measured collapse time of 2τ = 0.03 s from the shallowest source depths a cavity radius of r_{cav} = 0.023 m is estimated similar to the approach by Safar (1986). This is more than eight times the source depths z_s = 0.2 m and therefore we consider the effect of source-interface interaction as negligible for our experiments. Within seismic acquisition where the bubble of the air gun is much larger than the cavity in our experiments, this effect has to be considered. It should also be mentioned that further phenomena as cavitation and the shot effect (Loveridge, 1985) are expected during air gun operations at shallow source depths.

3.8 Conclusion

The experimental results indicate an increased transmission for smaller distances between the source and water-air interface. The measured data fits to the model and theory of a spherical wave reflection response which reveals a decreased reflection from the sea surface for shallow sources and large wavelength relative to the source-interface distance. It should be noted that the increased transmission from water to air might be also partly explained by the evanescent waves in water which could convert to homogeneous waves in air for certain wavenumbers. However, considering the results together with the model and theory, very shallow seismic sources seem to be beneficial for an enhanced very low frequency signal in marine seismic acquisition. As the highest noise levels in marine seismic acquisition are also in the low frequency range below 2 Hz, it depends on the source strength and low frequency noise level at the receivers whether the difference between the plane and spherical wave assumption can be recognized or not.

3.9 Acknowledgements

We acknowledge the European Union’s Horizon 2020 research and innovation programme under the Marie Skłodowska-Curie grant agreement No 641943 for the funding of Daniel Wehner’s PhD project within WAVES. We like to acknowledge the technical team at IGP for their support to the experimental setup. M. Landrø acknowledges financial support from the Norwegian Research Council. We thank Joshua (Shuki) Ronen and an unknown reviewer for their valuable comments which improved this paper.

Chapter 4

The Impact on Low Frequencies from Very Shallow Air Guns in Marine Seismic Acquisition - An Experimental Study

Daniel Wehner[1]**, Martin Landrø**[2] **and Lasse Amundsen**[3]
[1] *NTNU, Department of Geoscience and Petroleum, 7031 Trondheim, Norway*
[2] *NTNU, Department of Electronic Systems, 7491 Trondheim, Norway*
[3] *Statoil Research Centre, 7053 Trondheim, Department of Geoscience and Petroleum, Trondheim, 7031 Norway.*

submitted to Geophysics in October 2018

4.1 Abstract

In marine seismic acquisition the enhancement of the amplitude of frequencies below 5 Hz is of special interest since it improves the image of the subsurface. The frequency content of the air gun, the most common marine seismic source, is mainly controlled by its depth and the size. While the depth dependency on frequencies above 5 Hz is thoroughly investigated, for frequencies below 5 Hz it is less understood. However, recent results suggest that sources fired very close to the sea surface might enhance these very low frequencies. Therefore, dedicated tank experiments are conducted to investigate the changes of the source signal for very shallow sources in more detail. A small volume air gun is fired at different distances from the water-air interface including depths where the air bubble directly bursts into the surrounding air. The variations of the oscillating

bubble and surface disturbances, which can cause changes of the reflected signal from the sea surface, are explored to investigate whether an increased frequency signal below 5 Hz can be achieved from very shallow air guns. The results are compared with field measurements of a large volume air gun fired close to the sea surface. The results reveal an increased signal for frequencies below 5 Hz of up to 10 dB and 20 dB for the tank and field experiments, respectively, for the source depth where the air gun bubble directly bursts into the surrounding air. For large volume air guns an increased low frequency signal might also be achieved for slightly deeper source depths. From these observations new considerations in the geometry of air gun arrays in marine seismic acquisition can be suggested.

4.2 Introduction

The enhancement of signal amplitudes of frequencies below 5 Hz is a desirable objective in marine seismic data acquisition as it would have several benefits. The penetration depth of the signal increases and imaging below complex overburden structures like basalt or salt would be improved if low frequencies are enhanced. In addition, low frequencies are beneficial for waveform inversion as they increase the likelihood to find the correct velocity model (ten Kroode et al., 2013). However, the generation of low frequencies by seismic air guns, which are the most common marine seismic source, is a major issue due to two counteracting effects. These are the interference of the first reflected signal from the sea surface, referred to as the ghost, with the downgoing wavefield and the oscillating air bubble produced by the air gun (Hegna and Parkes, 2011). Deep towed sources give stronger low frequency amplitudes due to the ghost effect compared to shallow ones. In contrast, the oscillating air bubble generates stronger low frequency amplitudes at shallower source depths. This is due to longer oscillations of the bubble caused by less hydrostatic pressure. While the bubble time period controls the frequency output approximately between 5 Hz to 15 Hz depending on the source depth, the impact of the depth on frequencies below 5 Hz is less understood. However, a few studies indicate that shallow sources might be more likely to produce these very low frequencies (Mayne and Quay, 1971; Landrø and Amundsen, 2014a; Amundsen et al., 2017).

The behaviour of oscillating bubbles close to interfaces is studied by several authors for different sizes of air bubbles as mentioned in the following. The differences between air bubbles generated by sparks and explosives close to a solid and free surface is investigated by Hung and Hwangfu (2010) using high speed photography and pressure gauges. In a similar experimental set up Cui et al. (2016) study the behaviour of underwater explosions in the vicinity of one and two different boundaries, e.g. the free surface and a solid plate with a circular hole. The acoustic signal of small bubbles in the vicinity of interfaces generated by a discharge between two electrodes is discussed by Krieger and Chahine (2005). A numerical model for bubble oscillations close to a plane free surface is demonstrated by Oguz and Prosperetti (1990). An experimental study using a small scale air gun with a volume of 0.88 in^3 (14.5 cm^3) is presented by de Graaf et al. (2014b). They investigate the bubble oscillation period and pressure field for different distances to a steel plate and free surface. The variation of the bubble period from an air gun close to the free surface is also discussed by Haavik and Landrø (2016). The interaction of air bubbles in a clustered air gun array, when the sources are close to each other, is studied by Strandenes and Vaage (1992) and Barker and Landrø (2012). The general conclusion of all these studies is that the bubble period increases in the vicinity of a solid boundary, while it starts to decrease close to a free surface when the bubble surface distance reaches a critical point.

The ghost reflection depends on the water-air interface and when a seismic source is fired at very shallow depths the acoustic pressure that strikes the surface can be large. This could lead to disturbances of the water surface. The accompanying energy loss could lead to a reduced ghost reflection. In seismic acquisition the effect is referred to as the shot effect (Loveridge, 1984, 1985; Parkes and Hatton, 1986). The effect of pressure pulses on a free surface leading to disturbances is also discussed by Temperley and Trevena (1979). The estimated pressure amplitude needed to break the surface tension and disturb the surface varies for different studies between values of less than one bar to values over 100 bar (Weston, 1960; Nyborg et al., 1972). In addition to the disturbance of the interface, cavitation below the interface can occur caused by the negative reflected pressure pulse (Wentzell et al., 1969). This could also lead to energy losses from the ghost reflection. Another interesting effect that changes the interface shape are Faraday waves (Faraday, 1831). These surface waves can be generated at fluid-fluid interfaces by a periodic vertical motion within one of the fluids which in case of the air gun is caused by the oscillating bubble. Several experimental (Douady and Fauve, 1988; Douady, 1990) and numerical (Périnet et al., 2009, 2012) studies demonstrate the surface wave patterns generated due to harmonic motions in the fluid.

A few more studies should be mentioned that discuss different ways to enhance the low frequency output in marine seismic acquisition. Dellinger et al. (2016) present a vibrator-type source, called Wolfspar, that is designed to create specific ultra-low frequencies needed for the computation of velocity models in full waveform inversion (FWI). A marine dipole source is illustrated by Meier et al. (2015) which would change the ghost notches and hence would amplify the low frequency amplitudes. Ronen and Chelminski (2018) present a new pneumatic source, called the Tuned Pulse Source (TPS), that has much larger volumes and lower operating pressures compared to conventional airguns. They propose that this source enhances the low frequency signal while reducing the high frequency content which can be harmful for marine life. In addition, using the signal apparition approach in simultaneous source acquisition (Robertsson et al., 2016) could produce signals with more low frequencies and less high frequencies compared to conventional seismic source acquisition.

We investigate the effects on the air gun signal for sources fired very close to the sea surface in more detail by performing experiments in a water tank and compare those to field measurements (Amundsen et al., 2017). The variations of the bubble period and ghost effect are discussed for sources fired at these shallow depths. In the tank experiment a small volume air gun is fired at different depths including the point where the bubble bursts directly into the surrounding air, breaks the water surface and hence no oscillations occur in water. The surface disturbance caused by the acoustic pressure striking the water-air interface is also investigated further depending on the source depth. The results should reveal how valuable very shallow air guns could be for an enhanced low frequency signal below 5 Hz in marine acquisition and which depths might be optimal to achieve these increased low frequency signals.

4.3 Theory

The two main effects that are described in the following are the change of the bubble time period in the vicinity of the free surface and the impact of a reduced ghost reflection on the frequency spectrum. The mechanisms that could be responsible for a decreased ghost reflection are described. For the variation of the bubble time period we follow the explanation given by Haavik and Landrø (2016).

The first description of an oscillating bubble in an inviscid, incompressible and infinite medium is given by Rayleigh (1917) that neglects the effect of the free surface on the bubble. The maximum bubble radius can be estimated using the assumption of adiabatic expansion (Willis, 1941). This leads to the Rayleigh-Willis equation which is commonly used in seismic acquisition to estimate the bubble time period as (Rayleigh, 1917; Willis, 1941)

$$T_{\text{RW}} = C\,\frac{P_f^{1/3} V_g^{1/3}}{p_h^{5/6}} \tag{4.1}$$

where P_f is the firing pressure and V_g the volume of the air gun. The constant C is specific for the design of the gun and p_h is the hydrostatic pressure. The impact of an interface as the free surface was described first by Herring (1941) which corrects the Rayleigh-Willis equation leading to

$$T_{\text{He}} = T_{\text{RW}}\Big(1 + r\frac{R_a}{4z_s}\Big) \tag{4.2}$$

where R_a is the average bubble radius within one period and z_s is the distance from the interface to center of the bubble. In case of a free surface the reflection coefficient is r = -1 while for a rigid boundary r = 1. Similar to this Haavik and Landrø (2016) derive an expression to correct the bubble time period for the case where the bubble is close to an interface. They suggest to compute the bubble time period as (Haavik and Landrø, 2016)

$$T_{\text{HL}} = T_{\text{RW}}\frac{1}{2}\sqrt{A(\kappa, r)} \tag{4.3}$$

where

$$A(\kappa, r) = \frac{4\kappa + 4r - r^2 \ln\big(\frac{\kappa-1}{\kappa+1}\big)}{\kappa} + \frac{2r^2}{1-\kappa^2}\ , \kappa \geq 4. \tag{4.4}$$

The parameter κ describes the ratio of the distance to the interface and the equilibrium bubble radius R_{eq} as $\kappa = 2z_s/R_{eq}$. The radius R_{eq} is the bubble size when the pressure inside and outside the bubble is equal. The change of the bubble time period as a function of source depth z_s for different gun sizes is illustrated in Figure 4.1. We notice that the bubble time period increases for decreasing source depths z_s until a turning point (Figure 4.1, circles). For source depths shallower than this turning point the bubble period decreases again and hence the low frequency content is not increased anymore due to the oscillating bubble. An interesting observation is that the ratio z_s/R_{max} between source depth and maximum bubble radius, assuming an oscillating bubble after Rayleigh (1917) at the turning point decreases for increasing air gun sizes as z_s/R_{max} = 2.34 (100 in^3), 1.86 (500 in^3) and 1.67 (1200 in^3).

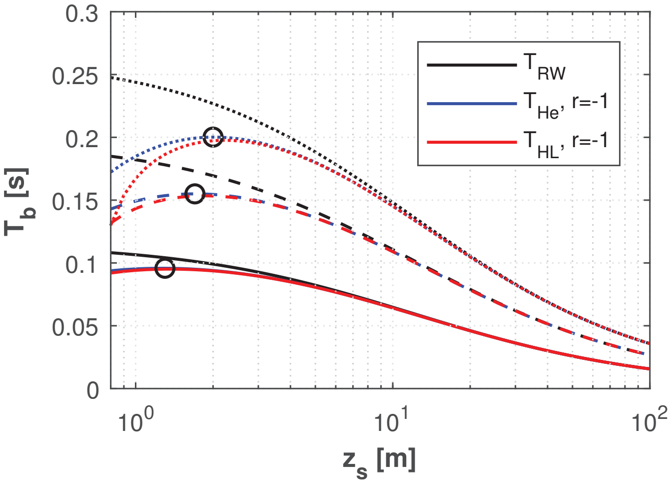

Figure 4.1: Change of bubble time period T_b in an infinite medium (T_{RW}) and close to a free surface (r = -1) for the different models, T_{He} and T_{HL}. T_b is modelled for different air gun sizes of 100 (solid), 500 (dashed) and 1200 (dotted) in^3 and a firing pressure of 137 bar. The circles indicate the maximum bubble period.

For a simple illustration of the ghost effect on the frequency content we assume a point source that emits a spike function. The frequency spectrum of this time signal $s(t)$ can be computed using the Fourier transform as (Ikelle and Amundsen, 2005)

$$s(t) = \frac{1}{2\pi} \int_{-\infty}^{+\infty} S(\omega)\, e^{(i\omega t)} d\omega \tag{4.5}$$

$$S(\omega) = \int_{-\infty}^{+\infty} s(t)\, e^{(-i\omega t)} dt \tag{4.6}$$

where t is the time of the signal and $\omega = 2\pi f$ is the angular frequency component, with f as the frequency. If we assume a perfect reflection at the water-air interface, with a reflection coefficient of r = -1, the signal and frequency spectrum can be computed for different source depths z_s as illustrated in Figure 4.2 (dashed line). The time delay t_d of the ghost reflection corresponds to $t_d = 2z_s/c$, where c = 1500 m/s is the sound velocity in water. This is valid in the far-field where the source-receiver distance is much larger than the source-interface distance and hence amplitude differences between the direct spike and ghost spike due to the distance $2z_s$ can be neglected. If we assume that the ghost amplitude

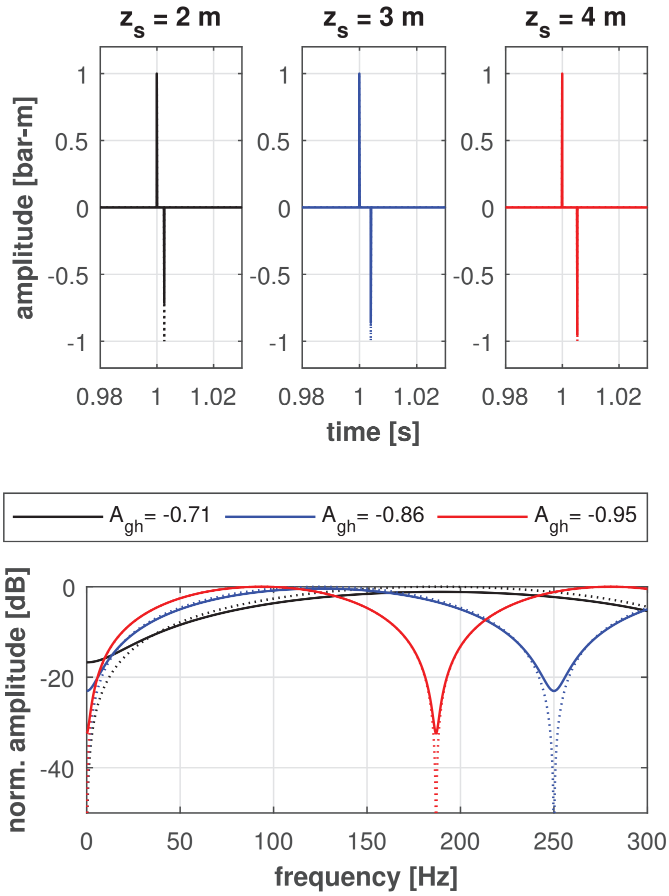

Figure 4.2: Spike functions and their ghost reflections from the sea surface (top) and the corresponding frequency spectra (bottom). Dashed lines indicate a prefect reflection at the surface. Solid lines indicate a reduced ghost reflection with amplitudes given as A_{gh}, computed from Equation 4.7.

is reduced due to energy losses at the surface related to the acoustic pressure that strikes the surface, we could assume a smaller ghost amplitude for shallower sources (Loveridge, 1984, 1985). For the reduced ghost shown in Figure 4.2 (solid line) we use the empirical relation presented by Hatton (2007) which leads to variations of the reflection coefficient r as

$$r = 1.3\left(\frac{p_p}{z_s}\right)^{1/5} - 1.7 \qquad (4.7)$$

where p_p is the zero to peak pressure in bar-m. For the example in Figure 4.2 a peak pressure of p_p = 1 bar-m is assumed for all source depths. It should be noted that the reflection coefficient might only vary temporarily when the acoustic pressure exceeds a critical value at the surface. The spectra in Figure 4.2 can also be described by the ghost function, assuming vertically travelling plane waves, as (Amundsen and Zhou, 2013)

$$|G| = |1 + r\, e^{(2i\frac{2\pi f z_s}{c})}| \tag{4.8}$$

where c is the sound velocity in water. We notice in Figure 4.2 that a reduced ghost reflection fills up the notches related to the source depth, e.g. at 187.5 Hz and 250 Hz for a source depth of 3 m and 4 m, respectively. This could also be of special interest for low frequencies. For the shallowest source at 2 m this leads to a higher frequency content of 5 - 15 dB between frequencies of 1 - 5 Hz compared to the deeper sources.

Potential mechanisms that lead to energy losses at the sea surface and therefore to a reduced ghost reflection are mentioned and further discussed in the Discussion section. These effects can be related to the pressure wave striking the interface, the physical interaction of the source (air bubble) with the interface as well as a rough surface caused by wind and weather. When the amplitude of the pressure wave at the sea surface is strong enough to break the surface tension, the reflected ghost signal is reduced by a certain amount as suggested in Figure 4.2 (Loveridge, 1984; Hatton, 2007). Secondly, if the air gun is so close to the surface that the bubble directly bursts into the air, the surface is highly disturbed and the water-air interface almost vanishes at the point where the bubble breaks. This could cause a strong decrease of the ghost reflection while it should be mentioned that the overall source signal strength is expected to decrease compared to deeper sources. In addition, a rough surface impacts the reflected signal as discussed by many authors (Brekhovskikh and Lysanov, 1991; Hovem, 2007; Jensen et al., 2011). However, this mostly effects higher frequencies in seismic acquisition and hence stronger sea states are expected to reduce the higher ghost notches (Jovanovich et al., 1983) but not the notch at 0 Hz. Therefore, we do not elaborate more on the effect of a rough sea surface.

4.4 Experiments

For a detailed investigation of very shallow sources we conduct experiments in a water tank where the source is fired almost at the water-air interface. In addition, we investigate data from a field experiment where a large volume air gun is fired in a fjord at different source depths (Amundsen et al., 2017).

4.4.1 Water tank experiments

The experiments are conducted in a water tank with the dimensions shown in Figure 4.3. The walls of the tank are equipped with 5 cm thick foam mattresses. This damping material leads to an improved signal reception with smaller side reflections indicated by previous tests, although they do not act as perfectly absorbing boundaries. The source is a Mini G. Gun with a chamber volume of 12 in^3 which is fired at different depths during the experiment, ranging from z_s = 0.8 m to z_s = 0.1 m (Figure 4.3). Brüel & Kjær hydrophones of the type 8105 are used as receivers for all experiments in the tank which have a frequency

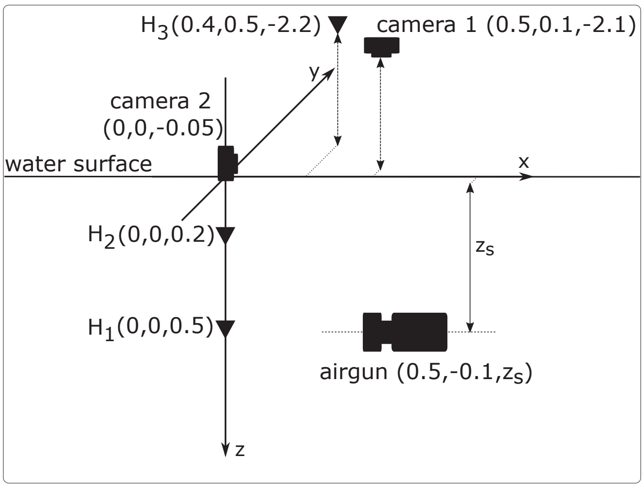

Figure 4.3: Sketch of experimental set up in the water tank. The hydrophones are indicated as H_1, H_2 and H_3 where the x-, y- and z-coordinates in meters are given in brackets. The water depth in the tank is 1.25 m and the width and length of the tank are 2.5 m and 6 m, respectively.

range from 0.1 Hz to 100 kHz. An additional hydrophone is located in air, denoted by H_3 (Figure 4.3), to record the signal transmitted through the water-air interface. The hydrophones of type 8105 have the same sensitivity in water and air for frequencies up to 3 kHz. Next to the hydrophone H_3 camera 1 is placed to film the water surface while the air gun is fired at different depths. For the same purpose the camera is also placed at a second location denoted as camera 2. The recording rate of the camera is 240 frames per second (fps) which allows to have a photo approximately every 4.2 ms. The video recordings might provide additional information about the impact on the ghost reflection when an air gun is fired very close to the water-air interface.

The experiment is also repeated several times where the hydrophones H_1 and H_2 are placed at different depths to investigate the impact of the tank size. It could be concluded that the main observations described in this paper are the same for all tests. The percentage of non-repeatability of the air gun shots at each source depth is described by

$$\delta A = \frac{\frac{1}{N}\sum_{n=1}^{N}(A_{rms} - A_{rms}^{n})}{A_{rms}} \cdot 100 \tag{4.9}$$

where A_{rms}^{n} is the root mean square amplitude of a single recorded trace where n indicates the shot number and N the total number of shots at one depth. A_{rms} is the root mean square amplitude of the stacked traces of all shots at one source depth. For an average number of 10 shots at each source depths, which are 300 Hz low-pass filtered, a non-repeatability of $\delta A \leq 5\%$ is found.

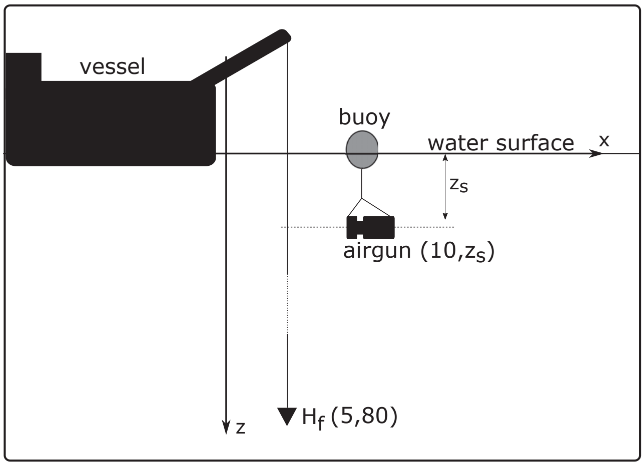

Figure 4.4: Sketch of experimental set up in the field. The hydrophone is indicated as H_f where the x- and z-coordinates in meters are given in brackets. The water depth in the fjord is around 390 m.

4.4.2 Field experiments

We analyze data from a field test conducted in a Norwegian fjord (Amundsen et al., 2017). The water depth at the test site is approximately 390 m and the weather conditions were excellent during the test. A Bolt 1500LL single air gun with a chamber volume of 1200 in^3, which is deployed from an A5 buoy, is fired at different source depths z_s below the sea surface (Figure 4.4). The signal is recorded with a Reson hydrophone TC4043 that is located at a constant depth of 80 m nearly vertically below the source. The rope with the hydrophone has a weight attached at the end to hold it straight. The x-coordinate for the receiver position given in Figure 4.4 is an estimation and might vary slightly. The hydrophone has a recommended frequency range between 2 Hz and 160 kHz. The air gun was fired at source depths of z_s = 1.3, 2.3, 3.3, 5.3, 7.3, 10.3, 20.3, 30.3 m. In addition, one shot is conducted between 1.3 m and 2.3 m. The source depths is not exactly known as the air gun is lowered due to a leakage in the A5 buoy. As the experiment was not designed to test very shallow sources, only one shot is performed for the source at 1.3 m. For all sources at a depth of 2.3 m and deeper at least six shots are fired. A more detailed description of the experiment is given by Amundsen et al. (2017).

4.5 Results

The pressure recordings of the tank and field experiment are investigated and compared. In addition, the variations of the oscillating bubble for different source depths and air gun sizes is investigated.

4.5.1 Water tank measurements

The measurements of the 12 in^3 air gun fired with a pressure of 80 bar at four different source depths are shown in Figure 4.5. The signal is corrected for geometrical spreading with $1/r$ where r is the source-receiver distance. The main peak of the air gun signature is reduced with decreasing source depth and the same can be observed for the peak of the oscillating bubble. For a source depth of 0.15 m only one bubble oscillation can be seen around 0.05 s. The signature of the shallowest source depths of 0.1 m does not have any bubble oscillation, indicating that the pressurized air from the gun directly bursts into the

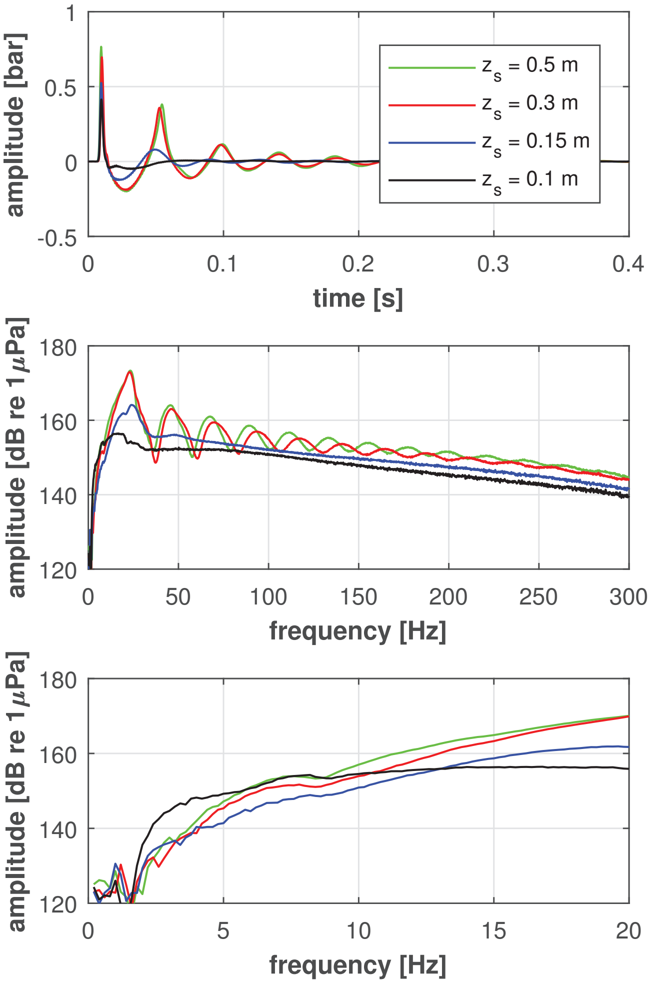

Figure 4.5: Measurements at H_1 of 12 in^3 air gun fired in water tank at different depths (top) and the corresponding frequency spectra (middle) and a zoom on the low frequency part (bottom). A 300 Hz low-pass filter is applied to the data.

air. The maximum bubble radius for the different source depths could be roughly estimated using Rayleigh's equation for the bubble period (Rayleigh, 1917) and the measured bubble period from the recordings. This reveals a maximum bubble radius for the different source depths of R_{max}(0.15 m) = 0.19 m, R_{max}(0.3 m) = 0.23 m and R_{max}(0.5 m) = 0.25 m. It should be noticed that the bubble radius is larger than the source depth for the the source at 0.15 m for this simple approximation. That the bubble vanishes for the shallowest source is visible in the frequency spectra (Figure 4.5, middle). While the source at 0.15 m still has energy at the first bubble peak at 23 Hz, peaks at higher frequencies related to a 2nd or 3rd bubble oscillation are not present. In addition, the first notches around 36 Hz and 58 Hz related to the bubble oscillation are not present for the source at 0.15 m compared to the deeper sources. The spectrum for the shallowest source at 0.1 m is nearly flat and has no energy related to the oscillating bubble. A close up on the low frequency end of the spectrum (Figure 4.5, bottom) illustrates that the energy drops for decreasing source depth except for the shallowest source without an oscillating bubble. For the shallowest source depth a higher low frequency signal between 2 Hz and 5 Hz can be observed with a gain up to 10 dB compared to the deeper sources. It should be mentioned that frequencies below 0.5 Hz are filtered out. Figure 4.6 shows photos taken when the air gun is fired at a source depth of 0.15 m in the water tank.

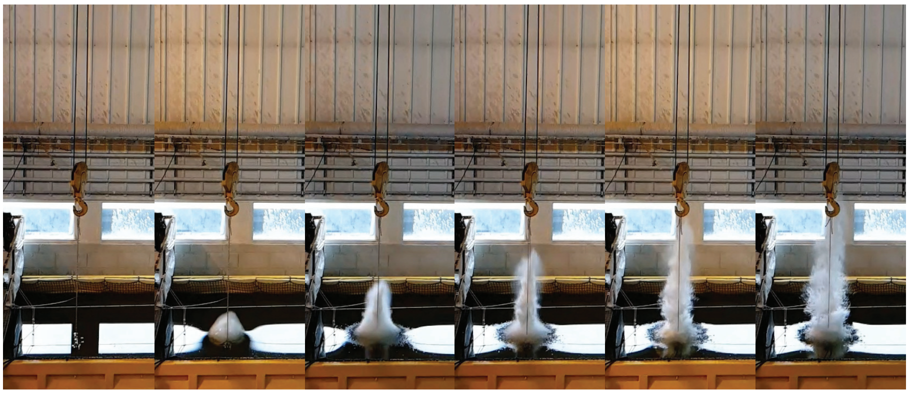

Figure 4.6: Photos of air gun fired at a depth of 0.15 m (taken by Stian Rørheim). The time between each photo is 13 ms.

A detailed investigation on the variation of the bubble period is shown in Figure 4.7. The minimum source depth on the x-axis is the depth where $z_s \approx R_{max}$. The measured bubble time period for source depths between 0.2 m and 0.8 m is compared to the modeled period following Equations 4.1, 4.2 and 4.3. The Rayleigh-Willis equation (T_{RW}) has the largest deviation as it assumes an infinite medium. The measured data has the best fit with Equation 4.3 given by Haavik and Landrø (2016). However, the difference to Equation 4.2 from Herring (1941) is small. In general, a decreasing bubble period with decreasing source depths can be observed for the measured data. Therefore, the highest peak in the spectrum, around 25 Hz, produced by the oscillating bubble is shifted towards higher frequencies as indicated in Figure 4.5 (middle) for the 12 in^3 used in the tank. The turning point where the bubble period starts to decrease with decreasing source depth is at $z_s \approx 3.2\ R_{max}$.

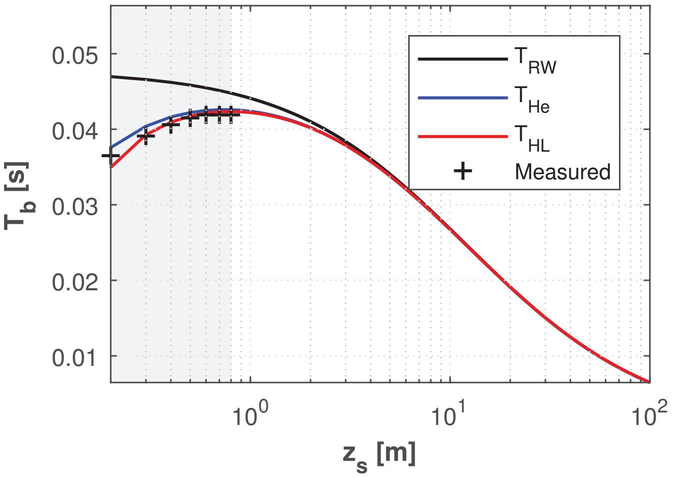

Figure 4.7: Measured bubble time period of 12 in^3 air gun for different depths fired in the water tank compared to theoretical curves from Rayleigh-Willis equation, Herring and Haavik (Eq. 4.1, 4.2, 4.3). The gray area indicates source depths which are smaller than four times the maximum bubble radius.

4.5.2 Field measurements

The measurements of the 1200 in^3 air gun fired with a pressure of 137 bar at four different source depths are shown in Figure 4.8. We estimate the source depth of the second shallowest source to be at 1.8 m from a notchlike event around 400 Hz and from the bubble period indicated by the peak around 5 Hz in the frequency spectrum (Figure 4.8, bottom). However, as it is not exactly known and only one shot is conducted we denote the depth in quotation marks. The main peak amplitude of the air gun signature is reduced with decreasing source depth from 7.4 bar at z_s = 3.3 m to 6 bar at z_s = 1.3 m. The signal is corrected for geometrical spreading using $1/r$ to get the amplitude at 1 m distance from the source. A large amplitude difference can be observed for the bubble peak which is also reduced for decreasing source depths. For the shallowest source at 1.3 m no oscillating bubble can be observed in the time recordings, again indicating that the pressurized air from the gun might directly burst into the air. For the source at ”1.8” m at least one bubble oscillation could be observed in the frequency spectrum (Figure 4.8, bottom) where the notch around 8 Hz is still pronounced compared to the shallowest depth, although the bubble oscillation is difficult to identify on the pressure recordings (Figure 4.8, top). The maximum bubble radius for the different source depths is estimated using Rayleigh’s equation (Rayleigh, 1917) and the measured bubble period from the recordings. This reveals a maximum bubble radius for the different source depths of R_{max}(1.8 m) = 1.19 m,

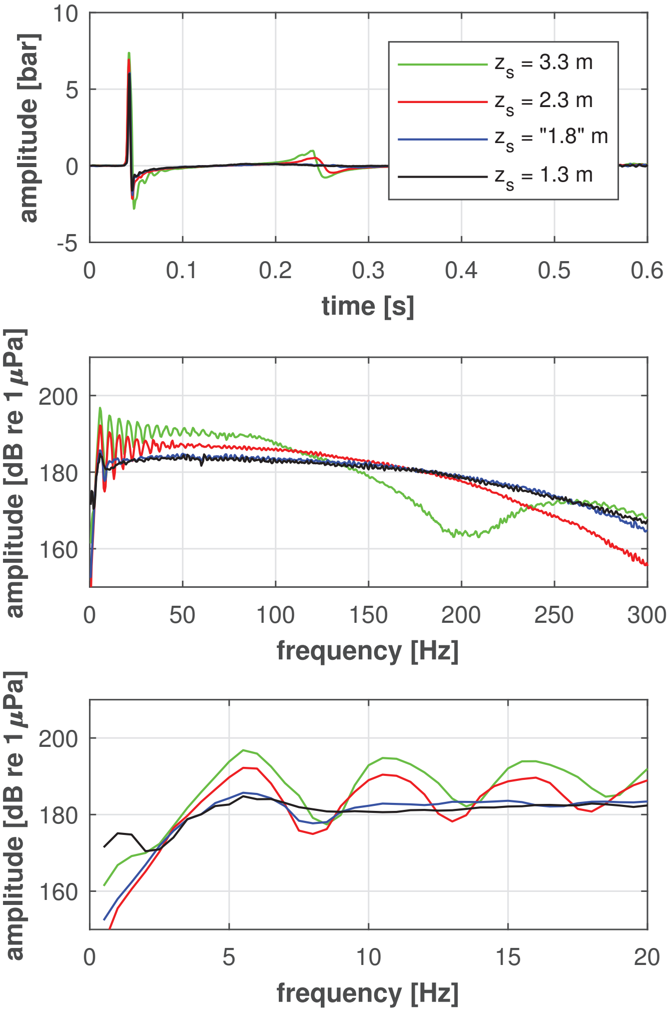

Figure 4.8: Measurements of 1200 in^3 air gun fired in the fjord at different depths (top) and the corresponding frequency spectra (middle) and a zoom on the low frequency part (bottom). A 300 Hz low-pass filter is applied to the data.

R_{max}(2.3 m) = 1.22 m and R_{max}(3.3 m) = 1.23 m. While the source at 2.3 m still has sufficient energy from the oscillating bubble visible at frequencies below 50 Hz, the spectrum for the shallowest source at 1.3 m is nearly flat according to the vanishing bubble oscillation (Figure 4.8, middle). In addition, the ghost notch for the source at 3.3 m is visible around 200 Hz. A close up on the low frequency end of the spectrum (Figure 4.8, bottom) illustrates that the energy drops for decreasing source depths related to the reduced energy of the bubble oscillation. For the shallowest source at 1.3 m a higher low frequency signal between 0.5 Hz and 2 Hz can be observed with a gain up to 20 dB compared to the deeper sources. It should be mentioned that frequencies below 0.5 Hz are filtered out. In addition, the recommended frequency range of the hydrophone used for the field test is between 2 Hz and 160 kHz and hence care must be taken when investigating these low frequencies. However, an enhanced low frequency content can be observed similar to the experiments in the tank (Figure 4.5).

A detailed investigation on the variation of the bubble period is shown in Figure 4.9. The measured bubble time period for source depths between 1.8 m and 30.3 m is compared to the theory. The best fit between the measured and modelled bubble time period for this data is given by Herring (1941). However, the difference between T_{He} and T_{HL} for the range of measured source depths is very small. In general, an increasing bubble time period T_b with decreasing source depths can be observed for the measured data which should lead to an enhanced low frequency signal produced by the oscillating bubble, assuming that the amplitude would be constant. It should be noted that the bubble period increases for source depths as shallow as $z_s \approx 1.6\ R_{max}$. Therefore, the turning point where the bubble period starts to decrease with decreasing source depth is shallower than for the small 12 in^3 air gun (Figure 4.7) relative to the maximum bubble radius.

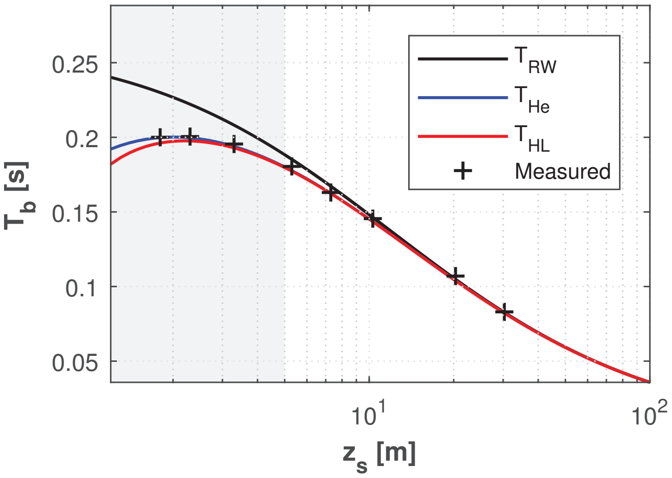

Figure 4.9: Measured bubble time period of 1200 in^3 air gun for different depths fired in the fjord compared to theoretical curves from Rayleigh-Willis equation, Herring and Haavik (Eq. 4.1, 4.2, 4.3). The gray area indicates source depths which are smaller than four times the maximum bubble radius.

4.5.3 Energy vs. Depth

The energy variation of the acoustic signal with source depths for the tank and field experiments is investigated for the measurements in water and air. The acoustic energy of the air gun for different source depths is estimated from the frequency spectra as

$$E = \int_{f_l}^{f_u} |S(f)|^2 df \tag{4.10}$$

where $S(f)$ is the Fourier transform of the recorded, stacked traces for each source depth z_s and f_l, f_u are the lower and upper frequency limit used for the integration. The stacked traces are corrected for geometrical spreading with $1/r$ where r is the source receiver distance. The results in Figure 4.10 illustrate the energy variations with source depths in the frequency band from 1 Hz (f_l) to 400 Hz (f_u). The energy in air, measured at H_3 (Figure 4.3), increases with decreasing source depth (Figure 4.10, top). In contrast to that, the energy in water from the tank experiment decreases with decreasing source depth. In general, the comparison between the energy in air and water illustrates that the loss in water anticorrelates well with the increase in air for the measurements in the tank, although the absolute energy difference between water and air is large. The field measurements (Figure 4.10, bottom) have the same trend as the results in the tank with a decrease in energy for shallower sources. Despite the increased energy for frequencies below 5 Hz and 2 Hz for the shallowest sources in Figure 4.5 (bottom) and Figure 4.8 (bottom), respectively, the acoustic energy can be expected to be smaller for very shallow sources compared to deeper ones. The main reason is the reduced energy of the oscillating air bubble for decreasing source depths. For air gun arrays that are tuned on the main peak and a reduced bubble oscillation the decrease of acoustic energy with source depth might be less pronounced.

4.6 Discussion

The effects and mechanisms that have an impact on the low frequency signal from very shallow air guns are discussed. This is the changing bubble time period with distance to the interface and the vanishing bubble oscillation when the bubble breaks the surface. In addition, as the source depth is decreased the water surface is disturbed caused by the pressure striking the surface and the expanding bubble. All these effects acting on the water-air interface can be expected to cause changes of the ghost reflection. We also discuss recommended depths and air gun volumes for a potential enhancement of frequencies below 5 Hz.

A possible mechanism for energy loss of the ghost reflection is the disturbance of the water surface caused by the acoustic pressure striking the interface. We follow the explanation by Weston (1960) and Loveridge (1985) that a critical pressure p_c is required to break the surface tension at the sea surface. We assume that the pressure radiates spherically from the source as shown in Figure 4.11(a). Video recordings are used to determine the radius d of the disturbed surface, estimated from marks along the rope in Figure 4.11(b). The critical distance r_c is calculated from the known source depth as $r_c = \sqrt{d^2 + z_s^2}$. For an estimation of the critical pressure we use measurements of 15 shots recorded at the receivers H_1 and H_2 for source depths of z_s = 0.2, 0.3, 0.4, 0.5, 0.6 m. The critical

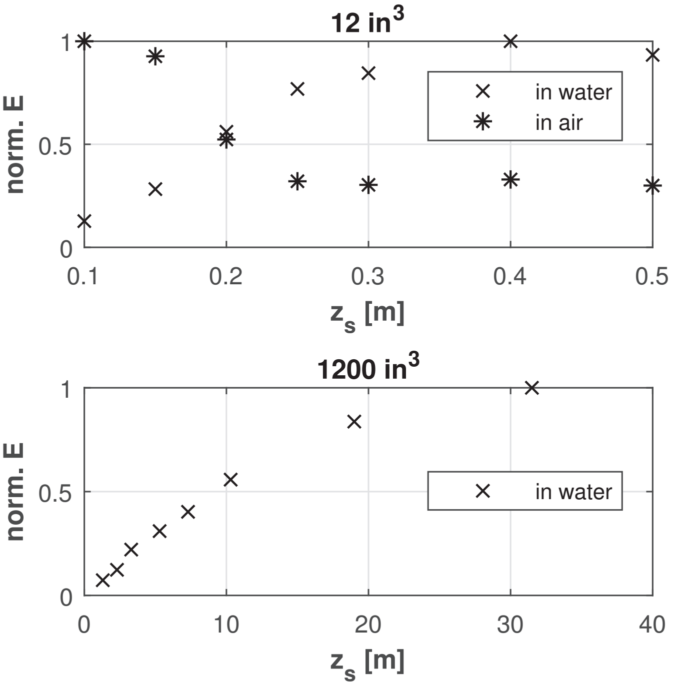

Figure 4.10: Estimated, normalized energy E using Equation 4.10 computed for different source depths for the tank experiments in air and water (top) and the field experiments (bottom).

pressure is computed as

$$p_c = \frac{1}{2} \sum_{i=1}^{2} \frac{1}{N} \sum_{n=1}^{N} \max(p_{i,n}) \left(\frac{r_i}{r_c}\right)^m \tag{4.11}$$

where $\max(p_{i,n})$ is the maximum measured pressure of shot number n at the receiver number i, where i = 1,2 and N is the number of recordings. The source-receiver distance is denoted by r_i as shown in Figure 4.11(a). The factor m = 1,2 accounts for a linear and quadratic spreading correction, respectively. Assuming a linear spreading correction for the amplitudes an average critical pressure from both hydrophones of p_c = 1.11±0.20 bar can be estimated for unfiltered pressure recordings. For the quadratic spreading correction, the critical pressure is p_c = 1.09±0.16 bar. The small variation between both results can be explained by small differences of the distances r_c and r_i. Although this is a rough estimation and the tank size could influence the measurements, the results agree with observations made from field tests. In a fjord test with a 600 in^3 air gun (Haavik and Landrø, 2016) the shot effect can be observed from video recordings down to a source depth of 5 m. A zero-to-peak pressure of approximately 5 bar-m is measured for these tests, which would result in a pressure of 1.25 bar striking the water surface for a source depth of 5 m when a linear spreading correction is assumed. It should be noted that the shot effect could lead to an increased low frequency signal for very shallow sources as indicated in

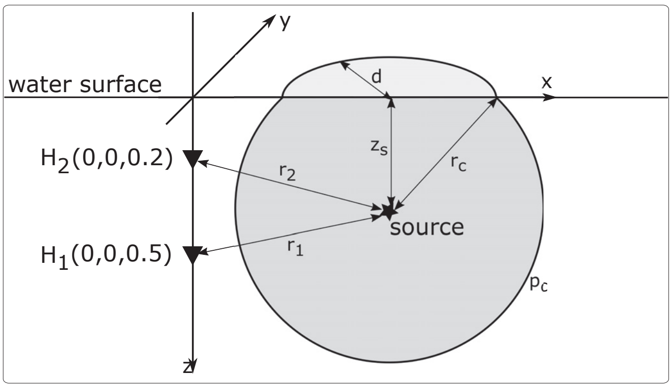

(a)

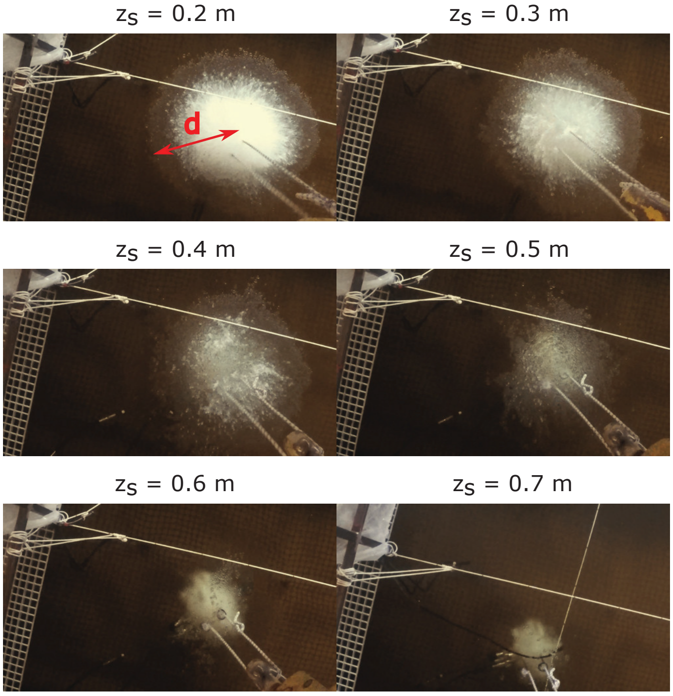

(b)

Figure 4.11: (a) Sketch illustrating the critical pressure p_c needed to disturb the surface area with the radius d. (b) Photos taken by camera 1 shown in Figure 4.3 of the air gun fired at different depths with a firing pressure of 80 bar. The photos are taken shortly after the main bubble radius was reached, at ca. 0.045 s (Figure 4.5).

Figure 4.2, especially for large volume air guns with a high zero-to-peak pressure amplitude.

Another effect is the bubble time period T_b and the amplitude of the bubble signal and its impact on the low frequencies with a peak at the bubble frequency f_b = 1/T_b. Although it is commonly assumed that the bubble enhances the low frequency signal due to an increasing period with decreasing source depths, at a specific depth close the surface the bubble period decreases again, indicated as the turning point in Figure 4.1 (circles). This turning point depends on the gun size and for larger gun volumes the sources can be towed shallower relative to its maximum bubble radius (z_s/R_{max}) before this point is reached. This hypothesis is supported by the measurements as the turning point for the 12 in^3 air gun is at z_s/R_{max} $\approx$ 3.2 (Figure 4.7) and for the 1200 in^3 air gun it is at z_s/R_{max} $\approx$ 1.6 (Figure 4.9).

In the tank experiment only near-field signatures are measured and it could be argued that the enhanced amplitudes at low frequencies vanish in the far-field due to the ghost effect. The far-field ghost is not added to the measured data as the effect of the reduced sea surface reflection caused by the surface disturbance is difficult to quantify. However, the similarities for the signal of the shallowest source in the tank, at 0.1 m (Figure 4.5), and in the field, at 1.3 m (Figure 4.8), at low frequencies indicate that the ghost is strongly reduced. Therefore, an enhanced low frequency signal in the far-field could still be expected.

As an attempt to summarize the impact of the source depth on the low frequency part of the signal, characteristic depths are defined (Figure 4.12) which are explained in the following.

I No relevant interactions between the source and the water-air interface are expected within this range that have an impact on the source signal.

II p_s = p_c: this depths indicates when the emitted acoustic pressure at the surface p_s equals the critical pressure p_c which was estimated in the experiments and is illustrated in Figure 4.11. Therefore, the surface can be disturbed by the shot effect for sources that are fired shallower. Although it is difficult to quantify this effect it could reduce the ghost impact as indicated in Figure 4.2 which could lead to increased low frequencies.

III $z_s < 4\ R_{max}$: for all depths smaller than $4 \cdot R_{max}$ the bubble is expected to interact with the sea surface (Chahine, 1977) which leads to a smaller increase of the bubble period than predicted by the Rayleigh-Willis equation (Figure 4.7 and 4.9). Therefore, the increase of low frequencies is lower than assumed, which would counteract the effect described in point 1. For large gun volumes the shot effect could be strong within this range while the bubble period still increases (Figure 4.9). This could be an explanation for the increased low frequencies between 0.5 Hz and 2 Hz for the 1200 in^3 air gun fired at a depth of 3.3 m (Figure 4.8, bottom).

IV T_b decreases: this depths indicates the turning point from which on the bubble period decreases with decreasing source depths (Figure 4.1, circles) and hence the low frequency enhancement due to the bubble is stopped. This effect is even more pronounced by a reduced bubble amplitude. Therefore, measurements within this range could have a reduced low frequency signal. This hypothesis can be supported by the

12 in^3 air gun fired at 0.15 m (Figure 4.5) and the 1200 in^3 air gun fired at ”1.8” m and at 2.3 m (Figure 4.8).

V $R_{max} \geq z_s \geq R_{max}/1.5$: within this range it is expected that the bubble breaks the surface. It can be observed from the measurements with the 12 in^3 air gun that the depth might has to be smaller than the maximum radius to break the surface. However, the value of 1.5 is a rough estimation from the observations. Within this range the low frequency signal below 5 Hz is expected to be enhanced the most. This could be due to a highly reduced ghost reflection as the surface is strongly altered by the bubble breaking the surface. For even shallower source depths the energy in water could be highly reduced and more energy goes into air as discussed (Figure 4.10). The other issue is that the low frequency content does not seem to be increased when the air gun is slightly deeper than this depth.

It should be mentioned that this is a simplified explanation as the shot effect and nonlinear effects, when the bubble breaks the surface, are difficult to quantify. The source depths for $p_s = p_c$ is estimated as $z_s = (p_p/p_c)$+1 m where p_p is the zero-to-peak amplitude in bar-m

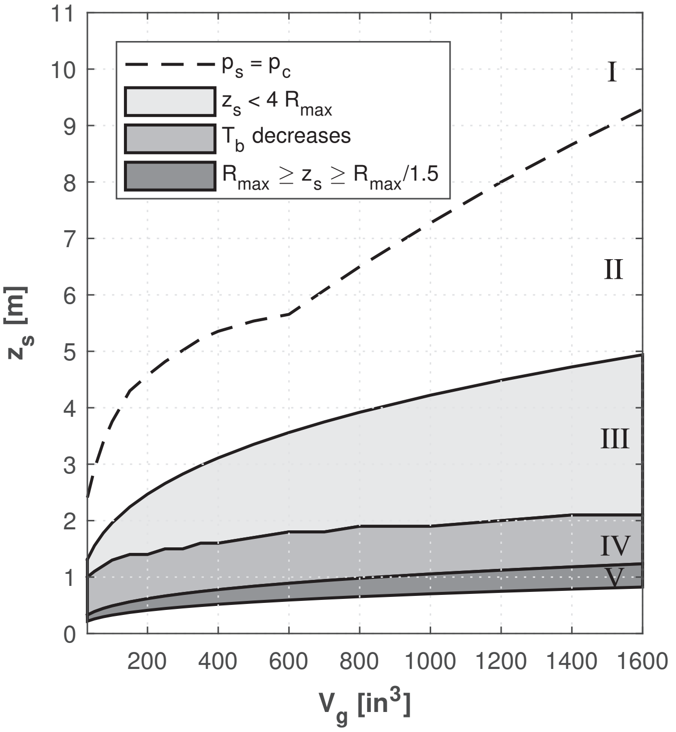

Figure 4.12: Characteristic depths for different gun volumes V_g and a firing pressure of 137 bar as explained in point I to V. R_{max} is the maximum bubble radius, T_b the bubble time period, z_s the source depth, p_s the emitted acoustic pressure at the surface and p_c the critical pressure as indicated in Figure 4.11(a).

computed at 4 m depths with a commercial software. This can be a valid assumption, at least for guns larger than 200 in^3, as the peak amplitude does not vary significantly with depth within the range between 5 m and 12 m (Vaage et al., 1983). The critical pressure p_c is estimated from experiments with a flat surface and this value could vary when the surface is already disturbed due to weather or waves. The maximum bubble radius R_{max} is estimated as a mean value of all maximum radii computed for source depths between 0.1 m and 10 m (increment 0.1 m) using a damped Kirkwood-Bethe equation as in Landrø and Sollie (1992). Despite all these simplifications the scheme (Figure 4.12) explains the main effects and observations in the measured data and could act as a guideline for further field experiments.

To enhance the frequency part below 5 Hz in marine seismic surveys it can be beneficial to place a few sources very shallow as suggested by Amundsen et al. (2017). The depths should be around the range $R_{max} \geq z_s \geq R_{max}/1.5$ as indicated in Figure 4.12. It is recommended to use large volume air guns due to several reasons. They do not loose as much energy from the oscillating bubble as smaller sources when towed that shallow. Only one or two big air guns (e.g. 1200 in^3) might be sufficient to increase the low frequency signal noticeable. They can be towed at depths around 1 m and not as shallow as 0.5 m or less which would make the towing even more complicated. In addition, it seems promising that a 1200 in^3 air gun also enhances the low frequency content for depth between 3 m to 4 m (Figure 4.8). It should be mentioned that the towing of air guns as shallow as 1 m or less is a challenging task, especially when the sea state is high. However, when this issue is solved the addition of a few very shallow sources to a conventional air gun array is very likely to enhance frequencies below 5 Hz. The energy related to the oscillating bubble that is lost for very shallow sources need to be compensated by the conventional part of the array.

To investigate the effect on the ghost in a field trial in more detail air guns with small bubble oscillations, e.g. GI Guns with two chambers, should be tested, while near- and far-field signals are recorded. This allows to focus on the main peak and its ghost as the bubble is a strong factor that impacts the signal very close to the sea surface. This test would continue the work done by Mayne and Quay (1971).

4.7 Conclusion

An enhanced low frequency signal for frequencies below 5 Hz can be observed in the experiments for sources at a depth where the air gun bubble bursts directly into the air and hence no oscillations occur. For large volume air guns the low frequency signal might be also increased for slightly deeper sources as the high zero-to-peak pressure leads to strong disturbances of the sea surface caused by the acoustic pressure. This could result in a reduced ghost reflection and enhanced low frequency signal as observed in the data. In comparison to small air guns, large volume air guns can be towed at shallower depths relative to their maximum bubble radius before the bubble period starts to decrease in the vicinity of the free surface. Recommended depths are given where guns of different volumes could be placed to achieve an increased signal for frequencies below 5 Hz. In addition, depths are indicated where the oscillating bubble looses most of its energy and where the ghost might start to be reduced. As very shallow air guns, which burst directly into the surrounding air, loose the energy related to the oscillating bubble, a combined source array of a few very shallow air guns and a conventional set up can be a good compromise. Further field trials are required to verify the results in common marine seismic acquisition surveys and to investigate the feasibility and source signal repeatability of towing air guns as shallow as 1 m, especially during higher sea states.

4.8 Acknowledgements

We acknowledge the European Union's Horizon 2020 research and innovation programme under the Marie Skłodowska-Curie grant agreement No 641943 for the funding of Daniel Wehner's PhD project within WAVES. We like to acknowledge the technical team at IGP for their support to the experimental setup. We like to thank Statoil ASA for contributing the air gun recordings where Å. S. Pedersen and M. Thomson have designed and conducted the field work. Martin Landrø acknowledges financial support from the Norwegian Research Council.

Chapter 5

The Coupling of Marine Seismic Source Signals into Air

Daniel Wehner[1], **Peter Svensson**[2] **and Martin Landrø**[2]
[1] *NTNU, Department of Geoscience and Petroleum, 7031 Trondheim, Norway*
[2] *NTNU, Department of Electronic Systems, 7491 Trondheim, Norway*

Extended investigation and discussion on Chapter 3 and 4; manuscript in preparation

5.1 Abstract

When a seismic airgun is fired very close to the water surface the oscillating bubble interacts strongly with the water-air interface. The main interest for seismic applications is how this effects the acoustic signal emitted into water. However, the signal that is radiated into air could be also influenced by the source-interface interaction. We elaborate more on the signal measured in air by expanding the discussion of chapter 3 and 4. In chapter 3 the acoustic source is a small cavity that is sufficiently far away from the water-air interface so that no interaction between the cavity and water surface occurs. Therefore, only the emitted acoustic pressure strikes the water surface. In chapter 4 the acoustic source is a large air bubble that is very close to the water-air interface and hence strong interaction between the bubble and water surface occurs. The main focus is on the source that directly interacts with the water-air interface. The effects on the water surface and oscillating air bubble for very shallow depths are discussed in more detail. We find that the moving surface could contribute to the signal that is measured in air.

5.2 Introduction

In marine seismic acquisition and underwater acoustics the focus is naturally on the signal that propagates in water. However, a part of the signal is also transmitted into the air. The signal amount that is transmitted depends, amongst other things, on the distance between the source and the water-air interface. For an oscillating bubble as the source, the bubble interacts and disturbs the water surface when excited close to the interface and the moving interface could emit further signal into the air. Hence, we might define two main effects that create a signal in air. First, the signal in air is transmitted through the interface. Second, the moving water surface, due to the interaction with the source, emits an acoustic signal into the air.

The signal that is transmitted through an interface depends on the transmission coefficient of the interface. For the water-air interface the transmission coefficient is low due to the high impedance contrast between water and air (Kinsler et al., 1962). For plane waves incident on the interface the transmission depends on the angle of incidence, while for spherical waves incident on the interface it depends also on the frequency, source-interface and interface-receiver distance (Brekhovskikh and Lysanov, 1991; Aki and Richards, 2002) as discussed in chapter 3. The strongest difference between a spherical transmission response and the plane wave transmission coefficient could be observed for low frequencies, or more precisely for wavelength larger than the source-interface distance as demonstrated by Li et al. (2017a), Li et al. (2017b) and Yan et al. (2017) for AVO (amplitude versus offset) analysis of seismic data between two acoustic media. In addition, an increased amount of signal could be transmitted into air caused by the evanescent component of the wave inside water which can be converted to a homogeneous wave in air for particular wave numbers. This is discussed in theory for monopole sound sources in water where the source depth is much less than the emitted acoustic wavelength by Godin (2006), McDonald and Calvo (2007), Godin (2008) or Glushkov et al. (2013). Experimental results verifying the increased transmission from water into air, when accounting for evanescent waves, for a frequency range between 1 and 20 kHz are presented by Calvo et al. (2013) and Voloshchenko and Tarasov (2013).

The behaviour of oscillating bubbles and explosions close to the water-air interface is studied by several authors for different sizes of air bubbles and an overview of bubble dynamics and potential applications is given by Wang et al. (2018). The interaction of the free surface with small bubbles, in the millimeter range up to a few centimeters, is demonstrated by Oguz and Prosperetti (1990), Chahine et al. (1995) or Krieger and Chahine (2005). A critical distance where the interaction between the bubble and free surface takes place is theoretically and experimentally investigated by Chahine (1977). The effect of surface tension on the water-air interface displacement caused by the bubble and acoustic pressure is demonstrated by Lu et al. (1989) and Cinbis et al. (1993). When small bubbles burst at the water-air interface a jet is formed as presented by Boulton-Stone and Blake (1993) in a numerical model and experimentally demonstrated by Blake and Gibson (1981) or Longuet-Higgins (1983). The interaction between the free surface and intermediate bubble radii, in the range of a few tens of centimeters, is demonstrated by Hung and Hwangfu (2010) and Cui et al. (2016) using small explosives. They also investigate the interaction with solid boundaries. High-speed photography for these experiments indicates cavitation near the surface due to the negative acoustic pressure reflected from the surface and the formation of a jet through the bubble (Cui et al., 2016). Experiments with a small laboratory scale airgun fired close to a solid boundary and free surface are conducted by de Graaf et al. (2014a). The interaction between the ocean surface and large spherical underwater blasts emitting a shock wave is theoretically described by Chan et al. (1968), Collins and Holt (1968) or Ballhaus Jr. and Holt (1974). Another example of the interaction between a fluid-air interface and large bubbles, in the range of a few meters, is related to volcanic eruptions. The infrasound signal recorded from gas bubbles breaking at the surface of a lava column is presented by Vergniolle and Brandeis (1994, 1996), Vergniolle et al. (1996) and Johnson (2003).

Here, we compare the two experiments from chapter 3 and 4 with a focus on the signal that is recorded in air. The main difference between the experiments is the bubble size of the source. In chapter 3 the radius of the cavity from the watergun is small, approximately 2-3 cm, and the distance between the source and water-air interface is large relative to the cavity radius. Therefore, no interaction between the source and the water surface is expected for the source depths in the experiment. In chapter 4 the radius of the bubble is much larger, approximately 20-25 cm, and hence the source strongly interacts with the water surface when excited at depths smaller than 4 times the maximum bubble radius.

5.3 Theory

The two main effects, signal transmission through the water-air interface and an acoustic signal emitted by a moving surface, are briefly discussed in the following.

The acoustic pressure from a source underwater transmitted through the water-air interface and measured in air can be described for a flat fluid-fluid interface and plane waves as (Kinsler et al., 1962)

$$p_t = p_i \, T_c \, \exp[i(\omega t - k_a x \sin(\theta_a) - k_a z \cos(\theta_a))] \tag{5.1}$$

where p_i is the pressure incident on the water-air interface, T_c is the transmission coefficient, θ_a is the angle of refraction in air and $k_a = \omega / c_a$ where c_a is the sound velocity in air and $\omega = 2\pi f$ with f as the frequency. The coordinates x and z are as shown in Figure 5.1. For the transmission plane waves or spherical waves might be assumed as discussed in chapter 3.

The acoustic pressure in air generated from a moving surface could be computed similar to a membrane as (Harris, 1981)

$$p_m(t) = \frac{\rho_a}{2\pi} \int_{dS} \frac{\ddot{h}\left(t - \frac{r_a}{c_a}\right)}{r_a} dS \tag{5.2}$$

where ρ_a is the density of air, dS is a surface element in the horizontal plane of the water surface, r_a is the distance from the water surface to the receiver and $\ddot{h}$ is the second time

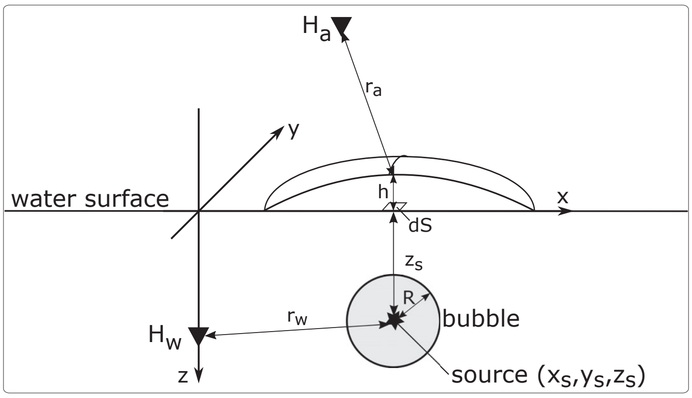

Figure 5.1: Sketch illustrating the displacement h of the water surface caused by an oscillating bubble underwater.

derivative of the water surface displacement h (Figure 5.1). The surface displacement caused by an oscillating bubble is related to the distance from the water surface and the bubble size (Chahine, 1977). Here, we use an ad-hoc model for the surface displacement accounting for those components, similar to the model presented by Chahine (1977), as

$$h = \frac{2}{(r^2+1)^{3/2}} \, \frac{4}{3}\pi R^3 \tag{5.3}$$

where $r = \sqrt{(x-x_s)^2 + (y-y_s)^2 + z_s^2}$ is the distance between the center of the bubble and the horizontal plane at the water-air interface and R is the bubble radius (Figure 5.1). The model presented from Chahine (1977) is valid under the assumption that the bubble is sufficiently far from the water-air interface, so that it can be represented as an oscillating source of variable intensity with time. The water surface displacement caused by an oscillating air bubble underwater is illustrated in Figure 5.1.

5.4 Experiments

The experiments are conducted in a water tank with the dimensions given in Figure 5.2 and 5.3. The walls of the tank are equipped with 5 cm thick foam mattresses. Brüel & Kjær hydrophones of the type 8105 are used as receivers for all experiments in the tank which have a frequency range from 0.1 Hz to 100 kHz. Additional hydrophones are located in air to record the signal transmitted through the water-air interface. The hydrophones of type 8105 have the same sensitivity in water and air for frequencies up to 3 kHz. Two different experiments are conducted that mainly differ in the seismic source used for the experiment.

In Experiment A, a S15 watergun with one cylindrical gun port and a gun volume of 15 in^3 (ca. 0.25 l) is used (Figure 5.2). The source creates a collapsing cavity caused by a

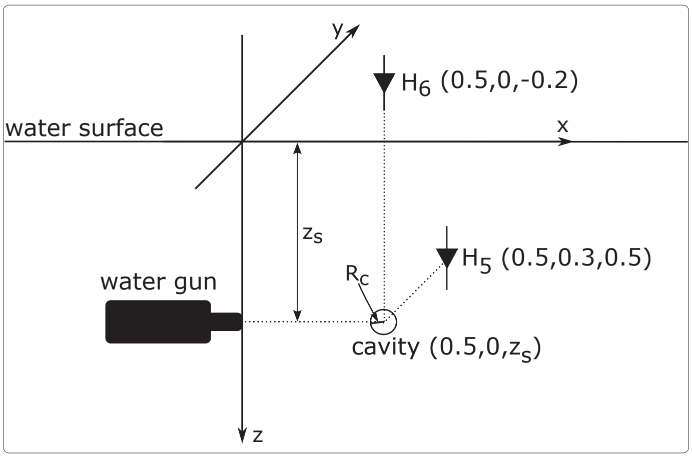

Figure 5.2: Sketch of experimental set up in the water tank for Experiment A. The hydrophones are indicated as H_5 and H_6 where the x-, y- and z-coordinates in meters are given in brackets. The water depth in the tank is 1.25 m and the width and length of the tank are 2.5 m and 6 m, respectively.

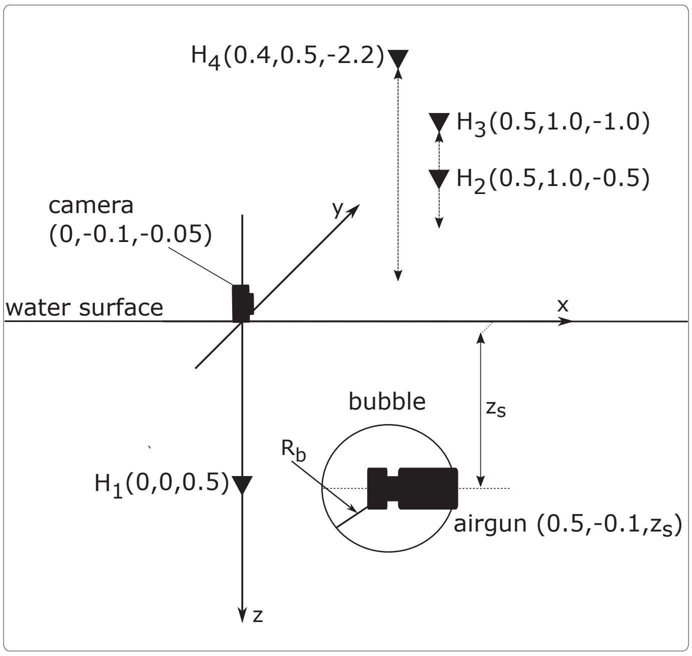

Figure 5.3: Sketch of experimental set up in the water tank for Experiment B. The hydrophones are indicated as H_1, H_2, H_3 and H_4 where the x-, y- and z-coordinates in meters are given in brackets. The water depth in the tank is 1.25 m and the width and length of the tank are 2.5 m and 6 m, respectively.

high velocity water jet that is pushed out of the gun port when fired. The maximum radius of the cavity in our experiment is in the range of approximately 2-3 cm (Figure 5.2). The source is fired at different depths ranging from z_s = 0.2 m to z_s = 0.7 m.

In Experiment B, a Mini G. Gun with four gun ports and a chamber volume of 12 in^3 (0.2 l) is used (Figure 5.3). The source creates an oscillating air bubble caused by the sudden release of highly compressed air from the gun chamber. The maximum radius of the bubble in our experiment is in the range of approximately 20-25 cm (Figure 5.3). The source is fired at different depths ranging from z_s = 0.1 m to z_s = 0.6 m. In addition to the pressure recordings a camera is placed slightly above the water-air interface during this experiment to film the water surface while the airgun is fired at different depths. The recording rate of the camera is 240 frames per second (fps) which allows to have a photo approximately every 4.2 ms.

5.5 Results

First, we compare the recordings in air from both experiments. Secondly, we investigate the results from experiment B in more detail as the source strongly interacts with the water-air interface which is not the case for experiment A. The pressure recordings in water and air are shown in Figure 5.4 and 5.5 for experiment A and B, respectively. The maximum bubble radius indicated in the figures for the cavity R_{mc} and airgun bubble R_{mb} is estimated from the measured collapse time τ (Rayleigh, 1917)

$$\tau = 0.915 R_m \sqrt{\frac{\rho_w}{p_0}} \tag{5.4}$$

where ρ_w is the water density, p_0 is the hydrostatic pressure and 0.915 is an exact number derived from gamma functions by Rayleigh (1917). The radius R_m is replaced by R_{mc} or R_{mb} for the respective experiment. It should be noted that the signals are corrected for geometrical spreading with 1/r and that the signal in air is enhanced by multiplication with a constant factor to make it comparable with the recordings in water.

For experiment A the signal in air is multiplied by 300 (Figure 5.4). The signal in air has nearly the same shape as the signal in water. The delay between the signals fits with the delay corresponding to the difference in source-receiver distances and different sound velocities in water and air. As the similarity between the signal in air and water is high, the signal in air is most likely caused by transmission through the interface only. This is also in agreement with the distance between the source and water-air interface where the shallowest source is still at a depth larger than 8 times the maximum cavity radius R_{mc}. Therefore, no interaction between the interface and source is expected (Chahine, 1977). That the signal reflected from the water-air interface does not alter the shape of the recordings in water too much is demonstrated in chapter 3. The measured transmitted signal is slightly stronger as expected from the theoretical plane wave transmission coefficient $T_p \approx$ 0.0006 which could be due to the spherical wavefront or evanescent waves as discussed in chapter 3.

For experiment B the signal in air is multiplied by 40 (Figure 5.5) which indicates that the signal in air is stronger than in experiment A relative to the signal strength in water. For the range with comparable source depths z_s in both experiments between 0.2 m and 0.6 m, the signal in air in experiment B is about 2 to 2.5 times stronger than in experiment A relative

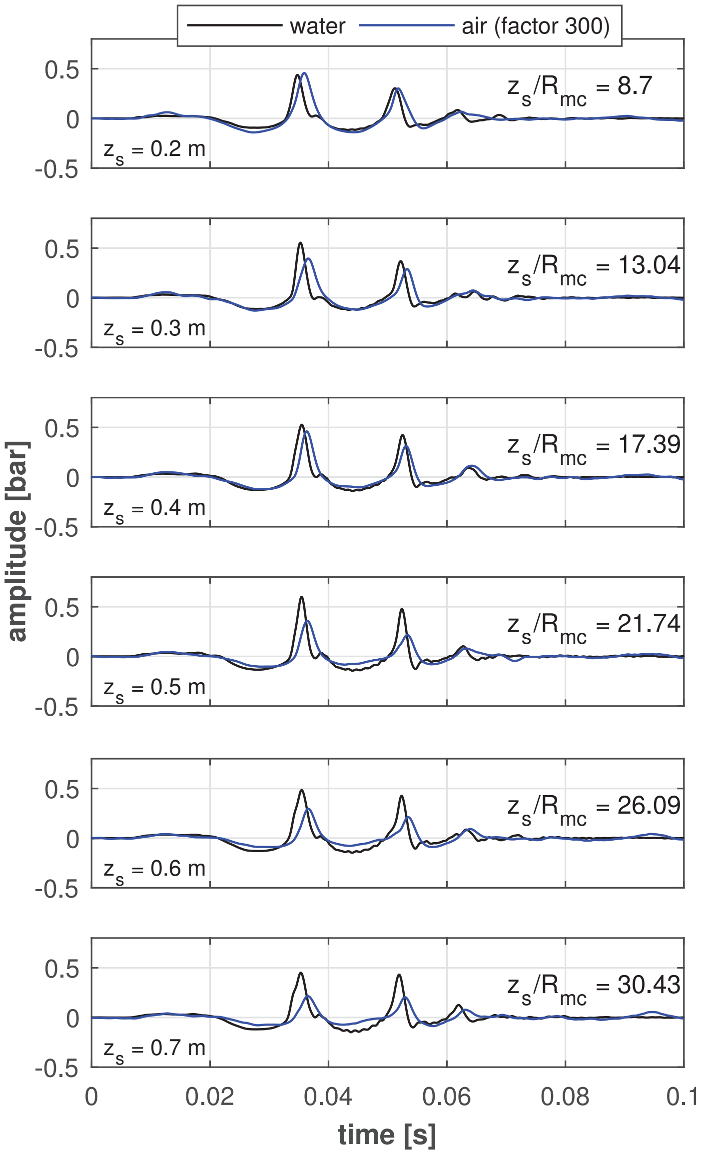

Figure 5.4: Measurements of watergun signature at H_5 and H_6 (Figure 5.2) for different source depths z_s. Indicated is also the ratio between the source depth z_s and maximum cavity radius R_{mc}. Signal is 300 Hz low-pass filtered.

to the signal in water. For shallower sources the increase of the signal in air is much stronger and for the shallowest depths of 0.1 m the amplitude in air is doubled compared to the second shallowest depths of 0.15 m (Figure 5.5). In addition, we observe that the signal shape is quite different between the measurements in air and water, especially for

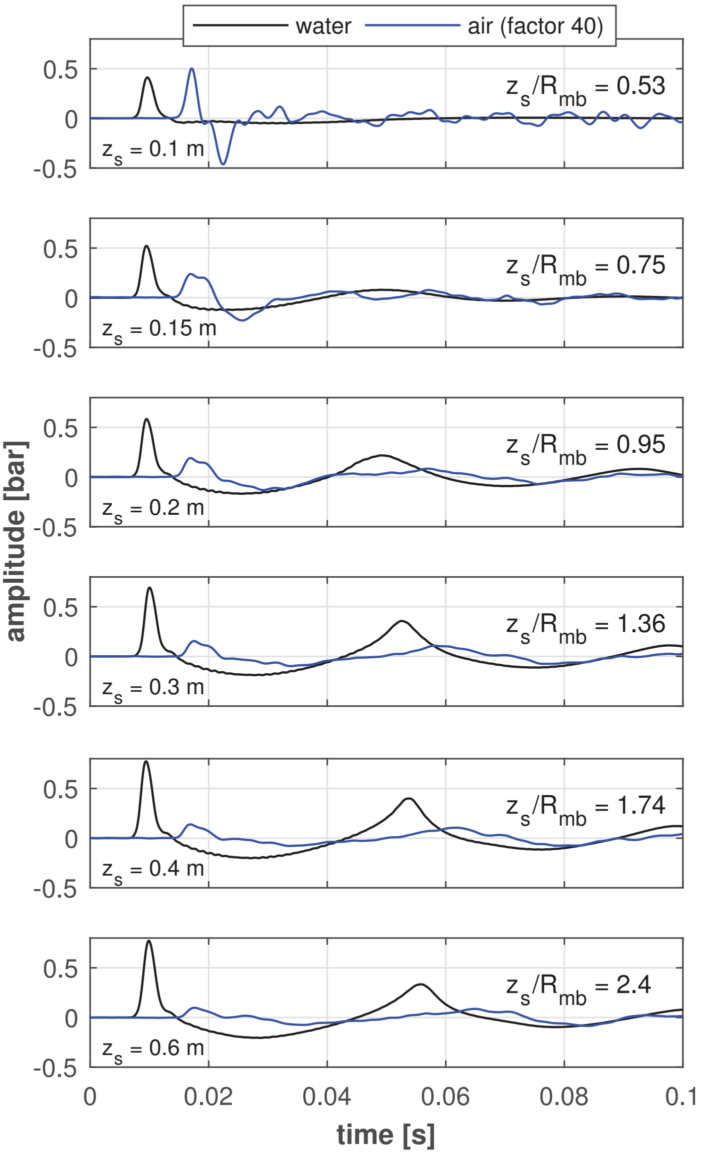

Figure 5.5: Measurements of airgun signature at H_1 and H_4 (Figure 5.3) for different source depths z_s. Indicated is also the ratio between the source depth z_s and maximum bubble radius R_{mb}. Signal is 300 Hz low-pass filtered.

the shallowest source depths. We note a strong negative peak around 0.23 s and 0.26 s in air for source depths of 0.1 m and 0.15 m which is not present in the measurements in water. The main peak in air around 0.18 s is also broadened for source depths between 0.15 m and 0.3 m compared to the signal in water and seems to consist of two peaks. The time delay between the main peak in water and air is about 7.3 ms which is slightly more than 6.5 ms which is expected from the source-receiver distance and sound velocity in air. If we account for an error in the acquisition geometry of $\pm$ 0.1 m for the position of the receivers the expected time delay can be 7 ms.

For a comparison of both experiments we estimate the signal that is transmitted into air depending on the source-interface distance as the ratio between the maximum amplitude in air and water (Figure 5.6). The errorbars indicate the computed standard deviation of the ratio from the measured data. The theoretical amplitude ratio using the plane wave transmission coefficient T_p is shown as a reference. The data seems to converge towards the plane wave transmission coefficient with increasing ratios of z_s/R_m which means that the source is at a large depths or the bubble radius of the source is small. The amplitude ratio strongly increases when $z_s/R_m < 1$. It should be noted that the source bubble interacts with the interface for small z_s/R_m values and hence the plane wave transmission coefficient might not be a fair comparison. However, it acts as a descriptive reference.

Two more observations from experiment B are discussed in the following. First, an interaction between the source and the water-air interface is expected for all depths as the the deepest source depth of 0.6 m is less than 2.5 times the maximum bubble radius R_{mb} and hence it is within the critical range for interaction (Chahine, 1977). The impact of the airgun bubble on the water-air interface can be observed in Figure 5.7(a). The photos il-

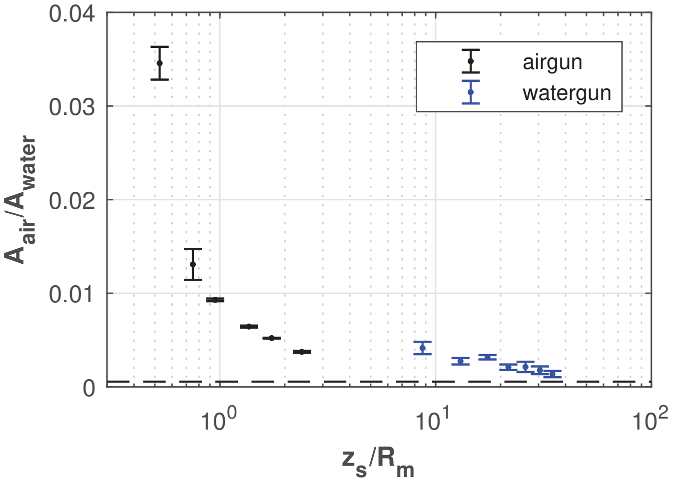

Figure 5.6: Ratio of maximum peak amplitude measured in air A_{air} and water A_{water} for both experiments depending on the ratio between the source depth z_s and maximum bubble size R_m. R_m is replaced with R_{mc} and R_{mb} for the respective experiment. Computed for a 300 Hz low-pass filtered signal. Dashed line shows theoretical ratio using the plane wave transmission coefficient T_p.

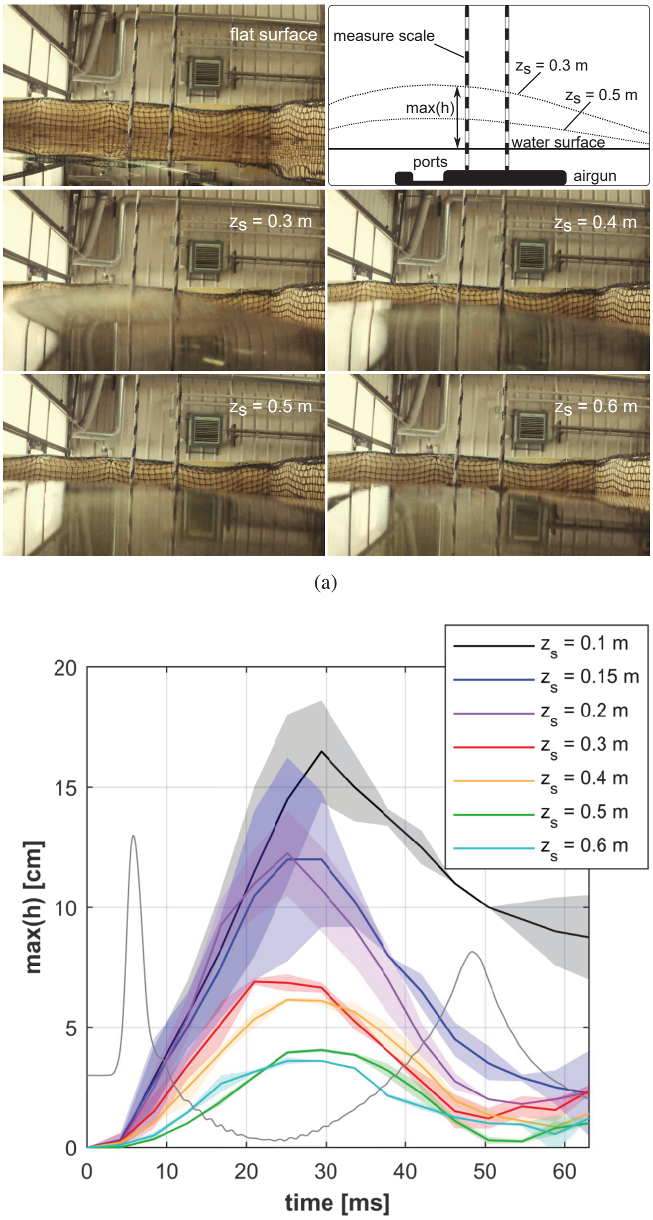

(a)

(b)

Figure 5.7: (a) Photos at water surface for airgun experiment B fired at different source depths z_s taken ca. 20 ms after airgun is fired, when bubble radius R is close to its maximum. Sketch shows the set up and how max(h) is measured. (b) Measured maximum surface displacement h for different source depths. Shaded area indicates the error. Grey line is the normalized measured acoustic pressure in water for the airgun fired at $z_s = 0.3$ m.

lustrate the surface lift due to the expanding airgun bubble. The variation of the maximum surface lift with time is measured from the videos and marks on the rope (Figure 5.7(b)). Only two videos for each source depth are evaluated and the estimation of the shallowest sources, $z_s < 0.3$ m, is more a guess due to the splash and other non-linear effects. However, we get a rough estimate for the surface elevation and the estimation for the deeper sources could be performed more accurately for the first bubble oscillation. We note how the surface lift decreases with increasing source depth. In addition, the correlation of the maximum bubble radius and maximum surface displacement can be observed. The maximum bubble radius is reached when the acoustic pressure has a minimum (Figure 5.7(b),

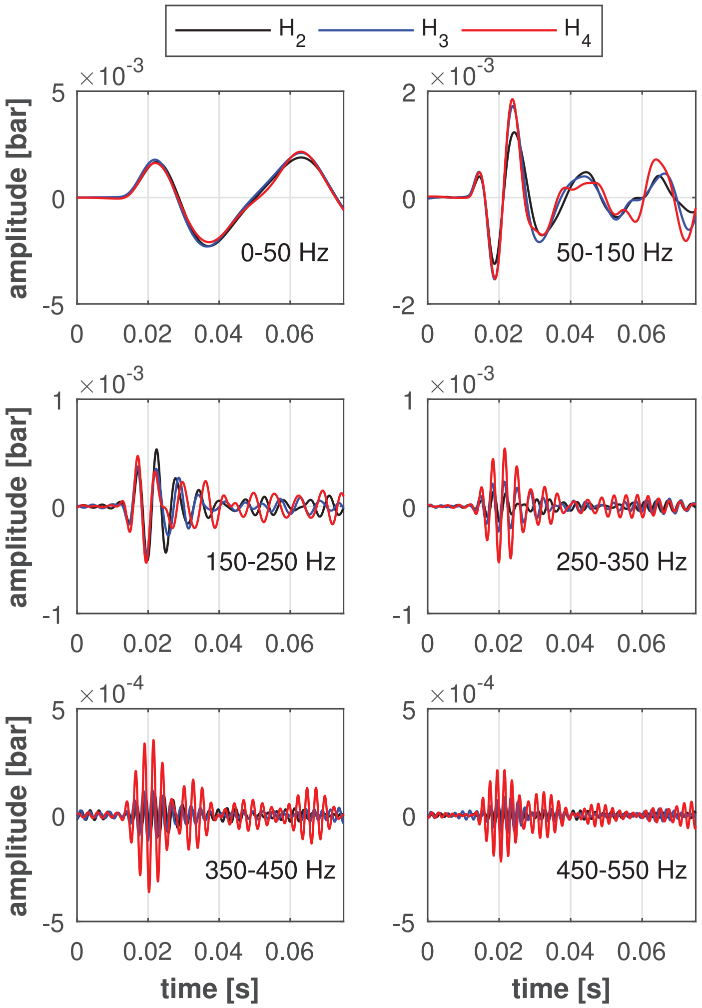

Figure 5.8: Measurements of airgun signature in air at H_2, H_3 and H_4 (Figure 5.3) with different band-pass filters applied as indicated, corrected for spreading with $1/r$ and aligned in time. The source depth is $z_s = 0.3$ m. Note the different amplitude scales for each plot.

grey line). We also note that the surface is almost instantly lifted when the gun is fired. It should be noted that the gun trigger and video recording are not synchronized. We estimate time zero for the video recordings from the first sign of released air from the gun.

Second, we investigate the measured signal in air at different refraction angles from the water-air interface location vertically above the source. Therefore, we compare the recorded signals measured at H_2, H_3 and H_4 (Figure 5.3) within different frequency bands (Figure 5.8). We observe that the signals are almost the same at all receivers for the lowest frequency band, below 50 Hz, while the difference increases with increasing frequency. That might be explained by different reflections of obstacles in air as the receivers are located at different positions. When comparing the amplitudes, we observe that receiver H_4 records stronger signals at higher frequencies compared to the other two receivers. While reflections might also impact this observation, evanescent waves could be another explanation as discussed in the next section.

5.6 Discussion

First, we discuss a potential mechanism to explain the amplitude differences observed in Figure 5.8. Secondly, we present a simple model that could explain the main features of the signal recorded in air from experiment B (Figure 5.5).

The higher amplitudes with higher frequencies measured at receiver H_4 compared to the receivers H_2 and H_3 might be explained by evanescent waves in water which are transmitted as homogeneous waves into air. As discussed for a monopole sound source by Godin (2008) and Calvo et al. (2013) more signal could be transmitted into air with decreasing frequencies and source depths when $z_s/\lambda \ll 1$, where λ is the wave length in water. Calvo et al. (2013) compute the transmitted signal into air using wavenumber integration which demonstrates that most of the signal is confined inside a cone, when only homogeneous waves in water are assumed (Figure 5.9). The angle of the cone corresponds to the critical angle between water and air. When evanescent waves are taken into account, the radiation into air is close to omnidirectional for small z_s/λ ratios as shown for an example with the ratio z_s/λ = 0.034 (Calvo et al., 2013). In our experiments (Figure 5.8) the ratio is z_s/λ = 0.005 for the lowest frequency band, assuming f = 25 Hz, while it is z_s/λ = 0.1 for the highest frequency range, assuming f = 500 Hz. Therefore, evanescent waves might be one explanation that we observe the same signal amplitude at all receivers for the lowest frequencies. For the highest frequencies, when the evanescent component is less pronounced, the amplitudes are stronger close to the 13.4^o cone, which is the case for receiver H_4 (Figure 5.8). It should be noted that the theory is developed for a monopole sound source which might not be fully valid for the airgun fired close to the interface.

The signal in air measured in experiment B might be partially explained by the movement of the water surface and the bubble venting into the surrounding air when it breaks the surface, in addition to the signal that is directly transmitted through the water-air interface. The effect is investigated using a phenomenological model that describes the movement of the water surface as a function of the bubble radius. We compute the airgun bubble in water using a damped Kirkwood Bethe equation as (Kirkwood and Bethe, 1942; Landrø and Sollie, 1992)

$$\ddot{R} = \frac{\left(1+\frac{\dot{R}}{C}\right)H + \left(1-\frac{\dot{R}}{C}\right)\frac{R}{C}\dot{H} - \frac{3}{2}\left(1-\frac{\dot{R}}{3C}\right)\dot{R}^2 - \alpha\dot{R} + \beta\dot{R}^2}{R\left(1-\frac{\dot{R}}{C}\right)} \tag{5.5}$$

where R, $\dot{R}$ and $\ddot{R}$ are the bubble radius, velocity and acceleration, respectively. The sound velocity in water at the bubble wall is denoted by C, H is the enthalpy and α and β are damping and empirical coefficients accounting for energy losses of the bubble oscillation. We adjust the damping parameters to fit the measurements in water at H_1 (Figure 5.3). In addition, we assume that the bubble breaks the surface and vents into the air when a critical bubble radius R_c is reached depending on the source depth. This radius is R_c = $1.5z_s$ estimated from the video observations and acoustic recordings in water. We assume that the bubble radius and hence the surface displacement stops abruptly when the critical radius is reached (Figure 5.10). Although this is a very simplistic model, we note that the bulge at the water surface for the shallowest source depth of z_s = 0.1 m is kept almost constant for a long time compared to the deeper sources (Figure 5.12 and 5.13). Similar observations for an almost stationary water surface displacement during a collapsing cavity are demonstrated by Robinson et al. (2001). The surface displacement h is computed

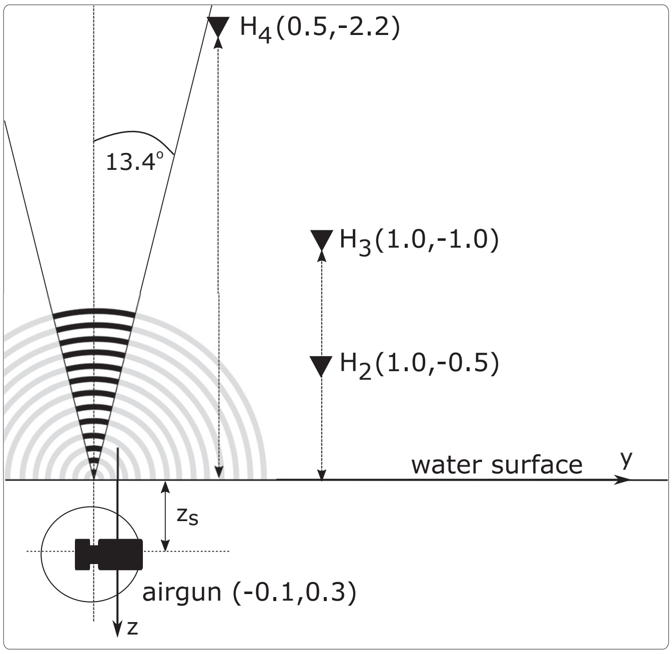

Figure 5.9: 2D section of experimental set up shown in Figure 5.3. The transmitted signal into air from a monopole sound source is sketched accounting only for homogeneous waves (black) and including the evanescent part (grey), adopted from Calvo et al. (2013).

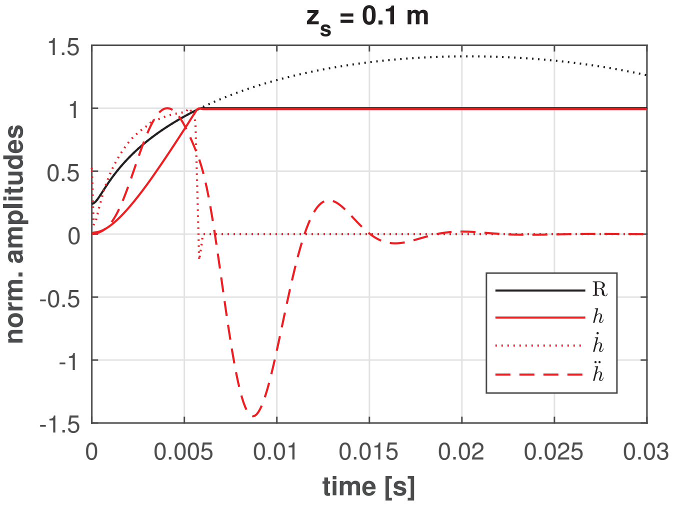

Figure 5.10: Modelled bubble radius R and surface displacement h vertically above the source. The critical radius R_c, when the bubble breaks the surface, is reached at 1. The black dashed line indicates the modelled bubble radius when it does not break the water-air interface. A 150 Hz low-pass filter is applied to $\ddot{h}$.

using equation 5.3 and the general shape of the water surface is explained well by the ad-hoc model. To fit the amplitude of the modelled surface displacement to the measurements (Figure 5.7(b)) we scale equation 5.3 with $0.3/z_s$. The acoustic signal at the receiver can be computed from the surface movement using equation 5.2. The model and measurements are compared in Figure 5.11 for normalized amplitudes. The negative peaks in air for the depths of 0.1 m and 0.15 m are explained by the negative acceleration of the surface displacement caused by the abrupt stop of the bubble (Figure 5.10). When the bubble does not break the surface, at 0.3 m, the signal in air is a repetition of the bubble movement in water. The amplitudes are normalized as the model predicts 5 times higher amplitudes than observed in the measurements. That could be due to the assumption of an abrupt stop of the bubble radius which is way more complex and the simple model used to describe the surface lift. In addition, the Kirkwood-Bethe model for the bubble does not account for a breaking bubble. These points need to be investigated in more detail to quantify the amplitudes as the breaking point is crucial for that purpose. However, the general shape with the negative peaks in air could be reproduced by the model (Figure 5.11) and hence the surface lift could contribute to the signal in air for very shallow source depths. Similar signals and mechanisms are discussed by Bowman et al. (2014) who conduct experiments with small explosives at different burial depths close to the surface. Although they investigate the coupling between an elastic medium and air, some phenomenons seem to be similar. Furthermore, investigations on volcanic eruptions conducted in the field of infrasound reveal similar signals received in air (Johnson, 2003; Yokoo and Iguchi, 2010).

In Figure 5.12 and 5.13 we note that the water surface has changed for all source depths between time 0 and 4.2 ms. A white foam lifted from the surface is visible at 4.2 ms for source depths of 0.1 m and 0.15 m that is not visible for the source depth of 0.3 m. That might be water vapor molecules lifted from the surface due to the high pressure incident on the water-air interface (Loveridge, 1985). In addition, we note that water droplets are created above the water surface starting at 21 ms. This observation can be best recognized when the photos at 21 ms (Figure 5.12) and 25.2 ms (Figure 5.13) for a source depth of 0.3

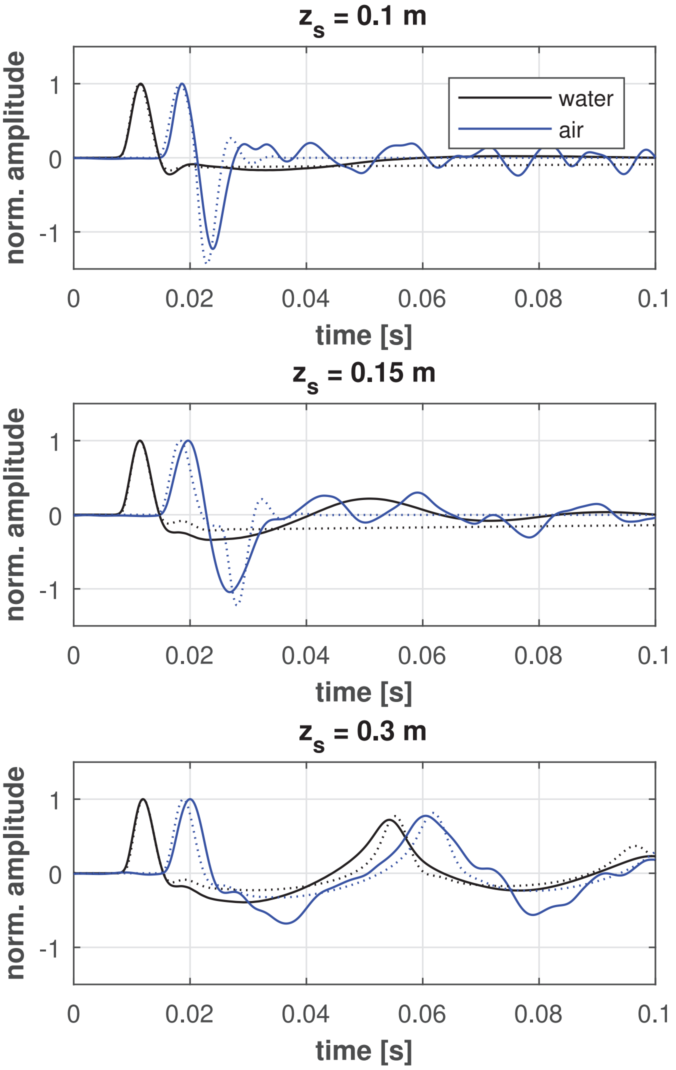

Figure 5.11: Measured (solid) and modelled (dotted) signals from the 12 in^3 airgun recorded in water at H_1 and in air at H_4 as indicated in Figure 5.3 for different source depths z_s. Measured and modelled data are normalized to each maximum value, respectively. A 150 Hz low-pass filter is applied to the data.

m are compared. The time correlates with the beginning contraction of the airgun bubble and hence the downward movement of the water-air interface (Figure 5.7(b)). The large surface spike at the center above the bubble, generated for source depths of 0.1 m and 0.15 m over time (Figure 5.12 and 5.13), is also demonstrated by many authors for the interaction of spark- or laser-induced cavities with the water-air interface (Blake and Gibson, 1981; Longuet-Higgins, 1983; Robinson et al., 2001) and for underwater explosions (Rogers and Szymczak, 1997). The strong surface lift is associated with a jet formation that is directed away from the free surface and propagates through the center of the bubble (Gibson, 1968; Robinson et al., 2001; Supponen et al., 2015; Zhang and Liu, 2015). The surface spike and jet are caused by a high pressure region between the bubble and free sur-

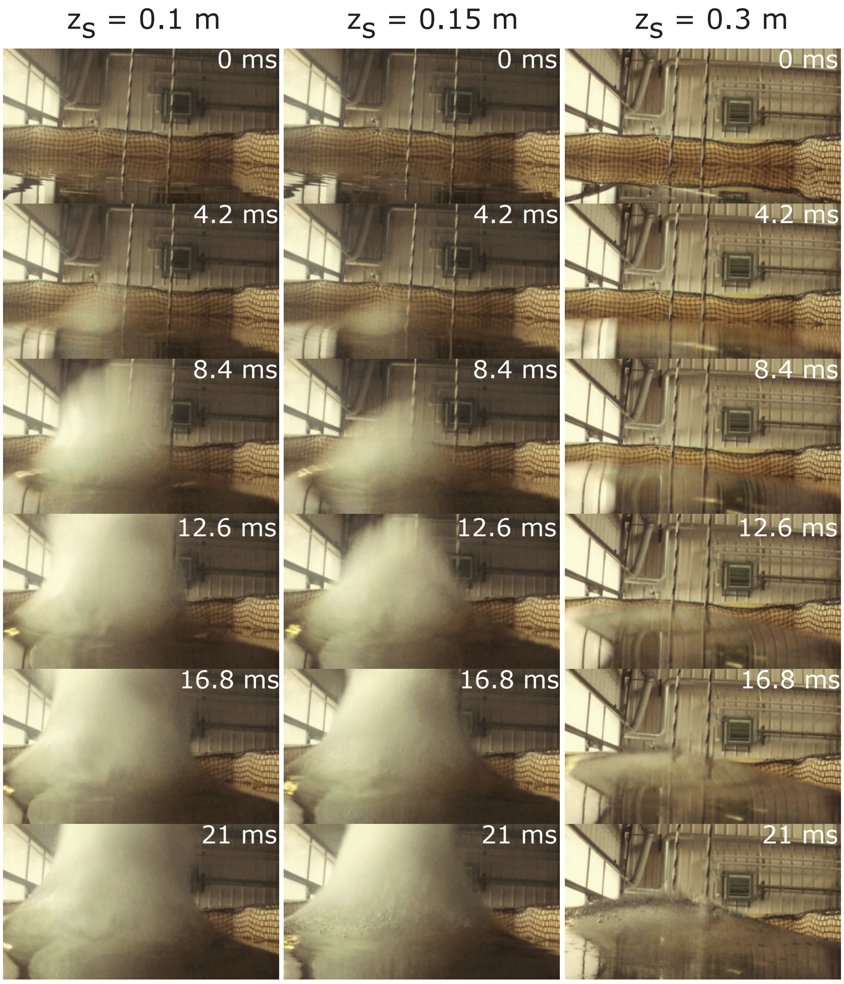

Figure 5.12: Photos of airgun fired at a different source depths z_s taken at different times as indicated. The source depths correspond to the recordings shown in Figure 5.11. Pressure recordings and camera are not synchronized.

face (Pearson et al., 2004) and hence the pressure above the bubble is larger than below. If we assume that the bubble directly bursts at the water-air interface, one might expect that the jet is directed towards the surface again. The evolution and height of the surface spike for collapsing cavities is investigated by Longuet-Higgins (1983) and Pearson et al. (2004). It should be noted that there are two main differences between cavities or underwater explosions and the bubble generated by an airgun. These are the existence of the airgun body at the bubble center and the shape of the bubble that is not exactly spherical due to the gun ports of an airgun (Langhammer and Landrø, 1996; de Graaf et al., 2014a). How this could impact the bubble oscillation in the vicinity of a free surface is experimentally investigated for a laboratory scale airgun by de Graaf et al. (2014a).

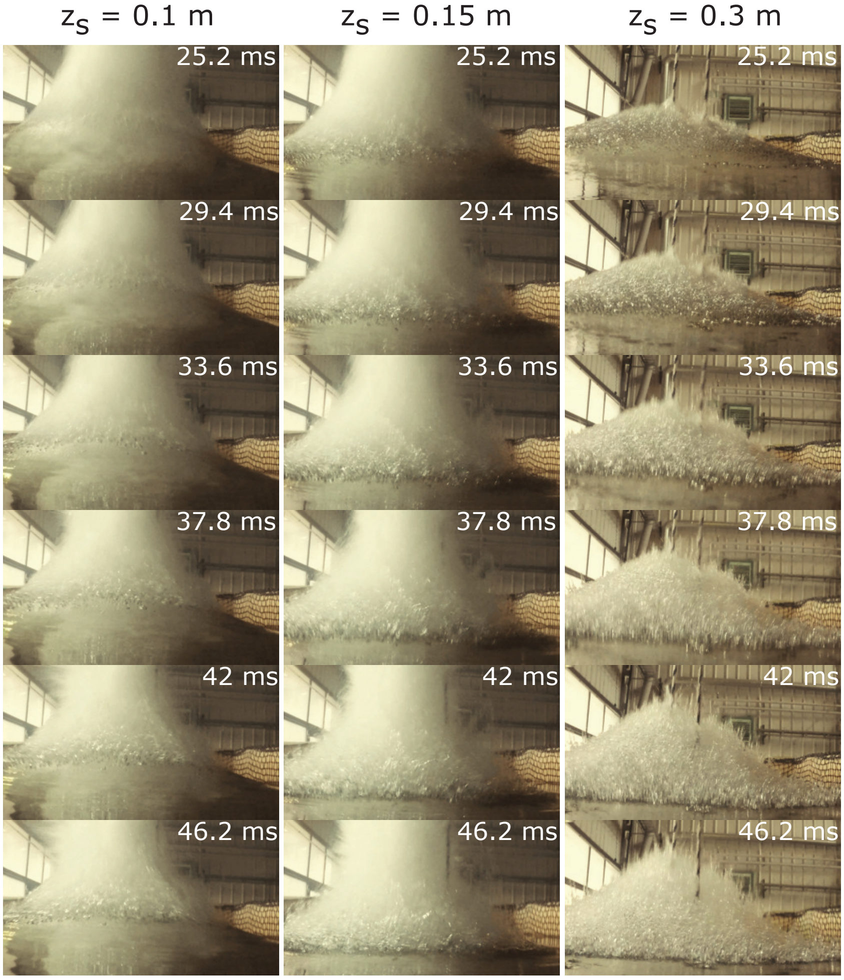

Figure 5.13: Continuation of Figure 5.12.

5.7 Conclusion

This investigation expanded on the signal in air generated by marine seismic sources, corresponding to chapter 3 and 4. The model and measurements indicate that the moving water surface, caused by the interaction with the oscillating bubble, could contribute to the signal measured in air for very shallow source depths. In addition, the radiation pattern in air might get closer to omnidirectional for decreasing source depths and frequencies. To quantify the contributions from the moving surface to the signal measured in air, the mechanism needs to be investigated in more detail. However, this extended discussion and the additional information can be helpful to understand the behaviour of seismic sources fired close to the surface and how the signal in air could be generated.

5.8 Acknowledgements

We acknowledge the European Union's Horizon 2020 research and innovation programme under the Marie Skłodowska-Curie grant agreement No 641943 for the funding of Daniel Wehner's PhD project within WAVES. We like to acknowledge the technical team at IGP for their support to the experimental setup. Martin Landrø acknowledges financial support from the Norwegian Research Council.

Chapter 6

The Impact of Bubble Curtains on Seismic Air Gun Signatures and its High Frequency Emission

Daniel Wehner[1] **and Martin Landrø**[2]
[1] *NTNU, Department of Geoscience and Petroleum, 7031 Trondheim, Norway*
[2] *NTNU, Department of Electronic Systems, 7491 Trondheim, Norway*

manuscript in preparation

6.1 Abstract

In marine seismic acquisition airguns are the most common source and in recent years research on the their impact on the marine environment has increased. The main focus is on the reduction of emitted high frequencies, approximately above 200 Hz, which are not useful for seismic imaging. Therefore, potential ways to reduce the high frequencies from airguns are investigated and the development of alternative source types has increased. We investigate the impact of bubble curtains on the source signature from seismic airguns as bubble curtains are know to mitigate high frequencies in other applications, e.g. pile driving for offshore windfarms. We conduct tank experiments with two different configurations of bubble curtains around a single airgun and compare the results to the conventional source signature without a bubble curtain. The two different bubble curtains vary in its size and the way they are fixed to the airgun. The amount of injected air into the bubble curtains is varied for both configurations. We compare the measured results to simulated data using a common model for airgun source signatures. The results indicate a reduced peak amplitude with an increasing air injection into the bubble curtain. This corresponds

to a gradually decreasing frequency content for frequencies above 50 Hz. The frequencies of the source signal below 50 Hz are nearly unaffected by the bubble curtain. In addition, the bubble time period of the source signal is slightly increased with an increasing amount of air injection into the bubble curtain. The main cause for the reduced peak amplitude is thought to be a buffer effect of the bubble curtain on the released air. Hence, a bubble curtain concentrated around the airgun ports could be the most efficient and practical solution to reduce the high frequency emission from airguns when bubble curtains are considered.

6.2 Introduction

Marine seismic acquisition is one of the major techniques to actively acquire geophysical data in the oceans. The most commonly used source for these surveys is the airgun which releases high pressure air within a few milliseconds from a metal chamber into the surrounding water. This leads to an acoustic signal starting with a sharp peak followed by an oscillation corresponding to the expanding and contracting air bubble. The advantages of the airgun are its signal repeatability and its reliability over long acquisition times. While the source produces a strong signal in the seismic frequency band between 5 Hz to 200 Hz it also emits energy above this range up to 5 kHz or more which could have an impact on the marine environment, e.g. disturbing the communication of marine mammals (Di Iorio and Clark, 2010). As these high frequencies are not used for seismic imaging and often are not even recorded as the data is commonly sampled with 1 kHz or less on the receiver side, a reduction of the emitted high frequency signals in marine seismic acquisition is of interest for research and commercial surveys.

The sound attenuation caused by air bubble curtains underwater is studied by several authors for different applications. An overview on historical applications for bubble curtains is given by Domenico (1982a). In a second paper, Domenico (1982b) demonstrates the impact on bubble barriers on watergun signatures in a pond experiment. Koschinski and Lüdemann (2013) and Würsig et al. (2000) describe different set ups for bubble curtains around pile driving operations for the construction of offshore wind farms. They report attenuated noise levels for frequencies starting at a few hundred hertz and a maximum in the range of a few kilohertz with a reduction of up to 20-25 dB. How these bubble curtains can reduce the impact on marine mammals, e.g. harbour porpoises, is discussed by Lucke et al. (2011). Mitigation effects of underwater explosions due to bubble curtains are experimentally investigated by Croci et al. (2014) and compared to modelled data (Grandjean et al., 2012) including gas fraction and bubble diameters. Modelled and measured results indicate a mitigation of the acoustic signal while the experimental data reveals a stronger mitigation than expected by the model. The difference in acoustic signal attenuation for different bubble sizes and distributions is investigated by Rustemeier et al. (2012). In addition, low frequency signals, smaller than approximately 200 Hz, might be reduced by encapsulated gas bubbles and resonance effects as indicated by dedicated tank experiments and modelled data (Lee et al., 2010, 2012).

The effect of bubble curtains on seismic airguns is not investigated in detail so far. However, the impact on airgun signatures of viscosity, heat transfer or mechanical effects is demonstrated by different authors. The effect of viscosity on the airgun signal, especially the behaviour of the oscillating bubble, is studied experimentally by Langhammer and Landrø (1993a) or numerically by de Graaf et al. (2014b) and King (2016). The impact of heat transfer at the interface between the bubble and the surrounding water is discussed by Ziolkowski (1982). Langhammer and Landrø (1993b) and Landrø (2014) discuss the impact of varying water temperatures on the acoustic signal produced by the airgun. How mechanical effects of the airgun itself, e.g. mass throttling, impact the source signature is demonstrated by de Graaf et al. (2014b) or Groenaas et al. (2016). An overview of the combined effects described above is given by Li et al. (2010) and de Graaf et al. (2014b). It should be mentioned that Coste et al. (2014), Gerez et al. (2015) and Groenaas et al. (2016) present a newly designed airgun, referred to as eSource, where the air release can be controlled to reduce the emission of high frequency signals. This source was developed to reduce the impact of seismic surveys on marine life.

We continue to investigate the impact of air bubbles in water on the source signature from airguns (Wehner and Landrø, 2018). We conduct experiments with a common airgun where an air bubble curtain is generated around the gun ports in two different settings. First, a tube ring is fixed around the gun ports that injects the air for the bubble curtain. In a second test, a metal frame with an injection tube is attached to the airgun and therefore the volume of the bubble curtain is increased. In contrast to most other applications where bubble curtains are used, the airgun is a moving source in water. This important practical issue needs to be considered when testing a bubble curtain for airguns. The bubble oscillation and main peak with an active bubble curtain are compared to the case without air injection. The results should demonstrate the impact of air saturated water on the airgun signature and if bubble curtains could reduce high frequency emission from airguns in marine seismic surveys.

6.3 Theory

When air is injected into the water surrounding the airgun, the source signature could be changed due to different mechanisms affecting the source directly or the propagation of sound in water. These effects can be complex and in the following general expected changes of the airgun signature are described. The source, especially the bubble oscillation, can change with varying medium parameters as density and compressibility. In addition, the air release from the chamber can be different when the piston and gun ports are surrounded by air saturated water which mainly has an impact on the main peak of the source signature. The propagation of the acoustic signal can be influenced by the air bubbles surrounding the seismic source.

The oscillation of an air bubble underwater is described by several authors, e.g. Kirkwood and Bethe (1942), Gilmore (1952), Plesset and Prosperetti (1977) or Ziolkowski (1970). We use the model from Kirkwood and Bethe (1942) with additional damping parameters

(Landrø and Sollie, 1992) that is given as

$$\ddot{R} = \frac{\Big(1 + \frac{\dot{R}}{C}\Big)H + \Big(1 - \frac{\dot{R}}{C}\Big)\frac{R}{C}\dot{H} - \frac{3}{2}\Big(1 - \frac{\dot{R}}{3C}\Big)\dot{R}^2 - \alpha\dot{R} + \beta\dot{R}^2}{R\Big(1 - \frac{\dot{R}}{C}\Big)} \tag{6.1}$$

where R, $\dot{R}$ and $\ddot{R}$ are the bubble radius, velocity and acceleration, respectively. The sound velocity in water at the bubble wall is denoted by C and α and β are damping and empirical coefficients accounting for energy losses on the bubble oscillation. We choose α = 3.5 and β = -0.18 in the following. H is the enthalpy at the bubble wall given as (Ziolkowski, 1970; Landrø and Sollie, 1992)

$$H = \frac{n(p_\infty + B)}{(n-1)\rho_\infty}\Big[\Big(\frac{P_b + B}{p_\infty + B}\Big)^{(n-1)/n} - 1\Big] \tag{6.2}$$

where n and B are constants depending on the fluid and for water $n \approx$ 7 and $B \approx$ 3000 bar (Gilmore, 1952). The hydrostatic pressure is denoted by p_∞, P_b is the pressure in the liquid at the bubble wall and ρ_∞ is the fluid density. The sound velocity at the bubble wall can be described as (Ziolkowski, 1970)

$$C = c_\infty\Big(\frac{P_b + B}{p_\infty + B}\Big)^{(n-1)/2n} \tag{6.3}$$

where c_∞ is the sound velocity in undisturbed water. The bulk modulus can be defined as (Ziolkowski, 1970)

$$K = n(p_\infty + B) \tag{6.4}$$

and the pressure at the bubble wall can be written as (Ziolkowski, 1970; de Graaf et al., 2014b)

$$P_b = p_0\Big(\frac{R_0}{R}\Big)^{3\gamma} \tag{6.5}$$

where R_0 and p_0 are the initial bubble radius and internal pressure, respectively. These values are assumed to be equal to the chamber volume and firing pressure of the airgun. The polymetric index is denoted by γ, which is $\gamma = 1$ for isothermal conditions between the bubble and surrounding water and $\gamma = 1.4$ for adiabatic conditions (de Graaf et al., 2014b).

We assume two different variations in these equations related to air saturated water. First, the heat transfer at the bubble wall could be increased due to increasing turbulences (Laws et al., 1990; de Graaf et al., 2014b) and hence γ would change. Second, the bulk modulus K, density ρ_∞ and velocity c_∞ in the water surrounding the airgun change due to an increased air saturation. The new parameters for air saturated water are estimated using Wood's equation as (Wood, 1941)

$$\rho'_\infty = \Phi\rho_a + (1 - \Phi)\rho_w \tag{6.6}$$

$$K' = \Big(\frac{\Phi}{K_a} + \frac{1 - \Phi}{K_w}\Big)^{-1} \tag{6.7}$$

$$c'_\infty = \sqrt{\frac{K'}{\rho'_\infty}} \tag{6.8}$$

where Φ is the air saturation in water. The density and bulk modulus of air and water are denoted by ρ_a, ρ_w and K_a, K_w, respectively.

The variations in the source signature with changing heat transfer and medium parameters are shown in Figure 6.1 (top, middle). We observe a reduced bubble amplitude and increased bubble time period with decreasing γ that is towards isothermal conditions at the bubble wall. For an increasing saturation, accompanying lower ρ'_∞ and c'_∞, the bubble time period and bubble amplitude is reduced. It has to be noted that the new bulk modulus K' is included in c'_∞ while the constants n and B in Equation 6.4 are derived for water. If the parameters in Equation 6.4 are reduced to $n \approx 0.5$ and $B \approx 214$ bar accounting for a change of the bulk modulus with an air saturation of 0.1% using Equation 6.7, the amplitude of the main peak is doubled and the bubble period is reduced by 3 ms compared to the conventional parameters. However, as we do not know the exact values of n and B for air saturated water, the effect is not included in the model.

When considering the release of pressurized air from the gun chamber into the water the bubble curtain surrounding the airgun could act as a buffer (Groenaas et al., 2016; Watson et al., 2018), similar as for a GI gun (Landrø, 1992). In the model this effect could be approximated by assuming a larger initial bubble volume than the chamber volume (Watson et al., 2018). The extended initial bubble radius could be estimated as

$$R'_0 = R_0 + \left(\frac{3V_{\text{bc}}\Phi}{4\pi}\right)^{1/3} = R_0 + (\Phi R_{\text{bc}}^3)^{1/3} \tag{6.9}$$

where V_{bc} and R_{bc} are the volume and radius of the bubble curtain surrounding the gun ports, assuming that it is spherical and Φ is the air saturation inside that volume. The variations for different initial radii R'_0 depending on the air saturation Φ are shown in Figure 6.1 (bottom). We observe a reduced bubble amplitude and bubble time period with increasing air saturation. In addition, the peak amplitude is noticeably reduced with increasing air saturation.

The propagation of sound from the source can be influenced by the air bubbles in water due to scattering and absorption. These effects are strongest at the resonance frequency of the injected air bubbles that depends on its size. For a single spherical bubble the resonance frequency f_r can be described as (Minnaert, 1933)

$$f_r = \frac{1}{2\pi a}\left(\frac{3\gamma p_\infty}{\rho_\infty}\right)^{1/2} \tag{6.10}$$

where a is the radius of the bubble and γ, p_∞ and ρ_∞ are the same parameters as described earlier. If a cloud of bubbles is treated as an effective medium the entire cloud can be described similar to a single bubble as (Carey and Fitzgerald, 1993; Hwang and Teague, 2000)

$$f_R = \frac{1}{2\pi R_b}\left(\frac{3\gamma p_\infty}{\Phi\rho_\infty}\right)^{1/2} \tag{6.11}$$

where R_b is the radius of the bubble cloud and Φ is again the air saturation. From the resonant frequency the damping effect of a pulsating bubble on an incident plane wave

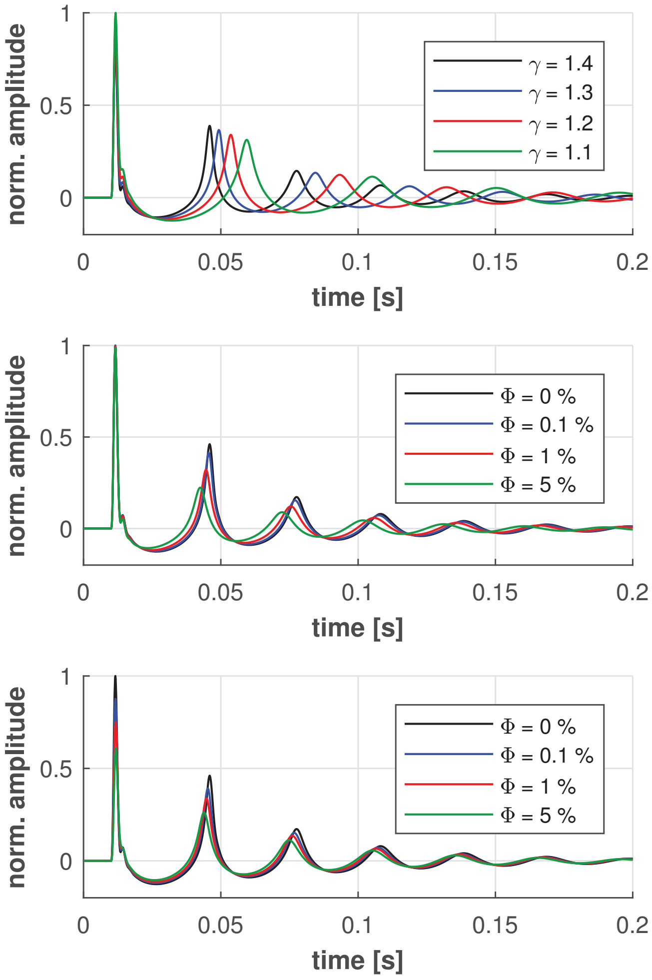

Figure 6.1: Modelled signature of 12 in^3 airgun fired with 80 bar at a depth of z_s = 0.6 m and 400 Hz low-pass filtered. Top: varying heat transfer γ. Middle: varying parameter c'_∞, ρ'_∞ with Φ (Eq. 6.6, 6.8). Bottom: varying initial radii R'_0 with Φ, assuming R_{bc} = 3 cm (Eq. 6.9).

can be computed by the extinction cross-section as (Medwin, 1977)

$$\sigma_e = \frac{4\pi a^2 \delta/(\kappa a)}{[(f_r/f)^2 - 1]^2 + \delta^2} \tag{6.12}$$

where κ is the wavenumber and δ is the damping constant (Medwin, 1977, 1997). The radius a and resonant frequency f_r might be replaced by the terms $R_b\sqrt{\Phi}$ and f_R for a bubble cloud. The extinction cross-sections illustrating the resonant frequency, and hence the strongest damping effect, for different radii of a single bubble are shown in Figure 6.2. It should be noted that quite large bubbles are needed to have an impact on the frequency range of interest that is approximately between 200 Hz and 5 kHz.

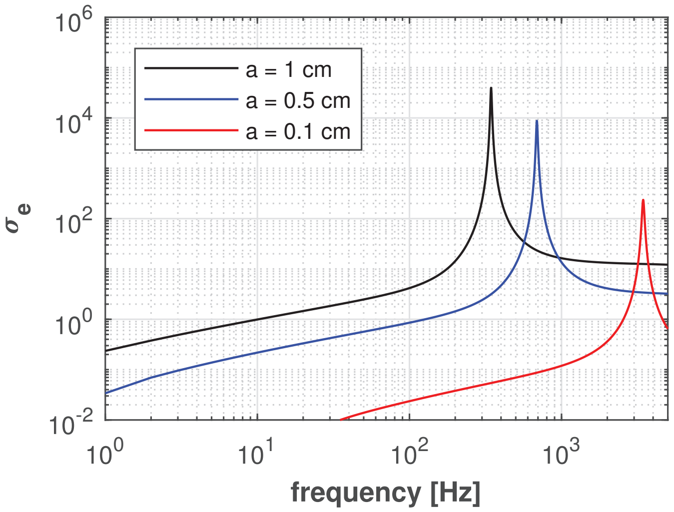

Figure 6.2: Extinction cross-section σ_e (Equation 6.12) that indicates the sound attenuation for different bubble radii a.

6.4 Experiments

The experiments are conducted in a water tank with the dimensions indicated in Figure 6.3. The walls of the tank are equipped with 5 cm thick foam mattresses. The source is a Mini G. Gun with a chamber volume of 12 in^3 (0.2 l) that is fired at a constant position (Figure 6.3) and firing pressure of 80 bar for all experiments. The experiments can be divided into three basic settings as

1. Airgun only: measurements of the acoustic signal from the airgun without any devices fixed to the source. 10 shots are fired.
2. Ring: a tube ring is fixed around the lower parts of the airgun ports (Figure 6.3). 20 holes with a spacing of 1 cm and a diameter of 3 mm are drilled into the tube to inject pressurized air to the gun ports. Measurements of the acoustic signal from the airgun without injected air and with three different amounts of injected air are conducted. 10 shots are fired for each test.
3. Frame: a cylindrical metal frame was built and fixed to the airgun (Figure 6.3). The length of the metal frame is L = 20 cm and the distance from the gun ports to the bars where the tube is fixed is 12 cm. The size of the metal frame is chosen to be slightly larger than the bubble radius that is reached when the main peak is emitted which is estimated from the model described in Equation 6.1. This is thought to give the best damping of the peak while still maintaining the frame as small as possible for practical considerations related to the towing of airguns in seismic acquisition. 40 holes with a diameter of 1.5 mm are drilled into the tube to inject pressurized air to the gun ports. The spacing between the holes is approximately between 3

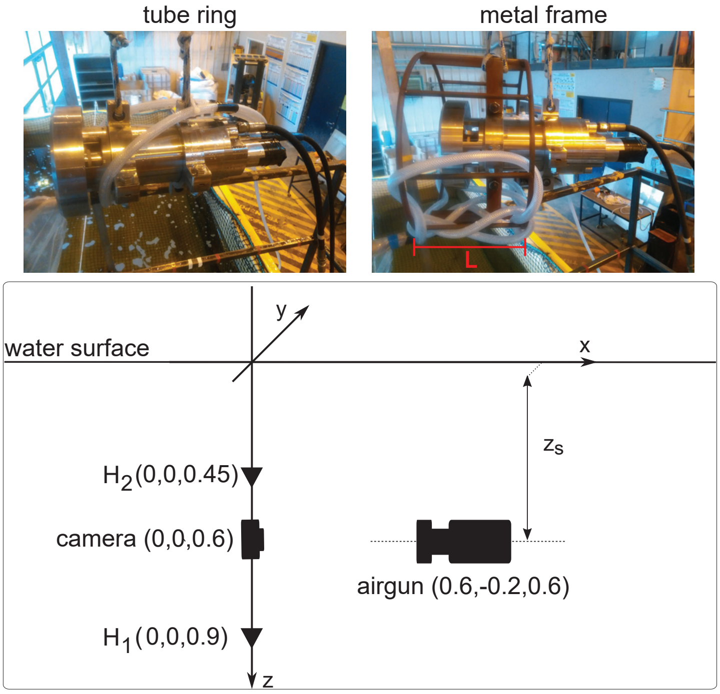

Figure 6.3: Photos and sketch of experimental set up in the water tank. The hydrophones are indicated as H_1 and H_2 where the x-, y- and z-coordinates in meters are given in brackets. The water depth in the tank is 1.25 m and the width (y-direction) and length (x-direction) of the tank are 2.5 m and 6 m, respectively.

cm and 5 cm. However, the distribution is more randomly than for the ring setting. Measurements of the acoustic signal from the airgun without injected air and with three different amounts of injected air are conducted. 10 shots are fired for each test.

Brüel & Kjær hydrophones of the type 8105 are used as receivers for all experiments in the tank which have a frequency range from 0.1 Hz to 100 kHz. A camera is placed in the water to capture the bubble curtain (Figure 6.3). The underwater photos for the different injected amounts of air for the ring and frame setting are shown in Figure 6.4 and 6.5, respectively. The photos illustrate the distribution of the bubble curtain and can be used to estimate the volume occupied by the air bubbles. In addition, noise measurements in the tank are taken when only the air injection is active and no airgun shots are fired. For the noise measurements an HTI-96 MIN hydrophone is used at the same position as H2. The HTI hydrophone has a higher sensitivity as the Brüel & Kjær hydrophones and hence is better suited for the noise recordings. The noise recordings are performed with two goals. The first is to estimate bubble sizes of the injected air. However, no clear peaks corresponding to the resonance frequencies of the bubbles could be observed on the noise recordings. The second goal is to ensure that the noise level from the injected air is below the signal from the airgun which could be confirmed from the noise measurements.

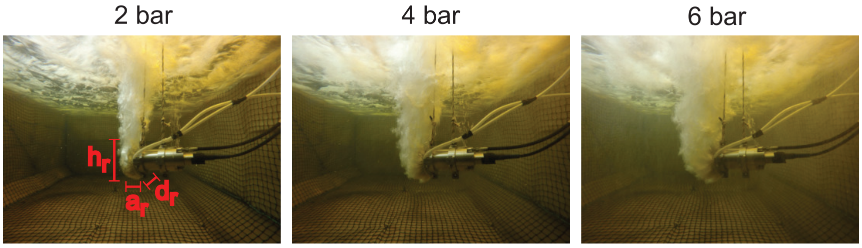
2 bar 4 bar 6 bar

Figure 6.4: Underwater photos of tube ring around air gun ports with different amounts of injected air. Pressure indicates the value measured at the inlet valve for the air supply.

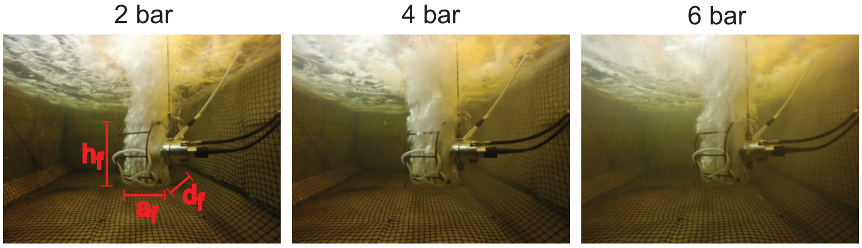
2 bar 4 bar 6 bar

Figure 6.5: Underwater photos of metal frame attached to air gun with different amounts of injected air. Pressure indicates the value measured at the inlet valve for the air supply.

6.5 Results

The measurements of the different experimental settings are investigated and the changes are described. First, the variation of the bubble oscillation and main peak of the airgun signature with active bubble curtains is investigated with a focus on the main peak of the signal. Then, the bubble curtain is characterized from the underwater photos, amount of injected air and acoustic measurements.

6.5.1 Acoustic Signal

First, we investigate the impact of the attached devices, the ring and metal frame, on the airgun signature. The stacked measured data for all three settings is illustrated in Figure 6.6. The signatures for the airgun without any device and with the tube ring fixed to the gun ports is almost the same. This can be expected as the tube ring does not change the shape of the airgun significantly. The signature with the metal frame attached has a reduced main peak, bubble peak and an increased bubble time period compared to the other two measurements (Figure 6.6, top). The damped bubble oscillation is also visible in the frequency spectrum between 10 and 200 Hz (Figure 6.6, bottom). The variation of the bubble oscillation can be related to the interaction between the metal frame and bubble. It should be mentioned that errorbars of the experiment are plotted in the frequency spectrum (Figure 6.6, bottom). However, there are small and hence not clearly visible.

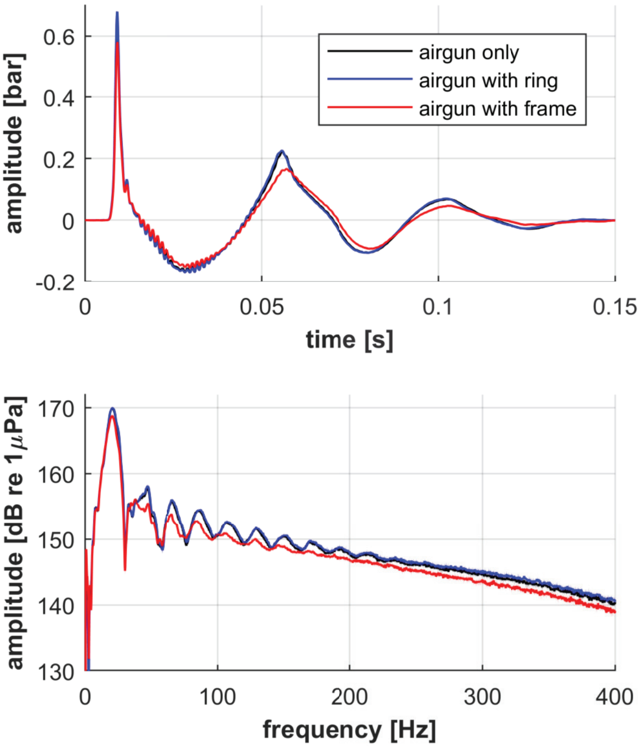

Figure 6.6: Comparison of signal measured at H_2 without devices, with tube ring and with metal frame attached to the gun. No air bubble curtain is present. Signal is 400 Hz low-pass filtered.

The impact of the bubble curtain, injected from the tube ring, on the airgun signature is shown in Figure 6.7 and 6.8 for different frequency bands. We notice that the peak amplitude and bubble amplitude are reduced with increasing air injection (Figure 6.7, top). In addition, the oscillation period of the bubble is slightly increased with increasing air injection. The frequency content is gradually reduced for higher air injection above approximately 50 Hz while the variation at frequencies below 50 Hz is low, less than 1.5 dB (Figure 6.7, bottom). The repeatability of the signal below 100 Hz is high for all air injection amounts as errorbars are difficult to identify. Above 100 Hz the signal repeatability decreases with increasing frequency and air injection which could be due to the time-varying medium around the gun ports caused by the bubble curtain. Including higher frequencies, reverberations in the signal with no bubbles can be observed within the first 0.1 s that could be due to side reflections from the tank wall (Figure 6.8, top). These reverberations are visible in the frequency spectrum as two distinct peaks at 710 and 792 Hz (Figure 6.8, bottom). We note that the two peaks in the spectrum are shifted towards lower frequencies and are strongly reduced with increasing air injection. For the highest

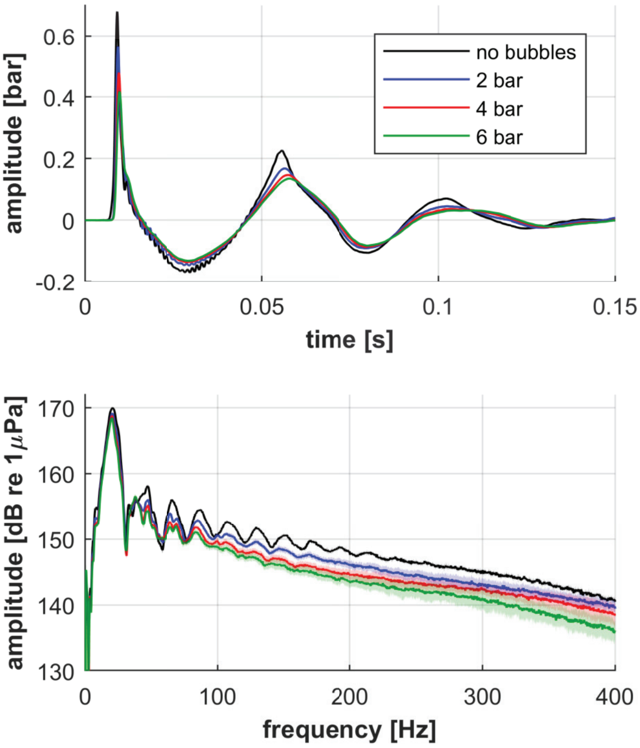

Figure 6.7: Comparison of signal measured at H_2 without and with bubble curtain of different amounts of injected air using the tube ring as shown in Figure 6.4. Signal is 400 Hz low-pass filtered and the shaded area indicates errorbars from the measurements (only in frequency spectrum).

injection of 6 bar the two peaks are not visible in the spectrum. The reduced reverberations can also be seen in the time signal (Figure 6.8, top).

The impact of the bubble curtain, injected from the metal frame, on the airgun signature is investigated in the same way as for the tube ring for two different frequency bands as shown in Figure 6.9 and 6.10. We notice that the peak amplitude is reduced for an air injection of 4 and 6 bar, but not for 2 bar. The bubble amplitude decreases and the oscillation period increases with increasing air injection (Figure 6.9, top). The frequency content is gradually reduced for higher air injection above approximately 50 Hz, except for the injection of 2 bar where the frequency content is increased above 250 Hz compared to the case with no bubbles (Figure 6.9, bottom). For frequencies below 50 Hz the changes in the signal are small, less than 2 dB (Figure 6.9, bottom). The repeatability of the signal below 200 Hz is high for all air injection amounts as errorbars are difficult to identify. Above 200 Hz the signal repeatability decreases with increasing frequency and air injection which might be caused by the varying bubble curtain. Including higher frequencies, reverberations in

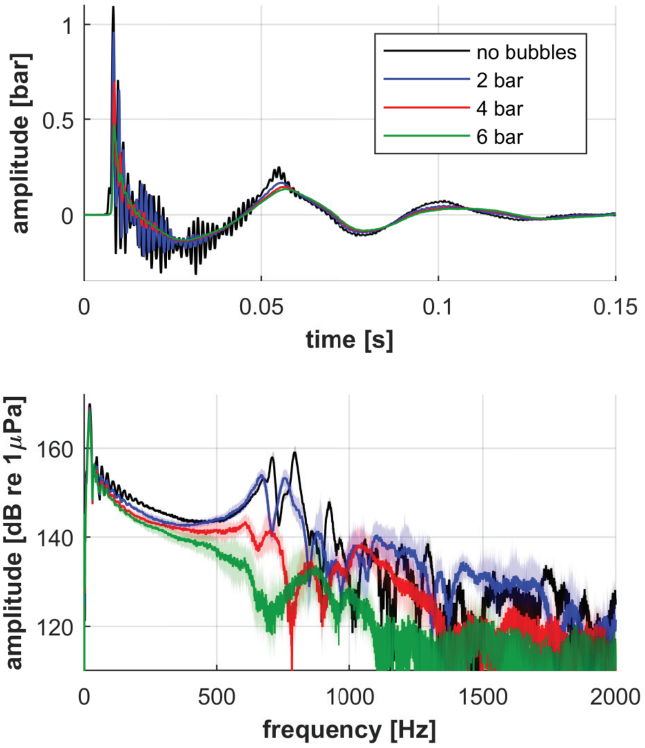

Figure 6.8: Comparison of signal measured at H_2 without and with bubble curtain of different amounts of injected air using the tube ring as shown in Figure 6.4. Signal is 2000 Hz low-pass filtered and the shaded area indicates errorbars from the measurements (only in frequency spectrum).

the signal with no bubbles can be observed within the first 0.1 s that are very similar to the recordings with the tube ring (Figure 6.8 and 6.10, top). These reverberations are visible in the frequency spectrum as two distinct peaks at 710 and 792 Hz (Figure 6.10, bottom). We note that the two peaks in the spectrum are shifted towards lower frequencies and are reduced with increasing air injection. However, the reduction of the peaks is less than for the tube ring (Figure 6.8, bottom). The lower reduction of these wall reflections is also visible in the time signal where reverberations are visible until 0.025 s for the signal with 6 bar air injection (Figure 6.10, top).

The changes of characteristic parameters of an airgun signature, the bubble time period T_b and primary-to-bubble ratio P/B, are summarized in Figure 6.11. We note the stronger variations of the bubble time period for the frame setting. This could be related to the larger volume covered by the bubble curtain and hence it has a stronger impact on the airgun bubble. The primary-to-bubble ratio is slightly increased for both settings with increasing air injection compared to the case without any bubbles around the gun ports.

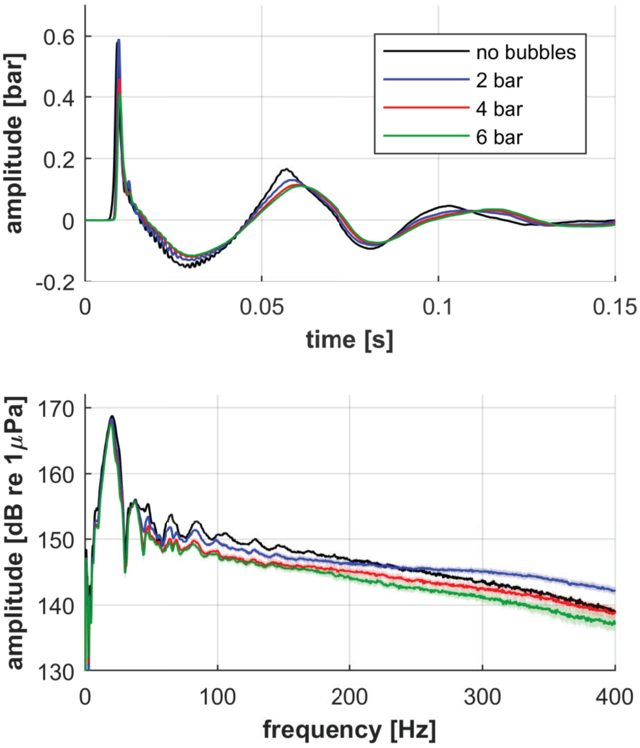

Figure 6.9: Comparison of signal measured at H_2 without and with bubble curtain of different amounts of injected air using the metal frame as shown in Figure 6.5. Signal is 400 Hz low-pass filtered and the shaded area indicates errorbars from the measurements (only in frequency spectrum).

Note the different filter compared to the previous figures. For Figure 6.11 a lower filter is chosen according to the common frequency range used in seismic imaging and to the stabilize the automatic picking of the parameters.

In the following investigation we focus more on the main peak of the signal. A zoomed plot of the 400 Hz low-pass filtered data and 2000 Hz low-pass filtered data is illustrated in Figure 6.12 and 6.13, respectively. In Figure 6.12 we note the decreasing trend of the main amplitude for the ring set up with increasing air injection. For the frame set up the amplitude increases first at 2 bar injection before it decreases at higher injection rates. This observation is similar for previous experiments (Wehner and Landrø, 2018). It should be noted that the errorbars for the measurements are quite small and hence barely visible. The slope of the main peak, shown in Figure 6.12, can be used as an indicator for the environmental impact (Ronen and Chelminski, 2018). For the ring set up the slope is reduced by 38 % from no injection to 6 bar of injection, while the reduction for the frame is about 28 %. It should be noted that the frame itself already reduces the peak amplitude

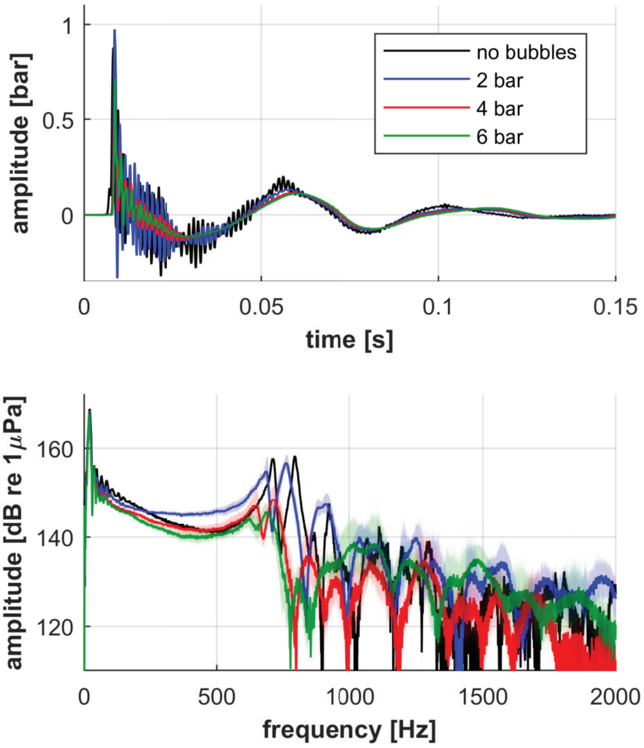

Figure 6.10: Comparison of signal measured at H_2 without and with bubble curtain of different amounts of injected air using the metal frame as shown in Figure 6.5. Signal is 2000 Hz low-pass filtered and the shaded area indicates errorbars from the measurements (only in frequency spectrum).

and hence the reduction of the frame set up with 6 bar injection is about 36 $\%$ compared to the airgun without any device. In Figure 6.13 a similar trend for the main peak amplitude can be observed as in Figure 6.12. Additionally, we observe a few more features in the signals. First, the reverberations are noticed as peaks with a time of 1.5 ms in between. The reverberations at 6 bar injection are almost vanished for the ring set up, while they are more preserved for the frame set up. In addition, the peak amplitude for the frame set up does not vary significantly between 4 and 6 bar injection. This leads to a larger slope of the peak for the frame setting with higher air injection compared to the ring set up. The reduction of the slope between no injection and 6 bar of injection is 57 $\%$ for the ring set up and 20 $\%$ for the frame. Compared to the case with no device fixed to the airgun the slope for the frame at 6 bar is reduced by 35 $\%$. Another observation is the small amplitude before the main peak, at 0.007 s, that only exists for the case with no bubbles (Figure 6.13). This precursor is related to air that escapes from the gun ports through tiny openings before the shuttle reaches the ports (Groenaas et al., 2016).

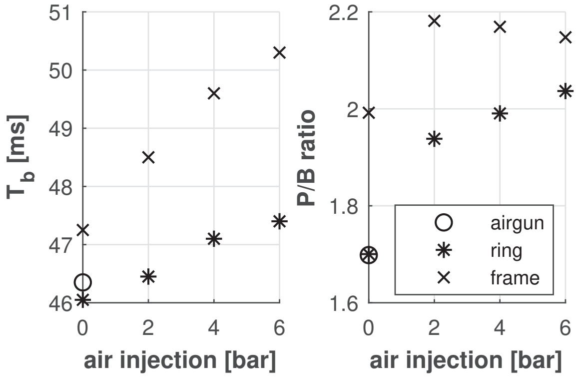

Figure 6.11: Bubble time period T_b and primary-to-bubble ratio P/B for all experimental settings as indicated. The signal is 150 Hz low-pass filtered.

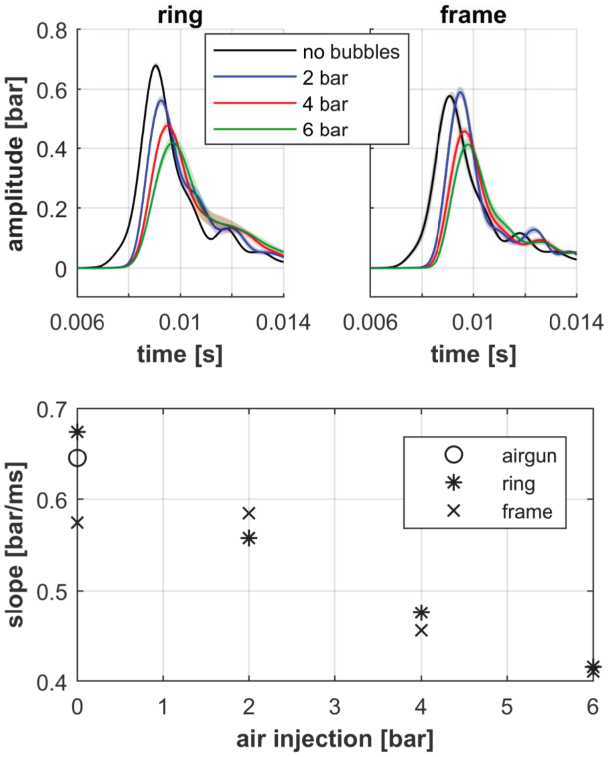

Figure 6.12: Zoom on main peak in Figure 6.7 and 6.9 and the slope of the main peak for all experiments. Errorbars are indicated as shaded area. Slope is computed as summed gradient between start of signal (t = 0 s) and main peak amplitude and signal is 400 Hz low-pass filtered.

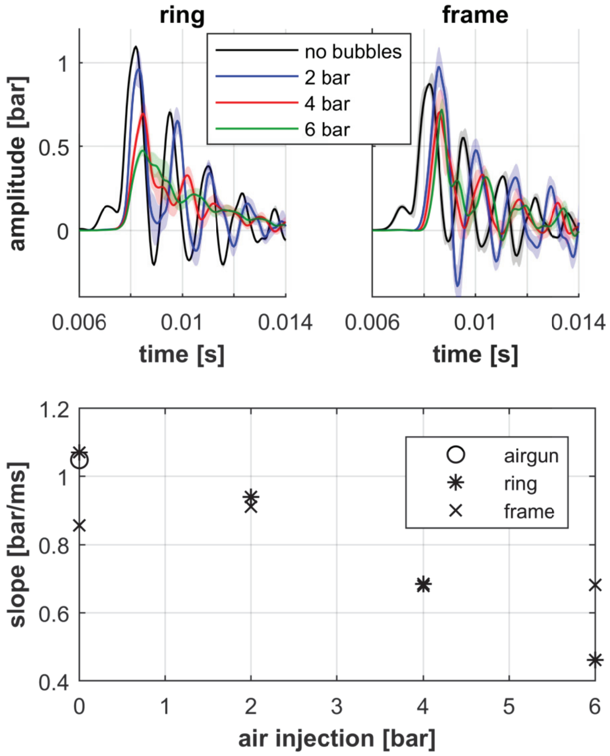

Figure 6.13: Zoom on main peak in Figure 6.8 and 6.10 and the slope of the main peak for all experiments. Errorbars are indicated as shaded areas. Slope is computed as summed gradient between start of signal (t = 0 s) and main peak amplitude and signal is 2000 Hz low-pass filtered.

6.5.2 Bubble Curtain

The bubble size of the injected air could be roughly estimated from the orifice size in the tube (Davidson and Amick, 1956; Kulkarni and Joshi, 2005) as

$$a = \left(\frac{3}{2}\frac{r_o\sigma}{\Delta\rho g}\right)^{1/3} \tag{6.13}$$

where r_o is the radius of the orifice, σ is the surface tension of water (72 dynes/cm) and g is the gravitational acceleration. The density difference between water ρ_w and air ρ_a is denoted as $\Delta\rho$. Equation 6.13 gives a mean bubble radius of $a = 0.31$ cm for the ring setting and $a = 0.23$ cm for the metal frame. These bubble radii have resonance frequencies of 1100 Hz and 1500 Hz according to Equation 6.12. The interpretation of the data above 800 Hz (Figure 6.8 and 6.10) is difficult due to the impact of side reflections. Therefore, the impact of the resonance bubble frequency on the signal is not evaluated here.

We estimate the volume occupied by the bubble curtain that is symmetric around the gun ports from the photos in Figure 6.4 and 6.5, assuming a simple rectangular shape. The area above that volume is neglected for the estimation. The volume estimate for the ring at 2 bar injection is $V_{r1} = h_r a_r d_r = 0.20$ m · 0.08 m · 0.20 m = 0.0032 m^3. For 6 bar injection the length a_r is doubled and hence $V_{r2} = h_r 2 a_r d_r = 0.0064$ m^3. For the frame setting the volume that is occupied by the bubble curtain is almost constant for the three injection rates and is estimated to be $V_f = h_f a_f d_f = 0.34$ m · 0.2 m · 0.3 m = 0.02 m^3.

We compute a rough estimation of the air saturation within this volume from the shift of the peaks between 700 and 800 Hz in the frequency spectrum (Figure 6.8 and 6.10). These peaks are due to wall reflections from the tank as mentioned before and illustrated in Figure 6.14(a). If we assume that the shift of the peaks is only caused by the decreased sound velocity inside the bubble curtain with radius $R_{\text{bc}} \approx a_r, a_f$ (Figure 6.4 and 6.5), we

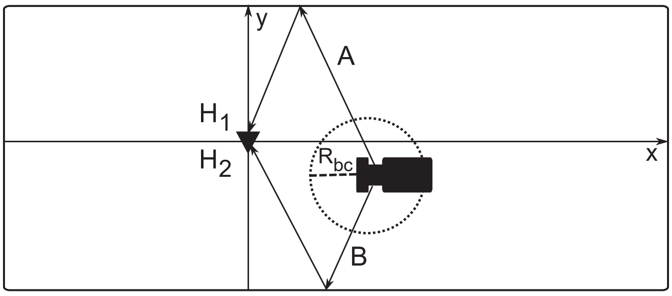

(a)

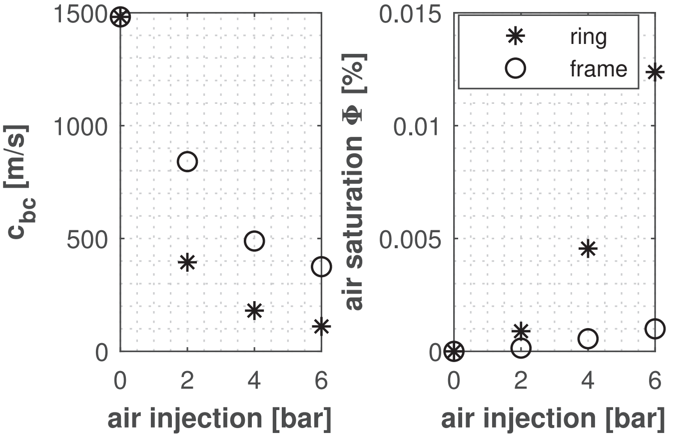

(b)

Figure 6.14: (a) Top view of Figure 6.3 showing the path for the wall reflections and the bubble curtain dimensions. (b) Estimated sound velocity and air saturation inside bubble curtain using Equation 6.14 and 6.8.

could compute the velocity inside the bubble curtain as (Landrø et al., 2017)

$$c_{\text{bc}} = \frac{f_p R_{\text{bc}} c_\infty}{f_p(R_{\text{bc}} - D) + c_\infty} \tag{6.14}$$

where c_∞ is the sound velocity in undisturbed water, f_p are the measured frequency peaks in the spectrum for all injection rates (Figure 6.8 and 6.10), R_{bc} the path inside the bubble curtain and D is the length of path A and B in Figure 6.14(a). To adopt the equation from Landrø et al. (2017) we use the relation $c = \lambda f$, where λ is the wavelength. The peak at the higher frequency is related to path B which is slightly shorter than path A. In addition, the peaks for the ring set up and 6 bar injection are extrapolated from the other injection amounts as they are hardly visible in the spectrum. The sound velocity c_{bc} and saturation Φ inside the bubble curtain can be estimated from Wood's equation (Eq. 6.8) using a density of ρ_w = 1500 kg/m^3, ρ_a = 1.25 kg/m^3 and bulk modulus of K_w = 2.15 GPa and K_a = 0.15 MPa for water and air, respectively. The estimated saturation is illustrated in Figure 6.14(b). Although simple estimations are made about the geometry and that the shift in the frequency peaks is only explained by the velocity difference inside the bubble curtain, the values seem reasonable as a higher saturation for the smaller volume from the tube ring can be expected.

6.6 Discussion

In the following a few aspects are discussed regarding the validity of the results and applicability of bubble curtains for airguns. This includes the potential cause for the observed reduction of the main peak with increasing air injection. In addition, the directivity and tank impact on the measured data is discussed. At the end, we shortly elaborate on the applicability of bubble curtains in field measurements.

In the results section the measurements at receiver H_2 are shown and a second receiver H_1 is positioned slightly deeper (Figure 6.3). Receiver H_1 is at an angle of δ_1 = 26^o from the horizontal plane where the source is located and receiver H_2 is at δ_2 = -14^o. By comparing the reduction of the main peak and slope of the peak at both receivers for increasing air injection we gain information about the directivity within this range. For the ring set up the reduction of the main peak at H_1 is about 3$\%$ less than at H_2 for both filter ranges, 400 and 2000 Hz low-pass filtered (Figure 6.7 and 6.8). For the frame set up the reduction of the main peak at H_1 is about 4$\%$ less than at H_2 for the 400 Hz low-pass filtered data (Figure 6.9) and about 16$\%$ less for the 2000 Hz low-pass filtered data (Figure 6.10). Hence, the ring reduces the amplitude consistently in that direction while the results for the frame are varying more with direction, especially at higher frequencies. This could be explained by the coverage of the bubble curtain around the gun ports. While the bubble curtain is nearly equally distributed around the gun ports for the ring set up as it is attached close to the gun, this is not the case for a bubble curtain generated further away from the ports. This issue could be even more important when the airgun is towed in water during seismic surveys.

The impact of the tank dimensions on the measured data can be observed on the reflections from the wall as discussed (Figure 6.8 and 6.10). It is difficult to draw conclusions for the variations in the frequency range above 700 Hz as several reflections might impact the signal. However, the reflections are reduced for higher air injection and the reflected peaks are completely vanished for the ring set up and an injection of 6 bar (Figure 6.8). This might indicate that the main peak is reduced similarly in different directions. This statement also includes that the tube ring leads to a more consistent reduction with directivity compared to the frame setting as reflected signals are still visible for the frame set up (Figure 6.10).

To investigate the main effect responsible for the reduced peak amplitude we compare the measured data to modelled results (Figure 6.15 and 6.16) using the estimated values for the air saturation Φ (Figure 6.14(b)). The bubble radius of the bubble curtain R_{bc} (Eq. 6.9) is assumed to be equal to a_r and a_f in Figure 6.4 and 6.5, respectively. The

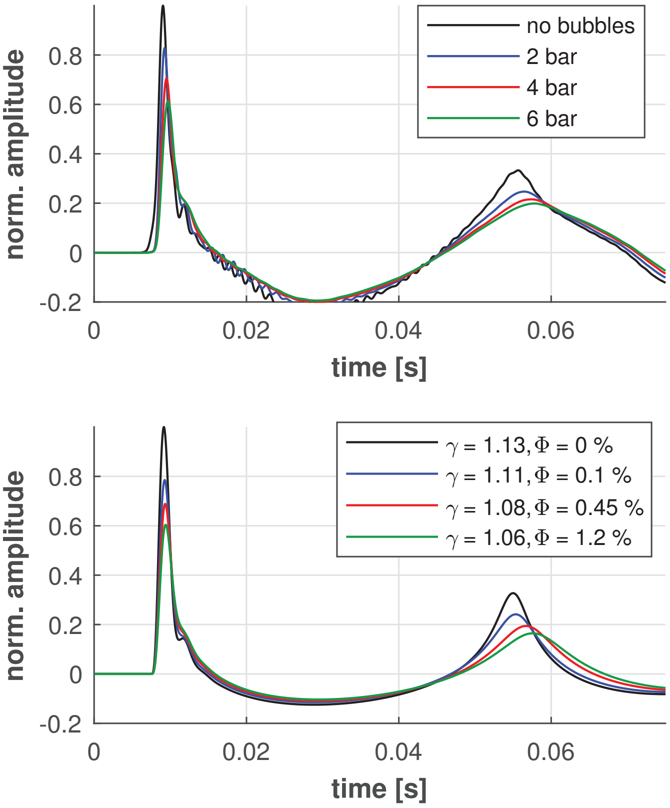

Figure 6.15: Comparison of measured (top) and modelled (bottom) acoustic pressure for the ring set up using the estimated saturation values Φ (Figure 6.14(b)) and dimensions of bubble curtain (Figure 6.4). Model accounts for all effects explained in Figure 6.1. Signal is 400 Hz low-pass filtered.

index γ for the heat transfer is fitted to the measured data. The modelled data agrees with the measurements quite well and explains the reduced main peak, except for the increased peak amplitude for the metal frame and 2 bar injection (Figure 6.16). Further deviations between the model and measurements can be due to the tank size, e.g. the small reverberations after the main peak in the measured data with no bubbles (Figure 6.15 and 6.16). The increase of the bubble period with increasing air injection is mainly caused by the variation of the heat transfer with changing γ. The reduced peak amplitude is mainly due to the increased initial radius R'_0 (Eq. 6.9) that buffers the mass flow from the airgun chamber to the bubble (Watson et al., 2018). The theory of an increased initial radius could be supported by the vanished precursor in Figure 6.13 (at 0.007 s) for an active bubble curtain as this signal might be fully buffered by the bubble curtain. The effect of varying medium parameters (ρ', c'_∞, K') on the airgun signature is low and might be even less pronounced in the measurements as the model assumes that the entire medium around the gun has changed. This is not valid for the experiments where only a small volume around

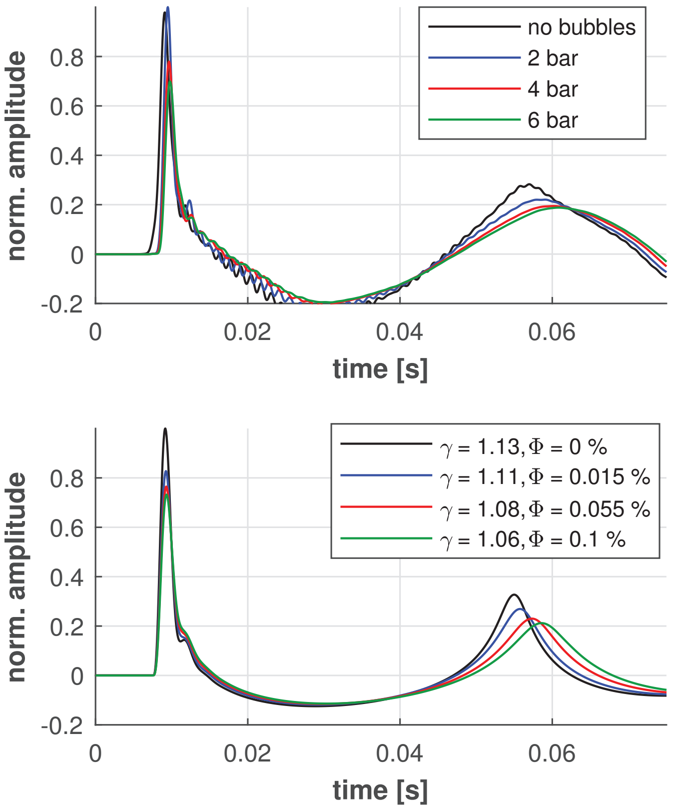

Figure 6.16: Comparison of measured (top) and modelled (bottom) acoustic pressure for the frame set up using the estimated saturation values Φ (Figure 6.14(b)) and dimensions of bubble curtain (Figure 6.5). Model accounts for all effects explained in Figure 6.1. Signal is 400 Hz low-pass filtered.

the gun ports is influenced by the bubble curtain. Scattering effects for the ring set up are expected to be negligible as the bubble expands way beyond this bubble curtain and hence the source dimensions exceed the bubble curtain. The bubble curtain from the ring set up covers approximately 10$\%$ from the volume occupied by the maximum airgun bubble. For the frame set up scattering might have a bigger impact on the data as it covers a larger space that is 45$\%$ of the volume covered by the maximum airgun bubble. Scattering might be an explanation for the variations of the main peak with changing air injection (Figure 6.10), which could also explain the larger deviations between the modelled and measured data (Figure 6.16). Watson et al. (2018) discuss further mechanisms that have an impact on the main peak. One explanation are increased turbulences in water which could be modelled by a varying damping factor $\alpha = \epsilon|\dot{R}|$ (Eq. 6.1), where ϵ is an empirically determined constant factor. However, this leads to a strongly reduced bubble oscillation which does not fit to the measured data and hence we keep the constant empirical factors $\alpha = 3.5$ and β = -0.18.

The observed reduction of the slope and amplitude of the main peak with increasing air injection is more consistent and slightly stronger for the ring set up compared to the frame set up. The main cause could be the buffer effect of a larger initial radius as discussed before. This observation is beneficial for practical applications, as a tube ring is easy to attach to a conventional airgun and does not interact with neighbouring guns which could happen for a larger metal frames. In addition, the injected air is focused around the gun ports and can be easily controlled from the vessel. A small bubble curtain around the gun ports also has the advantage that it is less influenced by currents and the movement of towed airguns. For larger frames it could be difficult to secure that the bubble curtain always surrounds the gun ports in a similar way.

6.7 Conclusion

The results indicate a reduction of the main peak in the source signal with an increasing amount of air injection into the bubble curtain surrounding an airgun. The emitted frequencies above 50 Hz are gradually reduced with an increasing air injection while the impact on the frequency content below 50 Hz is low. The main cause of the reduced peak amplitude is thought to be a buffer effect from the bubble curtain on the released air from the airgun. Therefore, a bubble curtain concentrated around the gun ports seems to be the most efficient and practical solution to reduce the high frequency emission from airguns when considering bubble curtains. Scattering and absorption effects are considered to be negligible in our experiments due to the small size of the bubble curtains. The impact of the bubble curtain on frequencies above 700 Hz is difficult to investigate in our experiment due to reflections from the test water tank. While the tests should be repeated in field experiments, the reduced main peak from airgun signatures caused by a small bubble curtain surrounding the gun ports could be demonstrated in the experiments. Therefore, bubble curtains could potentially be used to attenuate emitted high frequencies from seismic airguns. The maximum possible attenuation is also related to the amount of injected air that can be supplied by the compressors on the vessel.

6.8 Acknowledgements

We acknowledge the European Union's Horizon 2020 research and innovation programme under the Marie Skłodowska-Curie grant agreement No 641943 for the funding of Daniel Wehner's PhD project within WAVES. We like to acknowledge the technical team at IGP for their support to the experimental setup, especially Noralf Vedvik who built the metal frame. Martin Landrø acknowledges financial support from the Norwegian Research Council.

Chapter 7

Concluding remarks

Summary

Several experiments have been conducted to investigate the acoustic signal generated by single marine seismic sources, especially from airguns, and the mechanisms that can have an impact on the lower and upper end of the emitted frequency band. The focus is on the impact of the source depth on the ghost reflection from the water-air interface (Chapter 3, 4 and 5). In chapter 2 the impact of the rising airgun bubble on the source signature is investigated. In addition, the potential use of bubble curtains for seismic airguns is discussed in chapter 6. The changes of an airgun signature due to the mechanisms discussed in the chapters are schematically illustrated in Figure 7.1. The black line in Figure 7.1 is the frequency spectrum of a single airgun signature computed with a conventional airgun model. The colored lines sketch the deviations from this model caused by the mechanisms discussed in the chapters. As Figure 7.1 is only an illustration, the absolute variations between the signals should not be taken as a reference. The main mechanisms that impact the source signature in Figure 7.1 are summarized below.

I Source signature of a 200 in^3 airgun fired at a depth of z_s = 5 m, recorded in the far-field and assuming a reflection coefficient of R_c = -0.9994 for the water-air interface. The signal is modelled using the damped Kirkwood-Bethe equation (Eq. 1.11) which is commonly used for seismic airguns. This signal acts as a reference for the following deviations.

II The signal at the very low frequency end ($<$ 1-2 Hz) could be stronger than assumed in the conventional model if the rising airgun bubble (Chapter 2) and spherical wave front (Chapter 3) are taken into account which is commonly not the case. For the rising bubble the signal strength depends on the bubble size, where a larger bubble could lead to a stronger signal. However, the signal generated from the rising bubble seems to be insignificant in marine seismic acquisition as the bubble radius needs to be larger than 12 m to generate a signal above the noise level in calm weather conditions. This is demonstrated on a simple subsurface model considering a target depths at 3000 m (Chapter 2). The impact of the spherical wave front increases with decreasing source depth (decreasing distance between the source and interface). For source depths shallower than 3 m the signal strength for frequencies below 1 Hz could be increased by about 10 dB when the spherical wave front is considered compared to the conventional model where plane waves are assumed (Chapter 3). However, the noise level in the low frequency band is also high and a 10 dB increase below 1 Hz might not be noticeable on the receiver.

III When an airgun is fired very close to the water surface, the airgun bubble bursts directly into the air and hence there is no signal from an oscillating bubble (Chapter 4). Therefore, the signal in Figure 7.1 (red) is reduced at the peaks around 10 Hz, 20 Hz, etc. which are related to the oscillating bubble. In Figure 7.1 we assume that the bubble oscillation abruptly stops when a critical radius is reached as discussed in chapter 5. In addition, a reduced reflection from the water-air interface might be assumed as the interface is almost instantly altered when the source is fired. The reduced reflection could also be related to energy loss mechanisms of the acoustic signal at the water-air interface. A smaller reflected signal leads to reduced notches caused by the ghost, also for the ghost notch at 0 Hz (Chapter 4). For the signal

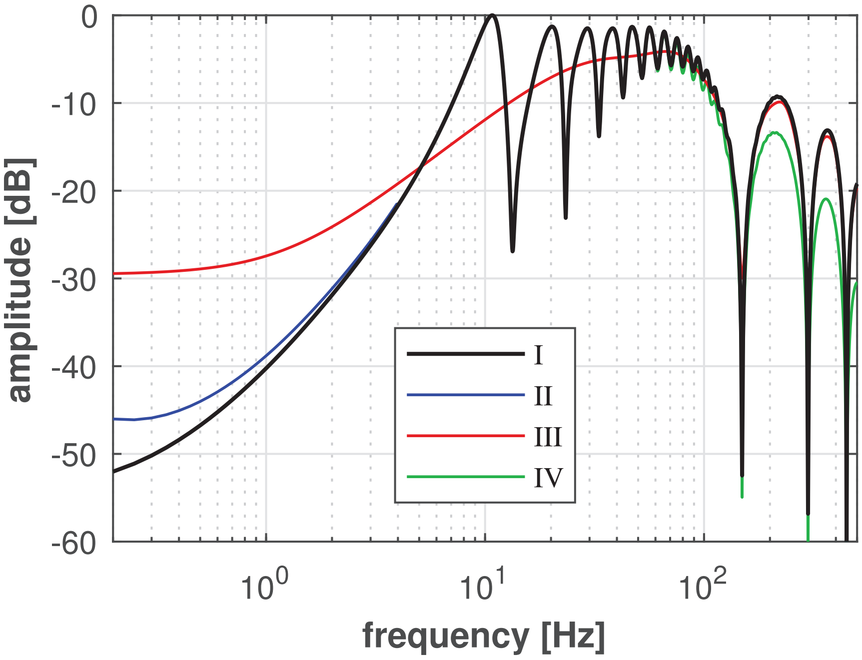

Figure 7.1: Sketch illustrating the frequency spectrum of a single airgun signature in the far-field computed with a conventional airgun model (I). The deviations from the model caused by mechanisms discussed in chapter 2, 3 (II), chapter 4 (III) and chapter 6 (IV) are shown and explained in more detail in the text.

in Figure 7.1 a randomly chosen reflection coefficient of R_c = -0.87 is assumed. It should be mentioned that the source depth is still 5 m for the model and the bubble would, in practice, not break the surface at this depth. However, the same source depth is used for all computations to have a direct comparison.

IV The use of bubble curtains surrounding the gun ports of seismic airguns could have a buffer effect on the released air from the gun chamber. This could lead to a reduced peak amplitude and therefore mitigate the high frequency emission from the source (Chapter 6). The experimental results indicate a gradually reduced signal for frequencies above 50 Hz with an increasing amount of air injection into the bubble curtain. The impact on the signal below 50 Hz is found to be low. In addition, a slightly increased bubble time period with stronger bubble curtains is found in the experiments. A reduction of 57% for the slope of the peak amplitude, which could act as an indicator for the environmental impact, is found for a bubble curtain that is directly injected at the gun ports with a pressure of 6 bar (Chapter 6).

Applicability

The mechanisms explained in point II (chapter 2 and 3) seem to be less important for marine seismic acquisition as the differences to the conventional model are negligible for frequencies above 2 Hz. For frequencies below 1-2 Hz the variations in the source signature could make a difference caused by the spherical wave front. However, the noise level is usually high at these low frequencies, especially on towed streamer data. The effect might be of importance in low noise environments, e.g. ocean bottom surveys.

The effect explained in point III (chapter 4) seems promising to have a positive impact on frequencies below 5 Hz in marine seismic acquisition. If an airgun is fired so close to the surface that the bubble directly bursts into the air, the experimental results indicate an increased signal of 10 - 20 dB for frequencies below 5 Hz. This could have direct implications in field applications and seismic imaging. It should be noted that the overall energy, especially at the main bubble frequency, is reduced due to the non-existence of the oscillating bubble. This could potentially be compensated by deploying sources in an array at different depths. Another important issue that needs to be solved is the towing of airguns that shallow. This could be feasible at calm weather conditions while it is a demanding task at higher sea states.

The test presented in point IV (chapter 6) might have some potential for reducing the high frequency emission, above 50-100 Hz, in marine seismic acquisition. The reduction of the main peak, and hence emitted high frequencies, could be feasible with a bubble curtain surrounding the gun ports. The experimental results indicate that the low frequency part, below 50 Hz, is barely influenced by the bubble curtain. In addition, a small frame for the bubble curtain concentrated around the gun ports, which seems to be sufficient for the peak amplitude reduction, can be easily attached to an airgun, even in airgun arrays.

Outlook

Potential extensions and future research ideas related to the presented work are mentioned below. One obvious continuation is the performance of field tests as most experiments were performed in the tank and near-field. Therefore, some experimental set ups for field experiments are suggested below and are illustrated in Figure 7.2.

A Similar to the field experiment presented by Amundsen et al. (2017) a single airgun is fired at several depths z_s between 0.5 m and 10 m, depending on the source volume. The minimum depth should be around $0.5R_{max}$ and the maximum depth should be larger than $4R_{max}$, where R_{max} is the maximum bubble radius. A GI Gun should be used to remove the bubble oscillation as good as possible. In this way the ghost effect can be investigated in more detail as the source signature is less influenced by the varying bubble oscillation in the vicinity of the free surface. A near-field (H_n) and far-field hydrophone (H_f) should be deployed in water (Figure 7.2). In addition, a hydrophone/microphone should be located in air (H_a) and a camera could film the water surface. The microphone and camera should be decoupled from the vessel as good as possible to reduce recorded noise and vibrations on the camera as indicated by the springs in Figure 7.2. The camera should have a frame rate above 240 fps to reveal some information about the surface disturbance. Ideally, all receivers and the camera should be synchronized with the trigger of the GI Gun. This test might be seen as an extension of the experiments from Mayne and Quay (1971).

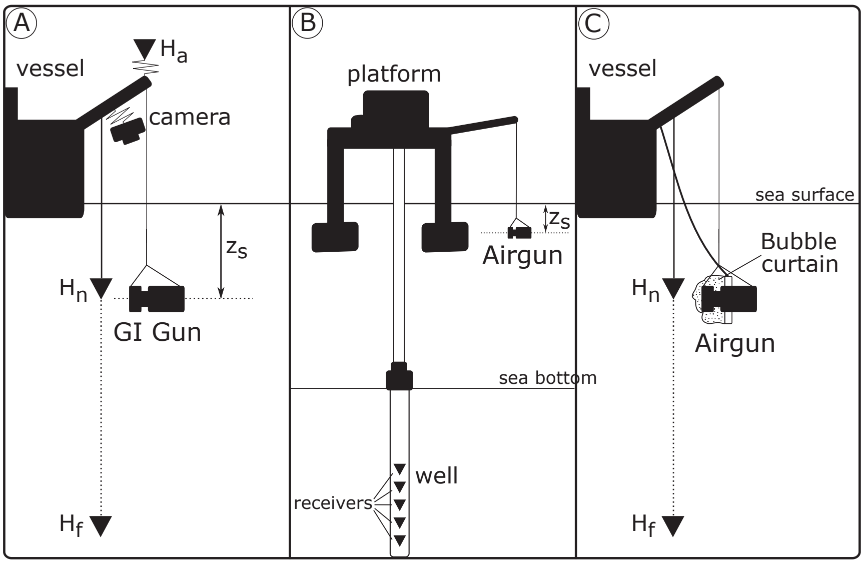

Figure 7.2: Field experiments suggested to continue the work presented in this thesis. The experiments A, B and C are explained in more detail in the text.

B As the towing of airguns at very shallow depths could be a difficult task, a possibly easier experiment can be a zero offset VSP measurement where the source is deployed from a platform. The VSP should be performed at least three times where only the source depth is changed. The shallowest source depth needs to be chosen so that the bubble directly bursts into the air and the deepest source depth should avoid interaction of the source with the water-air interface, e.g. at 10 m. In between, several source depths could be selected depending on the time available for the acquisition. The VSP recordings can be directly compared for variations, especially in the low frequency band.

C The bubble curtain attached to the airgun can be tested in a similar set up as explained in A. The frame or tube for the injection of the bubble curtain could be similar to those presented in chapter 6. The tube ring could be replaced by a metal tube which will have a longer lifetime. The source depth and firing pressure for the airgun should be kept constant. The variable that should be changed is the amount of injected air into the bubble curtain. It would be benefical to repeat the experiment with different airgun volumes. To investigate the directivity of the source signal with an active bubble curtain a source towed over one or several hydrophones is a variation to the suggested tests.

In addition to these field experiments, it could be of interest to investigate the water surface disturbances for very shallow sources in more detail to get a better estimation of energy loss mechanisms of the pressure signal that can impact the ghost reflection. The investigation could include movies from a high speed camera ($\sim$ 10000 fps) to clearly capture the effects from the acoustic pressure and oscillating bubble. In addition, more advanced modelling could be implemented which accurately accounts for the interaction with the free surface, e.g. based on the boundary element method as presented by Zhang and Liu (2015). That can improve the understanding of the acoustic signal emitted by the airgun for very shallow source depths.

The signal that is transmitted into air from marine seismic sources could be further exploited in comparison with investigations conducted in the field of infrasound (Vergniolle and Brandeis, 1994; Johnson et al., 2004; Mutschlecner and Whitaker, 2005). That could include measurements in air from large airgun arrays conducted with microphones and microbarometers to capture the low frequencies ($<$ 5-10 Hz). The receivers could be deployed on the vessel or on the nearby coast if applicable. This is mostly of academic interest.

The future of marine seismic acquisition in the industry is difficult to predict as it is mainly driven by its costs. Therefore, I do not expect that all airguns will be replaced by alternative sources in the near future, although marine vibrators are a promising option. Especially in academia the replacement of existing source systems for marine seismic acquisition could be too expensive. While exploration surveys might decrease in the future due to data sharing and less prospect areas, monitoring surveys might become more important in the fields of enhanced recovery and carbon sequestration.

Appendix A

Tube wave monitoring - detect shear modulus and S-wave velocity changes in the formations surrounding wells

Daniel Wehner[1], Filipe Borges[1,3], Yi Liu[2] and Martin Landrø[2]
[1] *NTNU, Department of Geoscience and Petroleum, 7031 Trondheim, Norway*
[2] *NTNU, Department of Electronic Systems, 7491 Trondheim, Norway*
[3] *Petróleo Brasileiro S/A (Petrobras)*

* *manuscript in preparation*

Bibliography

Aadnøy, B. S., 2010. Modern Well Design. CRC Press.

Abma, R., Howe, D., Foster, M., Ahmed, I., Tanis, M., Zhang, Q., Arogunmati, A., Alexander, G., 2015. Independent simultaneous source acquisition and processing. Geophysics 80 (6), WD37 – WD44.

Abma, R., Ross, A., 2013. Popcorn shooting: Sparse inversion and the distribution of airgun array energy over time. 83rd Annual International Meeting, SEG, Expanded Abstracts, 31–35.

Abma, R., Ross, A., 2015. Practical aspects of the popcorn source method. 85th Annual International Meeting, SEG, Expanded Abstracts, 164 – 169.

Achenbach, E., 1972. Experiments on the flow past spheres at very high Reynolds numbers. Journal of Fluid Mechanics 54 (3), 565–575.

Ainslie, M. A., Halvorsen, M. B., Dekeling, R. P. A., Laws, R., Duncan, A. J., Frankel, A. S., Heaney, K. D., Küsel, E. T., MacGillivary, A. O., Prior, M. K., Sertlek, H. O., Zeddies, D. G., 2016. Verification of airgun sound field models for environmental impact assessment. Proceedings of Meetings on Acoustics 4ENAL 27 (1), 1 – 13.

Aki, K., Richards, P. G., 2002. Quantitative Seismology. Universtiy Science Books.

Amundsen, L., 1993. Wavenumber-based filtering of marine point-source data. Geophysics 58 (9), 1335 – 1348.

Amundsen, L., Westerdahl, H., Pederson, A. S., Thompson, M., Landrø, M., 2017. On firing an air gun very shallow. Geophysics 82 (3), A25–A29.

Amundsen, L., Zhou, H., 2013. Low-frequency seismic deghosting. Geophysics 78 (2), WA15–WA20.

André, M., van der Schaar, M., Zaugg, S., Houégnigan, L., Sánchez, A. M., Castell, J. V., 2011. Listening to the deep: Live monitoring of ocean noise and cetacean acoustic signals. Marine Pollution Bulletin 63 (1-4), 18 – 26.

Avedik, F., Combe, R., 1973. New high-energy implosion seismic source. Ocean Industry, 51–52.

Bachrach, R., Nur, A., Agnon, A., 2001. Liquefaction and dynamic poroelasticity in soft sediments. Journal of Geophysical Research: Solid Earth 106 (B7), 13,515 – 13,526.

Bakulin, A., Smith, R., Hemyari, E., Ramadan, A., Jervis, M., Saragiotis, C., 2016. Processing and repeatability of 4D buried receiver data in a desert environment. 86th Annual International Meeting, SEG, Expanded Abstracts, 5405 – 5409.

Ballhaus Jr., W. F., Holt, M., 1974. Interaction between the ocean surface and underwater spherical blast wave. The Physics of Fluids 17 (6), 1068 – 1079.

Barker, D., Landrø, M., 2012. Simple expression for the bubble-time period of two clustered air guns. Geophysics 77 (1), A1 – A3.

Batzle, M., Wang, Z., 1992. Seismic properties of pore fluids. Geophysics 57 (11), 1396 – 1408.

Berkhout, A. J., 2008. Changing the mindset in seismic data acquisition. The Leading Edge 27 (7), 924 – 938.

Bertrand, A., Folstad, P. G., Luyngnes, B., Buizard, S., Hoeber, H., Pham, N., de Pierrepont, S., Schultzen, J., Grandi, A., 2014. Ekofisk life-of-field seismic: Operations and 4D processing. The Leading Edge 33 (2), 142 – 148.

Bjelland, C., 1993. Reduction of noise in seismic hydrophone arrays modeling of breathing waves and adaptive noise canceling. PhD thesis, University of Bergen.

Bjorlykke, K., 2010. Petroleum Geoscience. Springer Berlin Heidelberg.

Blake, J. R., Gibson, D. C., 1981. Growth and collapse of a vapour cavity near a free surface. Journal of Fluid Mechanics 111, 123 – 140.

Borges, F., Wehner, D., Landrø, M., 2018. Calculation of tube wave velocity in a shallow borehole using passive seismic recordings. 80th Annual Conference & Exhibition, EAGE, Extended Abstracts, ThP403.

Boulton-Stone, J. M., Blake, J. R., 1993. Gas bubbles bursting at a free surface. Journal of Fluid Mechanics 254, 437 – 466.

Bourgoyne Jr., A. T., Millheim, K. K., Chenevert, M. E., Young Jr., F. S., 1986. Applied Drilling Engineering. SPE Textbook Series. Society of Petroleum Engineers, Inc.

Bowman, D. C., Taddeucci, J., Kim, K., Anderson, J. F., Lees, J. M., Graettinger, A. H., Sonder, I., Valentine, G. A., 2014. The acoustic signatures of ground acceleration, gas expansion, and spall fallback in experimental volcanic explosions. Geophysical Research Letters 41 (6), 1916 – 1922.

Breitzke, M., Bohlen, T., 2012. Modeling cumulative sound exposure along a seismic line to assess the risk of seismic research surveys on marine mammals in the Antarctic Treaty area. Springer, New York, book section The Effects of Noise on Aquatic Life, pp. 609 – 611.

Brekhovskikh, L. M., Lysanov, Y. P., 1991. Fundamentals of Ocean Acoustics. Springer.

Brittan, J., Pidsley, L., Cavalin, D., Ryder, A., Turner, G., 2008. Optimizing the removal of seismic interference noise. The Leading Edge 27 (2), 166 – 175.

Bröker, K., Speirs, K., Hedgeland, D., Wolinsky, G., Gisiner, B., Adams, G., Jenkerson, M., Weissenberger, J., Campbell, J., 2018. The IOGP E&P sound and marine life joint industry programme - an international research programme to fill key data gaps. First Break 36 (11), 61 –63.

Bussat, S., Kugler, S., 2011. Offshore ambient-noise surface-wave tomography above 0.1 Hz and its applications. The Leading Edge 30 (5), 514 – 524.

Calvo, D. C., Nicholas, M., Orris, G. J., 2013. Experimental verification of enhanced sound transmission from water to air at low frequencies. Journal of the Acoustical Society of America 134 (5), 3403 – 3408.

Cambois, G., Long, A., Parkes, G., Lundsten, T., Mattsson, A., Fromyr, E., 2009. Multi-level airgun array: a simple and effective way to enhance the low frequency content of marine seismic data. 79th Annual International Meeting, SEG, Expanded Abstracts, 152–156.

Carcione, J. M., Poletto, F., 2008. Synthetic logs of multipole sources in boreholes based on the Kelvin-Voigt stress-strain relation. Geophysical Journal International 174, 808 – 814.

Carey, W. M., Fitzgerald, J. W., 1993. Low-frequency noise from breaking waves. Natural Physical Sources of Underwater Sound. Springer, Dordrecht.

Carlson, D., Long, A., Soellner, W., Tabti, H., Tenghamn, R., Lunde, N., 2007. Increased resolution and penetration from a towed dual-sensor streamer. First Break 25, 71–77.

Carroll, A. G., Przeslawski, R., Duncan, A., Gunning, M., Bruce, B., 2017. A critical review of the potential impacts of marine seismic surveys on fish & invertebrates. Marine Pollution Bulletin 114 (1), 9 – 24.

Cato, D. H., Noad, M. J., Dunlop, R. A., McCauley, R. D., Gales, N. J., Salgado Kent, C. P., Kniest, H., Paton, D., Jenner, K. C. S., Noad, J., Maggi, A. L., Parnum, I. M., Duncan, A. J., 2013. A study of the behavioural response of whales to the noise of seismic air guns: design, methods and progress. Acoustics Australia 41 (1), 88–97.

Chadwick, A., Arts, R., Eiken, O., Williamson, P., Williams, G., 2006. Geophysical Monitoring of the CO_2 plume at Sleipner, North Sea. Springer, book section Advances in the geological storage of carbon dioxide, pp. 303 – 314.

Chahine, G. L., 1977. Interaction between an oscillating bubble and a free surface. Journal of Fluid Engineering 99 (4), 709 – 176.

Chahine, G. L., Frederick, G. S., Lambrecht, C. J., Harris, G. S., Mair, H. U., 1995. Spark generated bubbles as laboratory-scale models of underwater explosions and their use for validation of simulation tools. Proceedings of the 66th Shock and Vibration Symposium, Biloxi, MS 2, 265 – 276.

Chan, B. C., Holt, M., Welsh, R. L., 1968. Explosions due to pressurized spheres at the ocean surface. The Physics of Fluids 11 (4), 714 – 722.

Chang, S. K., Liu, H. L., Johnson, D. L., 1988. Low-frequency tube waves in permeable rocks. Geophysics 53 (4), 519 – 527.

Chelminski, S., 2015. Device for marine seismic explorations for deposit. U.S. patent 8,971,152 B2 (to Chelminski Research LLC).

Cinbis, C., Mansour, N. N., Khuri-Yakub, B. T., 1993. Effect of surface tension on the acoustic radiation pressure-induced motion of the water-air interface. Journal of the Acoustical Society of America 94 (4), 2365 – 2372.

Collins, R., Holt, M., 1968. Intense explosions at the ocean surface. The Physics of Fluids 11 (4), 701 – 713.

Coste, E., Gerez, D., Groenaas, H., Hopperstad, J.-F., Larsen, O. P., Laws, R., Norton, J., Padula, M., Wolfstirn, M., 2014. Attenuated high-frequency emission from a new design of air-gun. 84th Annual International Meeting, SEG, Expanded Abstracts, 132–137.

Courant, R., Friedrichs, K., Lewy, H., 1928. Über die partiellen Differenzengleichungen der mathematischen Physik. Mathematische Annalen 100 (1), 32 – 74.

Crampin, S., 1985. Evaluation of anisotropy by shear-wave splitting. Geophysics 50 (1), 142 – 152.

Croci, K., Arrigoni, M., Boyce, P., Gabillet, C., Grandjean, H., Jacques, N., Kerampran, S., 2014. Mitigation of underwater explosion effects by bubble curtains: experiments and modelling. 23rd MABS (Military Aspects of Blast and Shock).

Cui, P., Zhang, A. M., Wang, S. P., 2016. Small-charge underwater explosion bubble experiments under various boundary conditions. Physics of Fluids 28 (117103), 1 – 24.

Dahl, P. H., Miller, J. H., Cato, D. H., Andrew, R. K., 2007. Underwater ambient noise. Acoustics Today 3 (1), 23 – 33.

Daley, T. M., Myer, L. R., Peterson, J. E., Majer, E. L., Hovertsen, G. M., 2008. Time-lapse crosswell seismic and VSP monitoring of injected CO_2 in a brine aquifer. Environmental Geology 54 (8), 1657 – 1665.

Davidson, L., Amick, E. H., 1956. Formation of gas bubbles at horizontal orifices. AlChE Journal 2 (3), 337 – 342.

de Graaf, K. L., Brandner, P. A., Penesis, I., 2014a. Bubble dynamics of a seismic airgun. Experimental Thermal and Fluid Science 55, 228 – 238.

de Graaf, K. L., Penesis, I., Brandner, P. A., 2014b. Modelling of seismic airgun bubble dynamics and pressure field using the Gilmore equation with additional damping factors. Ocean Engineering 76, 32 – 39.

de Ridder, S. A. L., Biondi, B. L., 2015. Near-surface Scholte wave velocities at Ekofisk from short noise recordings by seismic noise gradiometry. Geophysical Research Letters 42 (17), 7031 – 7038.

Dellinger, J., Ross, A., Meaux, D., Brenders, A., Gesoff, G., Etgen, J. T., Naranjo, J., 2016. Wolfspar, an FWI-friendly ultra-low-frequency marine seismic source. 86th Annual International Meeting, SEG, Expanded Abstracts, 4891–4895.

Deng, Y., Tao, J., Qiu, X., 2012. Sound radiation into air by a point source moving underwater. Journal of Sound and Vibration 331, 4481 – 4487.

Deri, C. P., 1987. A comparison of watergun/airgun sources for vertical seismic profiles. 19th Annual Offshore Technology Conference, 143 –151.

Dhelie, P. E., Lie, J. E., Danielsen, V., Evensen, A. K., Myklebostad, A., 2014. Broadband seismic − a novel way to increase notch diversity. 84th Annual International Meeting, SEG, Expanded Abstracts, 148–152.

Di Iorio, L., Clark, C. W., 2010. Exposure to seismic survey alters blue whale acoustic communication. Biology Letters 6, 51 – 54.

Digby, P., 1981. The effective elastic moduli of porous granular rocks. Journal of Applied Mechanics 48 (4), 803–808.

Dixon, N., D. Russell, V. J., 2005. Engineering properties of municipal solid waste. Geotextiles and Geomembranes 23 (3), 205 – 233.

Domenico, S. N., 1982a. Acoustic wave propagation in air-bubble curtains in water - part I: History and theory. Geophysics 47 (3), 345 – 353.

Domenico, S. N., 1982b. Acoustic wave propagation in air-bubble curtains in water - part II: Field experiment. Geophysics 47 (3), 354 – 375.

Dondurur, D., Karsli, H., 2012. Swell noise suppression by Wiener prediction filter. Journal of Applied Geophysics 80, 91–100.

Douady, S., 1990. Experimental study of Faraday instability. Journal of Fluid Mechanics 221, 383 – 409.

Douady, S., Fauve, S., 1988. Pattern selection in Faraday instability. Europhysics Letters 6 (3), 221 – 226.

Dowle, R., Maples, M., 2006. Solid streamer noise reduction. 76th Annual International Meeting, SEG, Expanded Abstracts, 85 – 89.

Dowling, A., 1998. Underwater flow noise. Theorectical and Computational Fluid Dynamics 10, 135 – 153.

Dragoset, B., 2000. Introduction to air guns and air-gun arrays. The Leading Edge 19 (8), 892 – 897.

Dragoset, B., Hargreaves, N., Larner, K., 1987. Air-gun source instabilities. Geophysics 52 (9), 1229 – 1251.

Dragoset, W. H., 1984. A comprehensive method for evaluating the design of air guns and air gun arrays. The Leading Edge 3 (10), 52 – 61.

Duffaut, K., Landrø, M., 2007. V_p/V_s ratio versus differential stress and rock consolidation - A comparison between rock models and time-lapse AVO data. Geophysics 72 (5), C81 – C94.

Dunlop, R. A., Noad, M. J., McCauley, R. D., Kniest, E., Paton, D., Cato, D. H., 2015. The behavioural response of humpback whales (megaptera novaeangliae) to a 20 cubic inch air gun. Aquatic Mammals 41 (4), 412–433.

Dunlop, R. A., Noad, M. J., McCauley, R. D., Kniest, E., Slade, R., Paton, D., Cato, D. H., 2016. Response of humpback whales (megaptera novaeangliae) to ramp-up of a small experimental air gun array. Marine Pollution Bulletin 103, 72–83.

Edgerton, H. E., Hayward, G. G., 1964. The 'boomer' sonar source for seismic profiling. Journal of Geophysical Research 69 (14), 3033 – 3042.

Elboth, T., 2010. Noise in marine seismic data. PhD thesis, University of Oslo.

Elboth, T., Lilja, D., Reif Pettersson, B. A. P., Andreassen, Ø., 2010a. Investigation of flow and flow noise around a seismic streamer cable. Geophysics 75 (1), Q1 – Q9.

Elboth, T., Presterud, I. V., Hermansen, D., 2010b. Time-frequency seismic data denoising. Geophysical Prospecting 58 (3), 441 – 453.

Elboth, T., Reif Pettersson, B. A. P., Andreassen, Ø., 2009. Flow and swell noise in marine seismic data. Geophysics 74 (2), Q17 – Q25.

Elboth, T., Reif Pettersson, B. A. P., Andreassen, Ø., Martell, M. B., 2012. Flow noise reduction from superhydrophobic surfaces. Geophysics 77 (1), P1 – P10.

Eriksrud, M., Langhammer, J., Nakstad, H., 2009. Towards the optical oil field. 79th Annual International Meeting, SEG, Expanded Abstracts, 3400 – 3404.

Fail, J. P., 1983. HWG 400 water gun: A new step toward power and resolution? 53rd Annual International Meeting, SEG, Expanded Abstracts, 227 – 229.

Faraday, M., 1831. On a peculiar class of acoustical figures; and on certain forms assumed by groups of particles upon vibrating elastic surfaces. Philososphical Transactions of the Royal Society of London 121, 299 – 340.

Ferre, M. C., 1960. Methods and apparatus for exploring earth formations. U.S. Patent 2,924,289 (to Schlumberger Well Surveying Corporation).

Fewtrell, J. L., McCauley, R. D., 2012. Impact of air gun noise on the behaviour of marine fish and squid. Marine Pollution Bulletin 64 (5), 984 – 993.

Finneran, J. J., Schlundt, C. E., Dear, R., Carder, D. A., Ridgway, S. H., 2002. Temporary shift in masked hearing thresholds in odontocetes after exposure to single underwater impulses from a seismic watergun. Journal of the Acoustical Society of America 111 (6), 2929 – 2940.

Fookes, G., Warner, C., Van Borselen, R., 2003. Practical interference noise elimination in modern marine data processing. 73rd Annual International Meeting, SEG, Expanded Abstracts, 1905 – 1908.

French, W. S., Henson, C. G., 1978. Signature measurements of the water gun marine seismic source. Offshore Technology Conference, 631 – 638.

Galperin, E. I., 1985. Vertical Seismic Profiling and its Exploration Potential. D. Reidel Publishing Company.

Gerez, D., Groenaas, H., Larsen, O. P., Wolfstirn, M., Padula, M., Bolt, T., 2015. Controlling air-gun output to optimize seismic content while reducing unnecessary highfrequency emissions. 85th Annual International Meeting, SEG, Expanded Abstracts, 154 – 158.

Gibson, D. C., 1968. Cavitation adjacent to plane boundaries. Proc. 3rd Australasian Conf. on Hydraulics and Fluid Mechanics, Sydney, 210 – 214.

Giles, B. F., 1968. Pneumatic acoustic energy source. Geophysical Prospecting 16 (1), 21 – 53.

Giles, B. F., Johnston, R. C., 1973. System approach to air-gun design. Geophysical Prospecting 21, 77 –101.

Gilmore, F. R., 1952. The growth or collapse of a spherical bubble in a viscous compressible liquid. Report, Hydrodynamics Laboratory, California Institute of Technology.

Girard, J. F., Coppo, N., Rohmer, J., Bourgeois, B., Naudet, V., Schmidt-Hattenberger, C., 2011. Time-lapse CSEM monitoring of the Ketzin (Germany) CO_2 injection using 2xMAM configuration. Energy Procedia 4, 3322 – 3329.

Glubokovskikh, S., Pevzner, R., Dance, T., Caspari, E., Popik, D., Shulakova, Gurevich, B., 2016. Seismic monitoring of CO_2 geosequestration: CO2CRC Otway case study using full 4D FDTD approach. International Journal of Greenhouse Gas Control 49, 201 – 216.

Glushkov, E. V., Glushkov, N. V., Godin, O. A., 2013. The effect of anomalous transparency of the water-air interface for a volumetric sound source. Acoustical Physics 59 (1), 6 – 15.

Godin, O. A., 2006. Anomalous transparency of water-air interface for low-frequency sound. Physical review letters 97 (16), 164301–1 – 164301–4.

Godin, O. A., 2008. Sound transmission through water-air interfaces: new insights into an old problem. Contemporary Physics 49 (2), 105 – 123.

Gordon, J., Gillespie, D., Potter, J., Frantzis, A., Simmonds, M., Swift, R., Thompson, D., 2003. A review of the effects of seismic surveys on marine mammals. Marine Technology Society Journal 37 (4), 16–34.

Grandjean, H., Jacques, N., Zaleski, S., 2012. Shock propagation in liquids containing bubbly clusters: a continuum approach. Journal of Fluid Mechanics 701, 304 – 332.

Grindheim, J. V., Revhaug, I., Pedersen, E., Solheim, P., 2017. Modellering, prediksjon og styring av slepte seismiske kabler. Kart og Plan, 1 – 16.

Groenaas, H., Larsen, O. P., Gerez, D., Padula, M., 2016. On the anatomy of the air-gun signature. 86th Annual International Meeting, SEG, Expanded Abstracts, 46 – 50.

Grude, S., Landrø, M., Dvorkin, J., 2014. Pressure effects caused by CO_2 injection in the Tubåen Fm., the Snøhvit field. International Journal of Greenhouse Gas Control 27, 178 – 187.

Gulunay, N., 2008. Two different algorithms for seismic interference noise attenuation. The Leading Edge 27 (2), 176 – 181.

Haavik, K. E., Landrø, M., 2015. Variable source depth acquisition for improved marine broadband seismic data. Geophysics 80, A69–A73.

Haavik, K. E., Landrø, M., 2016. Estimation of source signatures from air guns fired at various depths: A field test of the source scaling law. Geophysics 81 (3), P13–P22.

Halliday, D., Laws, R., Garden, M., 2015. Signal and noise in a shallow-water ocean-bottom cable survey. 85th Annual International Meeting, SEG, Expanded Abstracts, 120 – 124.

Halliday, D., Resnick, R., Jearl, W., 2003. Fundamentals of Physics. John Wiley and Sons, Inc.

Hardage, B. A., 1981. An examination of tube wave noise in vertical seismic profiling data. Geophysics 46 (6), 892 – 903.

Harris, G. R., 1981. Transient field of a baffled planar piston having an arbitrary vibration amplitude distribution. Journal of the Acoustical Society of America 70 (1), 186 – 204.

Hashin, Z., Shtrikman, S., 1963. A variational approach to the theory of the elastic behaviour of multiphase materials. Journal of the Mechanics and Physics of Solids 11, 127 – 140.

Hatch, L. T., Wright, A. J., 2007. A brief review of anthropogenic sound in the oceans. International Journal of Comparative Psychology 20 (2), 121 – 133.

Hatton, L., 2007. An empirical relationship between surface reflection coefficient and source array amplitude.
URL `http://www.leshatton.org/anelastic_surface_reflection_coefficient.html`

Hegna, S., Klüver, T., Lima, J., Wisløff, J. F., 2018. Making the transition from discrete shot records to continuous seismic records and source wavefields, and its potential impact on survey efficiency and environmental footprint. Geophysical Prospecting.

Hegna, S., Parkes, G., 2011. The low frequency output of marine air-gun arrays. 81st Annual International Meeting, SEG, Expanded Abstracts, 77–81.

Henriet, J. P., Schittekat, J., Heldens, P. H., 1983. Borehole seismic profiling and tube wave applications in a dam site investigation. Geophysical Prospecting 31, 72 – 86.

Herring, C., 1941. Theory of the pulsations of the gas bubble produced by an underwater explosion. Report, Columbia Univ., Divison of National Defense Research.

Hicks, E., Hoeber, H., Poole, G., King, B., 2014. An efficient 4D processing flow for variable-depth streamer data. The Leading Edge 33 (2), 172 – 180.

Hildebrand, J. A., 2009. Anthropogenic and natural sources of ambient noise in the ocean. Marine Ecology Progress Series 395, 5 – 20.

Hopperstad, J.-F., Laws, R., Kragh, E., 2012. Hypercluster of airguns − more low frequencies for the same quantity of air. 74th Annual Conference & Exhibition, EAGE, Extended Abstracts, Z011.

Hovem, J. M., 2007. Marine Acoustics, The Physics of Sound in Underwater Environments. Peninsula Publishing, Los Altos, California.

Huang, F., Bergmann, P., Juhlin, C., Ivandic, M., Lüth, S., Ivanova, A., Kempka, T., Henninges, J., Sopher, D., Zhang, F., 2018. The first post-injection seismic monitor survey at the Ketzin pilot CO_2 storage site: results from time-lapse analysis. Geophysical Prospecting 66, 62 – 84.

Hudimac, A. A., 1957. Ray theory solution for the sound intensity in water due to a point source above it. Journal of the Acoustical Society of America 29 (8), 916 – 917.

Hung, C. F., Hwangfu, J. J., 2010. Experimental study of the behaviour of mini-charge underwater explosion bubbles near different boundaries. Journal of Fluid Mechanics 651, 55 – 80.

Hutchinson, D. R., Detrick, R. S., 1984. Water gun vs air gun: A comparison. Marine Geophysical Research 6, 295–310.

Huygens, C., 1690. Treatise on light. Chicago: University of Chicago Press, 1955 [translated by Thompson SP].

Hwang, P. A., Teague, W. J., 2000. Low-frequency resonant scattering of bubble clouds. Journal of Atmospheric and Oceanic Technology 17, 847 – 853.

IAGC, 2013. Marine seismic operations - an overview. Report, Canadian Association of Geophysical Contractors.

IAGC, OGP, 2011. An overview of marine seismic operations. Report, International Association of Geophysical Contractors.

Ikelle, L. T., Amundsen, L., 2005. Introduction to Petroleum Seismology. Society of Exploration Geophysicists.

Jenkerson, M., Allen, P., Scott, H., Noss, T., 1999. Towed marine vibrator acquisition. Conference of the Brazilian Geophysical Society.

Jenkerson, M., Feltham, A., Henderson, N., Nechayuk, V., Girard, M., 2018. Geophysical characterization and reliability testing of the APS marine vibrator. 88th Annual International Meeting, SEG, Expanded Abstracts, 116 – 120.

Jennings, J., Clapp, R., Biondi, B. L., Ronen, S., 2018. Multicomponent deblending of marine data using a pattern-based approach. 88th Annual International Meeting, SEG, Expanded Abstracts, 136 – 140.

Jensen, F. B., Kuperman, W. A., Porter, M. B., Schmidt, H., 2011. Computational Ocean Acoustics. Springer.

JIP, Sound and Marine Life, 2018.
URL `http://www.soundandmarinelife.org/`

Johnson, J. B., 2003. Generation and propagation of infrasonic airwaves from volcanic explosions. Journal of Volcanology and Geothermal Research 121 (1-2), 1 – 14.

Johnson, J. B., Aster, R. C., Kyle, P. R., 2004. Volcanic eruptions observed with infrasound. Geophysical Research Letters 31 (14), L14604.

Johnston, R. C., 1982. Development of more efficient airgun arrays: theory and experiment. Geophysical Prospecting 30 (6), 752 – 773.

Jovanovich, D. B., Summer, R. D., Akins-Easterlin, S. L., 1983. Ghosting and marine signature deconvolution: A prerequisite for detailed seismic interpretation. Geophysics 48 (11), 1468 – 1485.

Kastelein, R. A., Helder-Hoek, L., Van de Voorde, S., Benda-Beckmann, A. M., Lam, F.-P. A., Jansen, E., de Jong, C. A. F., Ainslie, M. A., 2017. Temporary hearing threshold shift in a harbor porpoise (phocoena phocoena) after exposure to multiple airgun sounds. Journal of the Acoustical Society of America 142 (4), 2430 – 2442.

Keller, J. B., Kolodner, I. I., 1956. Damping of underwater explosion bubble oscillations. Journal of Applied Physics 27, 1152–1161.

Khodabandeloo, B., 2018. Modeling and charaterizing acoustic signals from cavity clouds generated by marine seismic air-gun arrays. PhD thesis, Norwegian University of Science and Technology.

King, J. R. C., 2016. Viscosity in air-gun bubble modelling. Geophysics 81 (1), T1–T9.

Kinsler, L. E., Frey, A. R., Coppens, A. B., Sanders, J. V., 1962. Fundamentals of Acoustics, 4th Edition. John Wiley & Sons, Inc., New York.

Kirkwood, J. G., Bethe, H. A., 1942. Shock and detonation waves. Report, OSRD Report 588.

Klüver, T., Tabti, H., 2015. Derivation of statistical sea-surface information from dual-sensor towed streamer data. 77th Annual Conference & Exhibition, EAGE, Extended Abstracts.

Korre, A., Imrie, C., May, F., Beaubien, S. E., Vandermeijer, V., Persoglia, S., Golmen, L., Fabriol, H., Dixon, T., 2011. Quantification techniques for potential CO_2 leakage from geological storage sites. Energy Procedia 4, 3413 – 3420.

Koschinski, S., Lüdemann, K., February 2013 2013. Development of noise mitigation measures in offshore wind farm construction. Report, Federal Agency for Nature Conservation.

Kragh, E., Laws, R., Hopperstad, J.-F., Kireev, A., 2012. Reducing the size of the seismic source with a 4C towed-marine streamer. 74th Annual Conference & Exhibition, EAGE, incorporating SPE EUROPEC, Z014.

Krauklis, P. V., Krauklis, A. P., 2008. Tube wave excitation by radial and vertical sources clamped to a borehole wall. Journal of Mathematical Sciences 148 (5), 721 – 727.

Krauklis, P. V., Molotkov, L. A., Krauklis, A. P., 2007. The tube wave generated by a point source located outside a borehole. Journal of Mathematical Sciences 142 (6), 2576 – 2588.

Krieger, J. R., Chahine, G. L., 2005. Acoustic signals of underwater explosions near surfaces. Journal of the Acoustical Society of America 118 (5), 2961 – 2974.

Kryvohuz, M., Campman, X., 2017. Source-side up-down wavefield separation using dual NFHs. 79th Annual Conference & Exhibition, EAGE, Extended Abstracts, TuA406.

Kugler, S., Bohlen, T., Bussat, S., Klein, G., 2005. Variability of Scholte-wave dispersion in shallow-water marine sediments. Journal of Environmental and Engineering Geophysics 10 (2), 203 – 218.

Kugler, S., Bohlen, T., Forbriger, T., Bussat, S., Klein, G., 2007. Scholte-wave tomography for shallow-water marine sediments. Geophysical Journal International 168, 551 – 570.

Kulkarni, A. A., Joshi, J. B., 2005. Bubble formation and bubble rise velocity in gas-liquid systems: A review. Industry and Engineering Chemistry 44, 5873 – 5931.

Landrø, M., 1992. Modelling of GI gun signatures. Geophysical Prospecting 40, 721 – 747.

Landrø, M., 2008. The effect of noise generated by previous shots on seismic reflection data. Geophysics 73 (3), Q9 – Q17.

Landrø, M., 2011. Seismic monitoring of an old underground blowout 20 years later. First Break 29, 39 – 48.

Landrø, M., 2014. A practical equation for air gun bubble time period including the effect of varying temperature. 76th Annual Conference & Exhibition, EAGE, Extended Abstracts, WeP0401.

Landrø, M., Amundsen, L., 2014a. Is it optimal to tow air guns shallow to enhance low frequencies? Geophysics 79, A13–A18.

Landrø, M., Amundsen, L., 2014b. Maximizing the ultra-low frequency output from air guns. 76th Annual Conference & Exhibition, EAGE, Extended Abstracts, TuELI209.

Landrø, M., Amundsen, L., 2018. Introduction to Exploration Geophysics with Recent Advances. Bivrost Geo.

Landrø, M., Amundsen, L., Langhammer, J., 2013. Repeatability issues of high-frequency signals emitted by air-gun arrays. Geophysics 78 (6), P19 – P27.

Landrø, M., Haavik, K. E., Amundsen, L., 2014. Using geophone components to obtain ultralow frequency seismic signals at long offsets. 84th Annual International Meeting, SEG, Expanded Abstracts, 233–237.

Landrø, M., Hansteen, F., Amundsen, L., 2017. Detecting gas leakage using high-frequency signals generated by air-gun arrays. Geophysics 82 (2), A7 – A12.

Landrø, M., Haugen, R., Sodal, A., Nielsen, E., Vaage, S., 1989. Study of marine seismic noise recorded by M/V Bernier July/August 1988. Report, SERES.

Landrø, M., Sollie, R., 1992. Source signature determination by inversion. Geophysics 57 (12), 1633 – 1640.

Landrø, M., Zaalberg-Metselaar, G., Owren, B., Vaage, S., 1993. Modeling of water-gun signatures. Geophysics 58 (1), 101–109.

Langhammer, J., 1994. Experimental studies of energy loss mechanisms in air gun bubble dynamics. PhD thesis, Norwegian University of Science and Technology.

Langhammer, J., Landrø, M., 1993a. Experimental study of viscosity effects on air-gun signatures. Geophysics 58 (12), 1801–1808.

Langhammer, J., Landrø, M., 1993b. Temperature effects on airgun signature. Geophysical Prospecting 41, 737–750.

Langhammer, J., Landrø, M., 1996. High-speed photography of the bubble generated by an airgun. Geophysical Prospecting 44, 153–173.

Laws, R., 2012. Cetacean hearing-damage zones around a seismic source. Springer, New York, book section The Effects of Noise on Aquatic Life, pp. 473 – 476.

Laws, R., 2013. Modifying the seismic source array spectrum to reduce the risk of injury to marine mammals. 75th Annual Conference & Exhibition, EAGE, incorparating SPE EUROPEC, Th1615.

Laws, R., Hatton, L., Haartsen, M., 1990. Computer modelling of clustered airguns. First Break 8 (9), 331 – 338.

Lee, K. M., Hinojosa, K. T., Wochner, M. S., Argo IV, T. F., Wilson, P. S., Mercier, R. S., 2010. Attenuation of low-frequency underwater sound using bubble resonance phenomena and acoustic impedance mismatching. Proceedings of Meetings on Acoustics 11, 1 – 17.

Lee, K. M., Wochner, M. S., Wilson, P. S., 2012. Mitigation of low-frequency underwater anthropogenic noise using stationary encapsulated gas bubbles. Proceedings of Meetings on Acoustics 17, 1–9.

LeVeque, R. J., 2007. Finite Difference Methods for Ordinary and Partial Differential Equations. Siam.

L'Heureux, J. S., Long, M., 2016. Correlations between shear wave velocity and geotechnical parameters in Norwegian clays. Proceedings of the 17th Nordic Geotechnical Meeting.

L'Heureux, J. S., Long, M., Vanneste, M., Sauvin, G., Hansen, L., Polom, U., Lecomte, I., Dehls, J., Janbu, N., 2013. On the prediction of settlement from high-resolution shear-wave reflection seismic data: The Trondheim harbour case study, mid Norway. Engineering Geology 167, 72 – 83.

Li, B., Bayly, M., 2017. Quantitative analysis on the environmental impact benefits from the bandwidth-controlled marine seismic source technology. Acoustics 2017 Perth, 1 – 10.

Li, G.-F., Cao, M.-Q., Chen, H.-L., Ni, C.-Z., 2010. Modeling air gun signatures in marine seismic exploration considering multiple physical factors. Applied Geophysics 7 (2), 158 – 165.

Li, J., Wang, S., Tao, Y., Dong, C., Tang, G., 2017a. A novel expression of the spherical-wave reflection coefficient at a plane interface. Geophysical Journal International 211, 700 – 717.

Li, J., Wang, S., Wang, J., Dong, C., Yuan, S., 2017b. Frequency-dependent spherical-wave reflection in acoustic media: Analysis and inversion. Pure and Applied Geophysics 174, 1759 – 1778.

Long, M., Donohue, S., 2007. In situ shear wave velocity from multichannel analysis of surface waves (MASW) tests at eight Norwegian research sites. Canadian Geotechnical Journal 44 (5), 533 – 544.

Longuet-Higgins, M. S., 1983. Bubble, breaking waves and hyperbolc jets at the free surface. Journal of Fluid Mechanics 127, 103 – 121.

Loveridge, M. M., 1984. A study of the marine ghost. 46th Annual Meeting of the European Association of Exploration Geophysicists, London.

Loveridge, M. M., 1985. Marine seismic source signatures, directivity and the ghost. PhD thesis, University of Oxford.

Lu, N. Q., Oguz, H. N., Prosperetti, A., 1989. The oscillations of a small floating bubble. Physics of Fluids A: Fluid Dynamics 1, 252 – 260.

Lubard, S. C., Hurdle, P. M., 1976. Experimental investigation of acoustic transmission from air into a rough ocean. Journal of the Acoustical Society of America 60 (5), 1048 – 1052.

Lucke, K., Lepper, P. A., Blanchet, M.-A., Siebert, U., 2011. The use of an air bubble curtain to reduce the received sound levels for harbor porpoises (phocoena phocoena). Journal of the Acoustical Society of America 130, 3406 – 3412.

Lugg, R., 1979. Developments in Geophysical Exploration. Vol. 1. Applied Science Publishers, book section Marine Seismic Sources, pp. 143 – 203.

Lugg, R. D., Brummitt, J. G., 1986. The P400 watergun source in the quest for improved resolution at all depths. Geophysical Prospecting 34, 665 – 685.

Lynn, W., Doyle, M., Larner, K., Marschall, R., 1987. Experimental investigation of interference from other seismic crews. Geophysics 52 (11), 1501 – 1524.

Marzetta, T. L., Schoenberg, M., 1985. Tube waves in cased boreholes. 55th Annual International Meeting, SEG, Expanded Abstract, 34 – 36.

Matter, J. M., Stute, M., Snæbjörnsdottir, S. Ó., Oelkers, E. H., Gislason, S. R., Aradottir, E. S., Sigfusson, B., Gunnarsson, I., Sigurdardottir, H., Gunnlaugsson, E., Axelsson, G., Alfredsson, H. A., Wolff-Boenisch, D., Mesfin, K., Fernandez de la Reguera Taya, D., Hall, J., Dideriksen, K., Broecker, W. S., 2016. Rapid carbon mineralization for permanent disposal of anthropogenic carbon dioxide emissions. Science 352 (6291), 1312 – 1314.

Mattson, A., 2010. OGP, E&P Sound and Marine Life, JIP, Svein Vaage Broadband Airgun Study. Report, PGS.

Mavko, G., Mukerji, T., Dvorkin, J., 1998. The Rock Physics Handbook. Cambridge University Press.

Mayhan, J. D., Weglein, A. B., 2013. First application of Greens theorem-derived source and receiver deghosting on deep-water Gulf of Mexico synthetic (SEAM) and field data. Geophysics 78 (2), WA77 – WA89.

Mayne, H. W., Quay, R. G., 1971. Seismic signatures of large air guns. Geophysics 36 (6), 1162 – 1173.

McDonald, B. E., Calvo, D. C., 2007. Enhanced sound transmission from water to air at low frequencies (L). Journal of the Acoustical Society of America 122 (6), 3159 – 3161.

Medwin, H., 1977. Acoustical determinations of bubble-size spectra. Journal of the Acoustical Society of America 62 (4), 1041 – 1044.

Medwin, H., 1997. Fundamentals of acoustical oceanography. Academic press.

Meier, M. A., Duren, R. E., Lewallen, K. T., Otero, J., Heiney, S., Murray, T., 2015. A marine dipole source for low frequency seismic acquisition. 85th Annual International Meeting, SEG, Expanded Abstracts, 176–180.

Meredith, J. A., 1990. Numerical and analytical modelling of downhole seismic sources: The near and far field. PhD thesis, Massachusetts Institute of Technology.

Meredith, J. A., Cheng, C. H., Toksöz, M. N., 1993. Secondary shear waves from source boreholes. Geophysical Prospecting 41 (3), 287 – 312.

Michelson, I., 1970. The science of fluids. Van Nostrand Reinhold Company.

Mindlin, R. D., 1949. Compliance of elastic bodies in contact. Journal of Applied Mechanics 16, 259–268.

Minnaert, M., 1933. On musical air bubbles and the sound of running water. The London, Edinburgh and Dublin Philosophical Magazine and Journal of Science 16 (104), 235 – 248.

Mitchell, J. K., ASCE, F., Solymar, V., 1984. Time-dependent strength gain in freshly deposited or densified sand. Journal of Geotechnical Engineering 110 (11), 1559 – 1576.

Moldoveanu, N., 2000. Vertical source array in marine seismic exploration. 70th Annual International Meeting, SEG, Expanded Abstracts, 53–56.

Mordret, A., Shapiro, N. M., Singh, S., 2014. Seismic noise-based time-lapse monitoring of the Valhall overburden. Geophysical Research Letters 41 (14), 4945 – 4952.

Morrison, F. A., 2013. An Introduction to Fluid Mechanics. Cambridge University Press.

Mosher, D. C., Simpkin, P. G., 1999. Environmental marine geoscience 1. status and trends in marine high-resolution seismic reflection profiling: Data acquisition. Geoscience Canada 26 (4), 174 – 188.

Mougenot, J.-M., Griswold, S., Jenkerson, M., Abma, R., 2015. Next-generation marine seismic sources: A report from the SEG 2015 postconvention workshop. The Leading Edge 36 (7), 598 – 603.

Müller, C., Milkereit, B., Bohlen, T., Theilen, F., 2002. Towards high-resolution 3D marine seismic surveying using Boomer sources. Geophysical Prospecting 50 (5), 517 – 526.

Mutschlecner, J. P., Whitaker, R. W., 2005. Infrasound from earthquakes. Journal of Geophysical Research 110 (D1), D01108.

Nigmatulin, R. I., Khabeev, N. S., Nagiev, F. B., 1981. Dynamics, heat and mass transfer of vapour-gas bubles in a liquid. International Journal of Heat and Mass Transfer 24 (6), 1033 – 1044.

Nooner, S. L., Eiken, O., Hermanrud, C., Sasagawa, G. S., Stenvold, T., Zumberge, M. A., 2007. Constraints on the in situ density of CO_2 within the Utsira formation from time-lapse seafloor gravity measurements. International Journal of Greenhouse Gas Control 1 (2), 198 – 214.

Norris, A. N., 1990. The speed of a tube wave. Journal of the Acoustical Society of America 87 (1), 414 – 417.

Nowacek, D. P., Clark, C. W., Mann, D., Miller, P. J., Rosenbaum, H. C., Golden, J. S., Jasny, M., Kraska, J., Southall, B. L., 2015. Marine seismic surveys and ocean noise:time for coordinated and prudent planning. Frontiers in Ecology and the Envrionment 13 (7), 378 – 386.

Nowacek, D. P., Thorne, L. H., Johnston, D. W., Tyack, P. L., 2007. Responses of cetaceans to anthropogenic noise. Mammal Review 37 (2), 81 – 115.

Nur, A. M., Mavko, G., Dvorkin, J., Gal, D., 1995. Critical porosity: The key to relating physical properties to porosity in rocks. 65th Annual International Meeting, SEG, Expanded Abstracts.

Nyborg, W. L., Scott, A. F., Ayres, F. D., 1972. Tensile strength and surface tension of liquids, in American Institute of Physics Handbook, 3rd Edition. McGraw-Hill Book Company, New York.

Ogilvy, J. A., 1987. Wave scattering from rough surfaces. Reports on Progress in Physics 50 (12), 1553 – 1608.

Oguz, H. N., Prosperetti, A., 1990. Bubble oscillations in the vicinity of a nearly plane free surface. Journal of the Acoustical Society of America 87 (5), 2085 – 2092.

Orange, A., Key, K., Constable, S., 2009. The feasibility of reservoir monitoring using time-lapse marine CSEM. Geophysics 74 (2), F21 – F29.

Overton, W. C. J., 1957. Shear modulus acoustic well logging. U.S. Patent 2,784,796 (to ExxonMobil Oil Corporation).

Ozasa, H., Mikada, H., Sato, F., Murakami, F., Takekawa, J., Asakawa, E., 2015. Development of hydraulic low frequency marine seismic vibrator. The 19th International Symposium on Recent Advances in Exploration Geophysics (RAEG 2015).

Parkes, G., Hatton, L., 1986. The Marine Seismic Source. Springer.

Parkes, G., Ziolkowski, A., Hatton, L., Haugland, T., 1984. The signature of an air gun array: Computation from near-field measurements including interactions - practical considerations. Geophysics 48 (2), 105–111.

Pavlenko, O., Irikura, K., 2002. Changes in shear moduli of liquefied and nonliquefied soils during the 1995 Kobe earthquake and its aftershocks at three vertical-array sites. Bulletin of the Seismological Society of America 92 (5), 1952 – 1969.

Pearson, A., Cox, E., Blake, J. R., Otto, S. R., 2004. Bubble interactions near a free surface. Engineering Analysis with Boundary Elements 28, 295 – 313.

Pedersen, E., Sørensen, A. J., 2001. Modelling and control of towed marine seismic streamer cables. IFAC Proceedings 34 (7), 89 – 94.

Peng, C., Lee, J. M., Toksöz, M. N., 1996. Pressure in a fluid-filled borehole caused by a seismic source in stratified media. Geophysics 61 (1), 43 – 55.

Périnet, N., Juric, D., Tuckerman, L. S., 2009. Numerical simulation of Faraday waves. Journal of Fluid Mechanics 635, 1 – 26.

Périnet, N., Juric, D., Tuckerman, L. S., 2012. Alternating hexagonal and striped patterns in Faraday surface waves. Physical Review Letters 109 (16), 164501–1 – 164501–5.

Petersen, C. J., Bünz, S., Hustoft, S., Mienert, J., Klaeschen, D., 2010. High-resolution P-cable 3D seismic imaging of gas chimney structures in gas hydrated sediments of an arctic sediment drift. Marine and Petroleum Geology 27, 1981 – 1994.

PGS, 2018. Nucleus.
URL `https://www.pgs.com/marine-acquisition/tools-and-techniques/acquisition-solutions/technology/nucleus/`

Planke, S., Berndt, C., 2002. Apparatus for seismic measurements. U.S. Patent 7,221,620. 22 (to P-Cable 3d Seismic As).

Planke, S., Eriksen, F. N., Berndt, C., Mienert, J., Masson, D., 2009. P-cable high-resolution seismic. Oceanography 22 (1), 85.

Plesset, M. S., Prosperetti, A., 1977. Bubble dynamics and cavitation. Annual Review of Fluid Mechanics 9, 145 – 185.

Plesset, M. S., Zwick, S. A., 1952. A nonsteady heat diffusion problem with spherical symmetry. Journal of Applied Physics 23 (1), 95 – 98.

Pool, R., Kanu, C., Brenders, A., Dellinger, J., 2018. The Wolfspar field trial: Design & execution of a low-frequency seismic survey in the Gulf of Mexico. 88th Annual International Meeting, SEG, Expanded Abstracts, 91 – 96.

Popper, A. N., 2005. Effects of exposure to seismic airgun use on hearing of three fish species. Journal of the Acoustical Society of America 117 (6), 3958 – 3971.

Pramik, B., Bell, M. L., Grier, A., Lindsay, A., 2015. Field testing the Aquavib: an alternate marine seismic source. 85th Annual International Meeting, SEG, Expanded Abstracts, 181–185.

Racca, R., Bröker, K., 2018. Monitoring and mitigation of sound exposure from seismic surveys for a feeding whale population. First Break 36 (11), 71 – 76.

Rafiee, R., 2013. Experimental and theoretical investigations on the failure of filament wound GRP pipes. Composites: Part B 45, 257 – 267.

Rayleigh, O. M., 1917. On the pressure developed in a liquid during the collapse of a spherical cavity. Philosophical Magazine Series 6 34 (200), 94 – 98.

Renard, V., Avedik, F., Combe, R., 1974. Simplon water gun, a new implosion type seismic source. Ocean Technology Conference, 773 – 777.

Reynolds, O., 1883. An experimental investigation of the circumstances which determine whether the motion of water shall be direct or sinuous, and of the law of resistance in parallel channels. Report, Proceedings of the Royal Society of London.

Richardson, W. J., Greene jr., C. R., Malme, C. I., Thomson, D. H., 1995. Marine Mammals and Noise. New York, Academic Press.

Ringrose, P. S., 2017. Principles of sustainability and physics as a basis for the low-carbon energy transition. Petroleum Geoscience 23 (3), 287–297.

Robertsson, J. O. A., Amundsen, L., Pederson, A. S., 2016. Signal apparition for simultaneous source wavefield separation. Geophysical Journal International 206, 1301 – 1305.

Robertsson, J. O. A., Ronen, S., Singh, S., van Borselen, R., 2013. Broadband seismology in oil and gas exploration and production − introduction. Geophysics 78, WA1–WA2.

Robinson, P. B., Blake, J. R., Kodama, T., Shima, A., Tomita, Y., 2001. Interaction of cavitation bubbles with a free surface. Journal of Applied Physics 89 (12), 8225 – 8237.

Rogers, J. C. W., Szymczak, W. G., 1997. Computations of violent surface motions: comparisons with theory and experiment. Philosophical Transactions of the Royal Society of London A: Mathematical, Physical and Engineering Sciences 355 (1724), 649 – 663.

Ronen, S., Chelminski, S., 2018. A next generation seismic source with low frequency signal and low environmental impact. 80th Annual Conference and Exhibition, EAGE, Extended Abstracts, TuE07.

Ronen, S., Denny, S., Telling, R., Chelminski, S., Young, J., Darling, D., Murphy, S., 2015. Reducing ocean noise in offshore seismic surveys using low-pressure sources and swarms of motorized unmanned surface vessels. 85th Annual International Meeting, SEG, Expanded Abstracts, 4956 – 4960.

Roy, D. A., Rekos, R., Brideau, C., Lawry, T., Corrado, C., 2018. A marine vibrator to meet the joint industry project specification. 88th Annual International Meeting, SEG, Expanded Abstracts, 97 – 101.

Rucci, A., Vasco, D. W., Novali, F., 2013. Monitoring the geologic storage of carbon dioxide using multicomponent SAR interferometry. Geophysical Journal International 193, 197 – 208.

Rustemeier, J., Grießmann, T., Rolfes, R., 2012. Underwater sound mitigation of bubble curtains with different bubble size distributions. Proceedings of Meetings on Acoustics 17, 1 – 10.

Safar, M. H., 1984. On the S80 and P400 water guns: a performance comparison. First Break, 20–24.

Safar, M. H., 1985a. On the calibration of the water gun pressure signature. Geophysical Prospecting 33, 97–109.

Safar, M. H., 1985b. Single water gun far-field pressure signatures estimated from near-field measurements. Geophysics 50 (2), 257–261.

Safar, M. H., 1986. A simple method for determining the S80 water gun depth. Geophysics 51 (2), 424 – 426.

Safarov, J., Millero, F., Feistel, R., Heintz, A., Hassel, E., 2009. Thermodynamic properties of standard seawater. Ocean Science Discussions 6, 689 – 722.

Schoenberg, M., Marzetta, T. L., Aron, J., Porter, R. P., 1981. Space-time dependence of acoustic waves in a borehole. Journal of the Acoustical Society of America 70 (5), 1496 – 1507.

Schonewille, M., Vigner, A., Ryder, A., 2008. Advances in swell noise attenuation. First Break 26, 103–108.

Schostak, B., Jenkerson, M., Mougenot, J.-M., 2015. The marine vibrator joint industry project. 85th Annual International Meeting, SEG, Expanded Abstracts.

Schulze-Gattermann, R., 1972. Physical aspects of the airpulser as a seismic energy source. Geophysical Prospecting 20 (1), 155 – 192.

Smith, J. G., 1999. Amplitude and phase effects of weather noise. 69th Annual International Meeting, SEG, Expanded Abstracts, 1485 – 1488.

Soubaras, R., Lafet, Y., 2013. Variable-depth streamer acquisition: Broadband data for imaging and inversion. Geophysics 78, WA27–WA39.

Southall, B. L., Bowles, A. E., Ellison, W. T., Finneran, J. J., Gentry, R. L., Greene jr., C. R., Kastak, D., Ketten, D. R., Miller, J. H., Nachtigall, P. E., Richardson, W. J., Thomas, J. A., Tyack, P. L., 2007. Marine mammal noise exposure criteria: Initial scientific recommendations. Aquatic Mammal 33 (4).

Stevens, J. L., Day, S. M., 1986. Shear velocity logging in slow formations using the Stoneley wave. Geophysics 51, 137 – 147.

Strandenes, S., Vaage, S., 1992. Signatures from clustered airguns. First Break 10 (8), 305 –312.

Supponen, O., Kobel, P., Obreschkow, D., Farhat, M., 2015. The inner world of a collapsing bubble. Physics of Fluids 27, 091113–1 – 09113–2.

Temperley, H. N. V., Trevena, D. H., 1979. Metastable effects associated with the reflection of a pressure pulse at the free surface of water. Journal of Applied Physics 12, 1887 – 1894.

ten Kroode, F., Bergler, S., Corsten, C., de Maag, J. W., Strijbos, F., Tijhof, H., 2013. Broadband seismic data – the importance of low frequencies. Geophysics 78, WA3–WA14.

Tenghamm, R., Long, A., 2006. PGS shows off electrical marine vibrator to capture 'alternative' seismic source market. First Break 24, 33–36.

Tenghamm, R., Vaage, S., Borresen, C., 2007. A dual-sensor, towed marine streamer; its viable implementation and initial results. 77th Annual International Meeting, SEG, Expanded Abstracts, 989 – 993.

Tree, E. L., Lugg, R. D., Brummitt, J. G., 1986. Why waterguns? Geophysical Prospecting 34, 302 – 329.

Troncoso, J. H., Garcés, E., 2000. Ageing effects in the shear modulus of soils. Soil Dynamics and Earthquake Engineering 19, 595 – 601.

Tulett, J., Laws, R., 2016. Seismic airgun sources: Clarifying the loudness. SPE International Conference and Exhibition on Health, Safety, Security, Environmental and Social Responsibility, 1 – 13.

Ursenbach, C. P., Haase, A. B., 2006. AVO modeling of monochromatic spherical waves: comparison to band-limited waves. Report, CREWES.

Vaage, S., Haugland, K., Utheim, T., 1983. Signatures from single airguns. Geophysical Prospecting 21, 87 – 97.

van Gestel, J.-P., Kommedal, J. H., Barkved, O. I., Mundal, I., Barke, R., Best, K. D., 2008. Continuous seismic surveillance of Valhall field. The Leading Edge 27 (12), 1616 – 1621.

van Melle, F. A., Weatherburn, K. R., 1953. Ghost reflections caused by energy initially reflected above the level of the shot. Geophysics 18 (4), 793 – 804.

Vanorio, T., Nur, A., Ebert, Y., 2011. Rock physics analysis and time-lapse rock imaging of geochemical effects due to the injection of CO_2 into reservoir rocks. Geophysics 76 (5), O23 – O33.

Vergniolle, S., Brandeis, G., 1994. Origin of the sound generated by Strombolian explosions. Geophysical Research Letters 21 (18).

Vergniolle, S., Brandeis, G., 1996. Strombolian explosions 1. A large bubble breaking at the surface of a lava column as a source of sound. Journal of Geophysical Research 101 (B9), 20433 – 20447.

Vergniolle, S., Brandeis, G., Mareschal, J.-C., 1996. Strombolian explosions 2. Eruption dynamics determined from acoustic measurements. Journal of Geophysical Research 101 (B9), 20449 – 20466.

Vialle, S., Vanorio, T., 2011. Laboratory measurements of elastic properties of carbonate rocks during injection of reactive CO_2-saturated water. Geophysical Research Letters 38 (1), L01302.

Voloshchenko, A. P., Tarasov, S. P., 2013. Effect of anomalous transparency of a liquid-gas interface for sound waves. Acoustical physics 59 (2), 163 – 169.

Walton, K., 1987. The effective elastic moduli of a random packing of spheres. Journal of the Mechanics and Physics of Solids 35 (2), 213–226.

Wang, Q. X., Yeo, K. S., Khoo, B. C., Lam, K. Y., 1996. Strong interaction between a buoyancy bubble and a free surface. Theoretical and Computational Fluid Dynamics 8, 73 – 88.

Wang, S. P., Zhang, A. M., Liu, Y. L., Zhang, S., Cui, P., 2018. Bubble dynamics and its applications. Journal of Hydrodynamics 30 (6), 975 – 991.

Wardle, C. S., Carter, T. J., Urquhart, G. C., Johnstone, A. D. F., Ziolkowski, A., Hampson, G., Mackie, D., 2001. Effects of seismic air guns on marine fish. Continental Shelf Research 21 (8 - 10), 1005 – 1027.

Watson, L. M., Dunham, E. M., Ronen, S., 2016. Numerical modeling of seismic airguns and low-pressure sources. 76th Annual International Meeting, SEG, Expanded Abstracts, 219 – 224.

Watson, L. M., Werpers, J., Dunham, E. M., 2018. What controls the initial peak of an air gun source signature?

Wehner, D., Borges, F., Landrø, M., 2018. Using well operation noise to estimate shear modulus changes from measured tube waves - a feasibility study. EAGE, Fifth CO2 Geological Storage Workshop, FrCO204.

Wehner, D., Landrø, M., 2018. The impact of bubbly water on airgun signatures. EAGE Marine Acquisition Workshop, Oslo, WeMA09.

Wei, Z., Hall, M. A., Phillips, T. F., 2012. Geophysical benefits from an improved seismic vibrator. Geophysical Prospecting 60, 466–479.

Wentzell, R. A., Scott, H. D., Chapman, R. P., 1969. Cavitation due to shock pulses reflected from the sea surface. Journal of the Acoustical Society of America 46 (789), 789 – 794.

Weston, D. E., 1960. Underwater explosions as acoustic sources. Proceedings of the Physical Society 76 (2), 233 – 249.

White, J. E., 1965. Seismic Waves: Radiation, Transmission, and Attenuation. International Series in the Earth Sciences. McGraw-Hill Book Company, New York.

Willis, H., 1941. Underwater explosions, time interval between successive explosions. Report, Royal Naval Scientific Service.

Winkler, K. W., Liu, H. L., Johnson, D. L., 1989. Permeability and borehole Stoneley waves: Comparison between experiment and theory. Geophysics 54 (1), 66 – 75.

Wood, A. B., 1941. Textbook of Sound. G. Bell & Sons LTD, London.

Würsig, B., Greene jr., C. R., Jefferson, T. A., 2000. Development of an air bubble curtain to reduce underwater noise of percussive piling. Marine Environmental Research 49, 79 – 93.

Yan, B. P., Wang, S. X., Yuan, S. Y., Ji, Y. Z., Tao, Y. H., 2017. Frequency-dependent reflection coefficient of spherical wave in acoustic medium. 79th Annual Conference & Exhibition, EAGE, Extended Abstracts, Tu P1 10.

Yokoo, A., Iguchi, M., 2010. Using infrasound waves from eruption video to explain ground deformation preceding the eruption of Suwanosejima volcano, Japan. Journal of Volcanology and Geothermal Research 196 (3-4), 287 – 294.

Young, R. W., 1973. Sound pressure in water from a source in air and vice versa. Journal of the Acoustical Society of America 53 (6), 1708 – 1716.

Zhang, A. M., Liu, Y. L., 2015. Improved three-dimensional bubble dynamics model based on boundary element method. Journal of Computational Physics 294, 208 – 223.

Zhu, H., Chang, M.-F., ASCE, P. E., 2002. Load transfer curves along bored piles considering modulus degradation. Journal of Geotechnical and Geoenvironmental Engineering 128 (9), 764 – 774.

Ziolkowski, A., 1970. A method for calculating the output pressure waveform from an air gun. Geophysical Journal of the Royal Astronomical Society 21, 137–161.

Ziolkowski, A., 1982. An air gun model which includes heat transfer and bubble interactions. 52nd Annual International Meeting, SEG, Expanded Abstracts, 187 – 189.

Ziolkowski, A., Parkes, G., Hatton, L., Haugland, T., 1982. The signature of an air gun array: Computation from near-field measurements including interactions. Geophysics 47 (10), 1413–1421.